Assist. Prof. Dr. Yelda TURKAN
Oregon State University,
USA

Dr. G. Sanka N. PERERA
Sabaragamuwa University Faculty of Geomatics
Sri Lanka

Dr. Hsiu-Wen CHANG
National Cheng Kung University, Department of Geomatics
Taiwan

The International Journal of Engineering and Geosciences (IJEG)

The International Journal of Engineering and Geosciences (IJEG) is a tri-annually published journal. The journal includes a wide scope of information on scientific and technical advances in the geomatics sciences. The International Journal of Engineering and Geosciences aims to publish pure and applied research in geomatics engineering and technologies. IJEG is a double peer-reviewed (blind) OPEN ACCESS JOURNAL that publishes professional level research articles and subject reviews exclusively in English. It allows authors to submit articles online and track his or her progress via its web interface. All manuscripts will undergo a refereeing process; acceptance for publication is based on at least two positive reviews. The journal publishes research and review papers, professional communication, and technical notes. IJEG does not charge for any article submissions or for processing.

CONTENTS
Volume 8 - Issue 3

RESEARCH ARTICLES

A benchmark dataset for deep learning-based airplane detection: HRPlanes

Tolga Bakirman *1 [ID], **Elif Sertel** 2 [ID]

1Yildiz Technical University, Geomatics Engineering Department, Türkiye
2Istanbul Technical University, Geomatics Engineering Department, Türkiye

Abstract

Airplane detection from satellite imagery is a challenging task due to the complex backgrounds in the images and differences in data acquisition conditions caused by the sensor geometry and atmospheric effects. Deep learning methods provide reliable and accurate solutions for automatic detection of airplanes; however, huge amount of training data is required to obtain promising results. In this study, we create a novel airplane detection dataset called High Resolution Planes (HRPlanes) by using images from Google Earth (GE) and labeling the bounding box of each plane on the images. HRPlanes include GE images of several different airports across the world to represent a variety of landscape, seasonal and satellite geometry conditions obtained from different satellites. We evaluated our dataset with two widely used object detection methods namely YOLOv4 and Faster R-CNN. Our preliminary results show that the proposed dataset can be a valuable data source and benchmark data set for future applications. Moreover, proposed architectures and results of this study could be used for transfer learning of different datasets and models for airplane detection.

1. Introduction

The rapid technological advancements in remote sensing systems have significantly improved [1] the availability of very high-resolution remote sensing imagery [2] to be used for the detection of geospatial objects such as airplanes, ships, buildings, etc. [3]. Airplane detection is essential in various fields such as airport surveillance [4], transportation activity analysis [5], defence and military applications and satellite imagery is a significant data source for this purpose with the advantages of covering large areas very quickly and periodically [6].

Airplane detection studies from earlier years are generally based on template matching and machine learning. For example, Liu et al. [7] and Xu and Duan [8] have utilized deformable templates for airplane detection. Although this method is flexible and outperforms rigid shape matching, it still needs various types of information for template design [9]. Compared to template matching, machine learning methods have

been used more widely for this purpose. Various feature extraction methods and classifiers are investigated in the literature. Sun et al. [10] utilized a spatial sparse coding bag of words (BOW) model combined with a linear support vector machine. This model uses sliding windows to extract features and employs a spatial mapping strategy to encode geometric information. Zhang et al. [11] proposed a rotation invariant histogram of oriented gradient (HOG) features for the detection of complex objects in high resolution imagery. They also improve their method further by using a generic discriminative part-based model later on [12]. Lei et al. [13] proposed a novel color-enhanced rotation-invariant Hough Forest to train a Pose-Estimation-based Rotation-invariant Texton Forest. Liu and Shi [14] investigated the airplane feature possessing rotation invariant that combined with sparse coding and radial gradient transform. Machine learning methods require manually extracted features and thus, their performance is heavily depending on selecting accurate hand-crafted features

---

* Corresponding Author

*(bakirman@yildiz.edu.tr) ORCID ID 0000-0001-7828-9666
(sertele@itu.edu.tr) ORCID ID 0000-0003-4854-494X

[15]. Deep learning approaches offer end-to-end solutions using automatic feature extraction.

Recent studies illustrate that deep learning-based airplane detection methods not only outperform conventional object detection algorithms but also provide feasible solutions. Chen et al. [16] combined classification and localization processes for better optimization using transfer learning. Xu et al. [17] proposed a multilayer feature fusion process that fuses the shallow and deep layer features in fully convolutional neural networks (FCN). Zhu et al. [18] utilized the L2 norm normalization, feature connection, scale scaling, and feature dimension reduction for more efficient fusion of low- and high-level features. Alganci et al. [6] assessed different deep learning approaches namely Faster Regional Convolutional Neural Network (Faster R-CNN), Single Shot Multi-box Detector (SSD) and You Only Look Once Version 3 (YOLOv3) for airplane detection from very high resolution satellite imagery. Wu et al. [19] proposed Weakly Supervised Learning in AlexNet which requires only image-level labelled data contrary to other object detection methods. Zhou et al. [20] introduced Multiscale Detection Network to detect small-scale aircrafts in a multiscale detection architecture manner. Ji et al. [21] developed a Faster R-CNN based model that combines multi-angle features driven and majority voting strategy. Shi et al. [22] introduced Deconvolution operation with a Position Attention mechanism (DPANet) that captures the external structural feature representation of aircraft during the feature map generation process. Wu et al. [23] proposed a self-calibrated Mask R-CNN model that performs perform object recognition and segmentation in parallel. Zeng et al. [24] utilize a top-down approach for aircraft detection in large scenes. Once the airport area is extracted with U-Net, Faster-RCNN with a feature enhancement module is applied for target detection. Chen et al. [25] have proposed two-stage aircraft detection network. The first stage creates region proposals using a circular intensity filter and the second stage detects targets by using a combination of rotation-invariant histogram of oriented gradient and vector of locally aggregated descriptors.

In order to train deep neural networks, huge amounts of images and corresponding labels are needed. Researchers have proposed datasets including airplanes for this purpose. Xia et al. [26] introduced the DOTA dataset with 15 classes including airplanes using imagery from Google Earth, Jilin-1 and Gaofen-2 satellites. This dataset has been then expanded, improved, and renamed as the iSAID dataset [27]. Lam et al. [28] utilized multi-source imagery to generate the xView dataset which has passenger/cargo planes and 59 other classes. More recently, Shermeyer et al. [29] took the advantage of synthetic data to create RarePlanes dataset. The dataset consists of 253 WorldView-3 real and 50,000 synthetic imageries, and corresponding 14,700 hand-annotated and 630,000 simulated plane labels, respectively.

In this study, we create a huge novel dataset solely for airplanes from very high-resolution Google Earth imagery using only hand-annotated labels. Our dataset, HRPlanes, includes images obtained from the biggest airports across the world to represent a variety of landscape, seasonal, and data acquisition geometry

conditions. We also evaluate our dataset using state-of-the-art deep neural networks namely YOLOv4 and Faster R-CNN to analyze the performance of two different object detection algorithms.

2. Dataset

The imagery required for the dataset has been obtained from Google Earth. We have downloaded 4800 x 2703 sized 3092 RGB images from the biggest airports of the world such as Paris-Charles de Gaulle, John F. Kennedy, Frankfurt, Istanbul, Madrid, Dallas, Las Vegas and Amsterdam Airports, and aircraft boneyards like Davis-Monthan Air Force Base.

Dataset images were annotated manually by creating bounding boxes for each airplane using HyperLabel software [30]. Quality control of each label was conducted by visual inspection of independent analysts who were not included in the labelling procedure. A total of 18,477 airplanes have been labelled. A sample image and corresponding minimum boxes for airplanes can be seen in Figure 1.

The dataset has been approximately split as 70% (2166 images), 20% (615 images) and 10% (311 images) for training, validation and testing, respectively.
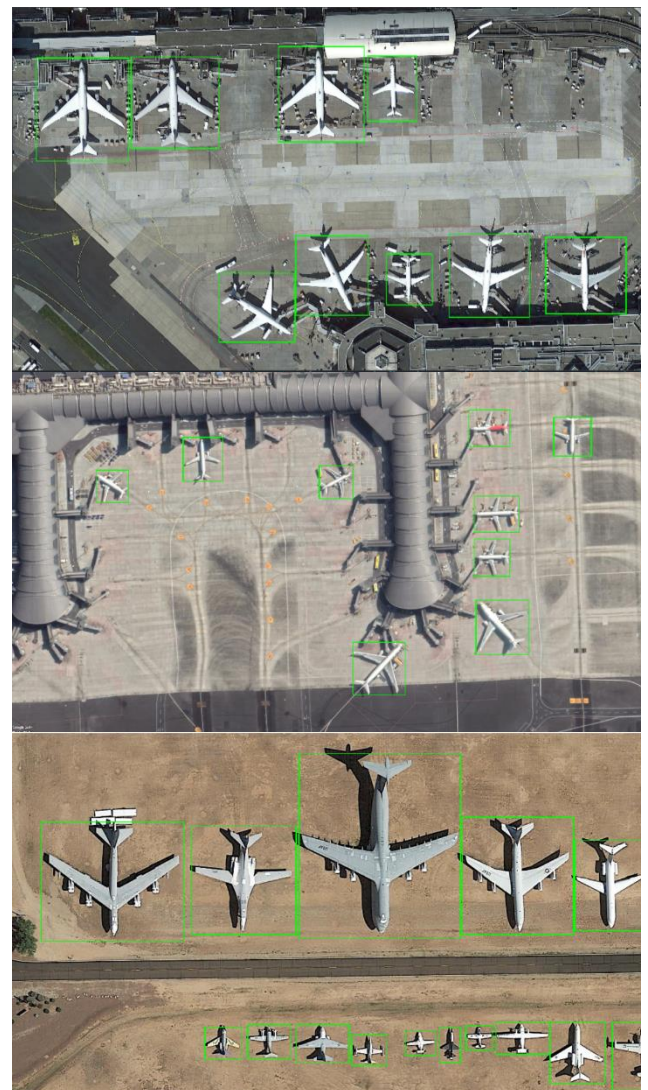
Figure 1. Sample images from the HRPlanes dataset

3. Methods

The proposed dataset has been evaluated using state-of-the-art YOLOv4 and Faster R-CNN methods. Both methods have been widely utilized in various object detection applications in the literature.

3.1. YOLOv4

The first version of YOLO is proposed by [31], which is highlighted to be extremely fast. The network which runs on Darknet framework is a global model since it uses features from the whole image to predict bounding boxes. Therefore, the model is able to learn general representations of the objects. The input image is divided by an S x S grid. The grid that covers the center of an object is responsible for detecting the object. The bounding boxes are predicted with a confidence score which is calculated by: $Pr(object) \times IoU_{GT}$. YOLO has a GoogLeNet [32] based architecture which has 24 convolutional and 2 fully connected layers. The network does not utilize the inception module, instead it uses a 1 x 1 reduction layer with a 3 x 3 convolutional layer. While the linear activation function is used in the final layer, leaky rectified linear activation is exploited in all other layers. Even though YOLO is fast and sensitive to false positives, it still has problems with localization and recall.

YOLOv2 [33] aims to improve the shortcomings of the first version of YOLO by simplifying the network with better representations. The first modification is adding batch normalization which also allows to removing dropouts from the model. YOLOv2's classification network is trained on 448 x 448 resolution, instead of 224 x 224. The network is then shrunk to 416 x 416 in order to obtain locations in the feature map as an odd number. The fully connected layers are removed in YOLOv2 and anchor boxes are added using dimension clusters to predict bounding boxes. Anchor boxes require manually determined box dimensions. To overcome this problem, k-means clustering is used to determine the bounding box priors. Even though the use of anchor boxes results in slight decrease in accuracy, an intermediate increase is obtained in the recall. The most significant improvement in YOLOv2 is the new backbone. Instead of using GoogLeNet based architecture, Darknet-19 is proposed which consists of 19 convolutional and 5 maximum pooling layers.

YOLOv3 [34] uses logistic regression to calculate the objectness score for each predicted bounding box. The bounding boxes are predicted at three different scales by extracting features in all scales using a modified feature pyramid network [35]. In order to extract more semantic information, features from the earlier layers of the network are concatenated with up-sampled features from layers at the later stages. The feature extraction network Darknet-19 is more extended with 3 x 3 and 1 x 1 convolutional layers and skip connections. The improved version has 53 convolutional layers and is referred as Darknet-53. Although YOLOv3 performs better with small objects compared to older YOLO versions, this is not the case for medium and large objects.

YOLOv4 [36] aims to reach the optimum balance between resolution, layers and parameters in order to obtain accurate results rapidly. The Darknet-53 backbone network is improved with Cross Stage Partial (CSP) module [37] which is called CSPDarknet-53 which contains 29 convolutional layers 3 × 3, a 725 × 725 receptive field and 27.6 M parameters. With high number of convolutional layers, a larger receptive field allows the network to obtain a better detector. In this scenario, the feature map of the base layer is partitioned and merged using a cross-stage hierarchy which provides more gradient flow. Additionally, Spatial pyramid pooling (SPP) [38] is integrated into the backbone of the network (CSPDarknet53 with Mish activation) in order to increase the receptive field even further. This helps to extract the main characteristic features without slowing the network. Path aggregation network (PANet) with Leaky activation is used for feature extraction instead of the FPN used in YOLOv3. Additionally, some CNN components have been integrated into the backbone and detector in order to improve the network further such as dropblock regularization, cross mini-batch normalization, CutMix and Mosaic data augmentation [36]. Whilst the authors select optimal hyper-parameters while applying genetic algorithms, they also provide some additional improvements to the network such as Self-Adversarial Training (SAT), modified spatial attention module, modified PAN, and Cross mini-Batch Normalization (CmBN). SAT is a data augmentation technique that consists of two forward-backward stages. In this way, the original image is altered to create the deception. Then, the network is trained using the modified images. SAM is modified by switching from spatial-wise attention to pointwise attention and the shortcut connection of PAN is replaced with concatenation. CmBN is a modified version of Cross-Iteration Batch Normalization that gathers information in mini-batches within a single batch.

3.2. Faster R-CNN

Regions with CNN features (R-CNN) [39] combines region proposal with high-capacity CNNs that allows for bottom-up region proposals for better localization and performance. R-CNN consists of three parts. The first part creates region proposals using selective search which are not dependent on the class. The first part of the network creates around 2000 region proposals. The second part performs feature extraction using Caffe [40] with shared parameters for all classes. Since proposed regions can be in any size, they are dilated and warped to 227 x 227. Caffe network extracts a fixed size low-dimensional feature vector for each proposed region using five convolutional and two fully connected layers. The final part of the network scores each extracted feature vector utilizing class-specific linear SVMs. All regions with scores are then analyzed with non-maximum suppression for each class to obtain the best region proposal with the highest IoU.

Feature extraction for each region proposal rather than a whole image increases computational cost and storage space. In order to overcome drawbacks, improve speed and increase the accuracy of the multi-stage

structured R-CNN method, a single-stage Fast-RCNN method that jointly learns the classification of proposal with refined localization is proposed [41]. The Fast R-CNN network processes the whole image to create a feature map. A region of interest (RoI) pooling layer similar to SPPnet [38] takes the feature map and extracts a fixed-size feature vector using maximum pooling applied on each channel. Softmax probability estimates and bounding box positions are then produced by feeding each feature vector into a series of fully connected layers. During the training of Fast R-CNN, stochastic gradient descent mini-batches are sampled hierarchically. Computation and memory costs are shared for RoIs created in the same images during forward-backward passes. Additionally, the network jointly optimizes the classifier and the regressor in a single stage.

Faster R-CNN [42] is based on a region proposal network (RPN). The detector in the network works with the rectangular object proposals by the RPN. Object proposals are then used by Fast R-CNN for detection. RPN also shares created features with Fast R-CNN thus, it does not increase computational cost. RPN also utilizes attention mechanisms that direct the Fast R-CNN detection network where to look. The anchors are created for each location as translation invariant and multi-scale. A multi-task loss is calculated by considering log loss and regression loss. Log loss is the classification loss between classes. For a single class airplane detection network, the classification loss calculates loss over airplane versus not plane. The regression loss is calculated once the anchor contains the desired object. Note that an object will have a defined maximum number of anchors. However, the anchor with the minimum loss will be attained as detection [42].

3.3. Accuracy Metrics

The results are assessed using Microsoft COCO [43] evaluation metrics, which consist of various Average Precision (AP) and Average Recall (AR) values. In this study, we have used the first 3 evaluation metrics of Microsoft COCO to assess test results. These are namely mean average precision (mAP), mAP at 50% Intersection over Union (IoU), and mAP at 75% IoU. AP is a summarization metric derived from the precision-recall curve. It is calculated by the weighted mean of precision values for different recall threshold values varying from 0 to 1 (Equation 1):

$$AP = \sum_n (R_n - R_{n-1}) \times P_n \qquad (1)$$

True Positives (TPs) are determined by IoU thresholds. For example, an IoU threshold of 50% means that the predicted bounding box will be counted as TP once it has equal to or greater than the IoU value of 50% with the ground truth, and AP is calculated based on this assumption which is the AP at 50% IoU threshold and referred as PASCAL VOC metric [44-45]. It is the same case for the AP at the 75% IoU threshold, which is stricter. The mAP is calculated by averaging APs calculated for 10 IoU thresholds from 50% to 95% with a 0.05 increment for all classes. Since we have only one class in this study, mAP and AP values are identical.

4. Results and Discussion

Experiments were conducted in an Intel Core i9-9900K 3.6 GHz CPU and an NVIDIA GeForce RTX 2080 Ti GPU. The training process for YOLOv4 was carried out in the Darknet framework. We conducted several initial experiments to find out the best hyperparameter configuration. Our results demonstrated that increasing batch size and subdivision affect the performance positively. This is similar for input image size as well. Higher image sizes provide better performance; however, computing load also increased for bigger image sizes, which is directly limited by the GPU. After manual hyper-tuning experiments, the best configuration for our hardware was found as; the input image of 416 x 416 pixels for the network size, 64 as the batch size, and 32 for the subdivision value. The learning rate, decay and momentum were input as 0.001, 0.0005 and 0.949, respectively. Complete-IoU loss was used as the loss function. YOLOv4 allows to apply various user-defined augmentation techniques namely mosaic, cut-mix, mix-up and blur. We have applied these augmentation methods however our results show that using only mosaic augmentation improved the results considerably.

Faster R-CNN network was trained on TensorFlow Object Detection API. The input image size was 1024 x 600. Momentum optimizer were utilized with a 0.0001 learning rate. We have used the random horizontal flip method for data augmentation. Both networks were trained using pre-trained weights from the MS COCO dataset. As explained for YOLOv4 experiments, Faster R-CNN hyperparameters for training have been determined empirically. YOLOv4 training took approximately 12 hours to complete while the Faster R-CNN training process was around 10 hours.

Deep neural networks have been evaluated using the same test dataset for two different models. The evaluation results are given in Table 1. The evaluation results show that both networks perform well up to 75% IoU threshold; the mAP value of YOLOv4 is 73.02%; whereas Faster R-CNN provided slightly better performance with 76.40%. Although YOLOv4 produces very high mAP at 50% IoU value of 99.15%, this value reduces with increasing IoU values and decreses to 91.82% for mAP at 75% IoU. YOLOv4 seems superior considering 50% and 75% IoU threshold. The decrease rate of AP with increasing IoU is higher for YOLOv4 compared to Faster R-CNN. This indicates that YOLOv4 cannot perform efficiently in higher IoU threshold levels higher than 80% in our dataset.

Table 1. Evaluation results based on average precision

	YOLOv4	Faster R-CNN
mAP	73.02%	76.40%
mAP@IoU=50%	99.15%	96.80%
mAP@IoU=75%	91.82%	90.00%

We present some figures to illustrate the obtained results with two different models; where purple boxes

represent YOLOv4 and green boxes represent Faster R-CNN results. Since images are collected from different satellites, the real-world coverage of the images is different with respect to spatial resolution while represented with 4800 x 2703 pixels. For very high-resolution images, the airplanes can be seen as very big objects within the scene with respect to image patch size. We will be using the term large scale for these examples such as Figure 2a, 2b, 2c, and 2d. For high resolution images, the image patch is covering a bigger area in which we will be using the term small scale such as Figure 2e and 2f. The assessment of Figure 2 including samples from Amsterdam Schiphol Airport shows that

airplanes represented with bigger object boxes could be clearly identified with both YOLOv4 and Faster R-CNN architectures as can be seen in Figure 2a, 2b, 2c and 2d. However, boundaries of bounding boxes for YOLOv4 seem better at this scale specifically in Figure 2d compared to Faster R-CNN of Figure 2c, in which the tails of some airplanes are not included within the bounding boxes. We have a small-scale image example in Figure 2e and 2f, in which there are also airplanes of different sizes available. Faster R-CNN (Figure 2e) produces better results compared to YOLOv4 specifically for small airplanes.

Figure 2. Prediction results of Faster R-CNN (green) and YOLOv4 (purple) from Amsterdam Schipol Airport

Figure 3 shows prediction results for a small-scale imagery from Istanbul Sabiha Gokcen Airport. On the contrary to Figure 2f, YOLOv4 seems to be performing better in this example (Figure 3b). Both architectures have also detected the small propeller aircraft which is located in the upper left of the image (Figure 3a and 3b). Figure 3c and 3d present predictions for commercial planes on large scale in the same airport. In this example, YOLOv4 seems to create better bounding boxes (Figure 3c) than Faster R-CNN (Figure 3d). This may be resulted due to boarding bridges near the planes.

Our HRPlanes dataset consists of imageries from airports around different parts of the world. Some prediction results from Chengdu Shuangliu International Airport are shown in Figure 4. Both methods performed sufficiently with similar bounding boxes under clear (Figure 4a and 4b) and hazy (Figure 4c and 4d) atmospheric conditions.

Military plane samples from Davis Monthan Air Force Base are shown in Figure 5. Both prediction results seem similar for fully visible airplanes in terms of both detection and bounding boxes as can be seen on the

center part of the image patch in Figures 5a and 5b; whereas, only YOLOv4 is able to detect tails of aircrafts on the southern part of the image patch (Figure 5b). Faster R-CNN could not able to capture parts of the aircrafts in this example. In another military planes example (Figure 5c and 5d), both architectures performed well and successfully detected seven military planes within the image patch. However, in some rare cases Faster R-CNN does not seem to create accurate bounding boxes for military planes and generate bounding boxes representing almost half of the airplanes (Figure 5e). Bounding boces of four out of six airplanes are not completely generated. YOLOv4 could detect all six airplanes and generate bounding boxes for all of them for the image patch (Figure 5f).

Figure 3. Prediction results of Faster R-CNN (green) and YOLOv4 (purple) from Istanbul Sabiha Gokcen Airport
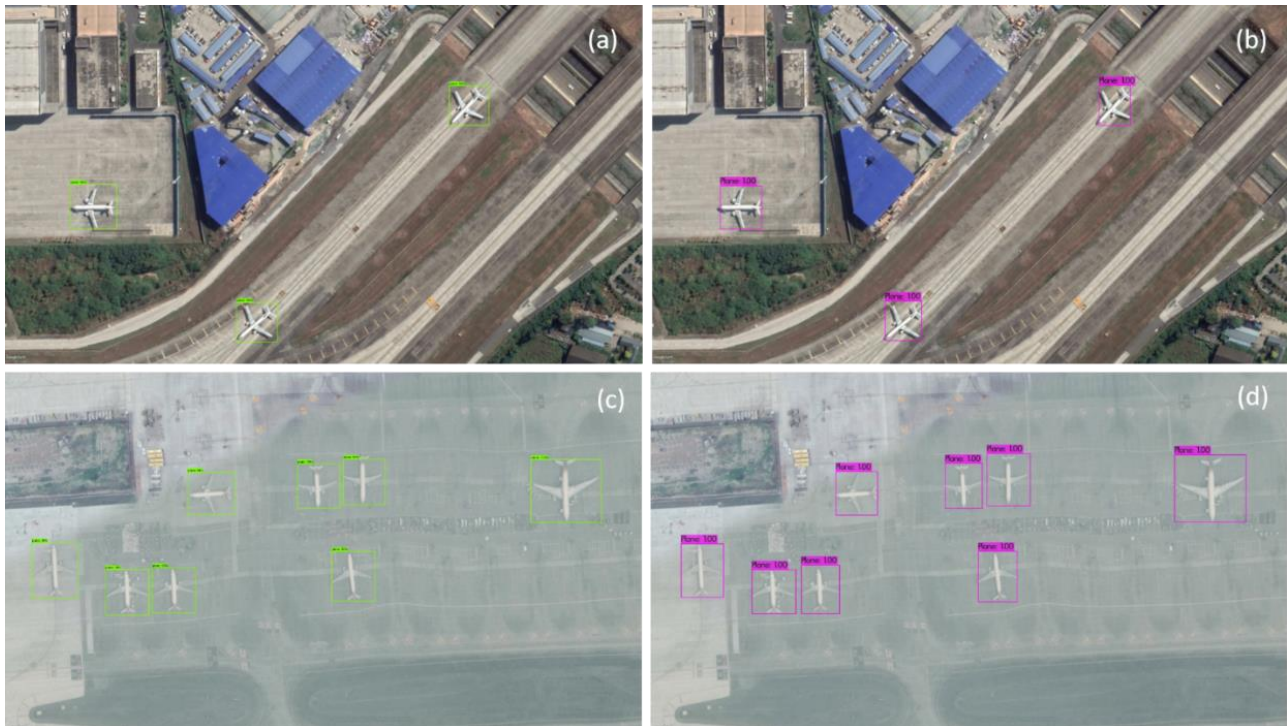
Figure 4. Prediction results of YOLOv4 (purple) and Faster R-CNN (green) from Chengdu Shuangliu International

Some small-scale examples which mostly consist of small propeller aircrafts are given in Figure 6. Faster R-CNN seems to have significantly performed better in these imageries considering YOLOv4 have created various False Positives (FP) in different parts of the image (Figure 6b, 6d, and 6f). Some FP detections have

lower confidence levels, which could be eliminated by increasing the confidence level to 0.50 such as cases in Figure 6b to improve the results of YOLOv4.

We show a plane graveyard example in Figure 7. Since the background is not complex and the planes are well aligned, both methods have performed efficiently in both examples. Even in small scale images, YOLOv4 was able to detect plane even though only their nose cones are visible which can be seen in upper right corner of Figure 7b.
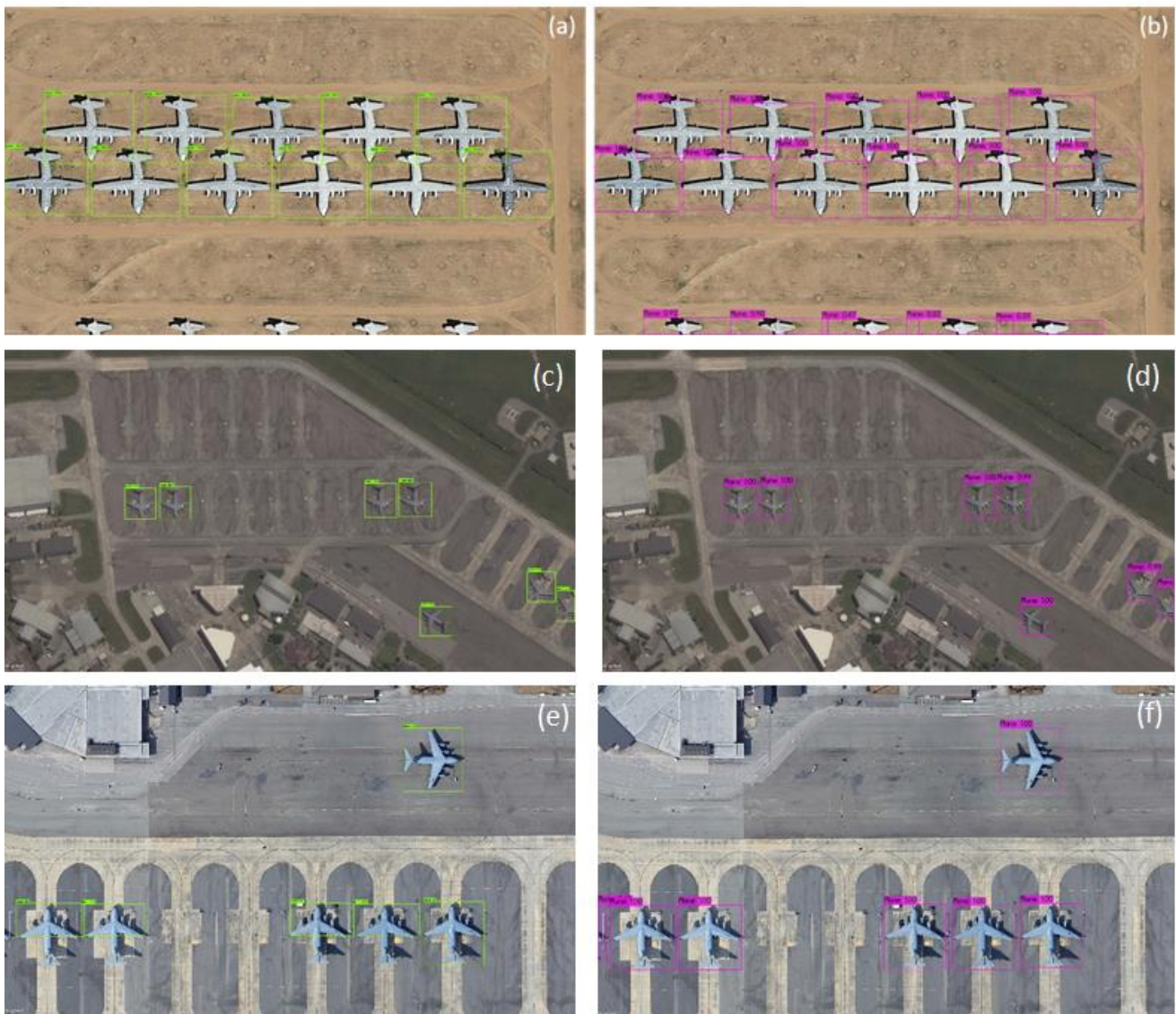
Figure 5. Prediction results of Faster R-CNN (green) and YOLOv4 (purple) from Davis Monthan for millitary planes

According to the prediction results, partly absent airplanes are generally detected by YOLOv4 (Figure 5b & Figure 7b). Only in some rare cases, Faster R-CNN is also able to detect them (Figure 8a). Additionally, it can be said that both methods can successfully identify airplanes in crowded scenes thanks to non-max suppression technique, even though Faster-RCNN has skipped one plane in Figure 8c. Both networks were even able to detect moving planes, which has a motion blur effect in the image (Figure 8e and 8f).

Compared to similar studies in the literature, our results show promising results. Chen et al. [16] have also created a plane detection dataset from Google Earth images and obtained 96.23% mAP at 50% IoU with their proposed network. Zhou et al. [20] have also used a similar dataset that consists of Google Earth and Tianditu images. They have achieved a mAP at 50% IoU value of 90.66% using the proposed deep and wider module. Ji et al. [21] trained a modified Faster R-CNN network with two datasets (RSOD and DIOR) that consist of Google Earth imagery and the calculated mAP at 50% IoU values are 94.82% and 95.25%. Shi et al. [22] have utilized DOTA and DIOR datasets with the developed DPANet and obtained mAP values of 89.95% and 66.21%, respectively. Wu et al. [23] obtained a mAP at 50% IoU value of 96.80% using an improved version of DOTA with their improved Mask R-CNN network. As can be seen from the accuracy values obtained in the other recent studies in the literature, our results are also encoraging for plane detection from high resolution imagery.
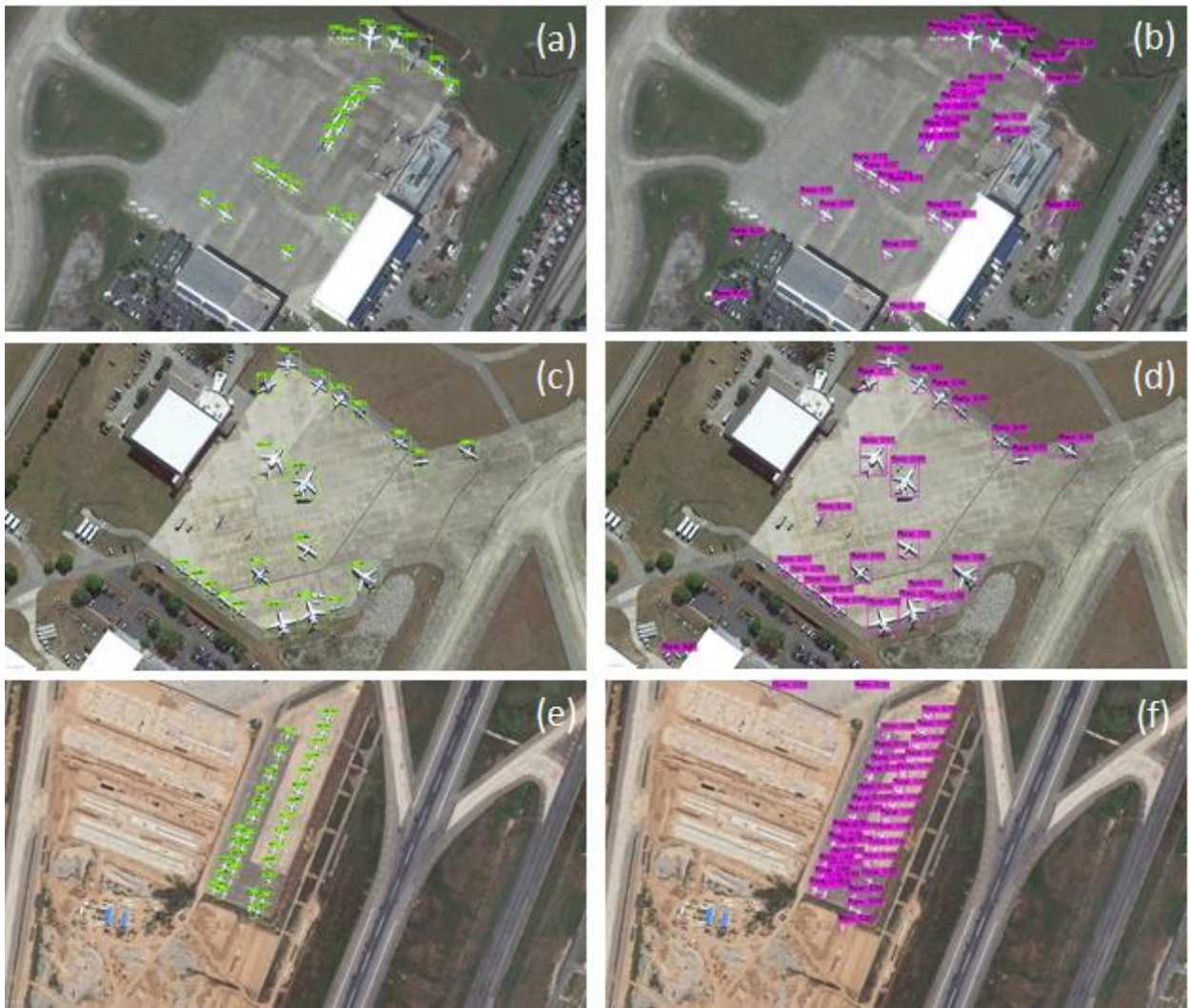
Figure 6. Prediction results of Faster R-CNN (green) and YOLOv4 (purple) from a small-scale image with small propeller aircrafts

Figure 7. Prediction results of Faster R-CNN (green) and YOLOv4 (purple) from a plane graveyard
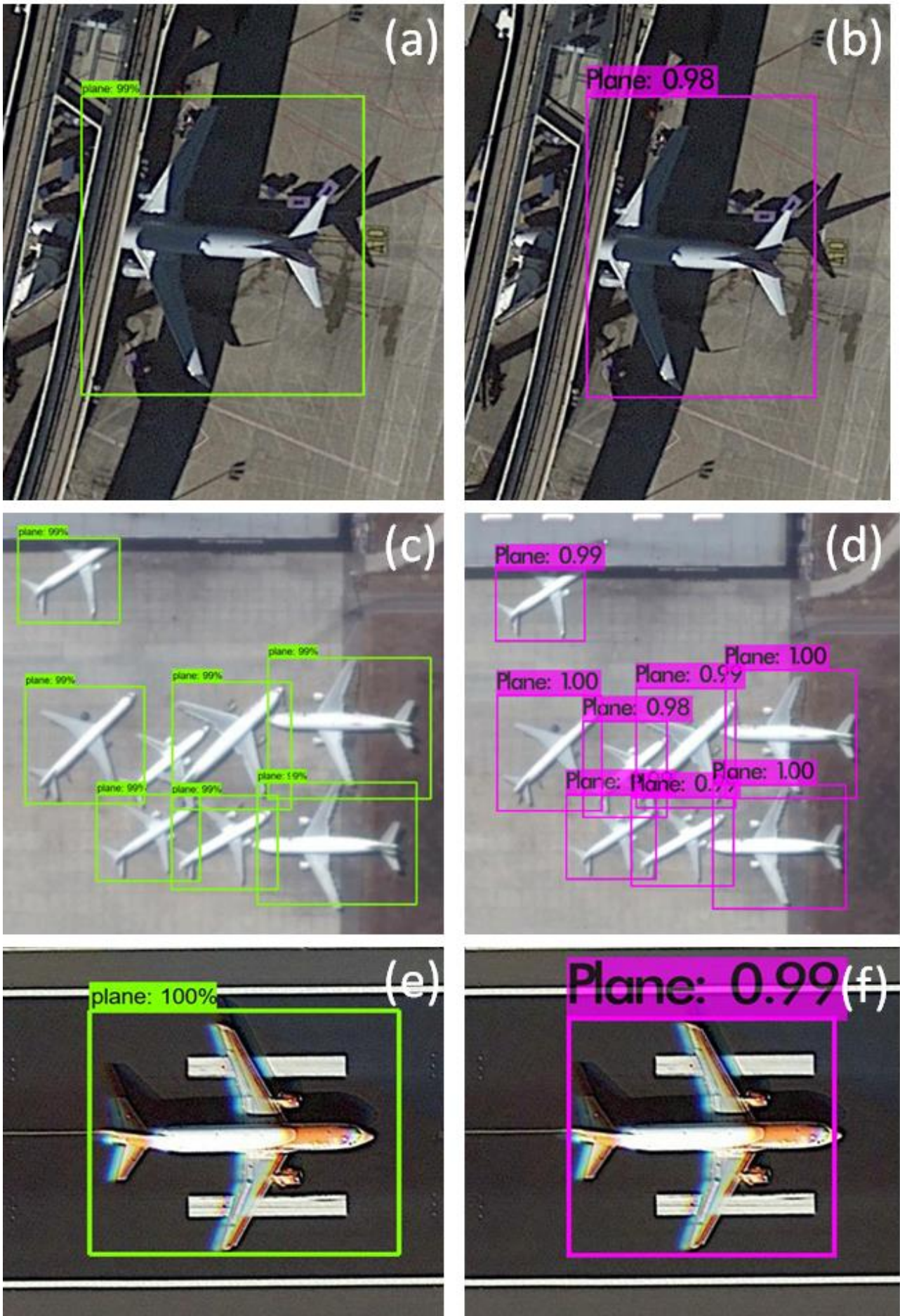
Figure 8. Visibility, density and motion blur examples

5. Conclusion

We created a novel airplane detection dataset, called HRPlanes, that includes image patches of commercial and military airplanes. We generated this new dataset to be a benchmark for deep learning-based object detection methods specifically for airplane cases. We evaluated the performance of YOLOv4 and Faster R-CNN on the created dataset with various experiments with different hyperparameters. Both models have provided satisfactory results for mAP at 75% IoU threshold above 90% which is quite high. Our results show that the dataset provides highly accurate information to train deep neural networks efficiently. Our proposed models and hyperparameter setting could be used for various remote sensing-based airplane detection tasks and our model weights could be directly used for the inference of similar datasets and transfer learning of different datasets. Moreover, our test dataset could be used by different researchers to evaluate the new model proposals. After further analysis and quality checks, it is planned to share the whole dataset publicly. Train and validation sets of the dataset are available upon request from the corresponding author. Currently, the weights of both networks and test dataset are available on: https://github.com/TolgaBkm/HRPlanes

Acknowledgement

Author contributions

Tolga Bakirman: Conceptualization, Data curation Methodology, Software, Validation, Writing-Original draft preparation **Elif Sertel:** Conceptualization, Data curation, Methodology, Software, Validation, Visualization, Investigation, Writing-Reviewing and Editing.

Conflicts of interest

The authors declare no conflicts of interest.

References

1. Kaynarca, M., Demir, N., & San, B. T. (2020). Yeraltı Suyu Kaynaklarının Uzaktan Algılama ve CBS Teknikleri Kullanarak Modellenmesine Yönelik bir Yaklaşım: Kırkgöz Havzası (Antalya). *Geomatik*, *5*(3), 241-245.

2. Efe, E., & Alganci, U. (2023). Çok zamanlı Sentinel 2 uydu görüntüleri ve makine öğrenmesi tabanlı algoritmalar ile arazi örtüsü değişiminin belirlenmesi. *Geomatik*, *8*(1), 27-34.

3. Li, K., Wan, G., Cheng, G., Meng, L., & Han, J. (2020). Object detection in optical remote sensing images: A survey and a new benchmark. *ISPRS journal of photogrammetry and remote sensing*, *159*, 296-307.

4. Körez, A. (2022). Divide and conquer object detection (DACOD) method for runway detection in remote sensing images. *International Journal of Engineering and Geosciences*, *7*(2), 154-160.

5. Biyik, M. Y., Atik, M. E., & Duran, Z. (2023). Deep learning-based vehicle detection from orthophoto and spatial accuracy analysis. *International Journal of Engineering and Geosciences*, *8*(2), 138-145.

6. Alganci, U., Soydas, M., & Sertel, E. (2020). Comparative research on deep learning approaches for airplane detection from very high-resolution satellite images. *Remote sensing*, *12*(3), 458.

7. Liu, G., Sun, X., Fu, K., & Wang, H. (2012). Aircraft recognition in high-resolution satellite images using coarse-to-fine shape prior. *IEEE Geoscience and Remote Sensing Letters*, *10*(3), 573-577.

8. Xu, C., & Duan, H. (2010). Artificial bee colony (ABC) optimized edge potential function (EPF) approach to target recognition for low-altitude aircraft. *Pattern Recognition Letters*, *31*(13), 1759-1772.

9. Cheng, G., & Han, J. (2016). A survey on object detection in optical remote sensing images. *ISPRS journal of photogrammetry and remote sensing*, *117*, 11-28.

10. Sun, H., Sun, X., Wang, H., Li, Y., & Li, X. (2011). Automatic target detection in high-resolution remote sensing images using spatial sparse coding bag-of-words model. *IEEE Geoscience and Remote Sensing Letters*, *9*(1), 109-113.

11. Zhang, W., Sun, X., Fu, K., Wang, C., & Wang, H. (2013). Object detection in high-resolution remote sensing images using rotation invariant parts based model. *IEEE Geoscience and Remote Sensing Letters*, *11*(1), 74-78.

12. Zhang, W., Sun, X., Wang, H., & Fu, K. (2015). A generic discriminative part-based model for geospatial object detection in optical remote sensing images. *ISPRS journal of photogrammetry and remote sensing*, *99*, 30-44.

13. Lei, Z., Fang, T., Huo, H., & Li, D. (2011). Rotation-invariant object detection of remotely sensed images based on texton forest and hough voting. *IEEE Transactions on Geoscience and Remote Sensing*, *50*(4), 1206-1217.

14. Liu, L., & Shi, Z. (2014). Airplane detection based on rotation invariant and sparse coding in remote sensing images. *Optik*, *125*(18), 5327-5333.

15. Ball, J. E., Anderson, D. T., & Chan, C. S. (2017). Comprehensive survey of deep learning in remote sensing: theories, tools, and challenges for the community. *Journal of applied remote sensing*, *11*(4), 042609

16. Chen, Z., Zhang, T., & Ouyang, C. (2018). End-to-end airplane detection using transfer learning in remote sensing images. *Remote Sensing*, *10*(1), 139.

17. Xu, Y., Zhu, M., Xin, P., Li, S., Qi, M., & Ma, S. (2018). Rapid airplane detection in remote sensing images based on multilayer feature fusion in fully convolutional neural networks. *Sensors*, *18*(7), 2335.

18. Zhu, M., Xu, Y., Ma, S., Li, S., Ma, H., & Han, Y. (2019). Effective airplane detection in remote sensing images based on multilayer feature fusion and improved nonmaximal suppression algorithm. *Remote Sensing*, *11*(9), 1062.

19. Wu, Z. Z., Weise, T., Wang, Y., & Wang, Y. (2020). Convolutional neural network based weakly supervised learning for aircraft detection from remote sensing image. *IEEE Access*, *8*, 158097-158106.

20. Zhou, L., Yan, H., Shan, Y., Zheng, C., Liu, Y., Zuo, X., & Qiao, B. (2021). Aircraft detection for remote sensing images based on deep convolutional neural networks. *Journal of Electrical and Computer Engineering*, *2021*, 1-16.

21. Ji, F., Ming, D., Zeng, B., Yu, J., Qing, Y., Du, T., & Zhang, X. (2021). Aircraft detection in high spatial resolution remote sensing images combining multi-angle features driven and majority voting CNN. *Remote Sensing*, *13*(11), 2207.

22. Shi, L., Tang, Z., Wang, T., Xu, X., Liu, J., & Zhang, J. (2021). Aircraft detection in remote sensing images based on deconvolution and position attention. *International Journal of Remote Sensing*, *42*(11), 4241-4260.

23. Wu, Q., Feng, D., Cao, C., Zeng, X., Feng, Z., Wu, J., & Huang, Z. (2021). Improved mask R-CNN for aircraft detection in remote sensing images. *Sensors*, *21*(8), 2618.

24. Zeng, B., Ming, D., Ji, F., Yu, J., Xu, L., Zhang, L., & Lian, X. (2022). Top-Down aircraft detection in large-scale scenes based on multi-source data and FEF-R-CNN. *International Journal of Remote Sensing*, *43*(3), 1108-1130.

25. Chen, X., Liu, J., Xu, F., Xie, Z., Zuo, Y., & Cao, L. (2022). A Novel Method of Aircraft Detection under Complex Background Based on Circular Intensity Filter and Rotation Invariant Feature. *Sensors*, *22*(1), 319.

26. Xia, G. S., Bai, X., Ding, J., Zhu, Z., Belongie, S., Luo, J., ... & Zhang, L. (2018). DOTA: A large-scale dataset for object detection in aerial images. In *Proceedings of the IEEE conference on computer vision and pattern recognition* (pp. 3974-3983).

27. Waqas Zamir, S., Arora, A., Gupta, A., Khan, S., Sun, G., Shahbaz Khan, F., ... & Bai, X. (2019). isaid: A large-scale dataset for instance segmentation in aerial images. In *Proceedings of the IEEE/CVF Conference on Computer Vision and Pattern Recognition Workshops* (pp. 28-37).

28. Lam, D., Kuzma, R., McGee, K., Dooley, S., Laielli, M., Klaric, M., ... & McCord, B. (2018). xview: Objects in context in overhead imagery. *arXiv preprint arXiv:1802.07856*.

29. Shermeyer, J., Hossler, T., Van Etten, A., Hogan, D., Lewis, R., & Kim, D. (2021). Rareplanes: Synthetic data takes flight. In *Proceedings of the IEEE/CVF Winter Conference on Applications of Computer Vision* (pp. 207-217).

30. HyperLabel. https://docs.hyperlabel.com/

31. Redmon, J., Divvala, S., Girshick, R., & Farhadi, A. (2016). You only look once: Unified, real-time object detection. In *Proceedings of the IEEE conference on computer vision and pattern recognition* (pp. 779-788).

32. Szegedy, C., Liu, W., Jia, Y., Sermanet, P., Reed, S., Anguelov, D., ... & Rabinovich, A. (2015). Going deeper with convolutions. In *Proceedings of the IEEE conference on computer vision and pattern recognition* (pp. 1-9).

33. Redmon, J., & Farhadi, A. (2017). YOLO9000: better, faster, stronger. In *Proceedings of the IEEE conference on computer vision and pattern recognition* (pp. 7263-7271).

34. Redmon, J., & Farhadi, A. (2018). Yolov3: An incremental improvement. *arXiv preprint arXiv:1804.02767*.

35. Lin, T. Y., Dollár, P., Girshick, R., He, K., Hariharan, B., & Belongie, S. (2017). Feature pyramid networks for object detection. In *Proceedings of the IEEE conference on computer vision and pattern recognition* (pp. 2117-2125).

36. Bochkovskiy, A., Wang, C. Y., & Liao, H. Y. M. (2020). Yolov4: Optimal speed and accuracy of object detection. *arXiv preprint arXiv:2004.10934*.

37. Wang, C. Y., Liao, H. Y. M., Wu, Y. H., Chen, P. Y., Hsieh, J. W., & Yeh, I. H. (2020). CSPNet: A new backbone that can enhance learning capability of CNN. In *Proceedings of the IEEE/CVF conference on computer vision and pattern recognition workshops* (pp. 390-391).

38. He, K., Zhang, X., Ren, S., & Sun, J. (2015). Spatial pyramid pooling in deep convolutional networks for visual recognition. *IEEE transactions on pattern analysis and machine intelligence*, *37*(9), 1904-1916.

39. Girshick, R., Donahue, J., Darrell, T., & Malik, J. (2014). Rich feature hierarchies for accurate object detection and semantic segmentation. In *Proceedings of the IEEE conference on computer vision and pattern recognition* (pp. 580-587).

40. Jia, Y., Shelhamer, E., Donahue, J., Karayev, S., Long, J., Girshick, R., ... & Darrell, T. (2014, November). Caffe: Convolutional architecture for fast feature embedding. In *Proceedings of the 22nd ACM international conference on Multimedia* (pp. 675-678).

41. Girshick, R. (2015). Fast r-cnn. In *Proceedings of the IEEE international conference on computer vision* (pp. 1440-1448).

42. Ren, S., He, K., Girshick, R., & Sun, J. (2015). Faster r-cnn: Towards real-time object detection with region proposal networks. *Advances in neural information processing systems*, *28*.

43. Lin, T. Y., Maire, M., Belongie, S., Hays, J., Perona, P., Ramanan, D., ... & Zitnick, C. L. (2014). Microsoft coco: Common objects in context. In *Computer Vision–ECCV 2014: 13th European Conference, Zurich, Switzerland, September 6-12, 2014, Proceedings, Part V 13* (pp. 740-755). Springer International Publishing.

44. Everingham, M., Van Gool, L., Williams, C. K., Winn, J., & Zisserman, A. (2010). The pascal visual object classes (voc) challenge. *International journal of computer vision*, *88*, 303-338.

45. Yaban, B., Alganci, U., & Sertel, E. (2022). Aircraft detection in very high-resolution satellite images using YOLO-based deep learning methods. *Intercontinental Geoinformation Days*, *4*, 270-273.

Identification of potential zones on the estimation of direct runoff and soil erosion for an ungauged watershed based on remote sensing and GIS techniques

Manti Patil [1] , **Arnab Saha** [*1,3] , **Santosh Murlidhar Pingale** [2] , **Devendra Singh Rathore** [1] , **Vikas Chandra Goyal** [1]

¹Research Management and Outreach Division, National Institute of Hydrology, Roorkee, Uttarakhand, 247 667, India
²Hydrological Investigations Division, National Institute of Hydrology, Roorkee, Uttarakhand, 247 667, India
³Institute of Infrastructure and Environment, The School of Energy, Geoscience, Infrastructure and Society, Heriot-Watt University, Edinburgh, EH14 5BU, UK

Abstract

An investigation of soil and water resources is essential to determine the future scenario of water management and water resources to attain food and water security. The improper management of watersheds results in a huge amount of sediment loss and surface runoff. Therefore, the present study was carried out to estimate the surface runoff and soil erosion using the Soil Conservation Service Curve Number (SCS-CN) method and RUSLE approach, respectively. These have been estimated using geospatial technologies for the ungauged Mandri river watershed from the Kanker district of Chhattisgarh State in India. The runoff potential zones, which are defined by the area's impermeable surfaces for a given quantity of precipitation were identified based on curve numbers at the sub-watershed levels. The land use data were collected from LISS IV images of 2009. The results showed that the average volume of runoff generated throughout the 16 years (2000-2015) was 14.37 million cubic meters (mM³). While average annual soil loss was found to be 17.23 tons/ha/year. Most of the eroded area was found to be around the major stream in a drainage system of Mandri River and on higher slopes of the terrain in the watershed. This study revealed that surface runoff and soil erosion are primary issues, which adversely affected the soil and water resources in this watershed. Therefore, suitable water harvesting sites and structures can be constructed based on the potential runoff zone and severity of soil erosion to conserve the soil and water in the watershed.

1. Introduction

Natural resource management and its proper utilization are considered a serious issue in the past few decades [1]. Precipitation is a vital source of water for human survival as well as for the basic requirement of flora and fauna, which is partially lost in huge amounts in the form of a direct runoff [2,3]. Runoff is one of the major components of the hydrologic cycle, which has a key role in addressing a wide range of issues interrelated to environment flow and social development [4,5]. The significance of rainfall-runoff modeling has long been intended [6,7]. For the transformation of rainfall into runoff, many previously developed models exist [8,9].

Out of these models, Soil Conservation Service Curve Number (SCS-CN) is used wide spreads for direct runoff estimation because of its acceptability [10]. The SCS-CN method is construed as an infiltration loss model [11-14]. It is essential for the protection and management of water resources mainly in drought-prone areas for watershed management and social development [15]. SCS-CN method can be used to estimate direct runoff from a small and ungauged agricultural watershed [16-19]. The curve number method is also used for water quality modeling and hydrologic simulation, etc. [20-28]. The application of the SCS-CN method has extended into the areas such as water quality modeling, urban hydrology, sediment, drainage, and baseflow, the

* Corresponding Author

(patilkgp@gmail.com) ORCID ID 0000-0003-4169-4785
*(arnab.dd@gmail.com) ORCID ID 0000-0002-3068-6774
(pingalesm@gmail.com) ORCID ID 0000-0002-7134-6012
(dsr.nih@gov.in) ORCID ID 0000-0001-8958-5591
(vcg.nih@gov.in) ORCID ID 0000-0003-0401-7881

coupling of remote sensing and geographical information system (GIS), in addition to rainfall-runoff modeling [1,29]. The integration of the SCS model and remote sensing has a good possibility to estimate runoff more accurately and faster [30-32]. Ibrahim-Bathis and Ahmed [33] did rainfall-runoff modeling using HEC-HMS and GIS techniques in the Doddahalla watershed in Southern India. He accomplished that the models can be applied in the ungauged watershed and water-scarce regions where the observed data are limited, and runoff estimation is mandatory to endure the water resources. Singh et al., [34] did rainfall-runoff modeling by applying a co-active neuro-fuzzy inference system (CANFIS) and multi-layer perception neural network (MLPNN) in the Naula catchment of river Ramganga in Uttarakhand, India. With the best results of CANFIS model, they suggested that present-day runoff depends on rainfall and runoff of the same and previous 2 days for that particular hilly watershed. Mishra et al. [35] integrated the SCS-CN method with the USLE model for computing the lumped quantity of event sediment load from watersheds. Soil erosion has been accepted as a serious problem arising from agricultural intensification, land degradation, and possibly due to global climatic change [36,37]. The productivity of some lands has declined by 50% due to soil erosion and desertification and degradation [38]. Meshram et al. [22] and Tyagi et al. [39] developed the relationship between curve number and sediment yield (SYI) using four watersheds of the Narmada basin. As per the best statistical outcomes, they proposed to compute SYI for the rest of the watersheds using curve numbers. Rather et al. [40] estimated the soil erosion vulnerability of eight watersheds in Jhelum basin Kashmir by applying a multicriteria analytical (MCA) framework using remote sensing and GIS techniques. The research discovered that three watersheds are highly erosion-prone and require immediate action to minimize the actual problem. The different studies on soil erosion and runoff estimation from gauged and ungauged watersheds have been carried out in different regions of the world [41-45].

The spatial distribution of several erosion-prone locations in the Mandri watershed was determined using the GIS-based RUSLE approach. The results would assist in implementing appropriate erosion control measures in the critically impacted areas. Therefore, the study has been conducted to (i) estimate the surface runoff as well as identify the runoff potential zone, which is the quantity of runoff generated by a specific area for a given amount of precipitation is mostly determined by the area's impermeable surfaces in Mandri watershed of Kanker district at Chhattisgarh, (ii) find out the optimal empirical model irrespective of SCS-CN method and GIS-based model for a generation of runoff in the ungauged agricultural watershed, (iii) estimate the average annual soil loss and potential erosion-prone areas in the watershed using the RUSLE method and suggested the remedial measures to minimize the erosion in higher runoff potential zones. The following outcomes may be used to create better management scenarios and focus on policymakers' choices for controlling soil erosion risks in the watershed's various areas in priority order for remediation.

2. Study area and data used

The study area is a micro-watershed of the Mandri river catchment (Figure 1) under the Chhattisgarh State Watershed Management Agency (CGWMA), the integrated watershed management program under the Government of India (CGWMA, 2014-15). This watershed lies in the Kanker block of district Kanker of Chhattisgarh, India. Its center is located at 20.1990° N latitude and 81.0755° E longitude and has a total geographical area of 6673.77 ha. The region comprises 9 villages and 10 sub-watersheds. It falls in the Middle Mahanadi basin, and Mandri Nadi is the major stream flowing through the area. On average, the region experiences an annual rainfall of around 1326 mm, approximately 90% of which falls from June to September. The majority of the rainfall occurs in the Kharif season, thereby making it a rainy region. The average annual rainfall has fluctuated greatly over the last six years (CGWMA, 2014-15). The topography of the watershed is undulating. The watershed has a maximum elevation of 711 m above mean sea level (a.m.s.l) and a minimum elevation of 330 m a.m.s.l. The climate of the watershed is semi-arid with four seasons. May is generally the hottest month with the mean daily maximum temperature at about 43 °C and December being the coolest with the minimum mean temperature of about 15 °C. The maximum relative humidity is generally around 80% during the monsoon season with a minimum of 35% during the dry season (Chhattisgarh Water Resources Department, CGWRD, 2014-15).

The specification of data used in the research work is presented in Table 1. The Digital elevation model (DEM) (12.5*12.5m) data was provided by the State Level Nodal Agency (SLNA). The land use data were collected from LISS IV images. The soil map was interpreted by the National Bureau of Soil Survey and Land Use Planning (NBSS&LUP). The daily rainfall data (add duration) were collected from the Indian Meteorology Department (IMD).

3. Method

3.1. SCS-CN Method

SCS-CN method developed by the United States Department of Agriculture (USDA) is the widely used approach for runoff computation because of its simplicity, accuracy, and its dependence on important parameter curve numbers (CN) [7,46]. To estimate runoff from storm rainfall, the United States Natural Resources Conservation Service (NRCS) based runoff CN method was used in this study. Determination of CN depends on the watershed's soil and land cover conditions, which the model represents as hydrologic soil group, cover type, treatment, and hydrologic condition [47]. This approach is based on a water balance hypothesis, which is expressed mathematically [48] in Equation 1.

$$\frac{F}{S} = \frac{Q}{P - I} \tag{1}$$
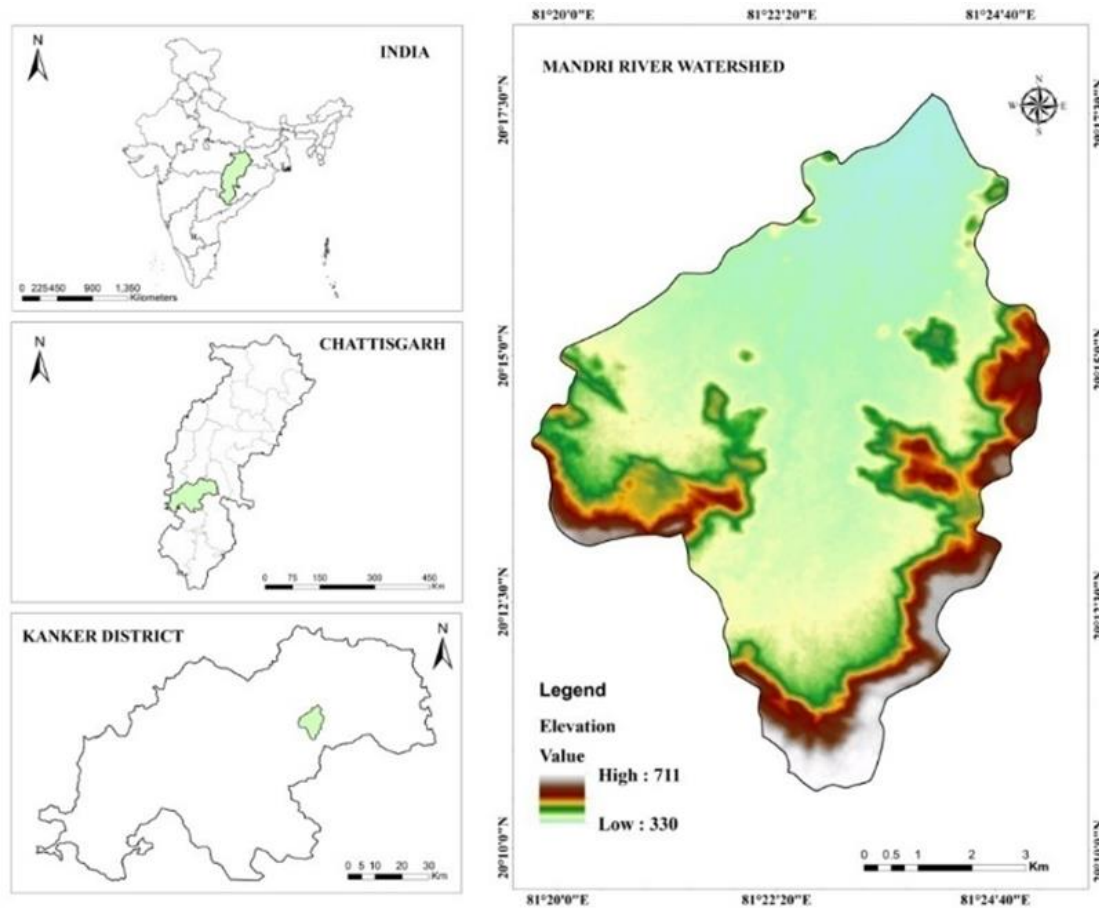
Figure 1. Study area map of Mandri river watershed

Table 1. Data specification and source of data

S.No.	Extracted Parameters	Data Specifications	Sources
1	Soil type	Soil Map Scale- 1:250,000	National Bureau of Soil Survey and Land Use Planning (NBSS & LUP), India
2	Land use	LISS IV images Resolution- 5.8 m Scale- 1:250,000 Year- 2009	National Remote Sensing Centre (NRSC), India
3	Slope and Elevation	ALOS Palsar DEM Resolution- 12.5 m Year- 2018	https://vertex.daac.asf.alaska.edu/
4	Rainfall	Daily Rainfall	Indian Meteorological Department (IMD)

Where, F is the actual amount of retention after runoff incited, mm; S is storage amount in a catchment, mm (S≥F); Q is the actual amount of runoff, mm; P is total precipitation, mm (P≥ Q), I is an initial abstraction in a catchment, mm

The amount of retention can be calculated by the Equation 2.

$$F = (P - I) - Q \qquad (2)$$

In studies of many small agricultural watersheds, I_a was found to be approximated by the following empirical Equation 3:

$$I = 0.2 * S \qquad (3)$$

Substituting Equation 3 from Equation 1 and Equation 2.

$$Q = \frac{(P - 0.2\,S)^2}{(P + 0.8\,S)}(P > Ia) \qquad (4)$$

This equation is used to estimate the direct runoff depth from rainfall. The variable used in this equation has rainfall P and S which is related to curve number CN:

$$S = \frac{25400}{CN} - 254 \qquad (5)$$

Where, CN is a dimensionless runoff indicator and values are in the range of 1 to 100. Higher values of CN indicate higher runoff and lower values of CN indicate lower runoff [49].

CN is an important decisive factor to define the surface runoff in the defined watershed. The major factors that determine CN are the hydrologic soil group (HSG) cover type, treatment, hydrologic condition, and

antecedent moisture conditions (AMC) [50]. The detailed description of the methodology to integrate the application of the SCS-CN method with RUSLE is shown in Figure 2.

AMC is mainly based on the following factors like land use, land treatment, hydrologic soil groups, hydrologic and climatic conditions. Direct runoff computation is based on the SCS-CN method due to its simplicity and flexibility. Soil texture is an important feature to classify the soil to its different characteristics like infiltration, soil texture, soil depth, water transmission rate, etc. (Table 2). AMC (Table 3) is a parameter to indicate the availability of soil moisture stored before a rainfall event. It is basically a wetness indicator and has a major effect on runoff generation in a catchment. Perceiving its significance, the soil conservation service (SCS) has prepared a guideline for adjusting the CN based on the total rainfall of the 5-day preceding event. AMC is bifurcated into three levels AMC-I for dry, AMC-II for normal, and AMC-III for wet conditions (Table 3). Based on weighted CN in Equation 6, CN_I and CN_{II} are computed in Equations 7 and 8, respectively. Because a curve number may also be termed AMC-I or CN_I or, dry soil moisture and AMC-II or CN_{II} or, average soil moisture and AMC-III or CN_{III} or, moist condition. The curve number can be adjusted by factors to CN_{II}, where CN_I factors are less than 1 (reduce CN and potential runoff), while CN_{III} factors are greater than 1 (increase CN and potential runoff). Here, the CN values are estimated according to the case of AMC-II [7,48].

$$CN_{II} = \frac{\sum A_i \times CN_i}{\sum_i^n A_i} \quad (6)$$

Where CN_{II} is the weighted CN, i is an index of watersheds subdivisions of uniform land use and soil type, CN_i is the CN for subdivision i, A_i is the drainage area of subdivision i and A is the total catchment area [51].

$$CN_I = \frac{CN_{II}}{(0.281 - 0.0128\, CN_{II})} \quad (7)$$

$$CN_{III} = \frac{CN_{II}}{(0.427 + 0.00573\, CN_{II})} \quad (8)$$

3.2. Soil erosion estimation

The present study uses the Revised Universal Soil Loss Equation (RUSLE), a predictive empirical model, to predict the annual soil loss rate in the Mandri catchment. The RUSLE, developed by the United States Department of Agriculture, is the most widely used erosion model for both agricultural and forest watersheds to predict the average annual soil loss by computing the soil erosion factors [54]. It is a revised version of the original Universal Soil Loss Equation [55] which had been tested and used for many years. RUSLE estimates annual average soil loss in tons per hectare per year using Equation 9:

$$A = R \times K \times LS \times C \times P \quad (9)$$
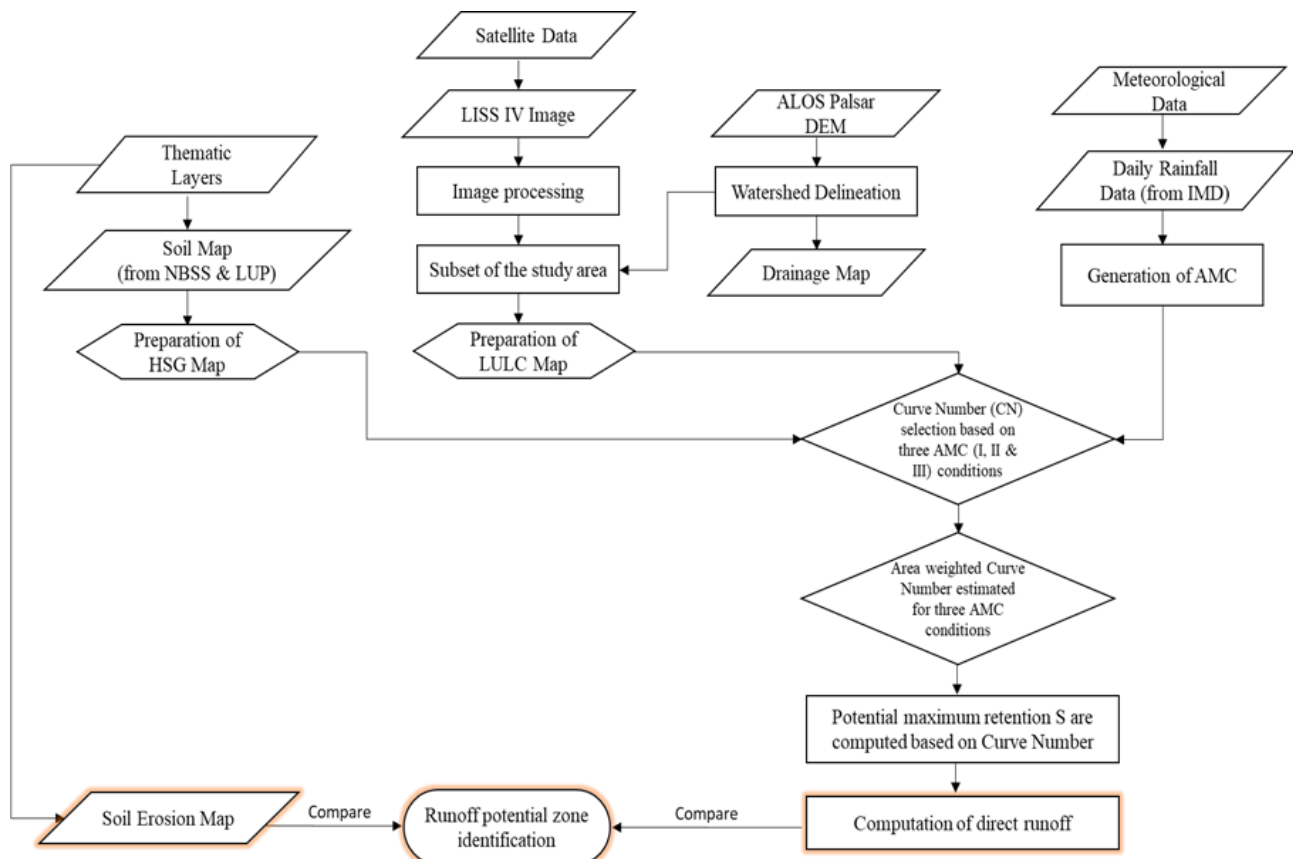
Figure 2. Methodology adopted to estimate runoff by using the SCS-CN method

Table 2. Soil characteristics have been classified into hydrologic soil groups [7,52,53]

Soil Characteristic	HSGs			
	A	B	C	D
Texture	Gravel/sand	Fine to moderate coarse texture	Moderate fine to fine texture	Mainly clay
Infiltration rate	Very high	High to moderate	Slow infiltration	Very slow
Drainage	Well-drained	Moderate to well drainage	Moderate to slow	Very slow
Water transmission rate	Very high	Moderate	Slow	Very slow
Assertion	Low runoff	Moderate runoff	Moderate to high runoff	High runoff

Table 3. Classification of antecedent moisture conditions (AMC) [52]

AMC	Total 5 days antecedent rainfall (mm)	
	Dormant season	Growing season
I	<12.5	<35.6
II	12.5-26	35.6-53.3
III	>26	>53.3

3.2.1. Rainfall-runoff erosivity factor (R)

Rainfall can erode the soil particles, the rainfall-runoff erosivity factor (Table 4) quantifies the effect of rainfall impact and also reflects the amount and rate of runoff likely to be associated with precipitation events it depends on the kinetic energy of the storm and the Intensity of the rainfall [56] Equation 10.

$$R = 81.5 + 0.385 * P_a \qquad (10)$$

Where R and P_a represent the average erosion index and mean annual rainfall in mm.

The methodology adopted for soil loss estimation is illustrated in Figure 3.

Table 4. Soil loss factors of RUSLE method

Parameter	Name	Unit
A	Computed spatial average soil loss over a period selected for R, usually on a yearly basis	[(t/ ha/y)]
R	Rainfall-runoff erosivity factor	[MJ mm/(ha h y^{-1})]
K	Soil erodibility factor	[t ha h/(ha MJ mm)]
LS	Slope length and slope steepness factor	[Dimensionless]
C	Cover and management factor	[Dimensionless]
P	Conservation support practices	[Dimensionless]
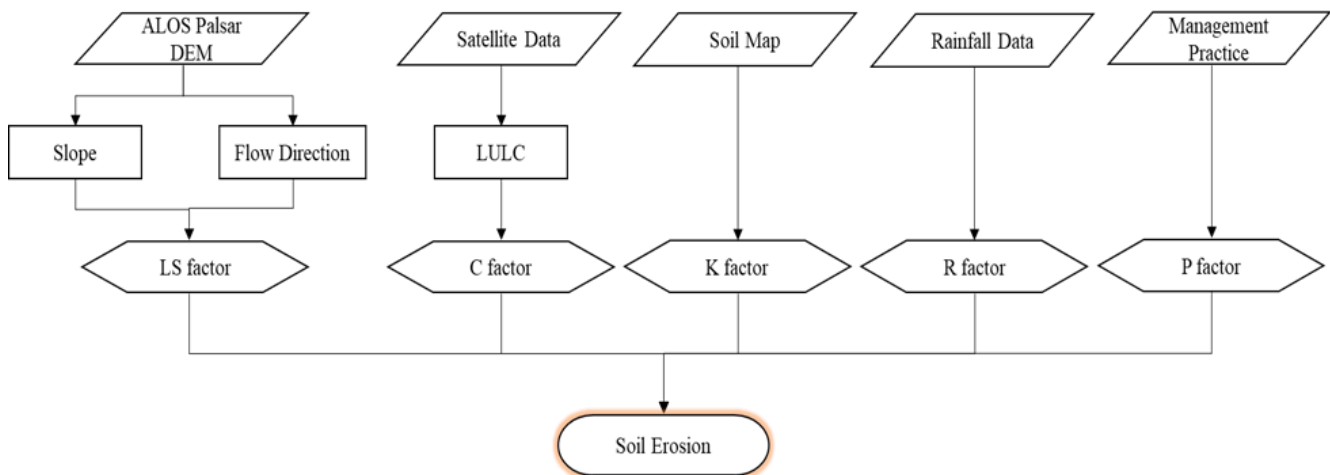
Figure 3. Methodology of soil loss estimation

3.2.2. Soil erodibility factor (K)

Soil erodibility (K) refers to the inherent susceptibility of soils to erosion by rainwater and runoff, and it is a function of a complex interaction of physical and chemical properties of soils affecting detachability, transportability, and infiltration capacity [57]. Clay-rich soils have low K values, ranging from 0.05 to 0.15, due to their resistance to detachment. Because of the low runoff, coarse-textured soils, such as sandy soils, have low K values, ranging from 0.05 to 0.2, despite the fact that these soils are effectively detachable. Medium and coarse soils, such as silt loam soils, possess moderate K values, ranging from 0.25 to 0.4, because they are relatively resistant to separation and generate moderate runoff. And for the higher values of K for high silt content soils tend to be greater than 0.4, because they are easily detached and generate high rates of runoff. In RUSLE,

factor K includes the whole soil, but factor Kf (for most soils, Kf = K.) only considers the fine-earth component or material with less than 2.00 mm equivalent diameter [58]. In the present study, the K factor map was prepared from the soil texture map of the NBSS&LUP, Nagpur. Soil texture is a measure of the particle size distribution in soil. Large particles are resistant to transport because of the greater force required to entrain them and fine particles are resistant to detachment because of their cohesiveness [45].

3.2.3. Slope length and slope steepness factor (LS)

The specific effects of topography on soil erosion are estimated by the dimensionless LS factor as the product of slope length (L) and steepness (S). In general, as slope length (L) increases, total soil erosion and soil erosion per unit area also increase due to the progressive accumulation of runoff in the downslope direction [59]. As the slope steepness (S) increases, the velocity and erosivity of runoff increase [60,61] Equation 11.

$$LS = (\text{flow accumulation} \times \text{cell size}/22.13)^{0.4} \times (\sin \text{slope}/0.0896)^{1.3} \qquad (11)$$

The computation of the LS factor requires flow accumulation and slope steepness factor which was computed from the Alos Palsar DEM (12.5m resolution).

3.2.4. Cover management factor (C)

Crop or land cover management factor (C) measures the combined effect of all the interrelated vegetative cover and management variables. This is one of the most important factors (after topography) in controlling soil erosion risk. It measures the protection of the soil surface from raindrop impact by vegetative material at some height above the soil surface and protection from raindrop impact and overland flow by the cover in contact with the soil surface, i.e., surface cover [62]. It is defined as the ratio of soil loss from a cropped field under a specific crop to soil loss from a continuous fallow field [63].

3.2.5. Conservation practice factor (P)

The support practice factor (P-factor) reflects the impact of support practices that will reduce the amount and rate of water runoff as well as the amount of soil erosion [64]. It is the ratio of soil loss from given conservation practices to soil loss obtained from up and down the slope. Where, conservation practices are contouring, strip cropping, and terracing [65]. The P-factor identifies differentiation between cropland and rangeland or permanent pasture. Both choices support terracing and contouring, however the cropland option includes a strip-cropping routine while the rangeland option includes an "other technological disruption" routine [58]. In the present study, the slope layer is generated where the slope is calculated in percent, and calculated the P factor layer [64] relates P factor value (Table 5) with the slope of the catchment.

Table 5. Relationship between slope and p factor [64]

Slope (%)	0-2	2-5	5-8	8-12	12-16	16-20	20-25	>25
P factor	0.6	0.5	0.5	0.6	0.7	0.8	0.9	1

4. Results and Discussion

4.1. LULC, soil, and drainage map

The LULC map shown in Figure 4a gives detailed information about the catchment area that was classified into 6 classes cropland, mixed forest, barren land, woody forest, built up, and water bodies. The majority of land uses are cropland (2545 ha), barren land (1975 ha), and mixed forest (1234 ha) (Figure 4a) (Table 6).

In accordance with various soil properties (like texture, drainage condition, infiltration rate, and depth), Soils are classified into different classes. Major soil classes are sand (2273.78 ha), loamy sand (2029.83 ha), and clay (1087.46 ha) as depicted in Figure 4b and Table 7. With respect to various soil classes hydrologic soil groups (HSG's) A, B, and D are defined (Figure 5). The soil

in the region originates from granite, gneiss, sand, and khedar. Most of the area is covered with sand and loamy-sand soil. The other soil types include clay-loamy, clay, sandy clay, and sandy-clay-loam (Figure 4b). The soil is faintly colored in the higher regions of the hilly tract, while in the river valleys; the soil is smooth and fertile.

The overall drainage pattern of the watershed is dendrite. Morphometric analysis showed that it had five order streams. Figure 4c shows the drainage network of the watershed. Drainage characteristic is a key input for watershed management and soil loss estimation [66]. Based on the soil characteristics of the study area, there are three HSG's were found as A, C, and D (Figure 5) in the Kanker district of Chhattisgarh. HSG group A covers 66% area of the whole watershed while C has 4.13% and HSG group D covers 23.81% area (Table 8). Soil group B does not exist in the study area.

(a)

(b)

(c)
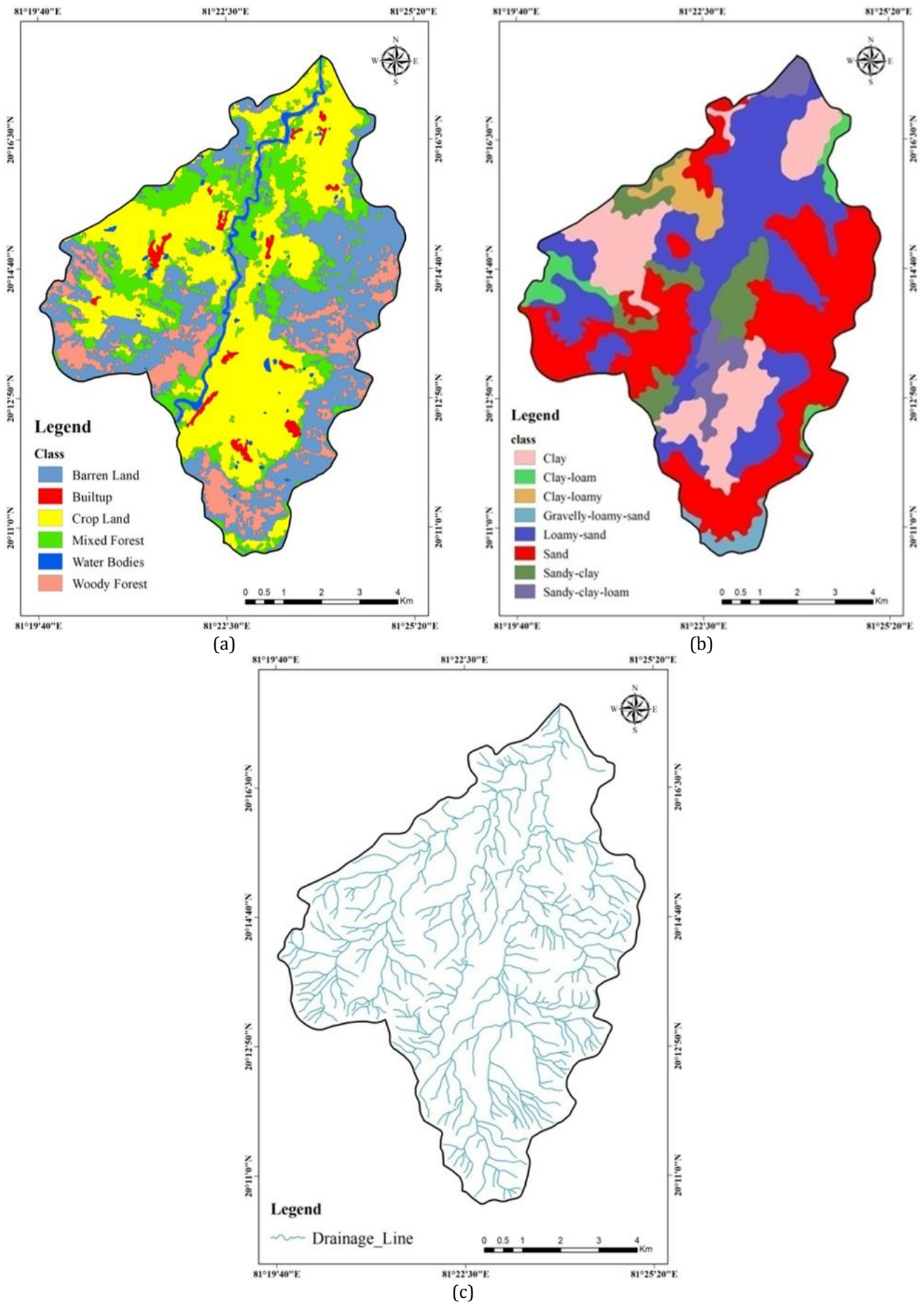
Figure 4. a) LULC map of the year 2009 **b)** Soil map **c)** Drainage map of the study area

4.2. Model verification

To validate the results of the SCS-CN method, we have used daily rainfall data for 16 years. The study was done on micro-watersheds so observed runoff data were not available. In this case, we used rainfall data as an alternative [18]. The applicability and validity of the SCS-CN method were confirmed by comparing computed runoff and daily runoff peaks [67]. In relation to rainfall and runoff, the runoff coefficient was computed for the monsoon season of 16 years data (2000-2015) (Table 9).

There were six major LULC classes identified in the study area (Table 10). In accordance with that, the curve number values are shown in Figure 6. The potential zone indicates that a higher curve number value requires minimum irrigation water requirement but has more erosion loss [68]. As per the slope ranges the possible remedial measures are suggested to minimize the erosion.

As depicted in Figure 7 and Table 11, the annual rainfall, runoff, annual volume of the area, and annual runoff coefficient were estimated as 1326.98 mm and 215.48 mm with an average runoff coefficient of 0.16. It indicated that 16.23% of average annual rainfall was converted into runoff during 2000-2015. The annual runoff volume was 14373537.6 m³ that was lost annually from the catchment between 2000 and 2015. In this study, it was concluded that the total annual rainfall of 21231.78 mm generated a runoff of 3447.77 mm, and the annual runoff coefficient was 0.16 (2000-2015).

Table 6. Classes of LULC in the study area

LULC type	Area (ha)	% Area
Barren land	1957.69	29.33
Build up	101.47	1.52
Crop land	2545.26	38.14
Mixed forest	1222.27	18.31
Water bodies	115.06	1.72
Woody forest	732.02	10.97
Total	6673.77	100

Table 7. Classification of soil type class in the study area

Soil type class	Area (ha)	Percentage of Area
Clay	1087.46	16.29
Clay-loam	206.83	3.1
Clay- loamy	192.83	2.89
Gravelly-loamy-sand	104.65	1.57
Loamy-sand	2029.83	30.42
Sand	2273.78	34.07
Sandy-clay	502.94	7.54
Sandy-clay-loam	275.96	4.13
Total	6674.28	100

Table 8. Classification of hydrologic soil groups

Hydrologic Soil Group (HSG)	Area (ha)	Area (%)
Group A	4408.27	66.05
Group C	275.96	4.13
Group D	1989.54	29.81
Total	6673.77	100
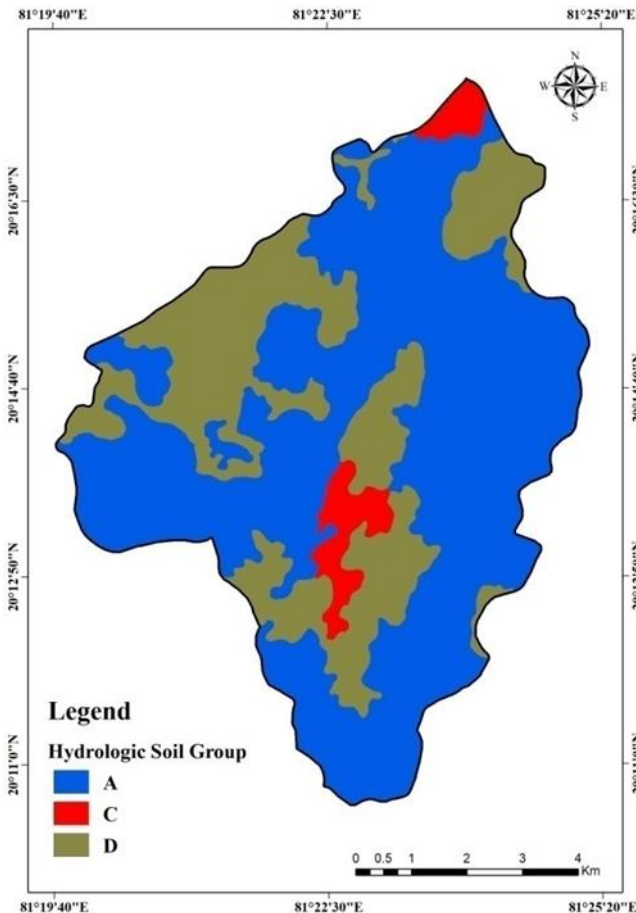
Figure 5. Hydrologic soil group map
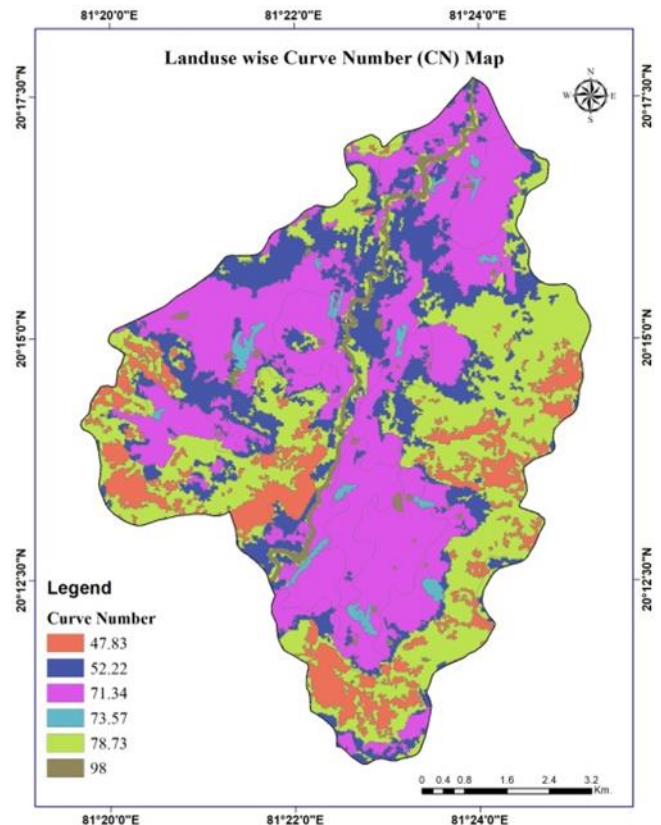
Figure 6. The CN map according to LULC classes

Table 9. Monsoon season rainfall and runoff

		June	July	August	September
2000	R	182.65	348.80	237.80	58.32
	Q	21.22	50.14	19.93	7.05
	CR	0.12	0.14	0.08	0.12
2001	R	526	502.9	672.77	40.05
	Q	93.59	145.87	237.61	0
	CR	0.18	0.29	0.35	0
2002	R	239.7	149.47	431.77	161.02
	Q	33.50	6.72	86.31	7.00
	CR	0.14	0.04	0.20	0.04
2003	R	106.02	377.15	562.42	277.82
	Q	0	50.31	128.80	42.93
	CR	0	0.13	0.23	0.15
2004	R	164.12	269.15	444.65	104.07
	Q	19.52	8.22	92.38	0
	CR	0.12	0.03	0.21	0
2005	R	159.22	322.12	378.70	283.50
	Q	14.65	14.85	55.11	82.23
	CR	0.09	0.05	0.15	0.29
2006	R	88.50	744.25	616.85	251.47
	Q	0	292.88	127.22	25.52
	CR	0	0.39	0.21	0.10
2007	R	518.40	230.37	390.55	270.25
	Q	186.65	14.04	12.40	13.06
	CR	0.36	0.06	0.03	0.05
2008	R	357.50	184.55	356.75	392.37
	Q	64.99	10.04	75.22	66.65
	CR	0.18	0.05	0.21	0.17
2009	R	59.59	487.07	266.42	87.87
	Q	0	110.26	30.95	8.41
	CR	0	0.23	0.12	0.10
2010	R	74.22	417.57	414.40	350.92
	Q	0	46.95	55.34	75.60
	CR	0	0.11	0.13	0.22
2011	R	120.70	285.77	419.27	390.97
	Q	0	16.76	63.14	99.27
	CR	0	0.06	0.15	0.25
2012	R	158.67	393.80	452.27	247.32
	Q	24.91	76.21	85.27	13.90
	CR	0.16	0.19	0.19	0.06
2013	R	289.62	318.24	371.32	125.87
	Q	49.84	26.88	74.87	0
	CR	0.17	0.08	0.20	0
2014	R	47.92	550.50	261.77	276.57
	Q	0	118.79	50.48	69.07
	CR	0	0.22	0.19	0.25
2015	R	271.25	117.65	203.67	270
	Q	56.09	4.09	11.98	85.59
	CR	0.21	0.03	0.06	0.32

*Note: R = Rainfall, mm, Q = Discharge, mm, and CR = Runoff coefficient

Figure 8 represents the variability of season rainfall, runoff, and runoff coefficient. The maximum runoff coefficient observed was 0.39 in July 2006 due to high rainfall were a minimum runoff coefficient of 0 in June 2014 and September 2001 in most of the months. As mentioned in Figure 5 and Table 8 that 66% area is under the HSG A soil group, which has high infiltration as well as a high-water transmission rate so the month of June in most of the years has a runoff coefficient of 0. The

average runoff coefficient was found to be 0.16 (Table 9). The rainfall trend in the monsoon season (Jun-Sep) is highly dominated to surface runoff.

In Figure 9, the scenario of rainfall to runoff for each CN condition is plotted. The CNI is CN for dry conditions, CNII is CN for normal conditions and CNIII is CN for wet conditions. Based on the previous 5 days' antecedent moisture condition and season, the runoff is generated for individual CN [53].

4.3. Curve number and soil loss relation

In practice, soil loss from upland areas is generally well correlated with observed runoff [35,69] than with rainfall. Runoff computation by SCS-CN methods is directly proportional to a CN value. With respect to land use, soil, and AMC conditions the CN are defined to each hydrologic response unit (HRU) [70]. Figure 6 and Table 10 show the value of CN for the growing season, which highlights the minimum CN is 36 in the mixed forest whereas the maximum CN is 98 in water bodies and paved surfaces. As per variability of curve number the higher value of CN generates maximum runoff which causes soil erosion risks whereas lowers CN generates minimum runoff [68]. Based on this CN map in Figure 6 runoff potential zone can be identified in the watershed as well as we can suggest the remedial measure to minimize the surface runoff and soil erosion.

The average annual soil loss map was prepared using the R, K, LS, C, P, and RUSLE methods. The soil erosion area is classified into 8 classes, in which very few areas have a high erosion rate (Figure 10b). Table 12 and Figure 10a shows that a few areas of the study area are very high runoff potential zones. The soil erosion classes indicated that around 54% area is under negligible or minimum erosion zone, but the rest of the area has runoff generating land use. Paddy, maize, tomato, gram, chickpea, etc. are the major crops grown in the watershed.

Table 10. LULC wise CN values

S. No	LULC	CN
1	Barren land	78.73
2	Build up	73.57
3	Cropland	77.70
4	Mixed forest	52.22
5	Water bodies	98
6	Woody Forest	47.83
	Average CN	71.3

Table 11. Annual rainfall and runoff depth and volume of the watershed in m^3

Year	Rainfall (mm)	Runoff (mm)	Runoff Coefficient	Volume (mM³)
2000	866.12	98.35	0.11	6.56
2001	1946.1	484.82	0.25	32.34
2002	1053.55	133.54	0.13	8.91
2003	1541.75	242.52	0.16	16.18
2004	1055.65	120.13	0.11	8.01
2005	1369.1	174.43	0.13	11.64
2006	1864.25	456.2	0.24	30.43
2007	1473.65	226.17	0.15	15.09
2008	1379.9	216.22	0.16	14.42
2009	959.4	149.63	0.16	9.98
2010	1489.3	193.42	0.13	12.90
2011	1280.8	179.18	0.14	11.95
2012	1323.9	200.28	0.15	13.36
2013	1327.82	158.09	0.12	10.55
2014	1249.72	257.03	0.21	17.14
2015	1050.77	157.76	0.15	10.52
Total	21231.78	3447.77	0.16	229.98
Average	1326.98	215.48	0.16	14.37

Remark: The highest annual runoff generation occurs in years of 2006 with a runoff coefficient of 0.24 whereas minimum runoff occurs in the year of 2000 with a runoff coefficient of 0.11
10% of rainfall amount
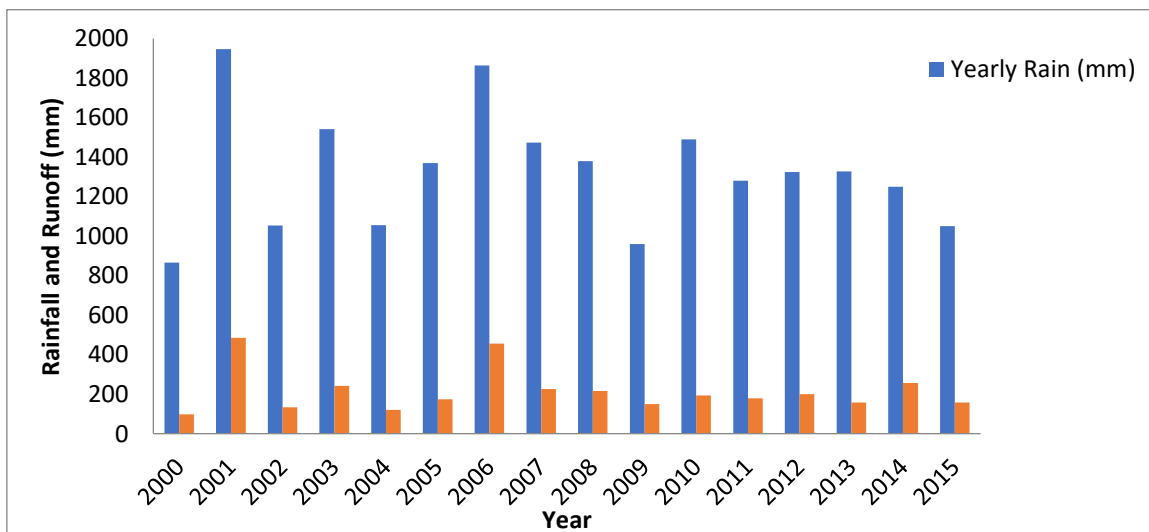
Figure 7. Rainfall-Runoff comparison from 2000-2015
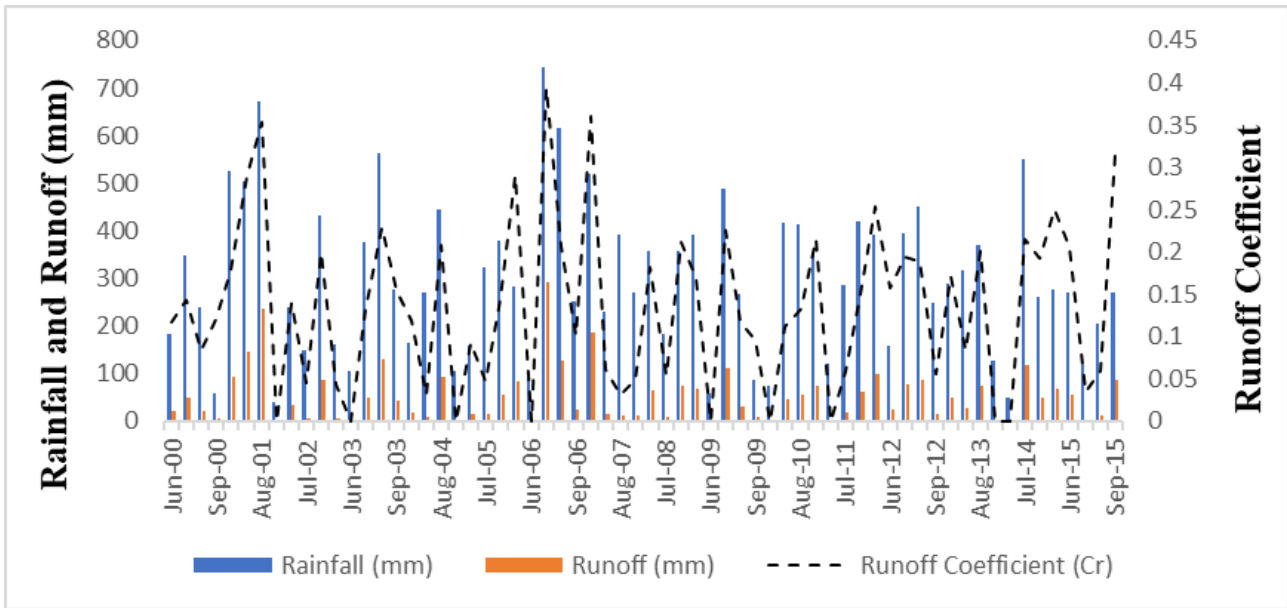
Figure 8. Surface runoff from storm rainfall
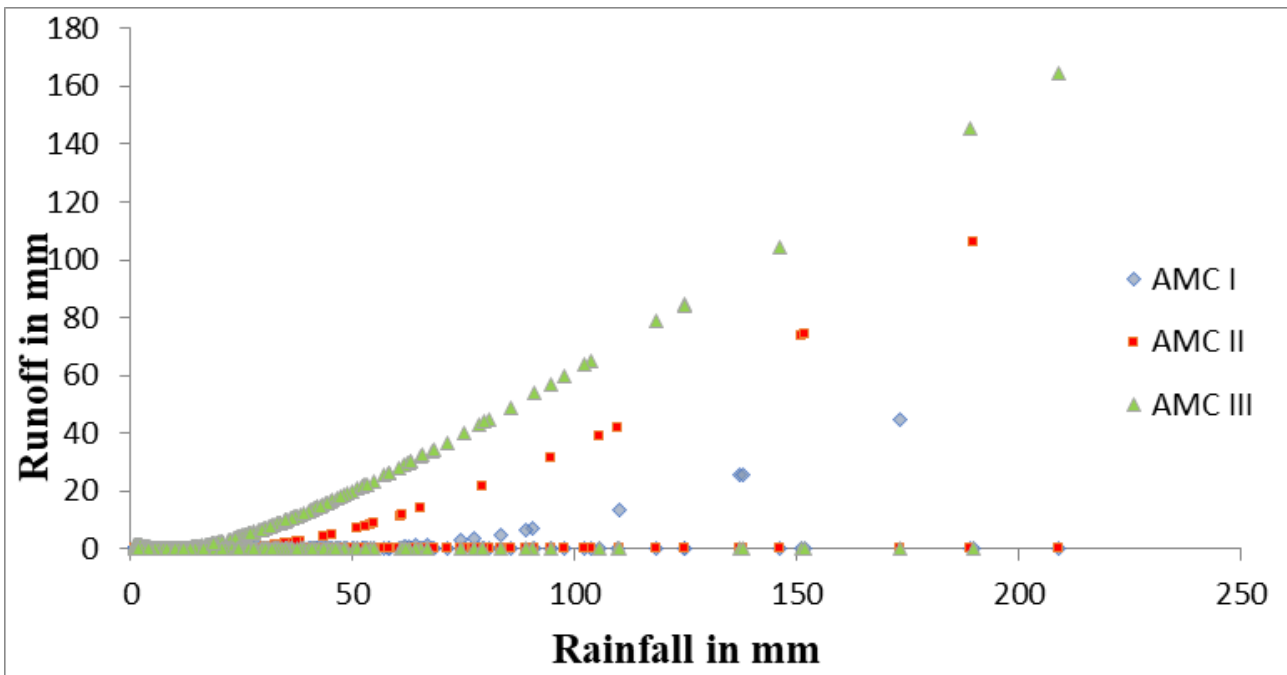
Figure 9. Rainfall-runoff comparison of each AMC conditions

Table 12. The possible remedial measures for erosion control [53]

Class t/ha/yr	Measures
< 2	Negligible
2 to 5	Negligible
5 to 10	Field bunding, Pasture Development
10 to 15	Contour Cultivation, Strip Cropping, Contour strip Cropping, intercropping, vegetative bunding
15 to 20	Intercropping, Contour bunding, Vegetative bunding, Diversion of drainage channels.
20 to 40	Graded bunding, land leveling, Gully Control Structure, Vegetative hedges, Pasture development
40 to 80	Afforestation, Gully Control Structure, Graded bunding, Pasture development

5. Conclusion

The study area is in an undulating agricultural watershed in the Mahanadi basin of Chhattisgarh, India. The area has decent rainfall (the average annual value of 1326 mm) with high intensity and the slope ranges from flat to steep. The watershed falls in a semi-arid region

and rainfed agriculture also exists. Due to the climatic and topographic features of the watershed, all four stages of erosion come into account in that particular area. Defining and sorting out the problems of soil and water at a point in agricultural watersheds is a big challenge. In this work, it was concluded that the integration of SCS-CN and RUSLE with the use of GIS and remote sensing

(i.e., the CN value, and soil loss rate) highlight the runoff potential zone and erosion-prone areas in the study area. For proper watershed management, the identification and estimation of runoff sources are necessary. Due to inadequate networks of stations, the observed data for hydrologic computation is usually not available at the micro-watershed level. In such cases, remote sensing and GIS are suitable techniques that give a reliable output of runoff and soil erosion. The spatial distribution of extreme average annual soil erosion is found along the stream and high altitudes of the watershed. Erosion is classified in the range from no erosion to extremely severe erosion range concerning that proper management practices are suggested to mitigate the problem. As a study conducted in the ungauged watershed with only the climatic and watershed characteristics, it was suggested that the probable zone for water harvesting structures enhance the water availability in terms of groundwater as well as surface water for crop production. This study emphasizes that proper watershed management could improve the cost-benefit ratio of the farmers as well as the living standard of the community.
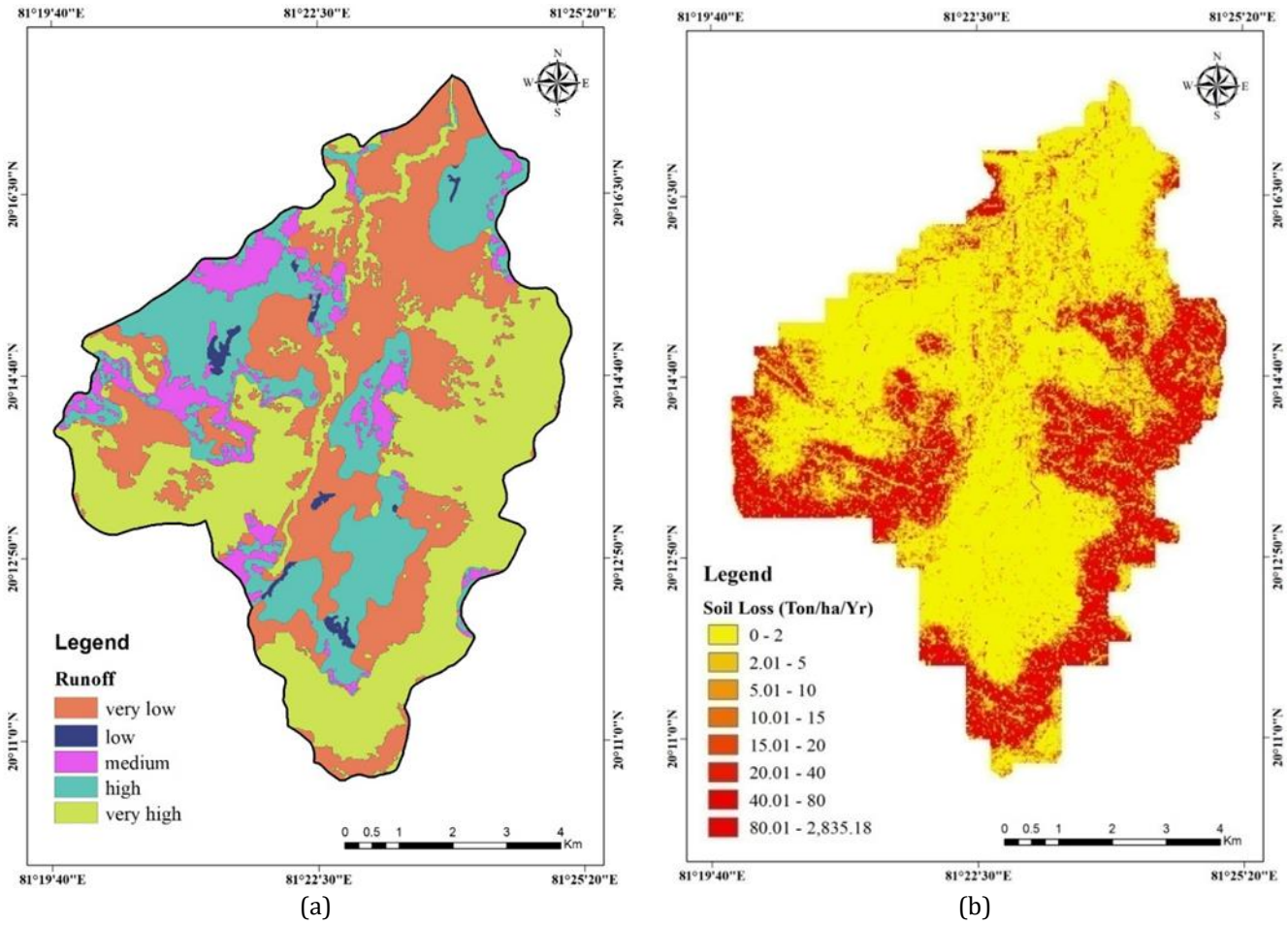
Figure 10. a) Runoff potential map **b)** Soil loss map of the study area

Figure 11. The relationship between rainfall and runoff in the study area

Author contributions

Manti Patil: Conceptualization, Methodology, Writing-Original draft preparation, Validation **Arnab Saha:** Conceptualization, Data curation, Visualization, Writing-Original draft preparation, Software, Validation **Santosh Murlidhar Pingale:** Methodology, Visualization, Investigation, Writing-Reviewing and Editing, **Validation Devendra Singh Rathore:** Investigation, Writing-Reviewing and Editing **Vikas Chandra Goyal:** Data curation, Investigation, Writing-Reviewing and Editing

Conflicts of interest

The authors declare no conflicts of interest.

References

1. Mishra, S. K., Pandey, A., & Singh, V. P. (2012). Special issue on soil conservation service curve number (SCS-CN) methodology. *Journal of Hydrologic Engineering*, *17*(11), 1157-1157. https://doi.org/10.1061/(ASCE)HE.1943-5584.0000694

2. Marshall, E. J. P., West, T. M., & Kleijn, D. (2006). Impacts of an agri-environment field margin prescription on the flora and fauna of arable farmland in different landscapes. *Agriculture, ecosystems & environment*, *113*(1-4), 36-44. https://doi.org/10.1016/j.agee.2005.08.036

3. Swain, S., Mishra, S. K., & Pandey, A. (2021). A detailed assessment of meteorological drought characteristics using simplified rainfall index over Narmada River Basin, India. *Environmental Earth Sciences*, *80*, 1-15. https://doi.org/10.1007/s12665-021-09523-8

4. Patil, M. (2016). Stream flow modeling for ranganadi hydropower project in India considering climate change. Current World Environment, 11(3), 834. https://doi.org/10.12944/CWE.11.3.19

5. Ramana, G. V., Viswanadh, G. K., & Gautam, N. C. (2011). Rainfall and Runoff process using by overland Time of Concentration Model and GIS Modules. In 12th ESRI India User Conference, New Delhi.

6. Mishra, S. K., & Singh, V. P. (2002). SCS-CN method. Part I: derivation of SCS-CN-based models. Available

electronically from http://hdl.handle.net/1969.1/164640

7. Mishra, S. K., & Singh, V. P. (2013). Soil conservation service curve number (SCS-CN) methodology (Vol. 42). Springer Science & Business Media

8. Rajurkar, M.P., Kothyari, U.C., & Chaube, U.C. (2004). Modeling of the daily rainfall-runoff relationship with artificial neural network. Journal of Hydrology, 285(1-4), 96-113. https://doi.org/10.1016/j.jhydrol.2003.08.011

9. Singh, V. P., Frevert, D. K., Rieker, J. D., Leverson, V., Meyer, S., & Meyer, S. (2006). Hydrologic modeling inventory: cooperative research effort. Journal of irrigation and drainage engineering, 132(2), 98-103. https://doi.org/10.1061/(ASCE)0733-9437(2006)132:2(98)

10. Guru, B. G. (2015). Critical Evaluation of MS (Mishra and Singh) Model for Runoff Estimation. Journal of Civil Engineering and Environmental Technology, 2(10), 11-14.

11. Aron, K., & Johnson, P. M. (1977). The multiphoton ionization spectrum of xenon: interatomic effects in multiphoton transitions. The Journal of Chemical Physics, 67(11), 5099-5104. https://doi.org/10.1063/1.434737

12. Chen, C. L. (1982). An evaluation of the mathematics and physical significance of the soil conservation service curve number procedure for estimating runoff volume. In Proc., Int. Symp. on Rainfall-Runoff Modeling, Water Resources Publ., Littleton, Colo (pp. 387-418).

13. Hjelmfelt Jr, A. T. (1980). Curve-number procedure as infiltration method. Journal of the Hydraulics Division, ASCE, 106(HY6), 1107-1111. https://doi.org/10.1061/JYCEAJ.0005445

14. Ponce, V.M., & Hawkins, R.H., 1996. Runoff curve number: has it reached maturity? Hydrol. Eng. ASCE 1 (1), 11–19. https://doi.org/10.1061/(ASCE)1084-0699(1996)1:1(11)

15. Siddiraju, R., Sudarsanaraju, G., & Rajsekhar, M. (2018). Estimation of rainfall-runoff using SCS-CN Method with RS and GIS Techniques for Mandavi Basin in YSR Kadapa District of Andhra Pradesh, India. Hydrospatial Analysis, 2(1), 1-15p. https://doi.org/10.21523/gcj3.18020101

16. Köylü, Ü. & Geymen, A. (2016). GIS and remote sensing techniques for the assessment of the impact of land use change on runoff. Arabian Journal of Geosciences, 9(7), 484. https://doi.org/10.1007/s12517-016-2514-7

17. Liu, X., & Li, J. (2008). Application of SCS model in estimation of runoff from small watershed in Loess Plateau of China. Chinese Geographical Science, 18(3), 235. https://doi.org/10.1007/s11769-008-0235-x

18. Rawat, K. S., & Singh, S. K. (2017). Estimation of surface runoff from semi-arid ungauged agricultural watershed using SCS-CN method and earth observation data sets. Water Conservation Science and Engineering, 1(4), 233-247. https://doi.org/10.1007/s41101-017-0016-4

19. Zelelew, D. G. (2017). Spatial mapping and testing the applicability of the curve number method for ungauged catchments in Northern Ethiopia.

International Soil and Water Conservation Research, 5(4), 293-301. https://doi.org/10.1016/j.iswcr.2017.06.003

20. Hawkins, R. H. (1973). Improved prediction of storm runoff in mountain watersheds. Journal of the Irrigation and Drainage Division, 99(4), 519-523. https://doi.org/10.1061/JRCEA4.0000957

21. Hawkins, R. H. (1978). Runoff curve numbers with varying site moisture. Journal of the irrigation and drainage division, 104(4), 389-398. https://doi.org/10.1061/JRCEA4.0001221

22. Meshram, S. G., Powar, P. L., Singh, V. P., & Meshram, C. (2018). Application of cubic spline in soil erosion modeling from Narmada Watersheds, India. Arabian Journal of Geosciences, 11(13), 362. https://doi.org/10.1007/s12517-018-3699-8

23. Mishra, S. K., & Singh, V. P. (1999). Another look at SCS-CN method. Journal of Hydrologic Engineering, 4(3), 257-264. https://doi.org/10.1061/(ASCE)1084-0699(1999)4:3(257)

24. Mishra, S. K., & Singh, V. P. (2003). Derivation of SCS-CN parameter S from linear Fokker-Planck equation. Acta Geophys Pol, 51(2), 180-202. Available electronically from http://hdl.handle.net/1969.1/164631

25. Mishra, S. K., & Singh, V. P. (2004). Long-term hydrological simulation based on the Soil Conservation Service curve number. Hydrological Processes, 18(7), 1291-1313. https://doi.org/10.1002/hyp.1344

26. Mockus, V. (1949). Estimation of total (and peak rates of) surface runoff for individual storms. Exhibit A of Appendix B, Interim Survey Rep. Grand (Neosho) River Watershed, USDA, Washington, DC.

27. Rallison, R. E. (1980) Origin and evolution of the SCS runoff equation. Proceedings of ASCE irrigation and drainage division symposium on watershed management, ASCE, New York, NY, 2, 912–924.

28. Williams, J. R., & LaSeur, W. V. (1976). Water yield model using SCS curve numbers. Journal of the hydraulics division, 102(9), 1241-1253. https://doi.org/10.1061/JYCEAJ.0004609

29. Guptha, G. C., Swain, S., Al-Ansari, N., Taloor, A. K., & Dayal, D. (2021). Evaluation of an urban drainage system and its resilience using remote sensing and GIS. Remote Sensing Applications: Society and Environment, 23, 100601. https://doi.org/10.1016/j.rsase.2021.100601

30. Guptha, G. C., Swain, S., Al-Ansari, N., Taloor, A. K., & Dayal, D. (2022). Assessing the role of SuDS in resilience enhancement of urban drainage system: A case study of Gurugram City, India. Urban Climate, 41, 101075. https://doi.org/10.1016/j.uclim.2021.101075

31. Nayak, T., Verma, M. K., &Bindu, S. H. (2012). SCS curve number method in Narmada basin. International Journal of Geomatics and Geosciences, 3(1), 219-228.

32. Sharma, I., Mishra, S. K., Pandey, A., Kumre, S. K., & Swain, S. (2020). Determination and verification of antecedent soil moisture using Soil Conservation Service Curve Number method under various land uses by employing the data of small Indian experimental farms. In Watershed Management 2020 (pp. 141-150). Reston, VA: ASCE. https://doi.org/10.1061/9780784483060.013

33. Ibrahim-Bathis, K., & Ahmed, S. A. (2016). Rainfall-runoff modelling of Doddahalla watershed—an application of HEC-HMS and SCN-CN in ungauged agricultural watershed. Arabian Journal of Geosciences, 9(3), 170. https://doi.org/10.1007/s12517-015-2228-2

34. Singh, A., Malik, A., Kumar, A., & Kisi, O. (2018). Rainfall-runoff modeling in hilly watershed using heuristic approaches with gamma test. Arabian Journal of Geosciences, 11(11), 261. https://doi.org/10.1007/s12517-018-3614-3

35. Mishra, S. K., Tyagi, J. V., Singh, V. P., & Singh, R. (2006). SCS-CN-based modeling of sediment yield. Journal of Hydrology, 324(1-4), 301-322. https://doi.org/10.1016/j.jhydrol.2005.10.006

36. Lal, M., Mishra, S. K., Pandey, A., Pandey, R. P., Meena, P. K., Chaudhary, A., ... & Kumar, Y. (2017). Evaluation of the Soil Conservation Service curve number methodology using data from agricultural plots. Hydrogeology Journal, 25(1), 151-167. https://doi.org/10.1007/s10040-016-1460-5

37. Swain, S., Mishra, S. K., Pandey, A., & Dayal, D. (2022). Spatiotemporal assessment of precipitation variability, seasonality, and extreme characteristics over a Himalayan catchment. Theoretical and Applied Climatology, 147, 817-833. https://doi.org/10.1007/s00704-021-03861-0

38. Kumar, S., & Kushwaha, S. P. S. (2013). Modelling soil erosion risk based on RUSLE-3D using GIS in a Shivalik sub-watershed. Journal of Earth System Science, 122(2), 389-398. https://doi.org/10.1007/s12040-013-0276-0

39. Tyagi, J. V., Mishra, S. K., Singh, R., & Singh, V. P. (2008). SCS-CN based time-distributed sediment yield model. Journal of hydrology, 352(3-4), 388-403. https://doi.org/10.1016/j.jhydrol.2008.01.025

40. Rather, M. A., Kumar, J. S., Farooq, M., & Rashid, H. (2017). Assessing the influence of watershed characteristics on soil erosion susceptibility of Jhelum basin in Kashmir Himalayas. Arabian Journal of Geosciences, 10(3), 59. https://doi.org/10.1007/s12517-017-2847-x

41. Haiyan, F., & Liying, S. (2017). Modelling soil erosion and its response to the soil conservation measures in the black soil catchment, Northeastern China. Soil and Tillage Research, 165, 23-33. https://doi.org/10.1016/j.still.2016.07.015

42. Kinnell, P. I. A. (2010). Event soil loss, runoff and the Universal Soil Loss Equation family of models: A review. Journal of Hydrology, 385(1-4), 384–397. https://doi.org/10.1016/j.jhydrol.2010.01.024

43. Mosbahi, M., Benabdallah, S., & Boussema, M. R. (2013). Assessment of soil erosion risk using SWAT model. Arabian Journal of Geosciences, 6(10), 4011-4019. https://doi.org/10.1007/s12517-012-0658-7

44. Pradeep, G. S., Krishnan, M. N., & Vijith, H. (2015). Identification of critical soil erosion prone areas and annual average soil loss in an upland agricultural watershed of Western Ghats, using analytical

hierarchy process (AHP) and RUSLE techniques. Arabian Journal of Geosciences, 8(6), 3697-3711. https://doi.org/10.1007/s12517-014-1460-5

45. Tirkey, A. S., Pandey, A. C., & Nathawat, M. S. (2013). Use of satellite data, GIS and RUSLE for estimation of average annual soil loss in Daltonganj watershed of Jharkhand (India). Journal of Remote Sensing Technology, 1(1), 20-30.

46. Soulis, K. X., & Valiantzas, J. D. (2012). SCS-CN parameter determination using rainfall-runoff data in heterogeneous watersheds–the two-CN system approach. Hydrology and Earth System Sciences, 16(3), 1001-1015. https://doi.org/10.5194/hess-16-1001-2012

47. Brady, S.J. (1985). Conservation compliance and wetlands conservation provisions of the omnibus farm acts of 1985, 1990, and 1996. A comprehensive review of Farm Bill contributions to wildlife conservation, 2000, 5-17.

48. Subramanya, K. (2013). Engineering Hydrology, 4e. Tata McGraw-Hill Education.

49. Suresh, R. (2012). Soil and water conservation engineering. Standard Publishers Distributors.

50. Lal, D., Patil, M., Kumar, S., Gotekar, Y., Karwariya, S., & Kumar, R. (2017) Land Degradation and Soil Loss Estimation by Rusle and GIS Technique: A Case Study. Journal of Climate Change and Water, 2(1), 34-46

51. Chow, V. T. (1964). Handbook of applied hydrology: a compendium of water-resources technology.

52. Miller, D. A., & White, R. A. (1998). A conterminous United States multilayer soil characteristics dataset for regional climate and hydrology modeling. Earth interactions, 2(2), 1-26. https://doi.org/10.1175/1087-3562(1998)002<0001:ACUSMS>2.3.CO;2

53. Das, G. (2008). Hydrology and Soil Conservation Engineering: Including Watershed Management. PHI Learning Pvt. Ltd, New Delhi.

54. Renard, K. G., Foster, G. R., Weesies, G. A., McCool, D. K., & Yoder, D. C. (1997). Predicting soil erosion by water: a guide to conservation planning with the Revised Universal Soil Loss Equation (RUSLE) (Vol. 703). Washington, DC: United States Department of Agriculture.

55. Wischmeier, W. H., & Smith, D. D. (1978). Predicting rainfall erosion losses: a guide to conservation planning (No. 537). Department of Agriculture, Science and Education Administration.

56. Kowal, J.M., & Kassam, A.H., (1976). Energy and instruments intensity of rainstorms at Samary, northern Nigeria. Tropical Agriculture (UK). 53, 185–198.

57. Stone, R. P., & Hilborn, D. (2000). Universal Soil Loss Equation (USLE). Ontario. Ministry of Agriculture. Food and Rural Affairs, 9.

58. RUSLE - an online soil erosion assessment tool. (2022). Msu.edu. http://www.iwr.msu.edu/rusle/kfactor.htm

59. Mishra, A., Kar, S., & Singh, V. P. (2007). Prioritizing structural management by quantifying the effect of land use and land cover on watershed runoff and sediment yield. Water Resources Management, 21(11), 1899-1913. https://doi.org/10.1007/s11269-006-9136-x

60. Le Roux, J. J. (2005). Soil erosion prediction under changing land use on Mauritius (Doctoral dissertation, University of Pretoria). URI: http://hdl.handle.net/2263/25468

61. Roose, E. J. (1977). Application of the universal soil loss equation of Wischmeier and Smith in West Africa. In Soil Conservation and Management in the Humid Tropics; Proceedings of the International Conference. In: Greenland, D.J.

62. De Jong, S. M. (1994). Derivation of vegetative variables from a Landsat TM image for modelling soil erosion. Earth Surface Processes and Landforms, 19(2), 165-178. https://doi.org/10.1002/esp.3290190207

63. Pandey, A., Chowdary, V. M., & Mal, B. C. (2009). Sediment yield modelling of an agricultural watershed using MUSLE, remote sensing and GIS. Paddy and Water Environment, 7(2), 105-113. https://doi.org/10.1007/s10333-009-0149-y

64. Shinde, V., Tiwari, K. N., & Singh, M. (2010). Prioritization of micro watersheds on the basis of soil erosion hazard using remote sensing and geographic information system. International Journal of Water Resources and Environmental Engineering, 5(2), 130-136. https://doi.org/10.5897/IJWREE.9000046

65. Sharma, A., Tiwari, K. N., & Bhadoria, P. B. S. (2011). Effect of land use land cover change on soil erosion potential in an agricultural watershed. Environmental monitoring and assessment, 173(1-4), 789-801. https://doi.org/10.1007/s10661-010-1423-6

66. Lal, D., Patil, M., Kumar, S., Gotekar, Y., Karwariya, S., & Kumar, R. (2017) Land Degradation and Soil Loss Estimation by Rusle and GIS Technique: A Case Study. Journal of Climate Change and Water, 2(1), 34-46

67. Ahmad, I., Vera, V., & Vera, M. K. (2015). Application of curve number method for estimation of runoff potential in GIS environment. In 2nd International Conference on Geological and Civil Engineering, IPCBEE (Vol. 80, pp. 16-20). https://doi.org/10.7763/IPCBEE

68. Chakraborty, S., Pandey, R.P., Mishra, S. K., & Chaube, U. C. (2015). Relation between Runoff Curve Number and Irrigation Water Requirement. Agricultural research, 4(4), 378-387. https://doi.org/10.1007/s40003-015-0184-4.

69. Singh, A., Chen, E. Y., Lugovoy, J. M., Chang, C. N., Hitzeman, R. A., &Seeburg, P. H. (1983). Saccharomyces cerevisiae contains two discrete genes coding for the α-factor pheromone. Nucleic acids research, 11(12), 4049-4063. https://doi.org/10.1093/nar/11.12.4049

70. Gajbhiye, S., Mishra, S. K., & Pandey, A. (2014). Relationship between SCS-CN and sediment yield. Applied Water Science, 4(4), 363-370. https://doi.org/10.1007/s13201-013-0152-8

Spatio-Temporal monitoring of Qeshm mangrove forests through machine learning classification of SAR and optical images on Google Earth Engine

Mostafa Mahdavifard[1], **Sara Kaviani Ahangar[2]**, **Bakhtiar Feizizadeh[*1]**, **Khalil Valizadeh Kamran[1]**, **Sadra Karimzadeh[1]**

[1]*University of Tabriz, Department of Remote Sensing and GIS, Iran*
[2]*University of Hormozgan, Department of Combat Desertification, Iran*

Abstract

Mangrove forests are considered one of the most complex and dynamic ecosystems facing various challenges due to anthropogenic disturbance and climate change. The excessive harvesting and land-use change in areas covered by mangrove ecosystems is critical threats to these forests. Therefore, the continuous and regular monitoring of these forests is essential. Fortunately, remote sensing data has made it possible to regularly and frequently monitor this forest type. This study has two goals. Firstly, it combines optical data of Landsat- 8 and Sentinel-2 with Sentinel-1 radar data to improve land cover mapping accuracy. Secondly, it aims to evaluate the SVM machine learning algorithms and random forest to detection and differentiate forest cover from other land types in the Google Earth Engine system. The results show that the support vector machine (SVM) algorithm in the S2 + S1 dataset with a kappa coefficient of 0.94 performs significantly better than when used in the L8 + S1 combination dataset with a kappa coefficient of 0.88. Conversely, the kappa coefficients of 0.89 and 0.85 were estimated for the random forest algorithm in S2 + S1 and L8 + S1 datasets. This again indicates the superiority of Sentinel-2 and Sentinel-1 datasets over Landsat- 8 and Sentinel-1 datasets. In general, the support vector machine (SVM) algorithm yielded better results than the RF random forest algorithm in optical and radar datasets. The results showed that using the Google Earth engine system and machine learning algorithms accelerates the process of mapping mangrove forests and even change detection.

1. Introduction

Mangrove forests are swampy plant communities located in tropical regions between sea and land on tropical and subtropical coastlines [1-2]. These forests are prolific ecosystems with significant ecological and economic consequences [3-4]. Mangrove forests help reduce coastal flooding and erosion and protect inland farms, livestock and aquaculture, and other coastal communities against natural hazards such as tornadoes and storms [5]. However, these forests are at high risk due to rapid population growth, poor planning, and unbalanced economic development. The increasing problems related to mangrove forests worldwide are serious issues faced by coastal ecosystems. Unfortunately, these forests are affected by human habitats, pollution, storms, and sea waves [6]. In Iran, this

type of forest is under threat due to the following factors: excessive harvesting in the branches of these forests, road development, the improper establishment of industries, forest use without proper recreational planning, pollution caused by oil hydrocarbons, increasing aquaculture activities and the general lack of environmental mechanisms in these forests [7].

It is impossible to monitor mangrove forests traditionally since they are located in intermedia areas [8]. Meanwhile, satellite remote sensing data can be used for large areas over time so that this technology can be used as an alternative to mangrove forest monitoring. Many researchers have mapped mangrove forests worldwide, using various satellite remote sensing data, including optical images [9-10] and SAR [11]. Mangrove forests can be monitored on a large scale, using high-resolution spatial images (less than 1 meter), such as

* **Corresponding Author**

(mostafamahdavi842@gmail.com) ORCID ID 0000-0001-9811-5428
(sarakaviani11@gmail.com) ORCID ID 0000-0003-0382-1480
*(feizizadeh@tabrizu.ac.ir) ORCID ID 0000-0002-3367-2925
(valizadeh@tabrizu.ac.ir) ORCID ID 0000-0003-4648-842X
(sadra.karimzadeh@gmail.com) ORCID ID 0000-0002-5645-0188

Worldview, Quickbird, and aerial photographs; however, due to cost constraints, data volume used by users is limited. As a result, freely accessible satellite images (e.g., Landsat-8 and Sentinel-2) and medium spatial resolution (30 and 10 m) are widely used for extracting data of large-scale mangrove forests [12]. Continuous cloud coverage and inundation of tidal lands in coasts prevent access to high-quality optical data [13-15]. With the advent of Sentinel-1 C-band synthetic aperture radar images, it is possible to provide land cover classifications in repetitive, cloud-covered environments [16]. SAR plays an essential role in monitoring the biophysical parameters of mangrove forests since its microwave energy can penetrate cloud masses formed continuously in tropical regions, making it possible to obtain data throughout the year [17]. Combining optical and SAR data can improve classification accuracy, contributing significantly to the protection of mangrove forests. This type of data combination provides more detailed information for studying the spatial distribution and dynamic changes of mangrove forests, which play an essential role in developing conservation and management policies [18]. The increase in the number of sensors and free satellite data has led to new platforms that help users select and process large volumes of spatial data. Google Earth Engine (GEE) is an excellent example of a cloud-based computing platform that provides easy access to satellite data sets on a planet-scale [19-20]. For example, GEE provides free preprocessed satellite series data (including Landsat-, Sentinel-2, and Sentinel-1), along with the required disk space and advanced machine learning classification algorithms [1]. The online GEE system offers more than 15 classification techniques, with most studies conducted rely on machine learning algorithms [21-22] CART, RF, and SVMs. This is because these methods have proved to be some powerful ways to classify land cover. Such methods based on free data and robust algorithms can be helpful for regular monitoring [23]. So far, many studies have been done on mangrove forests using optical and radar remote sensing methods worldwide. In West Africa, mangrove forests were mapped using machine learning algorithms in Google Earth and Sentinel-2 images, with thematic maps found to have an accuracy of 90% [23]. A comparative study to differentiate mangrove forests from non-mangrove forests using NDVI, NDWI, SAVI indices, SR, and CMRI showed that the combined CMRI index has better accuracy than other indicators used [5]. Multimodal mapping of mangrove forests in China showed that integrating RADARSAT-2 polarization data and Landsat-8 data can increase the overall accuracy (OA) by 95%, while optics classification alone can produce an OA of about 83% [18]. A study integrating Sentinel-2 multispectral time-series images with Sentinel-1 images for mapping Spartina alterniflora and Mangrove in Zhangjiang Est showed that the 10-meter maps produced represented a relatively stable spatial pattern mangrove and rapid expansion Spartina alterniflora [24]. Another study using Landsat- 8 multidimensional data to map and identify mangrove changes in Pong Vietnam showed that Landsat- multidimensional data, along with image segmentation and GIS approaches, has a high potential to

map mangrove forests in the coastal area [25]. Three spectral criteria (spectral match degree (SMD), normalized difference ° mangrove index (NDMI), and shortwave infrared absorption) were found to better differentiate mangrove forests from other vegetation in Landsat- images 8. The results showed that using spectral criteria (UA = 85%, PA = 94%, OA = 95%) is better than using raw band reflectance data (UA = 72%, PA = 82). ٪, OA = 90%) [26]. the changes in mangrove forests around Trat Province in Thailand were mapped by analyzing and processing 3-decade images via the GEE Web System. The results show that the use of a web-based monitoring system of GEE contributes to mapping and preserving the coastal ecosystems [27]. .Hu et al[12] used Sentinel-1 and Sentinel-2 time-series data in Google Earth Engine in China to map mangrove forests on a national scale. The results showed the significant capability of Sentinel-1 and Sentinel-2 images in producing accurate maps of mangrove forests with high resolution in GEE. Producing accurate thematic maps of mangroves with Sentinel 1 and Sentinel 2 data is important and necessary for planners. The result showed an increase in overall accuracy and kappa coefficient [28]. Ghorbanian et al. [29] used the combination of Sentinel 1 and Sentinel 2 images to create a functional index. The results of the researchers showed that the performance of the combined index was good in mangrove identification and it is widely used in large-scale mangrove mapping. In a study, the combination of optical and star data was used for mangrove mapping. The results showed that the combination of optical and SAR data can effectively improve the classification accuracy [30]. The present study uses the Cloud Google Earth Engine to monitor and map the Qeshm mangrove forests (southern Iran), which are designated as protected forests. The first purpose of this study was to combine images obtained from optics and radar (Sentinel-2 and Sentinel-1- Landsat-8 and Sentinel-1) systems with a different spatial resolution to compare them in terms of the accuracy of resulting thematic maps. The second purpose of this study was to compare and evaluate the performance of two algorithms, namely, SVM and RF machine learning, to identify mangrove forests and differentiate them from other land covers in the combined optics and radar images in the Google Earth Engine cloud platform. In previous studies, Sentinel-2 and Landsat-8 with optical nature were not integrated with Sentinel 1 SAR satellite with radar nature, which is superior to previous studies in the present study, and two RF and SVM machine learning classifiers were used simultaneously.

2. Material, Method and Case studies

2.1. Case studies

The case study is the mangrove forest in Hormozgan province in Iran (Figure 1a). Qeshm Island, with an area of approximately 1.491 square kilometers, is the largest island in the Persian Gulf and 2.5 times the size of Bahrain. Mangrove forests are located between Khamir City and Qeshm Island between latitude 26.45 ° - 27.00 ° and longitude 55.20 ° - 55.51 ° (Figure 1b). Figure 1c

shows the map of land cover in the protected mangrove area. These forests account for the largest area of forests in Iran and even in the Persian Gulf countries, covering 85% of Iranian mangroves. The majority of the mangrove forest cover in this area includes Avincina or mangrove. The mangrove biosphere has an area of 20 by 20 km, where several tidal channels have been identified [31].
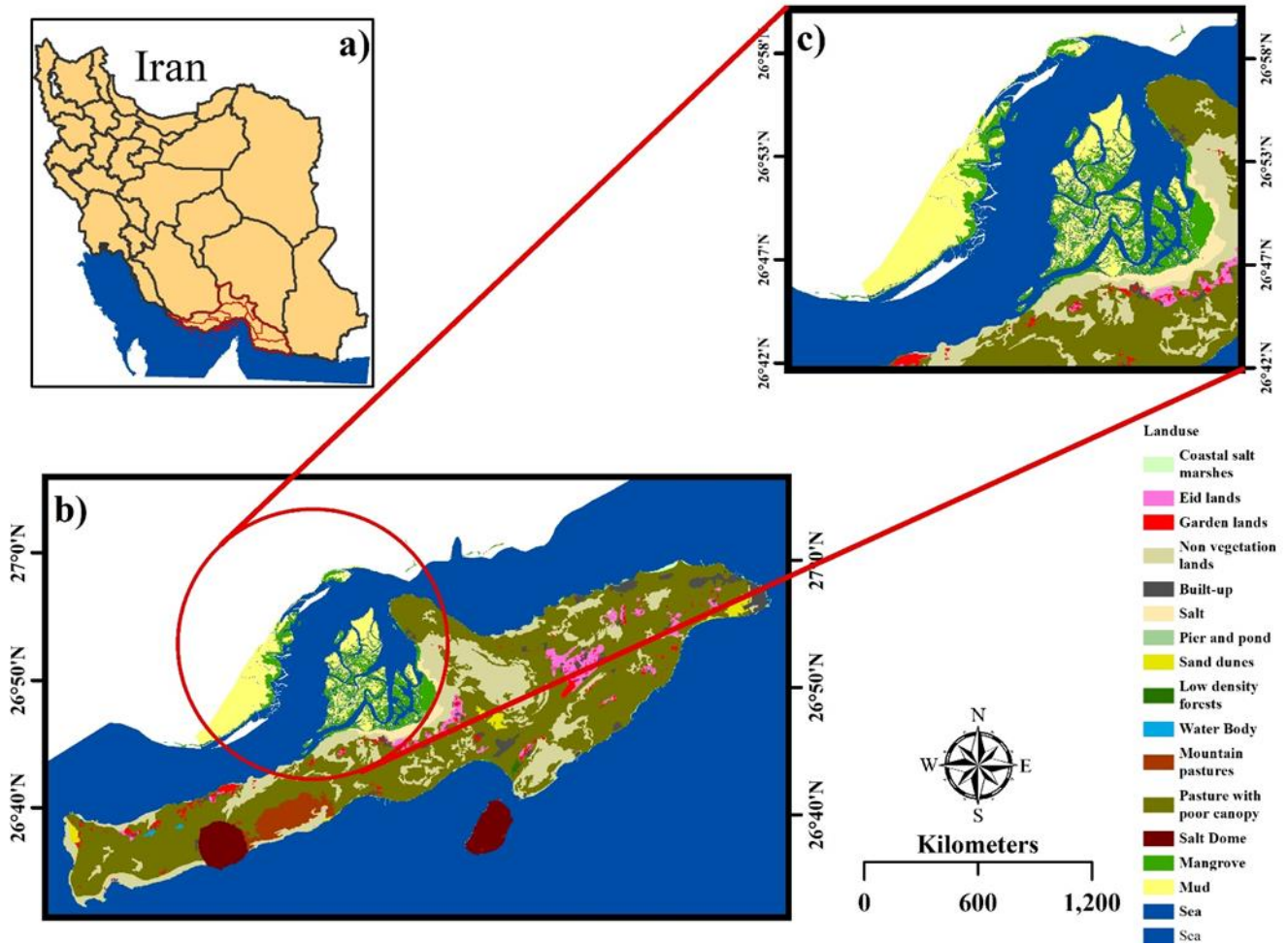
Figure 1. The geographical Location, Hormozgan Province in Iran (a), updated land use map of Qeshm Island (b), the land use map of the mangrove forests in the study area (c)

2.2. Data

2.2.1. Reference data

In this study, three datasets are as reference data. The land-cover map of the study area, global mangrove data [32], and high-resolution images obtained by Google Earth. To create a single data, the national land cover map was updated with global mangrove data in open-source QGIS software and was used as reference data and high-resolution Google Earth Images to choose validation samples. Samples of water classes and tidal areas were selected and collected from Google Earth photos, while samples of mangrove and mud classes were taken from the updated land cover map.

2.2.2. Satellite data

Launched on February 11, 2013, the Landsat-8 satellite is one of the new multispectral satellites, imagining the entire Earth every 16 days. This satellite has two OLI sensors and an infrared thermal sensor (TIRS). The Landsat-8 satellite has 11 spectral bands in the visible range, reflected infrared and thermal infrared with 15-, 30-, and 100-meters spatial resolution. The second satellite of the Sentinel series is called Sentinel-2, which began its operation on June 23, 2015. The Sentinel-2 satellite includes two Sentinel-2A and Sentinel-2B twin satellites. This satellite has 13 spectral bands in the visible range, near-infrared, and middle infrared with different resolutions of 10, 20, and 60 meters. Although this satellite is twin, its spatial resolution has been reduced to 5 days compared to the Landsat--8 satellite, which is unique.

Sentinel-1 is one of the Sentinel-satellites series that falls in the radar category, capturing the image of the Earth in the C band at two polarities VV and VH. This satellite has a spatial resolution of 5 to 20 meters per Azimuth and, like the Sentinel-2 optical satellite, has two types, A and B, which have reduced the review period of this satellite to 5 days.

This study uses the following: the average series images of monthly cloud-free combination (all months of 2016 except May due to severe cloudiness), Sentinel-2 Level1C atmosphere reflection in Google Earth Engine (ee.ImageColection ID: COPERNICUS / S2), monthly time series images of a cloud-free combination of Landsat-8

for the high reflection atmosphere in Google Earth Engine (ee.ImageColection ID: LANDSAT- / LC8 / C01 / T1_TOA) as well as GRD Sentinel-1 monthly time series images in Google Earth Engine (ee.ImageColection ID: COPERNICUS / S1). Many researchers have suggested VH polarization to monitor land cover [33-34], so in this study, the Backscatter value of VH polarization was used. Table 1 describes the data used.

Table 1. Characteristics of satellite data

Satellite	Landsat-8	Sentinel-2	Sentinel-1
Sensor (type)	OLI (Optical)	MSI (Optical)	SAR (Radar)
Data Level	Level 1	Level 1C	GRD
Spectral Band/ Polarization (um)	B3 (560) B4 (660) B5 (865)	B3 (560) B4 (665) B8 (842)	C-VH (5.62 cm)
Spatial Resolution (m)	30	10	5 * 10
Repeat Frequency (days)	16	5	6
Time Series	2016/1/1 – 2017/1/1		

2.3. Methods

As shown in the procedure flowchart (Figure 2), the spectral indices were initially calculated separately based on the time series satellite images in the Google Earth Engine system (Landsat-8 and Sentinel-2).

Secondly, the spectral indices used for each satellite were combined with the series images Sentinel-1 and placed in a dataset. Third, the mangrove forest cover was mapped using machine learning classification algorithms (RF and SVM) in GEE. Finally, to evaluate the classified maps, they were compared with the reference data.
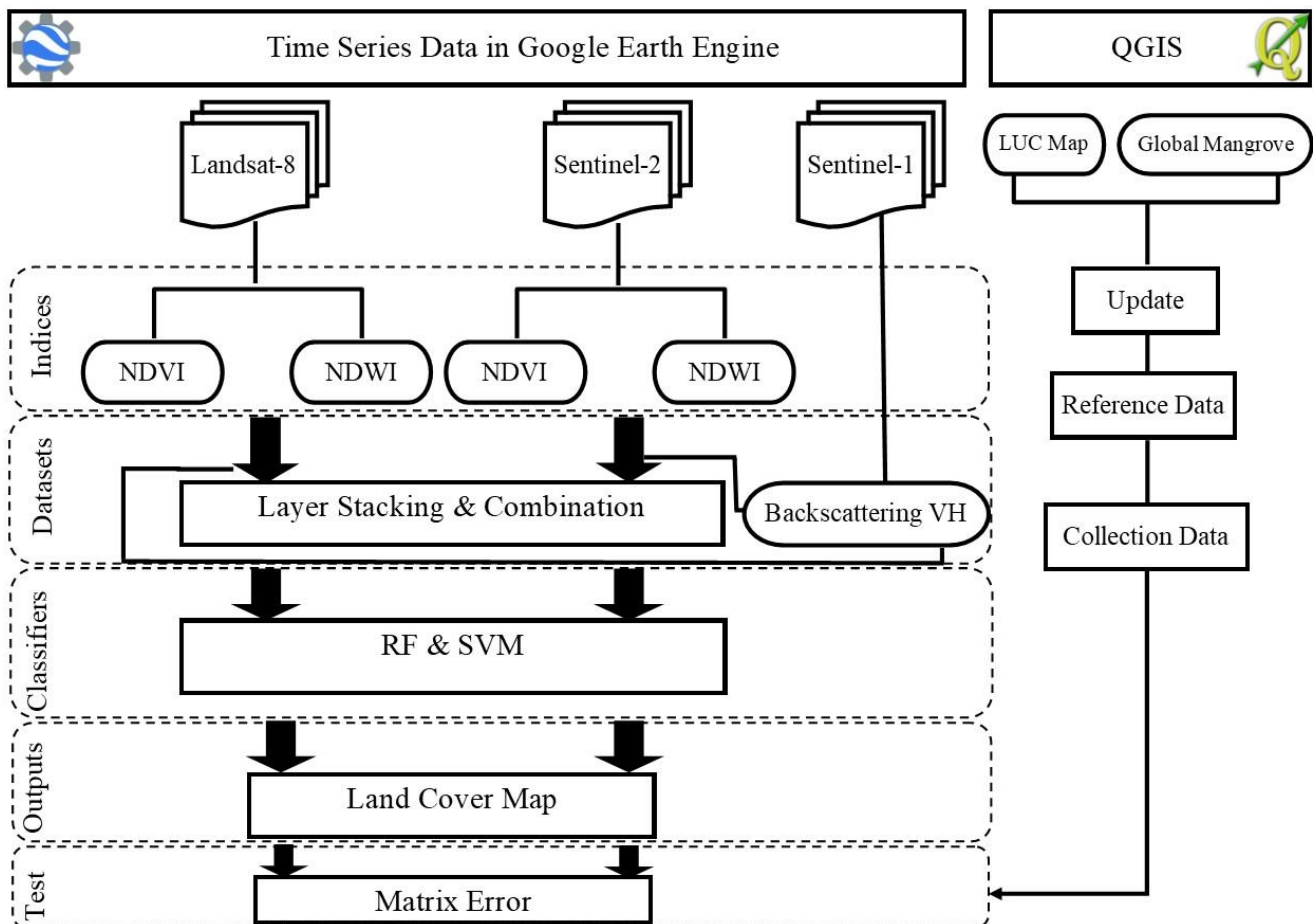
Figure 2. Research flowchart

2.3.1. Calculation of NDVI Time-Series

The present study detects and differentiates mangrove jungles from other vegetation and land, using the Normalized Differential Vegetation Index (NDVI). NDVI index was applied separately to the Sentinel-2 and Landsat-8 multispectral time-series images in Google Earth Engine. NDVI is one of the most common indicators used for vegetation dynamics at a regional and global scale [35-36]. This index developed by [37] (T) is calculated based on the ratio between the TOA reflectivity of the red band in the spectral range of 0.66

μm and the near-infrared band (NIR) in the range of 0.86 μm [38]. The value of NDVI ranges from - 1 to 1. Low NDVI values indicate vegetation under moisture pressure, and higher values indicate a higher level of green vegetation density [39-40]. This index is calculated based on Equation 1:

$$NDVI = \frac{NIR - Red}{NIR + RED} \qquad (1)$$

NIR represents the near-infrared band in the spectral range of 865 and 842 nm, and the red band ranges from 660 to 665 nm.

2.3.2. Calculation of NDWI Time-Series

Given the presence of water canals in the mangrove-covered area, water canals were identified and differentiated from other water bodies using the NDWI Normalized Differential Index in GEE. To this end, this index was calculated on time-series images (Landsat- 8 and Sentinel-2) to identify water channels. NDWI index is the best indicator for mapping water size. It is also a suitable index for monitoring the hydrological condition of wetlands. The value of NDWI ranges from 1 and-1, with negative values or near negative and positive values representing a water area with high humidity. NDWI was calculated using Equation 2 [41]:

$$NDWI = \frac{Green - NIR}{Green + NIR} \qquad (2)$$

NIR represents the near-infrared band in the spectral range of 865 and 842 nm, Green: the green band is in the range of 560 nm.

2.3.3. Data integration and combination

After calculating the spectral indices on the satellite imagery used, all the time series indices (NDWI, NDVI from the Sentinel-2 image) and the VH polarization time series redistribution image (Sentinel-1) were stacked and integrated into a single data set. Also, all the time series indices (NDWI and NDVI) calculated for Landsat-8 and the VH Sentinel-1 polarization time series redistribution image were stacked and integrated into a single data set. The Landsat-8 and Sentinel-1 combination datasets included 33 bands (11 NDVI indices, 11 NDWI indices, and 11 VH redistribution images), and the Sentinel-2 and Sentinel-1 combination datasets, had 33 bands. All these processes were performed in the GEE system.

2.3.4. Determining training data of classification

A total of 500 points in the area under study were selected in GEE to determine the training samples to classify four land cover classes (mangrove, tidal lands, mud, and seawater). The appropriate distribution of the samples was the primary criterion for selecting the sample. The data were collected using a combination of NDVI (Feb-Mar-Jan) and (Feb-Sep-Apr) in the images of Sentinel-2 and Landsat-8, respectively, due to unstable

environmental conditions such as submersion of tidal areas. This study used a completely random sampling method based on the visual evaluation of images and the ratio of different land cover in the study area. Jensen says that classes that are more important and have more importance are sampled more [42]. So, since the main purpose of the current paper was to separate mangroves from other lands by the mentioned method, we took more samples for the main purpose, which was mangroves, and less sampling should be done for other lands. So, 200 and 100 points were collected for the mangrove class and the other three land cover classes, respectively.

2.3.5. Image classification

Machine learning algorithms have been used in remote sensing for decades (e.g., from basic algorithms such as PCA and K-Means to more complex classifications and regression frameworks such as SVMs, decision trees, random forests, and artificial neural networks [43]. It has received special attention for land use and land cover [44-45]. There are many classification algorithms, but RF and SVM were also used in this paper due to their frequency and most use in previous studies. In a study to prepare a land cover map in the GEE system, they used machine learning classifications and concluded that RF and SVM algorithms have higher accuracy than other machine learning classifications [46].

Random Forest is a non-parametric "machine learning" algorithm [47-48]. Nowadays, RF is considered one of the most widely used algorithms for land cover classification, which uses remote sensing data [49-51]. This classification method uses bootstrap aggregating or bagging to generate random vectors with N samples (N: the size of the primary input training data) and select the training data for each class [52]. Each pixel is assigned to one class based on the popular votes of all tree predictors [23].

SVM methods have also been successfully applied in various classification approaches [53-54]. SVM is a machine learning method based on Vapnik Chervonenkis's dimension theory, drawing on the principle of minimum structural risk [55]. Generally, SVM is widely used and can turn nonlinear problems into linear problems by creating a different function in high-dimensional space; therefore, it is not affected by sample dimensions and can prevent misclassification [56]. The Classifier package manages and supports machine learning algorithms in the GEE system. These classifiers include CART, Random Forest, NaiveBayes, and SVM. In this research, RF and SVM classification in the classifier package of the GEE system was used to classify land cover. For this purpose, the datasets created for each satellite (Sentinel-2 + Sentinel-1 and Landsat-8 + Sentinel-1) containing calculated spectral indices and redistribution of radar VH polarization were each separately placed as the input of RF and SVM classification algorithms. Note: 1, 50 trees were taken into account using a trial-and-error method in order to perform the RF classification for the desired result. 2-100% of the points collected in the previous stage (determination of training data) were designated as

training points in the image classification process since we had access to reference data for the validation (testing) of RF and SVM classifiers.

2.3.6. Validation

In this study, the accuracy of land cover maps obtained from the classifiers was validated, using a reference map (combination of national land cover map and global forest cover); therefore, 30 samples (for each class: mangrove, mud, tidal areas, and sea) and a total of 120 samples as a control point on the reference map were selected and determined to assess the accuracy.

Researchers strongly suggest that one can't use the kappa coefficient parameter to compare and evaluate the accuracy of thematic maps obtained from image classification [50-57]. The advantage and capability of kappa coefficient is that it works well in unbalanced data. Another advantage of Kappa is that it can be used for multiple classes. Due to the unbalanced nature of the data, this coefficient is fruitful. Therefore, this study assesses the accuracy of classification methods using the optimal parameters extracted from the error matrix, such as overall accuracy (OA), producer's accuracy (PA), and user accuracy (UA). Table 2 shows the details of the assessment parameters used in this study.

Table 2. The statistical parameters of error matrix used in this study

Matrix Error	Formula	Description	Reference
Overall accuracy	$\dfrac{1}{N}\sum Pii$	Where OA defines the total accuracy of the model, test pixels are described by N, and P pii represents the total number of correctly classified pixels.	[58]
kappa	$\dfrac{N\sum_{i=1}^{r} xii - \sum_{i=1}^{r}(x_{i+} \times x_{+1})}{N^2 - \sum_{i=1}^{r}(x_{i+} \times x_{+1})}$	Where k is the number of rows (e.g., land-cover classes) in the error matrix, xii is the number of observations in row i and column i, and xi+ and x+j are the marginal totals for row i and column j, respectively, and N is the total number of samples.	
User's accuracy, UA	$\dfrac{x_{ii}}{x_{1+}}$	Where x_{ii} the number of correctly classified pixels is, x_{1+} is the number of pixels in a category. x_{+j} is the number of sample pixels in a category.	[42]
Producer's accuracy, PA	$\dfrac{x_{jj}}{x_{+j}}$		

3. Results

3.1. Mangrove phenology cycle and other vegetation

Figure 3 shows the monthly average of the NDVI time series of the Sentinel-2 and Landsat-8 satellites. The NDVI values of the mangrove cover and the typical vegetation in the Sentinel-2 images are much higher than the NDVI values calculated from the Landsat-8 images. In general, the NDVI of mangrove cover in Sentinel-2 and Landsat-8 was almost higher than that of normal vegetation per month, while the changes in typical vegetation fluctuated relatively highly per month. This factor is a distinguishing feature for identifying and differentiating mangroves from other vegetation in the area. As this figure shows, it can be concluded that spring is the best time to monitor mangrove forests in the study area (January, February, March) since the NDVI values in Landsat-8 and Sentinel-2 are 0.57 and 0.64 percent, respectively, indicating a high level of greenery of mangroves forests compare to other months of the year.

3.2. Accuracy assessment

Table 3 shows the resulting maps' accuracy obtained using the two classification methods for the combination datasets (S2 + S1 and L8 + S1). According to the tables, the mangrove class has the highest user accuracy among the four land cover classes based on the two algorithms

used on the 3 datasets; that is, the user accuracies of the mangrove class for SVM and RF algorithms related to the data (L8 + S1) are 100 and 96.30, respectively, while the user accuracies of the mangrove class related to dataset S2 + S1 are 100 and 93.55 for the SVM algorithm and the RF algorithm, respectively. Also, both classification methods in optical and radar satellite datasets had good performance in differentiating other classes (user accuracy above 81% for water, mud, and tidal land classes). The manufacturer's accuracy follows the same patterns for evaluating each class. The SVM and RF datasets (S2 + S1) are 95.79 and 92.43, respectively, and the accuracies of the SVM and RF datasets (L8 + S1) are 91.52 88.98, respectively. The kappa coefficients of the SVM algorithm for the datasets (S2 + S1) and (L8 + S1) are 0.94 and 0.88, respectively. The kappa coefficients of the RF algorithm for the datasets (S2 + S1) and (L8 + S1) are 0.89 and 0.85%, respectively.

Figures 4 and 5 illustrate the maps obtained from SVM and RF classifications of Optical and SAR datasets. As shown in the selected section of the S2 + S1 and L8 + S1 maps by the SVM algorithm, this algorithm, in addition to the acceptable classification of mangrove lands, has been able to distinguish well in both satellite scenarios of mud lands and tidal lands. However, the selected section in the S2 + S1 and L8 + S1 maps, classified by the RF algorithm, could not distinguish between tidal, mud lands, and sea. It has a potent mix of mud classes and tidal lands.
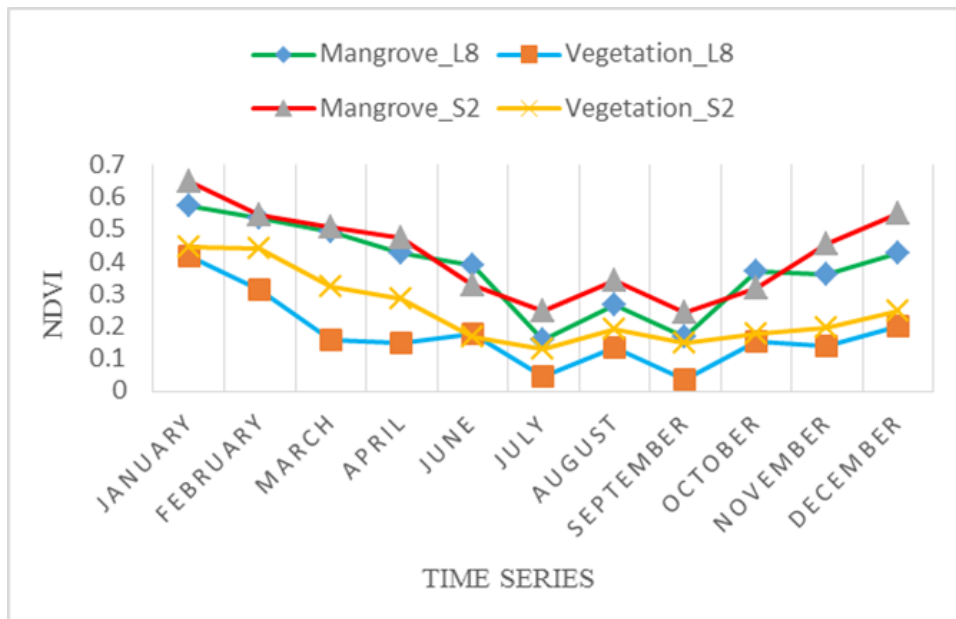
Figure 3. Comparing the average time-series images of NDVI for mangrove cover and typical vegetation cover in Landsat-8 and Sentinel-2

Table 3. The parameters of matrix for algorithms

Classification/Satellite	class	Mangrove	Mud	Tidal Zone	Sea	PA	UA
SVM-Sentinel2+Sentinel1	Mangrove	96.55	0	0	0	96.55	100
	Mud	3.45	100	0	0	100	96.77
	Tidal	0	0	96.67	10	96.67	90.63
	Sea	0	0	3.33	90	90	96.43
	Overall Accuracy = 95.79						
	Kappa Coefficient = 0.94						
RF-Sentinel2+Sentinel1	Mangrove	100	6.67	0	0	100	93.55
	Mud	0	93.33	0	0	93.33	100
	Tidal	0	0	93.33	16.67	93.33	84.85
	Sea	0	0	6.67	83.33	83.33	92.59
	Overall Accuracy = 92.43%						
	Kappa Coefficient = 0.89						
SVM-Landsat-8+Sentinel1	Mangrove	92.86	0	0	0	92.86	100
	Mud	7.14	100	0	3.33	100	90.91
	Tidal	0	0	96.67	20	96.67	82.86
	Sea	0	0	3.33	76.67	76.67	95.83
	Overall Accuracy = 91.52%						
	Kappa Coefficient = 0.88						
RF-Landsat-8+Sentinel1	Mangrove	92.86	3.33	0	0	92.86	96.30
	Mud	7.14	96.67	0	0	96.67	93.55
	Tidal	0	0	96.67	20	86.67	81.25
	Sea	0	0	3.33	80	80	85.71
	Overall Accuracy = 88.98%						
	Kappa Coefficient = 0.85						

3.3. Comparison of land cover area

Despite the increased improvement of map accuracy through combining radar and optics data in two machine learning methods (user accuracy greater than 81%), the resulting land cover maps differ in terms of area (Figure 6). As shown in Figure 6, the area of the land cover map obtained from the SVM algorithm for the combined dataset of Sentinel-2 and Sentinel-1 (mangrove area: 8333.41, mudflat: 25265.34, tidal areas: 13204.44, and sea: 27707.19 hectares) was nearly comparable with the area of the land cover map obtained from Landsat- 8 and Sentinel-1 datasets (mangrove area: 8544.72, mudflat: 24702.54, tidal areas: 12472.46 and sea: 287911.08 hectares).

However, the map obtained from the Landsat-8 and Sentinel-1 combination datasets based on the RF algorithm yielded a smaller estimate of the area of mangrove forests (7305.25 ha) compared to that obtained by the Sentinel-2 and Sentinel-1 datasets. The area of other lands based on RF algorithm in Sentinel-2 and Sentinel-1 combination datasets (mud area: 24674.31, tidal areas: 14051.36 and sea: 27209.9 hectares, respectively) gave results somewhat similar to those obtained from Landsat- 8 and Sentinel-1 combination datasets (244.85 mud area): Tidal zones: 12477.64, sea: 30301.07), but this classification method did not yield a better result compared to the SVM algorithm.
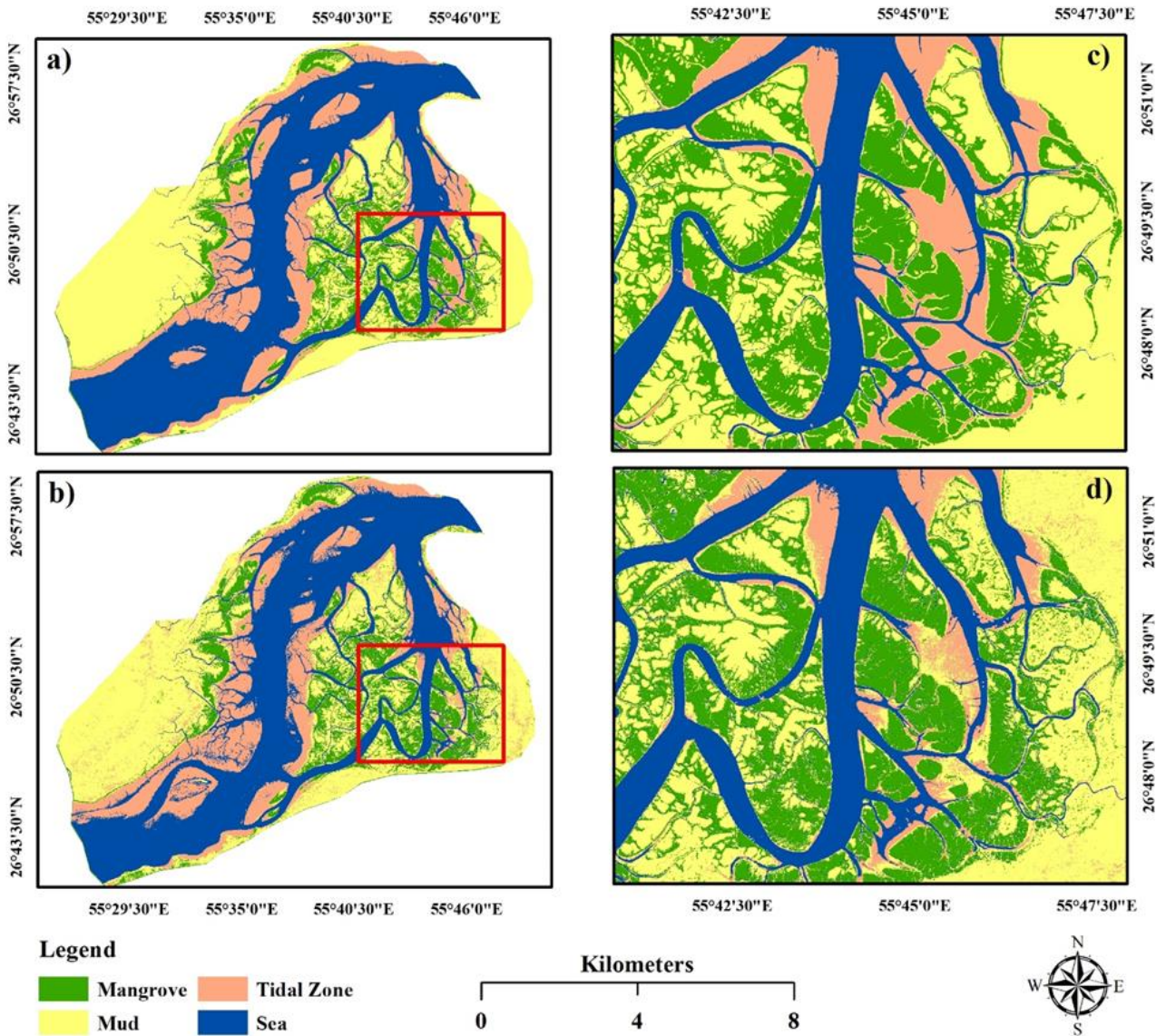
Figure 4 . Land cover map based on SVM algorithm related to S2 + S1 (a) combination dataset, SVM land cover map of S2 + S1 database in zoom-out mode (c), Land cover map based on RF algorithm related to S2 + S1 (b) combination database RF land cover data set S2 + S1 in zoom-out mode (d)

4. Discussion and Conclusion

This study aims to use a combination of optical and radar datasets (Landsat- 8 + Sentinel-and Sentinel-2 + Sentinel-1) to improve the accuracy of land cover maps and compare and assess them. Given the objectives of this study, the land cover was mapped using the new Google Earth Engine processor. Mondal et al. [23] used CART and RF machine learning algorithms to map mangrove forests. They stated that the accuracy of the maps obtained from the used algorithms is more than 90%, while in the current study, the land cover maps prepared based on the RF algorithm in GEE had an accuracy of less than 91%. Dong et al. [24] integrated the Sentinel-1 and Sentinel-2 images in the GEE to differentiate the Spartina alterniflora from the mangrove. Their results show that the combination of optics and radar data improved the accuracy of classified maps by about 99%. This theory is entirely consistent with our study because the use of a combination of optics and radar data in both 30-meter and 10-meter images has resulted in better differentiation of the mangrove

class from other land covers. Jahanbakhshi and Ekhtesasi [59] Applied SVM and RF algorithms to vegetation classification and land use. They concluded that the SVM algorithm is more valuable, providing logical results that confirm the current study results. Zhen et al. [2] used SAR data in the C and Landsat-8 bands to develop a suitable method for improving the classification of mangrove forests. Their results showed that the combination of optical data with radar yields an overall accuracy of up to 95%, confirming the current study results regarding the combination of Sentinel-1 and Sentinel-2 (SVM) and the overall accuracy of 95% resulting from such a combination. In general, managers and planners usually require frequent and regular monitoring of marine ecosystems such as mangrove forests monthly or annually. Such monitoring requires a large amount of satellite data and a powerful hardware system, which the GEE system has provided in recent years. EGG includes large amounts of satellite data (such as Landsat-8, Sentinel-2, and Sentinel-1) and advanced machine learning algorithms such as RF and SVM in the cloud and is available completely free. For this purpose, a

combination of free satellite data categorized as radar and optical data has improved land cover classification in the cloud-based GEE. Given the objectives of the present study, hybrid satellite data (Landsat-8 + Sentinel-1 and Sentinel-2 + Sentinel-1), SVM, and RF machine learning algorithms were used in the GEE. Due to their high spectral power and strong interpretation, optical data can achieve better classification results but requires more accurate spatial information concerning the biophysical properties of vegetation, which has been estimated by radar. In this study, the combined optical and radar variables (NDVI index, NDWI, and VH redistribution) helped improve the algorithms' results. This suggests that optical and radar properties can be combined to map mangrove forests using machine learning algorithms such as RF and SVM. In other words, radar data eliminates the problems of optical sensing and

improves the classification accuracy of thematic maps, especially mangrove mapping, when combined with optical data. In this study, the SVM algorithm in both combination datasets of Landsat-8 + Sentinel1 and Sentinel-2 + Sentinel-1 showed a very reasonable and good result compared to similar use of datasets with RF algorithm. This means that the SVM algorithm is one of the most desirable machine learning algorithms used in land use classification and land use. Thus, based on the results of this study, we recommend using the GEE system and other advanced machine learning algorithms in the cloud space to process time-series data for mapping the land cover. Moreover, it is better to use machine learning algorithms from radar data in-band L for achieving relevant results with high accuracy of 95% due to the very high penetration of such data up to about 25 cm in vegetation.
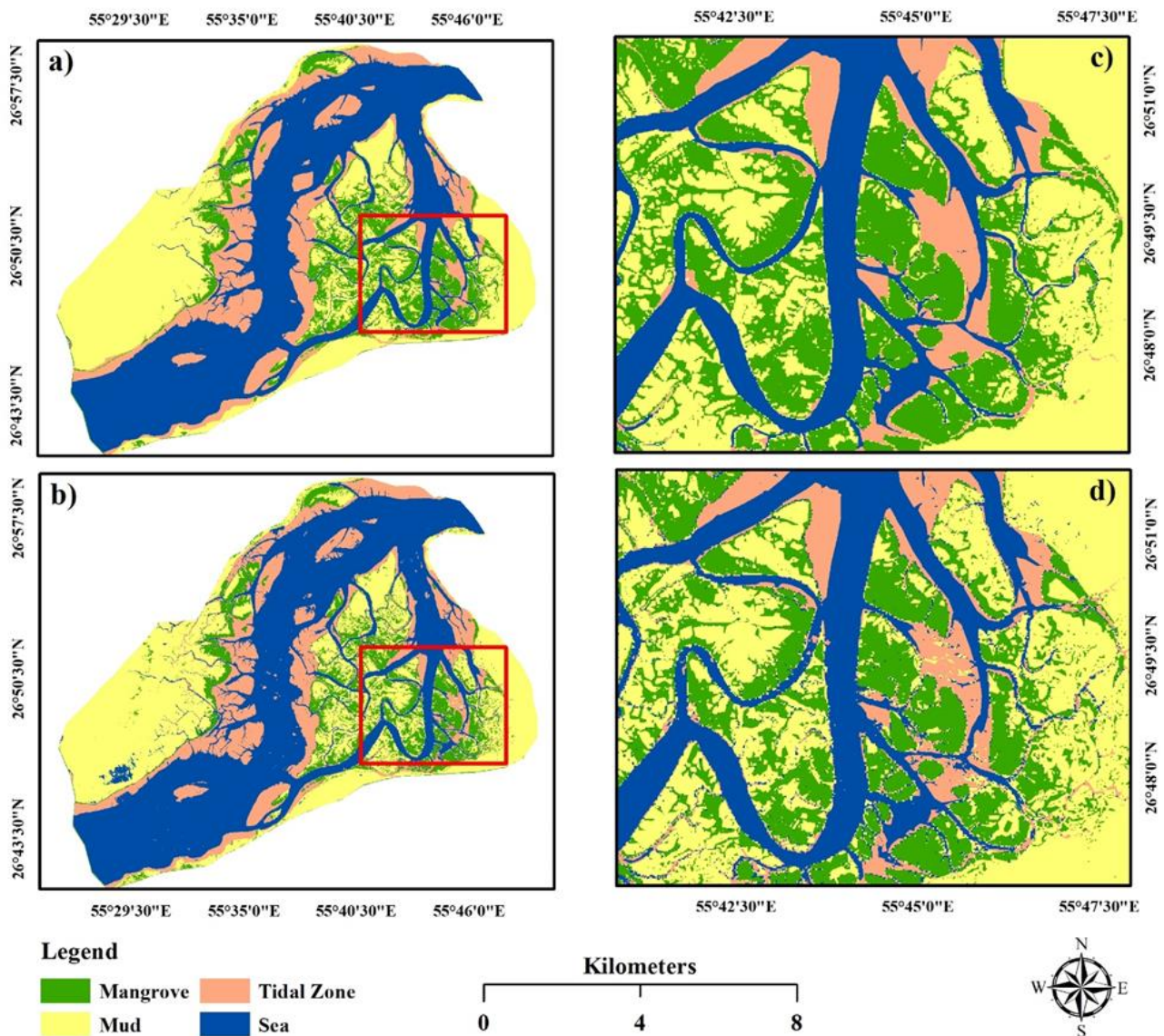
Figure 5. Land cover map based on SVM algorithm related to L8 + S1 (a) combination dataset, SVM land cover map of L8 + S1 combination dataset in zoom-out mode (c), Land cover map based on RF algorithm related to L8 + S1 (b) combination dataset RF land cover data set L8 + S1 in zoom-out mode (d),

	SVM	RF	SVM	RF
	S2 + S1		L8 + S1	
■ Mangrove	8333.41	8574.8	8544.72	7305.25
■ Mud	25265.34	24674.31	24702.54	24426.85
■ Tidal Zone	13204.44	14051.36	12472.46	12477.64
■ Sea	27707.19	27209.9	28791.08	30301.07
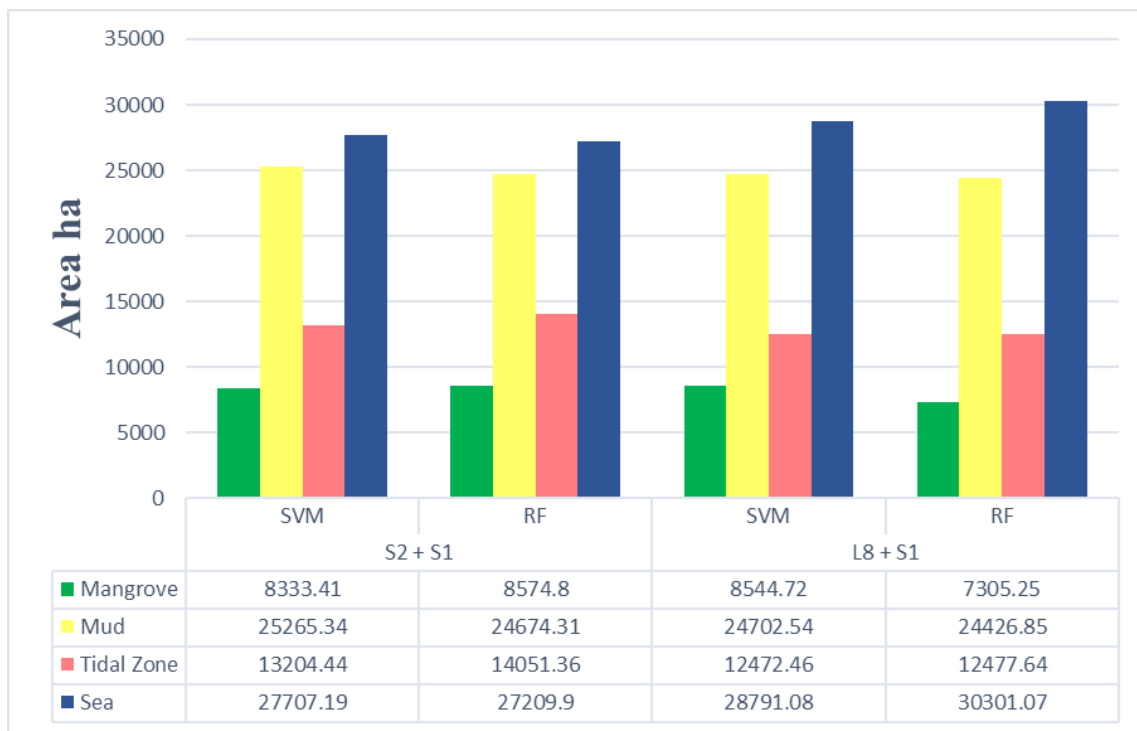
Figure 6. Comparing the area of land cover in combination dataset based on different machine learning algorithms

Author contributions

Mostafa Mahdavifard: Methodology, Data Collection, Image Processing, Validation **Sara Kaviani**: Writing-Original draft preparation, Reviewing and Editing. **Bakhtiar Feizizadeh**: Optic processing **Khalil Valizadeh Kamran:** Mangrove and Optic processing **Sadra Karimzadeh:** SAR processing.

Conflicts of interest

The authors declare no conflicts of interest.

References

1. Giri, C., Long, J., Abbas, S., Murali, R. M., Qamer, F. M., Pengra, B., & Thau, D. (2015). Distribution and dynamics of mangrove forests of South Asia. *Journal of environmental management*, *148*, 101-111.
2. Zhen, J., Liao, J., & Shen, G. (2018). Mapping mangrove forests of Dongzhaigang nature reserve in China using Landsat 8 and Radarsat-2 polarimetric SAR data. *Sensors*, *18*(11), 4012.
3. Collins, D. S., Avdis, A., Allison, P. A., Johnson, H. D., Hill, J., Piggott, M. D., ... & Damit, A. R. (2017). Tidal dynamics and mangrove carbon sequestration during the Oligo–Miocene in the South China Sea. *Nature communications*, *8*(1), 15698.
4. Jia, M., Wang, Z., Wang, C., Mao, D., & Zhang, Y. (2019). A new vegetation index to detect periodically submerged mangrove forest using single-tide Sentinel-2 imagery. *Remote Sensing*, *11*(17), 2043.
5. Gupta, K., Mukhopadhyay, A., Giri, S., Chanda, A., Majumdar, S. D., Samanta, S., ... & Hazra, S. (2018). An index for discrimination of mangroves from non-mangroves using LANDSAT 8 OLI imagery. *MethodsX*, *5*, 1129-1139.
6. Vaiphasa, C. (2006). *Remote sensing techniques for mangrove mapping*. Doctoral Dissertation, Wageningen University and Research.
7. Danehkar, A., Jalali, S.G., 2005. Avicennia marina forest structure using line plot method. Pajouhesh and Sazandegi 67, 18–24
8. Cárdenas, N. Y., Joyce, K. E., & Maier, S. W. (2017). Monitoring mangrove forests: Are we taking full advantage of technology?. *International Journal of Applied Earth Observation and Geoinformation*, *63*, 1-14.
9. Long, B. G., & Skewes, T. D. (1996). A technique for mapping mangroves with Landsat TM satellite data and geographic information system. *Estuarine, Coastal and Shelf Science*, *43*(3), 373-381.
10. Long, J. B., & Giri, C. (2011). Mapping the Philippines' mangrove forests using Landsat imagery. *Sensors*, *11*(3), 2972-2981.
11. Pasqualini, V., Iltis, J., Dessay, N., Lointier, M., Guelorget, O., & Polidori, L. (1999). Mangrove mapping in North-Western Madagascar using SPOT-XS and SIR-C radar data. *Hydrobiologia*, *413*, 127-133.
12. Hu, L., Xu, N., Liang, J., Li, Z., Chen, L., & Zhao, F. (2020). Advancing the mapping of mangrove forests at national-scale using Sentinel-1 and Sentinel-2 time-series data with Google Earth Engine: A case study in China. *Remote Sensing*, *12*(19), 3120.
13. Zhu, X., Meng, L., Zhang, Y., Weng, Q., & Morris, J. (2019). Tidal and meteorological influences on the growth of invasive Spartina alterniflora: evidence from UAV remote sensing. *Remote Sensing*, *11*(10), 1208.
14. Tarantino, C., Casella, F., Adamo, M., Lucas, R., Beierkuhnlein, C., & Blonda, P. (2019). Ailanthus altissima mapping from multi-temporal very high

resolution satellite images. *ISPRS Journal of Photogrammetry and Remote Sensing*, *147*, 90-103.

15. Campbell, A. D., & Wang, Y. (2020). Salt marsh monitoring along the mid-Atlantic coast by Google Earth Engine enabled time series. *PloS one*, *15*(2), e0229605.

16. Fonteh, M. L., Theophile, F., Cornelius, M. L., Main, R., Ramoelo, A., & Cho, M. A. (2016). Assessing the utility of sentinel-1 c band synthetic aperture radar imagery for land use land cover classification in a tropical coastal systems when compared with landsat 8. *Journal of Geographic Information System*, *8*(4), 495-505.

17. Zhu, Y., Liu, K., Liu, L., Wang, S., & Liu, H. (2015). Retrieval of mangrove aboveground biomass at the individual species level with worldview-2 images. *Remote Sensing*, *7*(9), 12192-12214.

18. Zhen, J., Liao, J., & Shen, G. (2018). Mapping mangrove forests of Dongzhaigang nature reserve in China using Landsat 8 and Radarsat-2 polarimetric SAR data. *Sensors*, *18*(11), 4012.

19. Carrasco, L., O'Neil, A. W., Morton, R. D., & Rowland, C. S. (2019). Evaluating combinations of temporally aggregated Sentinel-1, Sentinel-2 and Landsat 8 for land cover mapping with Google Earth Engine. *Remote Sensing*, *11*(3), 288.

20. Gorelick, N., Hancher, M., Dixon, M., Ilyushchenko, S., Thau, D., & Moore, R. (2017). Google Earth Engine: Planetary-scale geospatial analysis for everyone. *Remote sensing of Environment*, *202*, 18-27.

21. Shrestha, S., Miranda, I., Kumar, A., Pardo, M. L. E., Dahal, S., Rashid, T., ... & Mishra, D. R. (2019). Identifying and forecasting potential biophysical risk areas within a tropical mangrove ecosystem using multi-sensor data. *International Journal of Applied Earth Observation and Geoinformation*, *74*, 281-294.

22. Diniz, C., Cortinhas, L., Nerino, G., Rodrigues, J., Sadeck, L., Adami, M., & Souza-Filho, P. W. M. (2019). Brazilian mangrove status: Three decades of satellite data analysis. *Remote Sensing*, *11*(7), 808.

23. Mondal, P., Liu, X., Fatoyinbo, T. E., & Lagomasino, D. (2019). Evaluating combinations of sentinel-2 data and machine-learning algorithms for mangrove mapping in West Africa. *Remote Sensing*, *11*(24), 2928.

24. Dong, D., Wang, C., Yan, J., He, Q., Zeng, J., & Wei, Z. (2020). Combing Sentinel-1 and Sentinel-2 image time series for invasive Spartina alterniflora mapping on Google Earth Engine: A case study in Zhangjiang Estuary. *Journal of Applied Remote Sensing*, *14*(4), 044504.

25. Pham, T. D., & Yoshino, K. (2015, March). Mangrove mapping and change detection using multi-temporal Landsat imagery in Hai Phong city, Vietnam. In *International symposium on cartography in internet and ubiquitous environments* (pp. 17-19).

26. Shi, T., Liu, J., Hu, Z., Liu, H., Wang, J., & Wu, G. (2016). New spectral metrics for mangrove forest identification. *Remote Sensing Letters*, *7*(9), 885-894.

27. Pimple, U., Simonetti, D., Sitthi, A., Pungkul, S., Leadprathom, K., Skupek, H., ... & Towprayoon, S. (2018). Google earth engine based three decadal landsat imagery analysis for mapping of mangrove forests and its surroundings in the trat province of Thailand. Journal of Computer and Communications, 6, 247-264

28. Gessesse, A. A., & Melesse, A. M. (2019). Temporal relationships between time series CHIRPS-rainfall estimation and eMODIS-NDVI satellite images in Amhara Region, Ethiopia. In *Extreme hydrology and climate variability* (pp. 81-92). Elsevier.

29. Ghorbanian, A., Zaghian, S., Asiyabi, R. M., Amani, M., Mohammadzadeh, A., & Jamali, S. (2021). Mangrove ecosystem mapping using Sentinel-1 and Sentinel-2 satellite images and random forest algorithm in Google Earth Engine. *Remote Sensing*, *13*(13), 2565.

30. Huang, K., Yang, G., Yuan, Y., Sun, W., Meng, X., & Ge, Y. (2022). Optical and SAR images Combined Mangrove Index based on multi-feature fusion. *Science of Remote Sensing*, *5*, 100040.

31. Shen, Z., Miao, J., Wang, J., Tang, A., & Zhen, J. (2023). Combining Optical and Sar Data for Mapping Mangrove Forests Using Feature Selection and Machine Learning Methods. SSRN

32. Bihamta Toosi, N., Soffianian, A. R., Fakheran, S., Pourmanafi, S., Ginzler, C., & T. Waser, L. (2020). Land cover classification in mangrove ecosystems based on VHR satellite data and machine learning—an upscaling approach. *Remote Sensing*, *12*(17), 2684.

33. Worthington, T. A., Zu Ermgassen, P. S., Friess, D. A., Krauss, K. W., Lovelock, C. E., Thorley, J., ... & Spalding, M. (2020). A global biophysical typology of mangroves and its relevance for ecosystem structure and deforestation. *Scientific reports*, *10*(1), 1-11.

34. Walker, W. (2014). Introduction to RADAR Remote Sensing for Vegetation Mapping and Monitoring. *A Ph. D. presentation: Woods Hole Research Center*, *22*.

35. Baghdadi, N., El Hajj, M., Zribi, M., & Bousbih, S. (2017). Calibration of the water cloud model at C-band for winter crop fields and grasslands. *Remote Sensing*, *9*(9), 969.

36. Vrieling, A., De Leeuw, J., & Said, M. Y. (2013). Length of growing period over Africa: Variability and trends from 30 years of NDVI time series. *Remote sensing*, *5*(2), 982-1000.

37. Tucker, C. J. (1979). Red and photographic infrared linear combinations for monitoring vegetation. *Remote sensing of Environment*, *8*(2), 127-150.

38. Zhu, Z., Bi, J., Pan, Y., Ganguly, S., Anav, A., Xu, L., ... & Myneni, R. B. (2013). Global data sets of vegetation leaf area index (LAI) 3g and fraction of photosynthetically active radiation (FPAR) 3g derived from global inventory modeling and mapping studies (GIMMS) normalized difference vegetation index (NDVI3g) for the period 1981 to 2011. *Remote sensing*, *5*(2), 927-948.

39. Viana, C. M., Oliveira, S., Oliveira, S. C., & Rocha, J. (2019). Land use/land cover change detection and urban sprawl analysis. In *Spatial modeling in GIS and R for earth and environmental sciences* (pp. 621-651). Elsevier.

40. Javadnia, E., Mobasheri, M. R., & Kamali, G. A. (2009). MODIS NDVI quality enhancement using ASTER images. Journal of Agricultural Science and Technology, 11, 549-558.

41. McFeeters, S. K. (1996). The use of the Normalized Difference Water Index (NDWI) in the delineation of open water features. *International journal of remote sensing*, *17*(7), 1425-1432.

42. Jensen, J. R. (1996). *Introductory digital image processing: a remote sensing perspective* (No. Ed. 2). Prentice-Hall Inc..

43. Schulz, K., Hänsch, R., & Sörgel, U. (2018). Machine learning methods for remote sensing applications: an overview. *Earth resources and environmental remote sensing/GIS applications IX*, *10790*, 1079002.

44. Liu, K., Li, X., Shi, X., & Wang, S. (2008). Monitoring mangrove forest changes using remote sensing and GIS data with decision-tree learning. *Wetlands*, *28*, 336-346.

45. Heumann, B. W. (2011). An object-based classification of mangroves using a hybrid decision tree—Support vector machine approach. *Remote Sensing*, *3*(11), 2440-2460.

46. Feizizadeh, B., Omarzadeh, D., Kazemi Garajeh, M., Lakes, T., & Blaschke, T. (2023). Machine learning data-driven approaches for land use/cover mapping and trend analysis using Google Earth Engine. *Journal of Environmental Planning and Management*, *66*(3), 665-697.

47. Torres, M., & Qiu, G. (2014). Automatic habitat classification using image analysis and random forest. *Ecological informatics*, *23*, 126-136.

48. Fu, B., Wang, Y., Campbell, A., Li, Y., Zhang, B., Yin, S., ... & Jin, X. (2017). Comparison of object-based and pixel-based Random Forest algorithm for wetland vegetation mapping using high spatial resolution GF-1 and SAR data. *Ecological indicators*, *73*, 105-117.

49. Millard, K., & Richardson, M. (2015). On the importance of training data sample selection in random forest image classification: A case study in peatland ecosystem mapping. *Remote sensing*, *7*(7), 8489-8515.

50. Phan, T. N., Kuch, V., & Lehnert, L. W. (2020). Land cover classification using Google Earth Engine and random forest classifier—The role of image composition. *Remote Sensing*, *12*(15), 2411.

51. Amani, M., Mahdavi, S., Afshar, M., Brisco, B., Huang, W., Mohammad Javad Mirzadeh, S., ... & Hopkinson, C. (2019). Canadian wetland inventory using Google Earth Engine: The first map and preliminary results. *Remote Sensing*, *11*(7), 842.

52. Tappan, G. G., Sall, M., Wood, E. C., & Cushing, M. (2004). Ecoregions and land cover trends in Senegal. *Journal of arid environments*, *59*(3), 427-462.

53. Mountrakis, G., Im, J., & Ogole, C. (2011). Support vector machines in remote sensing: A review. *ISPRS journal of photogrammetry and remote sensing*, *66*(3), 247-259.

54. Toosi, N. B., Soffianian, A. R., Fakheran, S., Pourmanafi, S., Ginzler, C., & Waser, L. T. (2019). Comparing different classification algorithms for monitoring mangrove cover changes in southern Iran. *Global Ecology and Conservation*, *19*, e00662.

55. Andrew, A. M. (2000). An Introduction to Support Vector Machines and Other Kernel-Based Learning Methods by Nello Christianini and John Shawe-Taylor, Cambridge University Press, Cambridge, 2000, xiii+ 189 pp., ISBN 0-521-78019-5 (Hbk,£ 27.50). *Robotica*, *18*(6), 687-689.

56. Ding, H. Y., & Bian, Z. F. (2008). Theory of support vector machine and its applications in remote sensing image processing. Computer *Engineering Design*, *5*, 62.

57. Foody, G. M. (2020). Explaining the unsuitability of the kappa coefficient in the assessment and comparison of the accuracy of thematic maps obtained by image classification. *Remote Sensing of Environment*, *239*, 111630.

58. Mohammadi, A., Karimzadeh, S., Valizadeh Kamran, K., & Matsuoka, M. (2020). Extraction of land information, future landscape changes and seismic hazard assessment: A case study of Tabriz, Iran. *Sensors*, *20*(24), 7010.

59. Jahanbakhshi, F., & Ekhtesasi, M. R. (2019). Performance evaluation of three image classification methods (Random Forest, Support Vector Machine and the Maximum Likelihood) in land use mapping. *Journal of Water and Soil Science*, *22*(4), 235-247

Investigation of the capability of multi-GNSS PPP-AR method in detecting permanent displacements

Mert Bezcioglu [1] , **Tayyib Ucar** [1] , **Cemal Ozer Yigit** *[1]

[1]Gebze Technical University, Department of Geomatics Engineering, Türkiye

Abstract

The traditional-precise point positioning (PPP) technique may provide a positioning as precise as the relative positioning technique in long-term observation durations. However, since it cannot provide high-precision positioning due to ambiguity problem in short-term observations, the interest in the PPP-AR (Ambiguity Resolution) technique has increased. The main purpose of this study is to investigate the performance of traditional-PPP and PPP-AR techniques for monitoring permanent displacements, considering different observation durations based on different satellite combinations. For this purpose, a displacement simulator that can move precisely in one direction and in the horizontal plane over a small distance was used. 6 different displacements were simulated, and all collected GNSS observations were evaluated with traditional-PPP, PPP-AR, and relative methods. Moreover, these methods were examined by considering the Global Positioning System (GPS), European Global Navigation Satellite System (Galileo), and GPS/Galileo satellite combinations. The findings clearly demonstrated the superiority of the PPP-AR technique outperformed the traditional-PPP technique in short-term observation durations and emphasize the contribution of multi-GNSS (Global Navigation Satellite System) combinations to both methods.

1. Introduction

GNSS technology has been widely used in the detection of horizontal and vertical displacement components of surface deformations such as landslides [1-2], earthquakes [3-5], and engineering structures [6-8]. The estimation of the displacements employed the GNSS technique is usually realized using the repeated campaigns or continuous monitoring stations. The permanent deformation of surfaces such as tectonic faults, landslides, volcanoes, and some engineering structures such as dams can be determined by employing repeated campaigns with the GNSS method. Moreover, real-time deformations of structures such as towers, high-rise buildings, long-span suspension bridges can be predicted by obtaining high-rate GNSS observations with the continuous monitoring stations. Furthermore, high-rate continuous monitoring stations can also be utilized in applications such as GNSS-seismology. Although GNSS measurements in static mode provides millimeter level accuracy in long-term observation durations, the accuracy level decreases in short-term due to effects such as satellite geometry and multipath error [9].

The relative positioning method is widely used to detect permanent deformations at millimeter level precision with repeated campaigns. However, it requires at least two GNSS receivers, one of which is outside the deformation zone. In recent years, however, the traditional-PPP technique, which enables centimeter-level positioning precision by using precise orbit/clock products and employing the stand-alone GNSS receiver, has emerged. Therefore, it has become very popular in the scientific world as a very cost-effective technique [10-13]. The effectiveness of the traditional-PPP technique has been proven in many applications such as characterization of seismic waveforms, structural health monitoring, GNSS buoy, precise orbit determination of low orbit satellites and determination of position of moving objects [14-21]. Furthermore, the performance of determining permanent deformations of the traditional-PPP technique has also been examined [22-26].

* **Corresponding Author**

(mbezcioglu@gtu.edu.tr) ORCID ID 0000-0001-7179-8361
(t.ucar2018@gtu.edu.tr) ORCID ID 0000-0002-4070-4024
*(cyigit@gtu.edu.tr) ORCID ID 0000-0002-1942-7667

In the traditional-PPP technique, the observation duration must be long enough for the ambiguity resolution to converge to the integer value [27]. Compared to the traditional-PPP method, the ambiguity parameter is resolved as an integer in the PPP-AR technique, which makes the PPP-AR technique more effective than the traditional-PPP technique, especially in short-term observation durations. Li et al. [28] examined the PPP and PPP-AR techniques in terms of convergence time and position accuracy by evaluating the GPS and BeiDou satellite combinations in static and kinematic mode, and clearly stated the superiority of the multi-GNSS PPP-AR technique over traditional-PPP method. Li et al. [29] compared the multi-GNSS PPP-AR method using GPS, GLONASS, Galileo and BeiDou satellite combinations with the PPP-AR technique obtained with single and dual satellite combinations. They clearly emphasized that the most accurate position information in the East, North and Up components was obtained with the multi-GNSS PPP-AR technique. Geng et al. [30] used triple frequency observations with GPS, BeiDou, Galileo and QZSS satellite systems to examine how fast the ambiguity resolution is resolved with the PPP-AR technique. The results showed that the more satellites included in the triple frequency, the shorter time to obtain the ambiguity as an integer. Katsigianni et al. [31] examined the contribution of only-Galileo, only-GPS and multi-GNSS satellite observations to traditional-PPP and PPP-AR methods in kinematic mode. The findings clearly stated that the accuracy obtained from only-Galileo and only-GPS techniques is at the same level, and multi-GNSS observations increase the accuracy of position information obtained from traditional-PPP and PPP-AR techniques. Psychas et al. [32] examined the effect of different frequency and satellite combinations on position accuracy and ambiguity resolution. The outcomes demonstrated that the increase in the frequency number improves the position accuracy and ambiguity resolution. Bezcioglu et al. [33-34] collected GNSS observations both static and kinematic mode on two different days with a Zodiac boat on Livingston Island on the Antarctic Peninsula, and the GNSS data processed by the traditional-PPP and PPP-AR technique were compared with the relative positioning technique. The results obtained in the study clearly expressed the superiority of the PPP-AR technique over the traditional-PPP method.

Considering the existing literature, it is seen that the positioning performances of traditional-PPP and PPP-AR techniques were investigated. However, the capabilities of both methods in detecting permanent displacements that occur at a point were not comparatively examined by considering different satellite combinations and observation durations. In this contribution, the ability of traditional-PPP and PPP-AR techniques to detect permanent displacements were evaluated for the first time. A displacement simulator that can precisely move in one direction and in the horizontal plane over a small distance was used in the study, and 6 different displacements of 10, 15, 20, 25, 35 and 40 mm were generated. Observation data collected with only-GPS, only-Galileo and GPS/Galileo satellite combinations were evaluated by both traditional-PPP and PPP-AR

techniques by considering the 12-, 6-, 4-, 3-, 2.5-, 2-, 1.5-, and 1-hour observation durations. The ability of both methods that allow obtaining position information with a stand-alone GNSS receiver to estimate the simulated permanent displacements, were validated by considering the relative GNSS positioning technique data obtained from 12-hour observations as ground truth. The outline of this paper is as follows: In section 2, the design of the experiment and the data processing strategy are described; the results are presented in section 3, and finally, section 4 concludes the paper.

2. Method

The displacement simulator apparatus used in the study, the collection and processing of GNSS data, and the mathematical model of geocentric to topocentric coordinate transformation are detailed in the following sections.

2.1. The displacement simulator, GNSS data collection and processing

For the purpose of this study, a displacement simulator, which is shown in Figure 1 and has the ability to move in the horizontal plane, was used. The simulator can produce displacement at sub-mm level precision with the help of a screw and the value of displacement is controlled with the help of a digital caliper. Moreover, geodetic devices such as GNSS receiver, total station and reflector can be mounted on the upper part of the simulator.

Linux-based open-source Pride PPP-AR software was used for traditional-PPP and PPP-AR solutions in this study. The detailed mathematical model of traditional-PPP and PPP-AR techniques were described in detail in Atiz et al. [35]. Processing parameters were also given in Table 1. In the PPP-AR and Network-Adjustment evaluations, the ratio values were chosen as 3.0 for the ambiguity resolution [36].

The experiments were carried out on the roof of the Faculty of Economics of Gebze Technical University in November 2021 and lasted for 8 days. GNSS data for all simulated displacement cases were collected at 10° elevation angle in static mode using a Leica GR30 receiver and a Leica CGA60 antenna and recorded at 20 Hz (0.05 sec) sampling rate. Experiments were performed minimum multipath effect. After collecting 24-hour static data for the reference period (initial position), the antenna was moved 10, 15, 20, 25, 35 and 40 mm in successive days using the simulator. Approximately 12 hours of GNSS observations were collected for each simulated displacement cases. In order to evaluate the effect of the observation durations in both traditional-PPP and PPP-AR techniques, the collected observation data were evaluated with Pride PPP-AR software, by considering the 12-, 8-, 6-, 4-, 3-, 2.5-, 2-, 1.5- and 1-hour observation durations.

Furthermore, to examine the effect of different satellite combinations on the traditional-PPP and PPP-AR methods, solutions were also realized with only-GPS, only-Galileo and GPS/Galileo satellite combinations. The examination and verification of the performance of traditional-PPP and PPP-AR techniques under the effect

of different observations durations and different satellite combinations in the detection of permanent displacements were performed with the relative positioning technique. GAMIT/GLOBK software was used for relative positioning method solutions. Network-adjustment solution for relative positioning method was realized by considering BOR1, BUCU, DRAG, DYNG, GANP, GLSV, GRAZ, JOZ2, MAT1, MDVJ, MEDI, POLV, POTS and SOFI GNSS stations. During the 8-day experiments, it rained at some time intervals. Since the simulator apparatus used in the study is made of wood,

considering that there may be an expansion in the apparatus due to wetting, the displacements estimated from the relative method were used as reference, not the displacements produced. In other words, for each network adjustment solution, we used the coordinate from H-files generated by GAMIT, the loosely constrained daily solution and considered them as reference. Finally, the coordinates from the relative positioning, traditional-PPP and PPP-AR methods were transformed to the topocentric coordinate system to calculate the point displacement.

Table 1. Processing strategies of GAMIT/GLOBK and Pride PPP-AR

Options	Network Adjustment	Traditional-PPP	PPP-AR
Sampling Rate	30 sec	0.05sec / 20 Hz	0.05sec / 20 Hz
Elevation Mask	10°	10°	10°
Basic Observable	Code+Phase	Code+Phase	Code+Phase
Tropospheric Model	GMF	GPT3+VMF3	GPT3+VMF3
Weighting Model	$1/\sin(ele)^2$ "ele:elevation"	$W = 1$, ele > 30° $W = 4\sin(ele)^2$, ele < 30°	$W = 1$, ele > 30° $W = 4\sin(ele)^2$, ele < 30°
Ionosphere	Ionosphere-free linear combination	Ionosphere-free linear combination	Ionosphere-free linear combination
Orbit / Clock	IGS	WUHAN	WUHAN
AR Products		-	WUHAN
Satellite Phase Centre Calibration	Corrected (IGS14)	Corrected (IGS14)	Corrected (IGS14)
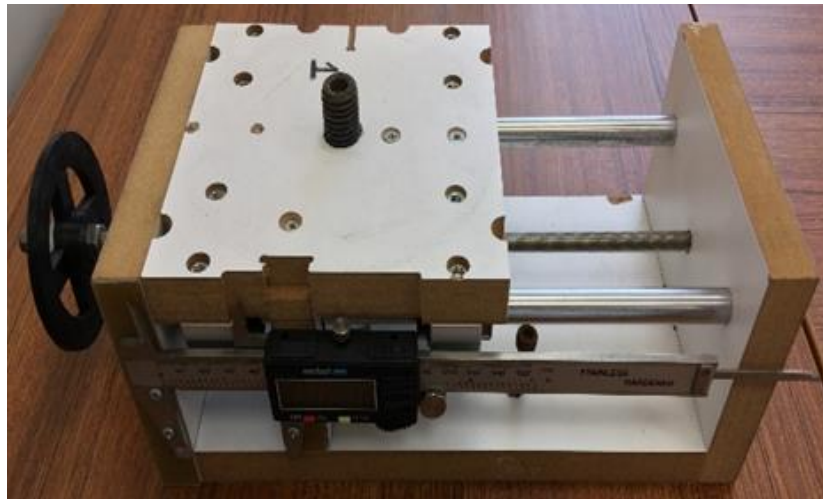
Figure 1. Displacement simulator

2.2. The Coordinate transformation

The GNSS technique provides a position information in the International Terrestrial Reference Frame (ITRF). ITRF is Earth Centered Earth Fixed (ECEF) system, and to calculate the displacement components using the GNSS method, the point coordinates derived from the GNSS technique must be transformed to the local topocentric coordinate system corresponding to the geocentric ITRF system due to the necessity of decomposition of the position and height errors [26]. The common equations between these two systems can be written as Equation 1 and 2.

$$\begin{bmatrix} n_i \\ e_i \\ h_i \end{bmatrix} = R(\varphi_0, \lambda_0) \begin{bmatrix} \Delta x_i \\ \Delta y_i \\ \Delta z_i \end{bmatrix}, \quad \begin{bmatrix} \Delta x_i \\ \Delta y_i \\ \Delta z_i \end{bmatrix} = \begin{bmatrix} x_i - x_0 \\ y_i - y_0 \\ z_i - z_0 \end{bmatrix} \quad (1)$$

$$R(\varphi_0, \lambda_0) = \begin{bmatrix} -\sin\varphi_0\cos\lambda_0 & -\sin\varphi_0\sin\lambda_0 & \cos\varphi_0 \\ -\sin\lambda_0 & \cos\lambda_0 & 0 \\ \cos\varphi_0\cos\lambda_0 & \cos\varphi_0\sin\lambda_0 & \sin\varphi_0 \end{bmatrix} \quad (2)$$

In Equation 1, x_0, y_0, z_0 ($\varphi_0, \lambda_0, h_0$) represents the reference point coordinates, and x_i, y_i, z_i is the coordinates obtained from the GNSS technique. $R(\varphi_0, \lambda_0)$ denotes the rotation matrix that provides the transformation from the ITRF coordinate system to the local topocentric coordinate system and is expressed as Equation 2.

The variance-covariance matrix of each solution in the local geodetic system can be calculated using the error propagation formula as shown in Equation 3.

$$R\sum_{n,e,h} = R(\varphi_0, \lambda_0)\sum_{x,y,z}R^T(\varphi_0, \lambda_0) \quad (3)$$

The terms $\sum_{n,e,h}$ and $\sum_{x,y,z}$ in Equation 3 are given in Equation 4.

The displacement of a point can be defined as the statistically significant difference in position between two different periods. For example, assuming that the position of a point P with the covariance matrix $\sum P_t$ at

time t is $P_t(n_t, e_t, h_t)$, and the position of the same point P with the covariance matrix $\sum P_{t+\Delta t}$ at time $t + \Delta t$ is $P_{t+\Delta t}(n_{t+\Delta t}, e_{t+\Delta t}, h_{t+\Delta t})$, the value of the permanent displacement of this point between these two times can be obtained by taking the difference of the coordinates between the times t and $t + \Delta t$ are given in Equation 5.

$$\sum_{n,e,h} = \begin{bmatrix} \sigma_{nn}^2 & \sigma_{ne} & \sigma_{nh} \\ \sigma_{en} & \sigma_{ee}^2 & \sigma_{eh} \\ \sigma_{hn} & \sigma_{he} & \sigma_{hh}^2 \end{bmatrix}, \sum_{x,y,z} = \begin{bmatrix} \sigma_{xx}^2 & \sigma_{xy} & \sigma_{xz} \\ \sigma_{yx} & \sigma_{yy}^2 & \sigma_{yz} \\ \sigma_{zx} & \sigma_{zy} & \sigma_{zz}^2 \end{bmatrix} \quad (4)$$

$$P_{t+\Delta t} - P_t = \begin{bmatrix} \Delta n \\ \Delta e \end{bmatrix} = \begin{bmatrix} n_{t+\Delta t} - n_t \\ e_{t+\Delta t} - e_t \end{bmatrix} \quad (5)$$

As a result, the permanent displacement value of point P between two different times can be calculated as shown in Equation 6.

$$d = \sqrt{\Delta n^2 + \Delta e^2} \quad (6)$$

The covariance matrix of the point coordinates for two different times is given in Equation 7.

$$\sum_{P_t} = \begin{bmatrix} \sigma_{n_t}^2 & \sigma_{n_t e_t} \\ \sigma_{n_t e_t} & \sigma_{e_t}^2 \end{bmatrix} \& \sum_{P_{t+\Delta t}} = \begin{bmatrix} \sigma_{n_{t+\Delta t}}^2 & \sigma_{n_{t+\Delta t} e_{t+\Delta t}} \\ \sigma_{n_{t+\Delta t} e_{t+\Delta t}} & \sigma_{e_{t+\Delta t}}^2 \end{bmatrix} \quad (7)$$

Assuming that the coordinates between the times t and $t + \Delta t$ are uncorrelated, the covariance matrix of the point coordinates is shown in Equation 8.

$$\sum_{P_t P_{t+\Delta t}} = \begin{bmatrix} \sigma_{n_t}^2 & \sigma_{n_t e_t} & 0 & 0 \\ \sigma_{n_t e_t} & \sigma_{e_t}^2 & 0 & 0 \\ 0 & 0 & \sigma_{n_{t+\Delta t}}^2 & \sigma_{n_{t+\Delta t} e_{t+\Delta t}} \\ 0 & 0 & \sigma_{n_{t+\Delta t} e_{t+\Delta t}} & \sigma_{e_{t+\Delta t}}^2 \end{bmatrix} \quad (8)$$

The variance of the permanent displacement occurring at the point is determined as in Equation 9.

$$\sigma_d^2 = J_d \sum_{P_t P_{t+\Delta t}} J_d^T \quad (9)$$

The Jacobi matrix J_d in Equation 9 is expressed as in Equation 10.

$$J_d = \begin{bmatrix} \dfrac{\delta d}{\delta n_t} & \dfrac{\delta d}{\delta e_t} & \dfrac{\delta d}{\delta n_{t+\Delta t}} & \dfrac{\delta d}{\delta n_{t+\Delta t}} \end{bmatrix} = \begin{bmatrix} -\dfrac{\Delta n}{d} & -\dfrac{\Delta e}{d} & \dfrac{\Delta n}{d} & \dfrac{\Delta e}{d} \end{bmatrix} \quad (10)$$

The standard deviation (σ_d) of the estimated displacement is obtained as follows in Equation 11.

$$\sigma_d = \left(\left(\frac{\Delta n}{d} \right)^2 \left(\sigma_{n_t}^2 + \sigma_{n_{t+\Delta t}}^2 \right) + 2 \frac{\Delta n}{d} \frac{\Delta e}{d} \left(\sigma_{n_t e_t} + \sigma_{n_{t+\Delta t} e_{t+\Delta t}} \right) + \left(\frac{\Delta e}{d} \right)^2 \left(\sigma_{e_t}^2 + \sigma_{e_{t+\Delta t}}^2 \right) \right)^{1/2} \quad (11)$$

2.3. The Pride PPP-AR Software

Pride PPP-AR, developed by the PRIDE Laboratory at the GNSS Research Center of Wuhan University, is an open-source software that allows to obtain solutions with traditional-PPP and PPP-AR techniques. Pride PPP-AR software has been designed according to the principles of readability, modularity, extensibility, and sustainability. Within the framework of these principles, Pride PPP-AR software is used flexibly and comfortably. Pride PPP-AR supports Linux and Mac OS operating system. It also has a module that works on Windows system. Pride PPP-AR software basically consists of undifferenced processing and ambiguity resolution modules. The undifferenced processing module includes data cleaning and parameter estimations and is responsible for detecting ambiguities in the wide-lane and narrow-lane. Traditional-PPP solutions can be obtained after this stage, and using these ambiguities estimates. The initial ambiguity module then uses phase clock bias products to fix these uncertainties to integer resolution [37].

3. Results

The capability of traditional-PPP and PPP-AR techniques to detect permanent deformations under the effect of different observation durations and different satellite combinations is examined in this part of the contribution. As mentioned in the above sections, the accuracy of traditional-PPP and PPP-AR techniques based on 12-, 8-, 6-, 4-, 3-, 2.5-, 2-, 1.5- and 1-hour GPS,

Galileo and GPS/Galileo satellite combinations were investigated employing the relative positioning technique as a reference. Moreover, the superiority of these methods over each other is also discussed.

Table 2 shows the results from both methods discussed in this study, based on 1-hour observations. Table 2 also includes the calculated displacements according to Equation 6 and the standard deviation of the displacements obtained according to Equation 11 for all simulation cases. Furthermore, error column of Table 2 shows how close the permanent displacements obtained from the traditional-PPP and PPP-AR techniques are to the displacements obtained from the relative method. As can be seen from the table, the errors obtained from the PPP-AR technique are quite small compared to the traditional-PPP technique. The differences between the relative method and the traditional-PPP technique range from -13.9 mm to 110.5 mm. Moreover, the differences between the PPP-AR technique and the relative method are between -4.1 mm and 7.5 mm. The average of the errors obtained from the traditional-PPP technique are 21.9 mm, 66.9 mm and 11.6 mm for the only-GPS, only-Galileo and GPS/Galileo satellite combinations, respectively. These differences were obtained as 3.9 mm, 2.3 mm and 2.7 mm for the PPP-AR technique. These results clearly indicate the contribution of multi-satellite combinations to both methods. Furthermore, considering the mean standard deviations obtained from the traditional-PPP technique, the standard deviation of the solutions obtained from the GPS/Galileo satellite combination is 4 times and 2 times smaller, respectively,

than the mean standard deviations derived from the only-GPS-only and only-Galileo solutions. For the PPP-AR technique, on the other hand, the standard deviation values obtained for all satellite combinations are quite similar. These outcomes clearly indicate that the superiority of the PPP-AR technique over the traditional-PPP technique in short-term observation durations.

Table 3 contains results based on 1.5-hour GNSS observations, similar to Table 2. As can be seen from the table, the errors obtained from the PPP-AR technique are also very small at this observation duration compared to the traditional-PPP technique. The differences between the relative method and the traditional-PPP technique are between -7.4 mm and 26 mm, while the differences between the PPP-AR technique and the relative method range from -4.0 mm to 5.7 mm. The mean values of errors derived from the traditional-PPP technique are 4.3 mm, 9.8 mm and 4.4 mm for the only-GPS, only-Galileo and GPS/Galileo satellite combinations, respectively. These differences were obtained as 1.4 mm, 2.7 mm and 1.3 mm for the PPP-AR technique. Also, considering the mean standard deviations from the traditional-PPP technique, similar to the 1-hour measurement time, the standard deviation of the solutions obtained with the GPS/Galileo satellite combination is 4 times and 2 times smaller, respectively, than the mean standard deviations obtained with the GPS-only and Galileo-only solutions. The standard deviation values obtained for all satellite combinations are similar for the PPP-AR technique. Moreover, the mean standard deviation values for only-GPS, only-Galileo and GPS-Galileo satellite combinations are 0.2, 0.2 and 0.1 mm, respectively. These findings clearly demonstrate that the superiority of the PPP-AR technique over the traditional-PPP technique in short observation duration times of 1.5 hours, similar to the 1-hour observations. The main reason for this outcome is that the ambiguity is known as an integer in the PPP-AR technique.

Table 4 represents the results obtained by both methods discussed in the study, based on 2-hour GNSS observations. The errors derived from the PPP-AR technique are smaller than the traditional-PPP technique. The differences between the relative method and the traditional-PPP technique are vary between -1.2 mm and 26.8 mm. These values are range from -5.0 mm to 3.4 mm for the PPP-AR technique. Furthermore, while the mean error value for only-GPS observations in the traditional-PPP technique is 5.3 mm, these values are 14.0 mm and 2.9 mm for only-Galileo and GPS/Galileo satellite combinations, respectively. These values clearly indicate that the contribution of the multi-GNSS combination on both methods. Moreover, as the measurement time increases, the decrease in the error values obtained from the traditional-PPP technique also demonstrate the importance of the observation duration in the traditional-PPP technique. Considering the standard deviations derived from the traditional-PPP technique, the standard deviations of the GPS/Galileo satellite combination are smaller than the derived from the only-GPS and only-Galileo solutions, as in the 1- and 1.5-hour observation durations. The standard deviations of PPP-AR technique, on the other hand, are similar to the prior observation durations. These results clearly

revealed that the superiority of the PPP-AR technique over the traditional-PPP technique in 2-hour observation durations.

The results based on different satellite combinations based on 2.5-hour satellite observations are presented in Table 5. From the table, it can be seen that the errors of the Galileo-only satellite observations for the Traditional-PPP technique are 13 times and 9 times higher, respectively, than the errors of the only-GPS and GPS/Galileo satellite combination. Although the differences between the relative method and the traditional-PPP technique range from -5.7 mm to 33 mm, the differences between the PPP-AR technique and the relative method are between -6.0 mm and 3.7 mm. The standard deviation of GPS/Galileo satellite combination for the traditional-PPP technique is smaller than the only-GPS and only-Galileo solutions, and the mean standard deviation values obtained from these satellite combinations are 0.7 mm, 0.4 mm and 0.3 mm, respectively. For PPP-AR technique, the mean standard deviation values are 0.1 mm for all satellite combinations. These results indicate that the PPP-AR technique outperforms the traditional-PPP technique in the 2.5-hour satellite observations, similar to 1-, 1.5- and 2-hour observation durations.

Table 6 contains the results obtained from both methods based on 3-hour GNSS observations. The differences between the relative method and the traditional-PPP technique range from -7.3 mm to 16.5 mm. However, the differences between the PPP-AR technique and the relative method are vary between -5.4 mm and 2.6 mm. Considering the standard deviations obtained from the traditional-PPP technique, it is seen that the average standard deviations obtained from all satellite combinations are comparable to each other, similar to the standard deviations obtained from the PPP-AR technique. These results differ from the prior observations durations, especially considering the traditional-PPP technique based on GPS/Galileo satellite combinations. These results indicate that the necessity of using multi-GNSS satellite observations with a minimum observation duration of 3 hours in estimating permanent displacements employing the traditional-PPP technique.

The results from traditional-PPP and PPP-AR techniques based on 4-hour observation duration are presented in Table 7. As can be seen from the table, the differences between the relative method and the traditional-PPP technique range from -5.0 mm to 11.0 mm. However, the differences between the PPP-AR technique and the relative method are between -32.8 mm and 5.9 mm. Considering that this difference of -32.8 mm is in the value of the first simulated displacement, and the errors obtained from the other cases is vary between -5.1 mm and 5.9 mm, it is clear that this error is an outlier. The average error derived from the GPS/Galileo satellite combination for the traditional-PPP technique is 0.6 mm, also this value is smaller than the errors obtained from the only-GPS and only-Galileo solutions. Moreover, the results of the GPS/Galileo satellite combination performed better as with other observation durations.

The results of both methods discussed in the study based on 6-hour GNSS observations are given in Table 8. With the increase in the observation duration, the errors

obtained from the traditional-PPP technique have decreased considerably. The differences between the traditional-PPP technique and the relative method range from -8.1 mm to 4.5 mm, and the differences between the PPP-AR technique and the relative method are between -7.9 mm and 0.7 mm. The average error values of the only-GPS, only-Galileo, and GPS/Galileo satellite combinations are -1.8 mm, -1.4 mm and -1.9 mm for the traditional-PPP technique, and -3.3 mm, -2.5 mm and -2.7 mm for the PPP-AR technique, respectively. The standard deviations obtained from both methods are similar to each other.

Table 9 shows the results from traditional-PPP and PPP-AR techniques based on 8-hour observation duration. The differences between the relative method and the traditional-PPP technique range from -9.1 mm to 9.5 mm, while the differences between the relative method and the PPP-AR technique are between -9.0 mm and 2.6 mm. Considering the standard deviations derived from both methods, the values obtained from both methods are similar, as in the 4- and 6-hour observation durations.

Table 10 includes outcomes from traditional-PPP and PPP-AR techniques based on 12-hour GNS observations. From the table, it can be seen that the standard deviations of both discussed methods are similar for all satellite combinations. On the other hand, there are slight differences between the estimated permanent displacement derived from the traditional-PPP and PPP-AR techniques and those obtained from the relative method. The differences between the relative method and the traditional-PPP technique range from -9.1 mm to 19.7 mm, while the differences between the PPP-AR technique and the relative method vary between -9.1 mm and 14.4 mm. Although the mean error values are -2.3, 4.6 and 0.4 mm for only-GPS, only-Galileo and GPS-Galileo satellite combinations, respectively, for the traditional-PPP technique, these values are -3.2, 1.00 and 0.0 mm, respectively, for the PPP-AR technique. These results clearly indicate the contribution of multi-satellite combination to the detection of permanent displacements by traditional-PPP and PPP-AR techniques. Furthermore, considering the standard deviation values obtained from both methods, it is clear that both methods are similar in the 12-hour observation duration.

The bar graph of the mean standard deviations of the simulated displacements obtained based on different observation durations and satellite combinations employing the traditional-PPP and PPP-AR techniques is

illustrated in Figure 2. As can be seen from the figure, the PPP-AR technique performed better than the traditional-PPP technique for all satellite combinations at observation durations up to 6 hours. The standard deviations obtained from both methods are similar for the 8- and 12-hour observation durations. Considering the mean standard deviation obtained at observation durations up to 6 hours, for only-GPS, only-Galileo, and GPS/Galileo satellite combinations, the PPP-AR technique has, on average, 77.2%, 70.6% and 52.6% smaller standard deviations, respectively, compared to the traditional-PPP technique. For GPS-only observations, the PPP-AR technique has between 55.6% and 90.1% smaller standard deviations than the traditional-PPP technique, 58.7% and 91.2% for Galileo-only observations, and 8.9% and 69.5% for multi-GNSS satellite combinations. These results clearly revealed that the PPP-AR technique is more reliable than the traditional-PPP technique in the determination of permanent displacements at observation durations of 6 hours and less. Moreover, from the Figure 2, it can be seen that the contribution of multi-GNSS satellite combinations for the traditional-PPP technique, especially at short-term observation durations. The multi-GNSS satellite observations improve the standard deviations from only-GPS observations between 7.7% and 82.7%, while it improves the standard deviations from only-Galileo observations between 19.0% and 79.8%. These results clearly demonstrate that the contribution of multi-GNSS observations in short-term observation durations.

Figure 3 represents the differences between the simulated displacements in this contribution and determined employing the relative method and the displacements estimated from the traditional-PPP and PPP-AR techniques, based on different observation durations. From the figure, it can be seen that the PPP-AR technique has slightly smaller error values compared to the traditional-PPP technique, especially at short-term observation durations of up to three hours. In terms of permanent displacement detection applications, the superiority of the PPP-AR technique over the traditional-PPP technique becomes more evident as the observation duration decreases, while the errors of both methods are similar to each other, as the observation time increases. Furthermore, it can be seen that the multi-GNSS observations are in agreement with relative method, especially for observation durations up to 6-hour.

Table 2. Displacements and its statistics obtained from 1-hour GNSS observations employing PPP and PPP-AR methods (RD: Reference Displacement, ED: Estimated Displacement, SD: Standard Deviation, E: Error).

| | Traditional-PPP | | | | | | | | | | PPP-AR | | | | | | | | | |
| | GPS | | | Galileo | | | GPS/Galileo | | | | GPS | | | Galileo | | | GPS/Galileo | | |
RD (mm)	ED (mm)	SD (mm)	E (mm)	ED (mm)	SD (mm)	E (mm)	ED (mm)	SD (mm)	E (mm)		ED (mm)	SD (mm)	E (mm)	ED (mm)	SD (mm)	E (mm)	ED (mm)	SD (mm)	E (mm)
42.5	28.6	1.4	-13.9	116.4	2.1	73.9	47.8	0.4	5.3		38.4	0.1	-4.1	44.8	0.3	2.3	39.5	0.2	-3.1
35.4	23.3	1.8	-12.1	82.9	1.8	47.5	52.6	0.5	17.2		41.4	0.2	6.0	36.5	0.2	1.1	39.1	0.2	3.7
26.7	58.8	1.2	32.1	75.7	1.9	49.0	40.3	0.3	13.6		34.2	0.1	7.5	30.7	0.1	4.0	32.6	0.1	5.9
21.1	44.3	1.1	23.2	114.9	2.9	93.8	39.8	0.2	18.7		24.3	0.1	3.2	22.7	0.1	1.6	23.6	0.0	2.5
16.6	55.5	1.8	38.9	43.5	2.3	26.9	18.6	0.7	2.0		21.1	0.2	4.5	16.9	0.3	0.3	19.3	0.2	2.7
10.8	74.0	2.4	63.2	121.3	2.4	110.5	23.3	0.6	12.5		16.9	0.3	6.1	15.5	0.3	4.7	15.2	0.2	4.4

Table 3. Displacements and its statistics obtained from 1.5-hour GNSS observations employing PPP and PPP-AR methods (RD: Reference Displacement, ED: Estimated Displacement, SD: Standard Deviation, E: Error)

| | Traditional-PPP | | | | | | | | | PPP-AR | | | | | | | | |
| | GPS | | | Galileo | | | GPS/Galileo | | | GPS | | | Galileo | | | GPS/Galileo | | |
RD (mm)	ED (mm)	SD (mm)	E (mm)	ED (mm)	SD (mm)	E (mm)	ED (mm)	SD (mm)	E (mm)	ED (mm)	SD (mm)	E (mm)	ED (mm)	SD (mm)	E (mm)	ED (mm)	SD (mm)	E (mm)
42.5	35.1	0.4	-7.4	50.2	0.3	7.7	42.9	0.1	0.4	38.2	0.2	-4.4	45.5	0.3	3.0	38.9	0.2	-3.6
35.4	32.2	0.2	-3.2	39.9	0.5	4.5	38.2	0.1	2.8	39.0	0.2	3.6	36.3	0.2	0.9	37.4	0.2	2.0
26.7	38.7	0.3	12.0	34.1	0.5	7.4	34.1	0.1	7.4	31.7	0.1	5.0	30.9	0.1	4.2	31.6	0.1	4.9
21.1	26.1	1.9	5.0	36.1	0.4	15.0	33.0	0.3	11.9	21.4	0.1	0.3	22.5	0.0	1.4	21.8	0.0	0.7
16.6	22.9	0.3	6.3	14.6	0.3	-2.0	15.4	0.1	-1.2	17.6	0.2	1.0	17.6	0.2	1.0	16.9	0.2	0.3
10.8	24.1	2.0	13.3	36.8	1.4	26.0	16.0	0.3	5.2	13.3	0.3	2.5	16.5	0.2	5.7	14.2	0.2	3.4

Table 4. Displacements and its statistics obtained from 2-hour GNSS observations employing PPP and PPP-AR methods (RD: Reference Displacement, ED: Estimated Displacement, SD: Standard Deviation, E: Error)

| | Traditional-PPP | | | | | | | | | PPP-AR | | | | | | | | |
| | GPS | | | Galileo | | | GPS/Galileo | | | GPS | | | Galileo | | | GPS/Galileo | | |
RD (mm)	ED (mm)	SD (mm)	E (mm)	ED (mm)	SD (mm)	E (mm)	ED (mm)	SD (mm)	E (mm)	ED (mm)	SD (mm)	E (mm)	ED (mm)	SD (mm)	E (mm)	ED (mm)	SD (mm)	E (mm)
42.5	42.0	0.6	-0.5	69.3	0.6	26.8	42.3	0.3	-0.2	37.8	0.2	-4.7	43.7	0.2	1.2	37.5	0.1	-5.0
35.4	41.8	0.6	6.4	42.9	0.5	7.5	40.1	0.3	4.7	38.3	0.2	2.9	36.7	0.1	1.3	37.1	0.1	1.7
26.7	27.2	0.3	0.5	44.4	0.4	17.7	31.3	0.2	4.6	30.2	0.1	3.5	29.2	0.1	2.5	29.9	0.1	3.2
21.1	22.0	1.3	0.9	42.1	0.8	21.0	22.8	0.2	1.7	20.5	0.1	-0.7	21.0	0.1	-0.1	20.7	0.1	-0.4
16.6	16.4	1.2	-0.2	17.7	0.5	1.1	15.5	0.4	-1.2	16.4	0.2	-0.2	15.1	0.1	-1.6	15.6	0.1	-1.0
10.8	35.7	1.1	24.9	20.6	0.9	9.8	18.4	0.5	7.6	14.2	0.2	3.4	13.5	0.2	2.7	14.2	0.2	3.4

Table 5. Displacements and its statistics obtained from 2.5-hour GNSS observations employing PPP and PPP-AR methods (RD: Reference Displacement, ED: Estimated Displacement, SD: Standard Deviation, E: Error)

| | Traditional-PPP | | | | | | | | | PPP-AR | | | | | | | | |
| | GPS | | | Galileo | | | GPS/Galileo | | | GPS | | | Galileo | | | GPS/Galileo | | |
RD (mm)	ED (mm)	SD (mm)	E (mm)	ED (mm)	SD (mm)	E (mm)	ED (mm)	SD (mm)	E (mm)	ED (mm)	SD (mm)	E (mm)	ED (mm)	SD (mm)	E (mm)	ED (mm)	SD (mm)	E (mm)
42.5	36.9	0.6	-5.7	75.1	0.5	32.6	43.1	0.3	0.6	37.4	0.1	-5.1	41.6	0.2	-0.9	36.6	0.2	-5.9
35.4	47.0	0.6	11.6	43.8	0.3	8.4	36.7	0.3	1.3	38.2	0.1	2.8	34.9	0.2	-0.5	36.5	0.1	1.1
26.7	23.9	0.4	-2.8	44.7	0.4	18.0	27.7	0.3	1.0	28.9	0.1	2.2	27.2	0.1	0.5	27.8	0.1	1.1
21.1	15.9	0.8	-5.2	32.2	0.4	11.1	19.2	0.2	-1.9	19.7	0.1	-1.4	19.4	0.1	-1.7	19.5	0.0	-1.6
16.6	15.0	0.8	-1.6	13.7	0.3	-2.9	15.5	0.3	-1.1	16.3	0.1	-0.3	14.1	0.2	-2.5	14.7	0.1	-1.9
10.8	20.0	0.9	9.2	18.0	0.8	7.2	18.9	0.4	8.1	14.5	0.2	3.7	13.2	0.2	2.4	14.4	0.2	3.6

Table 6. Displacements and its statistics obtained from 3-hour GNSS observations employing PPP and PPP-AR methods (RD: Reference Displacement, ED: Estimated Displacement, SD: Standard Deviation, E: Error)

| | Traditional-PPP | | | | | | | | | PPP-AR | | | | | | | | |
| | GPS | | | Galileo | | | GPS/Galileo | | | GPS | | | Galileo | | | GPS/Galileo | | |
RD (mm)	ED (mm)	SD (mm)	E (mm)	ED (mm)	SD (mm)	E (mm)	ED (mm)	SD (mm)	E (mm)	ED (mm)	SD (mm)	E (mm)	ED (mm)	SD (mm)	E (mm)	ED (mm)	SD (mm)	E (mm)
42.5	35.2	0.5	-7.3	59.0	0.1	16.5	40.7	0.3	-1.8	37.5	0.1	-5.0	39.8	0.2	-2.7	37.1	0.1	-5.4
35.4	47.1	0.5	11.7	40.4	0.4	5.0	36.8	0.3	1.4	37.2	0.1	1.8	35.1	0.2	-0.3	36.1	0.1	0.7
26.7	28.5	0.5	1.8	36.2	0.3	9.5	27.6	0.3	0.9	27.3	0.0	0.6	26.5	0.1	-0.2	26.7	0.1	-0.1
21.1	16.1	0.4	-5.1	26.3	0.3	5.2	17.8	0.3	-3.4	18.2	0.1	-2.9	18.3	0.1	-2.8	17.7	0.1	-3.4
16.6	14.1	0.0	-2.5	11.4	0.4	-5.2	12.9	0.3	-3.7	14.4	0.1	-2.2	13.3	0.2	-3.3	13.2	0.1	-3.4
10.8	10.3	0.7	-0.5	13.9	0.6	3.1	13.3	0.3	2.5	13.0	0.1	2.2	13.4	0.2	2.6	12.8	0.1	2.0

Table 7. Displacements and its statistics obtained from 4-hour GNSS observations employing PPP and PPP-AR methods (RD: Reference Displacement, ED: Estimated Displacement, SD: Standard Deviation, E: Error)

| | Traditional-PPP | | | | | | | | | PPP-AR | | | | | | | | |
| | GPS | | | Galileo | | | GPS/Galileo | | | GPS | | | Galileo | | | GPS/Galileo | | |
RD (mm)	ED (mm)	SD (mm)	E (mm)	ED (mm)	SD (mm)	E (mm)	ED (mm)	SD (mm)	E (mm)	ED (mm)	SD (mm)	E (mm)	ED (mm)	SD (mm)	E (mm)	ED (mm)	SD (mm)	E (mm)
42.5	46.6	0.4	4.1	42.6	0.3	0.1	45.0	0.3	2.5	9.7	0.1	-32.8	40.1	0.1	-2.4	40.0	0.1	-2.5
35.4	46.0	0.4	10.6	36.1	0.3	0.7	39.1	0.2	3.7	37.0	0.1	1.6	41.3	0.1	5.9	37.0	0.1	1.6
26.7	31.6	0.4	4.9	27.0	0.3	0.3	28.0	0.2	1.3	26.5	0.1	-0.2	25.6	0.1	-1.1	26.5	0.1	-0.2
21.1	18.6	0.4	-2.5	18.0	0.3	-3.1	17.7	0.2	-3.4	16.2	0.1	-4.9	17.0	0.1	-4.2	16.2	0.1	-4.9
16.6	14.5	0.3	-2.1	11.6	0.4	-5.0	11.4	0.1	-5.2	12.5	0.1	-4.1	11.5	0.1	-5.1	12.5	0.1	-4.1
10.8	7.5	0.4	-3.3	5.6	0.5	-5.2	8.4	0.3	-2.4	10.6	0.2	-0.2	11.4	0.1	0.6	10.6	0.2	-0.2

Table 8. Displacements and its statistics obtained from 6-hour GNSS observations employing PPP and PPP-AR methods (RD: Reference Displacement, ED: Estimated Displacement, SD: Standard Deviation, E: Error)

	Traditional-PPP									PPP-AR								
	GPS			Galileo			GPS/Galileo			GPS			Galileo			GPS/Galileo		
RD	ED	SD	E	ED	SD	E	ED	SD	E	ED	SD	E	ED	SD	E	ED	SD	E
(mm)	(mm)	(mm)	(mm)	(mm)	(mm)	(mm)	(mm)	(mm)	(mm)	(mm)	(mm)	(mm)	(mm)	(mm)	(mm)	(mm)	(mm)	(mm)
42.5	45.3	0.2	2.8	46.6	0.2	4.1	45.0	0.2	2.5	40.7	0.1	-1.8	41.8	0.1	-0.7	42.5	0.1	0.0
35.4	39.9	0.2	4.5	34.2	0.2	-1.2	37.7	0.2	2.3	35.6	0.1	0.2	35.7	0.1	0.3	36.1	0.1	0.7
26.7	26.5	0.2	-0.2	27.5	0.2	0.8	26.4	0.2	-0.3	25.5	0.1	-1.2	25.8	0.1	-1.0	25.9	0.1	-0.8
21.1	14.2	0.2	-6.9	18.0	0.3	-3.1	15.3	0.2	-5.8	14.4	0.1	-6.7	16.0	0.1	-5.2	15.0	0.0	-6.1
16.6	8.5	0.1	-8.1	10.7	0.2	-5.9	8.7	0.1	-7.9	8.7	0.1	-7.9	10.3	0.0	-6.3	9.2	0.1	-7.4
10.8	7.8	0.3	-3.0	7.5	0.3	-3.3	8.4	0.2	-2.4	8.7	0.1	-2.1	8.8	0.1	-2.0	8.4	0.1	-2.4

Table 9. Displacements and its statistics obtained from 8-hour GNSS observations employing PPP and PPP-AR methods (RD: Reference Displacement, ED: Estimated Displacement, SD: Standard Deviation, E: Error)

	Traditional-PPP									PPP-AR								
	GPS			Galileo			GPS/Galileo			GPS			Galileo			GPS/Galileo		
RD	ED	SD	E	ED	SD	E	ED	SD	E	ED	SD	E	ED	SD	E	ED	SD	E
(mm)	(mm)	(mm)	(mm)	(mm)	(mm)	(mm)	(mm)	(mm)	(mm)	(mm)	(mm)	(mm)	(mm)	(mm)	(mm)	(mm)	(mm)	(mm)
42.5	47.6	0.1	5.1	52.0	0.3	9.5	48.4	0.2	5.9	42.5	0.1	0.0	44.0	0.1	1.5	44.3	0.1	1.8
35.4	40.8	0.1	5.4	38.3	0.2	2.9	39.7	0.2	4.3	37.5	0.1	2.1	36.6	0.1	1.2	38.0	0.1	2.6
26.7	27.5	0.1	0.8	30.7	0.2	4.0	28.4	0.2	1.7	26.6	0.1	-0.1	29.1	0.1	2.4	27.7	0.1	1.0
21.1	12.0	0.0	-9.1	21.3	0.2	0.2	14.1	0.2	-7.0	13.4	0.0	-7.7	19.1	0.1	-2.0	15.3	0.1	-5.8
16.6	8.0	0.1	-8.6	11.7	0.3	-4.9	8.9	0.2	-7.7	7.6	0.0	-9.0	11.6	0.1	-5.0	9.2	0.1	-7.4
10.8	3.4	0.2	-7.4	2.7	0.3	-8.1	3.6	0.2	-7.2	4.6	0.1	-6.2	5.3	0.1	-5.5	4.6	0.1	-6.2

Table 10. Displacements and its statistics obtained from 12-hour GNSS observations employing PPP and PPP-AR methods (RD: Reference Displacement, ED: Estimated Displacement, SD: Standard Deviation, E: Error)
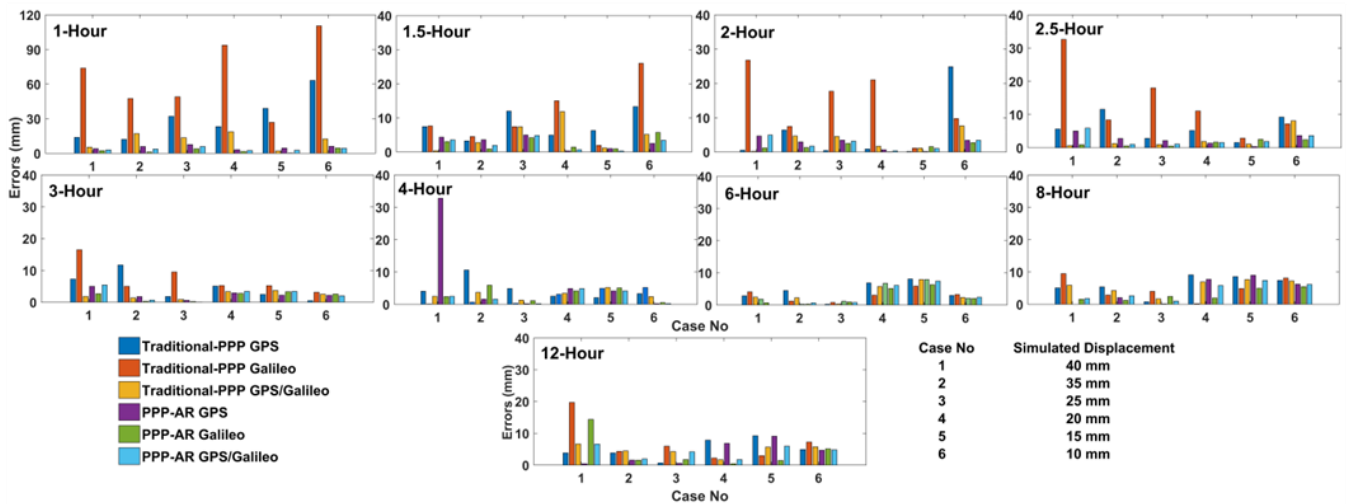
	Traditional-PPP									PPP-AR								
	GPS			Galileo			GPS/Galileo			GPS			Galileo			GPS/Galileo		
RD	ED	SD	E	ED	SD	E	ED	SD	E	ED	SD	E	ED	SD	E	ED	SD	E
(mm)	(mm)	(mm)	(mm)	(mm)	(mm)	(mm)	(mm)	(mm)	(mm)	(mm)	(mm)	(mm)	(mm)	(mm)	(mm)	(mm)	(mm)	(mm)
42.5	46.3	0.2	3.8	62.2	0.2	19.7	49.2	0.2	6.7	42.9	0.1	0.4	56.9	0.2	14.4	49.1	0.2	6.6
35.4	39.2	0.2	3.8	39.7	0.1	4.3	39.9	0.1	4.5	37.0	0.1	1.6	37.0	0.1	1.6	37.3	0.1	1.9
26.7	27.4	0.2	0.7	32.6	0.4	5.9	31.0	0.2	4.3	26.1	0.1	-0.6	28.4	0.1	1.7	30.9	0.2	4.2
21.1	13.3	0.1	-7.8	23.3	0.4	2.2	19.4	0.1	-1.7	14.3	0.1	-6.8	20.7	0.2	-0.4	19.4	0.1	-1.7
16.6	7.4	0.1	-9.2	19.6	0.4	3.0	10.9	0.2	-5.7	7.5	0.0	-9.1	15.2	0.2	-1.4	10.7	0.0	-6.0
10.8	5.9	0.1	-4.9	3.6	0.1	-7.3	5.1	0.1	-5.7	6.1	0.0	-4.7	5.7	0.1	-5.1	6.0	0.0	-4.8
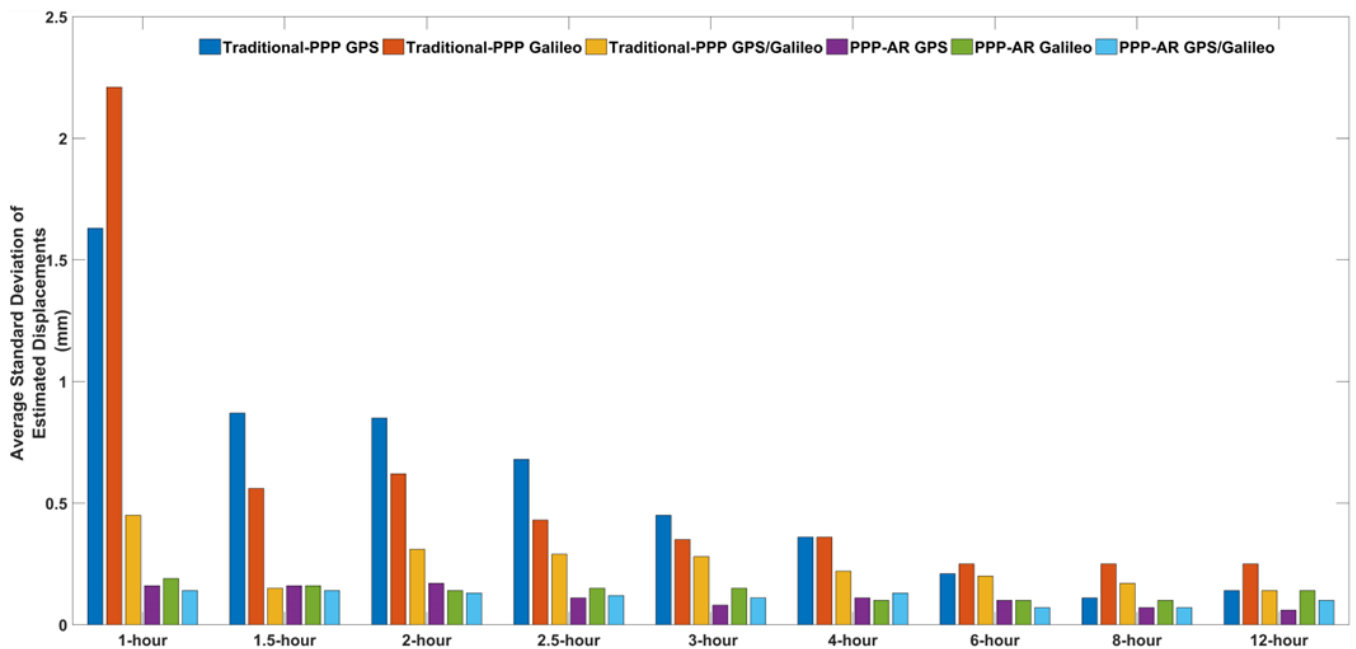
Figure 2. Average standard deviation of estimated displacements based on observation durations and satellite combinations for both methods

Figure 3. Differences between estimated displacements employing the relative method and displacements obtained from traditional-PPP and PPP-AR techniques based on different observation durations.

4. Conclusion

This study evaluates the capability of traditional-PPP and PPP-AR techniques to detect permanent displacements, by considering the different satellite combinations and observation durations. The results obtained by both methods based on 12-, 6-, 4-, 3-, 2.5-, 2-, 1.5- and 1-hour GNSS observations and the only-GPS, only-Galileo and GPS/Galileo satellite combinations were examined by considering the relative GNSS positioning technique as reference. To investigate the performance of both methods in determining permanent displacements, 6 different permanent displacements of 10, 15, 20, 25, 35 and 40 mm were generated by using a displacement simulator capable of moving in one direction and in the horizontal plane. Considering the mean standard deviation values obtained in the study, the PPP-AR technique for only-GPS, only-Galileo and GPS/Galileo satellite combinations outperformed the traditional-PPP technique on average by 77.2%, 70.6% and 52.6%, respectively. For both methods, the multi-GNSS technique, on the other hand, improves the standard deviations obtained from only-GPS observations by 51.4% on average, while it improves the standard deviations derived from only-Galileo observations by 45% on average. While these results clearly demonstrated the superiority of the PPP-AR technique over the traditional-PPP technique, especially in short observation durations, they also revealed that the multi-GNSS observations improve the results obtained, compared to single-system. It is worth about mentioning that some biases may come from GAMIT solutions, therefore, the displacements error obtained from traditional-PPP and PPP-AR may also include some biases. The findings of the study confirm the contribution of multi-GNSS to the traditional-PPP and PPP-AR methods, similar to previous studies. The outcomes also show the superiority of the PPP-AR technique over the traditional-PPP technique, especially in short-time observation durations, and differ from previous studies in this regard. However, as the observation duration increases, it is worth noting that the traditional-PPP and PPP-AR techniques are similar and comparable to each other.

Author contributions

Mert Bezcioglu: Analyses, Methodology, Writing-Reviewing and Editing. **Tayyip Ucar:** Data curation, Analyses, Writing-Original draft preparation, Validation, Field study. **Cemal Ozer Yigit:** Supervision, Methodology, Writing-Reviewing and Editing.

Conflicts of interest

The authors declare no conflicts of interest.

References

1. Hastaoglu, K. O., & Sanli, D. U. (2011). Monitoring Koyulhisar landslide using rapid static GPS: a strategy to remove biases from vertical velocities. *Natural hazards*, *58*, 1275-1294.
2. Malet, J. P., Maquaire, O., & Calais, E. (2002). The use of Global Positioning System techniques for the continuous monitoring of landslides: application to the Super-Sauze earthflow (Alpes-de-Haute-Provence, France). *Geomorphology*, *43*(1-2), 33-54.
3. Erdoğan, S., Şahin, M., Tiryakioğlu, İ., Gülal, E., & Telli, A. K. (2009). GPS velocity and strain rate fields in Southwest Anatolia from repeated GPS measurements. *Sensors*, *9*(3), 2017-2034.
4. Hager, B. H., King, R. W., & Murray, M. H. (1991). Measurement of crustal deformation using the Global Positioning System. *Annual Review of Earth and Planetary Sciences*, *19*(1), 351-382.

5. Tiryakioğlu, I. (2015). Geodetic aspects of the 19 May 2011 Simav earthquake in Turkey. *Geomatics, Natural Hazards and Risk*, *6*(1), 76-89.

6. Celebi, M. (2000). GPS in dynamic monitoring of long-period structures. *Soil Dynamics and Earthquake Engineering*, *20*(5-8), 477-483.

7. Lovse, J. W., Teskey, W. F., Lachapelle, G., & Cannon, M. E. (1995). Dynamic deformation monitoring of tall structure using GPS technology. *Journal of surveying engineering*, *121*(1), 35-40.

8. Moschas, F., & Stiros, S. (2011). Measurement of the dynamic displacements and of the modal frequencies of a short-span pedestrian bridge using GPS and an accelerometer. *Engineering structures*, *33*(1), 10-17.

9. Genrich, J. F., & Bock, Y. (1992). Rapid resolution of crustal motion at short ranges with the Global Positioning System. *Journal of Geophysical Research: Solid Earth*, *97*(B3), 3261-3269.

10. Bulbul, S., Bilgen, B., & Inal, C. (2021). The performance assessment of Precise Point Positioning (PPP) under various observation conditions. *Measurement*, *171*, 108780.

11. Kouba, J., & Héroux, P. (2001). GPS precise point positioning using IGS orbit products. *GPS solutions*, *5*(2), 12-28.

12. Li, T., Wang, J., & Laurichesse, D. (2014). Modeling and quality control for reliable precise point positioning integer ambiguity resolution with GNSS modernization. *GPS solutions*, *18*, 429-442.

13. Zumberge, J. F., Heflin, M. B., Jefferson, D. C., Watkins, M. M., & Webb, F. H. (1997). Precise point positioning for the efficient and robust analysis of GPS data from large networks. *Journal of geophysical research: solid earth*, *102*(B3), 5005-5017.

14. Alçay, S., & Atiz, Ö. (2021). Farklı yazılımlar kullanılarak gerçek zamanlı hassas nokta konum belirleme (RT-PPP) yönteminin performansının incelenmesi. *Geomatik*, *6*(1), 77-83.

15. İnyurt, S., & Ulukavak, M. (2020). Web tabanlı GNSS Yazılımlarının (CSRS-PPP, Trimble-RTX) Performansının Araştırılması. *Geomatik*, *5*(2), 120-126.

16. Uçarlı, A. C., Demir, F., Erol, S., & Alkan, R. M. (2021). Farklı GNSS uydu sistemlerinin hassas nokta konumlama (PPP) tekniğinin performansına etkisinin incelenmesi. *Geomatik*, *6*(3), 247-258.

17. Pırtı, A., & Yazıcı, D. (2022). İnternet tabanlı GNSS yazılımlarının doğruluk açısından değerlendirilmesi. *Geomatik*, *7*(2), 88-105.

18. Ogutcu, S. (2020). Performance assessment of IGS combined/JPL individual rapid and ultra-rapid products: Consideration of Precise Point Positioning technique. *International Journal of Engineering and Geosciences*, *5*(1), 1-14.

19. Ogutcu, S. (2020). Performance analysis of ambiguity resolution on PPP and relative positioning techniques: consideration of satellite geometry. *International Journal of Engineering and Geosciences*, *5*(2), 73-93.

20. Öğütcü, S., Shakor, A., & Farhan, H. (2022). Investigating the effect of observation interval on GPS, GLONASS, Galileo and BeiDou static PPP. *International Journal of Engineering and Geosciences*, *7*(3), 294-301.

21. Özdemir, E. G. (2022). Bağıl ve mutlak (PPP) konum çözüm yaklaşımı sunan Web-Tabanlı çevrimiçi veri değerlendirme servislerinin farklı gözlem periyotlarındaki performanslarının araştırılması. *Geomatik*, *7*(1), 41-51.

22. Alcay, S., Ogutcu, S., Kalayci, I., & Yigit, C. O. (2019). Displacement monitoring performance of relative positioning and Precise Point Positioning (PPP) methods using simulation apparatus. *Advances in Space Research*, *63*(5), 1697-1707.

23. Aydin, C., Uygur, S. Ö., Cetin, S., Özdemir, A., & Dogan, U. (2019). Ability of GPS PPP in 2D deformation analysis with respect to GPS network solution. *Survey review*, *51*(366), 199-212.

24. Capilla, R. M., Berné, J. L., Martín, A., & Rodrigo, R. (2016). Simulation case study of deformations and landslides using real-time GNSS precise point positioning technique. *Geomatics, Natural Hazards and Risk*, *7*(6), 1856-1873.

25. Farzaneh, S., Safari, A., & Parvazi, K. (2022). Precise estimation of horizontal displacement by combination of multi-GNSS (Galileo and GPS) observations via the LS-VCE method. *Applied Geomatics*, *14*(2), 267-286.

26. Yigit, C. O., Coskun, M. Z., Yavasoglu, H., Arslan, A., & Kalkan, Y. (2016). The potential of GPS Precise Point Positioning method for point displacement monitoring: A case study. *Measurement*, *91*, 398-404.

27. Choy, S., Bisnath, S., & Rizos, C. (2017). Uncovering common misconceptions in GNSS Precise Point Positioning and its future prospect. *GPS solutions*, *21*, 13-22.

28. Pan, L., Xiaohong, Z., & Fei, G. (2017). Ambiguity resolved precise point positioning with GPS and BeiDou. *Journal of geodesy*, *91*, 25-40.

29. Li, X., Li, X., Yuan, Y., Zhang, K., Zhang, X., & Wickert, J. (2018). Multi-GNSS phase delay estimation and PPP ambiguity resolution: GPS, BDS, GLONASS, Galileo. *Journal of geodesy*, *92*, 579-608.

30. Geng, J., Guo, J., Meng, X., & Gao, K. (2020). Speeding up PPP ambiguity resolution using triple-frequency GPS/BeiDou/Galileo/QZSS data. *Journal of Geodesy*, *94*, 1-15.

31. Katsigianni, G., Loyer, S., & Perosanz, F. (2019). Ppp and ppp-ar kinematic post-processed performance of gps-only, galileo-only and multi-gnss. *Remote sensing*, *11*(21), 2477.

32. Psychas, D., Verhagen, S., & Teunissen, P. J. (2020). Precision analysis of partial ambiguity resolution-enabled PPP using multi-GNSS and multi-frequency signals. *Advances in Space Research*, *66*(9), 2075-2093.

33. Bezcioğlu, M., Yiğit, C. Ö., & Bodur, M. N. (2019). Kinematik PPP-AR ve Geleneksel PPP Yöntemlerin Performanslarının Değerlendirilmesi: Antarktika Yarımadası Örneği. *Afyon Kocatepe Üniversitesi Fen ve Mühendislik Bilimleri Dergisi*, *19*(1), 162-169.

34. Bezcioglu, M., Yigit, C. O., & El-Mowafy, A. (2019). Kinematic PPP-AR in Antarctic. *Sea technology*, *60*(2), 20-23.

35. Atiz, O. F., Ogutcu, S., Alcay, S., Li, P., & Bugdayci, I. (2021). Performance investigation of LAMBDA and bootstrapping methods for PPP narrow-lane ambiguity resolution. *Geo-Spatial Information Science*, *24*(4), 604-614.

36. Verhagen, S., & Teunissen, P. J. (2013). The ratio test for future GNSS ambiguity resolution. *GPS solutions*, *17*, 535-548.

37. Geng, J., Chen, X., Pan, Y., Mao, S., Li, C., Zhou, J., & Zhang, K. (2019). PRIDE PPP-AR: an open-source software for GPS PPP ambiguity resolution. *GPS Solutions*, *23*, 1-10.

The plight of urban settlements based on the proliferation of dichotomy in Tanzania

Amani Michael Uısso *[1] , **Sibel Canaz Sevgen** [1] , **Harun Tanrıvermiş** [1]

[1]Ankara University, Department of Real Estate Development and Management, Türkiye

Abstract

The observation of the juxtaposition of formal and informal urban settlements in the commonwealth and sub-Saharan developing countries has been trending as a common mundane phenomenon in emerging and fast-growing cities. Dar Es Salaam is one of the largest, and most populous cities in Tanzania; the dichotomy of informal and formal settlement is ubiquitous in peri-urban areas and its urban vicinities where land evolves from village to urban. The dichotomy of urban settlements occurs when the public authorities do not satisfactorily provide public urban services which are customarily attributed to poor governance and policies formulated, financial deficiencies, and nonstrategic urban land development. Different strategies and approaches have been applied by the government for at least providing the proper infrastructure; however, most of the approaches are not well successful and deliver the expected results following the high cost of urban land development. To comprehend the urban typology and land development characteristics of Dar es Salaam, urban land transformation, and to detect the change in the built-up area, data from 1975-2020 were examined through remote sensing, and images with ArcView GIS and LADER. The field survey data analysis supported the cause of unplanned settlements and the limitation of urban land acquisition and development. The aim of this study is to analyze the built-up area growth through the years for the study area. The result showed that rapid urbanization and dramatic growth in built-up areas especially between 1990-2000 years were easily observed, financial deficiencies and conventional urban land development policies have a significant contribution to the thriving of dichotomy settlement. The study suggested that innovative urban land development must be integrated with conventional approaches to leverage urban land development and cater to sustainable urban development.

1. Introduction

The informal land rights seem to hamper the effective functionality of respective authorities over land development for so long when the rapid urbanization evolves, and the outpour of population increase does not match with the acute serviced urban land supply and decent social infrastructures [1,2]. Without effective land governance and urban management, the social infrastructures, and environmental amenities in the urban vicinities are predominated by informal land rights which tend to be over-consumed; hence, open spaces continue to have encroached upon the urban growth [3]. It is well noticed that necessary urban infrastructures are far from adequate, and urban plots fetch high prices due to their scarcity in most of the growing urban areas of Tanzania. Residents' quality of life has remained low, if not deteriorating. The arguments stance that the juxtaposition of informal urban land settlements and formal suburban gated housing estates in most of the Tanzanian cities is a result of the dominancy of informal land rights over formal land rights without the presence of effective land governance over the rapid urbanization [2-7].

For many years urbanization is considered to cost the developing countries in contrast to the developing countries which reap a lot of benefits from the cause of urbanization just because most of the urbanization

process comes with a lot of costs strings which out weight the benefits due to poor infrastructures facilities, crime rates, congestions, lack of resources to provide basic services, overcrowdings, environmental deteriorations, just to mention few [8]. Factors such as lack of planning, poor land governance, and difficulties in obtaining the serviced land with title deeds, lead to cities growing horizontally (outward) rather than vertically (upward) making commutes to be longer and costlier with insufficient infrastructure [9]. On the other hand, a total estimate of a loss of TZS 655 billion of money every year in Tanzania from traffic congestion-related delays and extra fuel use associated with poor urban infrastructure facilities [10,11]. In addition, research shows that most of the roads in Dar es Salaam are operating above capacity during pick hours [12], while other researchers [7,13,14], identified that congestion is a major source of air pollution in the city.

Many countries in Sub-Saharan Africa are still undergoing land reforms since independence and they are still experiencing the juxtaposition of informal and formal settlement [15,16]. The informal settlements are prevalent to the extent that about half and three-quarters of all newly constructed houses in African cities have been developed in un-serviced and unplanned lands without having formal land administration and legal compliance, land use planning, construction permits, and transfer of ownership right [17,18,19,59,60]. For example, only 15% of the population in Tanzania is living in a well-serviced and well-planned formal settlement only [20,21]. The challenges of urban land development in Tanzania in meeting the demands of urban serviced plots have led to the development of unplanned urban land settlements more obviously in the urban periphery where land is cheap and people run after it [4,63,69]. The development of informal settlements or interchangeably referred to as unplanned settlements, appeared when the private interests override the public interest whereby private land is developed and compromises with the fundamental urban land use planning role of the government [4,29,68].

The main characteristic of the informal settlement is mainly associated with inadequate infrastructure which can't allow the smooth habitable and healthy environment of the space occupiers more specifically wider and networked roads, lack of allocated public spaces such as open and green spaces, the social infrastructures notably schools, health facilities, graveyards and may be fostered by lack of clean and safe water, sanitary sewerage systems and electricity to mention few [4,6,19,22]. However, the revolving question to many is that despite being unplanned and even some of the areas regarded as hazardous, why do most of them continue to receive public services such as water and electricity from the main which is regarded as legal-illegal conduct in these unplanned areas [23]. They are not only receiving services such as water and electricity from the main but also, they are regarded as a source of tax to the local and central authorities [23]. These precedents impair the efforts of ensuring sustainable cities as stipulated in goal no.11 of the sustainable development goals, which target investment in public transport, creating green public spaces, and

improving urban planning and management in a participatory and inclusive way. Consequently, the flourishing of dichotomy urban settlements in fast-growing cities which are exorbitant and unmanageable towards efforts of ensuring sustainable urban land development. Analysis of land use and land cover change offers useful results for determining and implementing land management policies [24,25].

The dichotomy of urban and development structure has different historical reasons whereby formal and customary land ownership runs simultaneously [2,49]. On the other hand, the dichotomy of urban land development has an inherent effect due to the colonial land laws which accommodated the dual tenure system of customary land or quasi-customary land ownership and formal or statutory land ownership, especially in the peri-urban areas [2,4,53]. The other reason for the dichotomy of urban land development is the speed of the government to supply buildable service land is lower compared to the demand of people [62,63,65,73]. Furthermore, the existence of a land black market and informal marketization of public land development operationalized by the landowners at the urban fringes subdividing land and selling it to other buyers who seek land for dwelling purposes deter the sustainable urban land development and hence dichotomy urban settlement [2,28,58,63,67]. Land cover studies has been studying over the years by many researchers [79,80]. This study aims to examine the cause and challenges of duo settlement urban partners in Dar es Salaam and track the urban land development land cover typology using remotely sensed images and investigate the situation of the land cover and its dichotomy flourishment.

2. Urban land development regulation

Urban land development in Tanzania is governed by various regulations from land management and administration, land acquisition, planning, surveying, titling, and registration. The constitution of the United Republic of Tanzania is the overall of human rights and land rights; the Land Act No. 4 of 1999 and The Village Land Act No. 5 of 1999 (as amended in 2004, 2005, 2008, and 2009) to manage urban and village land respectively. The Land Use Planning Act (LUPA) 2007 and the Urban Planning Act (UPA) No. 6 of 2007 (revised in 2002), also facilitates land administration processes specifically for planning before titling and registration. The Land Acquisition Act, 1967 for compulsory land acquisition matters; The Land Survey Act of 1975, Cap 324 (Revised in 2002) for the cadastral survey and geodetic referencing procedures; The Local Government (Urban Authorities) Development Control Regulations, 2008 which delegate the responsibilities for Local government and Urban authorities, The Human Settlement and Development Policy of 2000 and National Land Policy of 1995 [74]. Once the area is declared as a planning or zoning area, especially for the provision of public facilities and other infrastructure community needs, the landowners have no option rather than waiting for the compensation and reallocation processes to take place. The President can resort to compulsory urban land

acquisition on the condition of compensation, for the public interest and this will include investment in the national interest and urban land development [49]. The operating modal in question which is expropriation or eminent domain in urban land development is being debated now and then due to dissatisfaction allegations, unfair compensation claims, land dispossession of claims, and in other places land squabbles and claims for the unjust spatial land development with little inclusiveness and participation. However, the land development process faced with challenges right away from the land acquisition stage due to a lack of diversity in land acquisition and development. Compulsory land acquisition had extensively used as a development approach without proper resettlement plans because of financial deficits. Financial deficits make people receive a little amount of money as compensation after land acquisition and make them go to the periphery to seek unplanned cheaper land which they can afford. On the other hand, the national land policy of 1995 has identified the unplanned settlement by making the provision to all residents found in the unplanned settlements for their land rights to be recognized and registered [71]. The upgrading of the informal settlements in urban settings had been recognized through the National Human Settlements Development Policy of 2000 as the result of the high birth rate which cause population increases and rural-urban migration [78]. The two policy stances had been supported by Land Act No.4 of 1999, under sections 57 to 60 by the provision of a regularization process which is the upgrading of informal settlements, hence supporting the dichotomy of urban settlements [74].

3. Local and central government initiatives and role of international organization

Urban development and resettlement had been faced with several challenges that are affecting urban portfolio performance due to the exercising of the conventional approaches in land acquisitions and urban land development [52,62,66]. The rapid urbanization in Tanzania exposes its emerging cities and the process appeared to cause a burden and challenge to local and central governments which have the responsibility and overseer of any urban land development in their jurisdictions [5,6,23,64,70]. In the land development process, there is a close relationship between compulsory land acquisition and land development or urban planning [26]. The acquisition of the private land properties and resettlements actions of the project affected people in the cause of urban land development seems to be thorny and challenge to government authorities [27]. The settlement actions for most of the cities in developing urban vicinities, especially peri-urban areas in Tanzania, are not identified early enough, and the challenges of the (re)settlements outcomes are not well contained and addressed [4,5,19].

The influence of the government, the World Bank, and other international counterparts towards urban development and infrastructure provisions, in African countries and Tanzania in particular, is of greater importance. The number of projects introduced in

Tanzania through direct intervention or sector loans is increasing rapidly. However, most of the projects normally adopt the conventional approaches in dealing with land acquisition and resettlement actions which in most cases have limited successful and promising future results [28,29]. It is nothing short of axiomatic that problems of urban management and resettlement were not likely to be contained through conventional land development approaches due to underlying factors such as; land acquisition and relocation of project-affected people due to the rapid urbanization process, exorbitant land prices, and paucity of resources for large scale public land development and supply of low-cost housing programs, especially at this time where the country is facing with many urban developmental challenges with limited available financial resources [4,30-32].

4. The description of the study area and data

Dar es Salaam is in the eastern part of Tanzania, on the western shores of the Indian Ocean. It is the largest business city in Tanzania. It is situated in the coastal region of Tanzania, and it serves as a prominent business hub and site for public and private administrative offices and agencies. It is the richest city in the country and saves as an important economic center in the region due to its geographical location, concentration of trade, and other services including manufacturing compared to other regions. Dar es Salaam, which serves as the capital of the country until the mid-1970s, remains the center for the central government bureaucracy, although Dodoma is the new capital and political city of Tanzania since 1974. The study area was based on the analysis of all municipalities of Dar es Salaam, which includes: Temeke, Kinondoni, Ilala, Ubungo, and Kigamboni municipal councils (Figure 1) represented the selected study area which is around 1641 km² surface area.

To support the rising challenges in urban land development, the study used observational, documentary, and green literature review together with field survey data. The examination of the flourishing of unplanned settlements and hence the dichotomy of urban settlement, and the limitation of the applicability of expropriation were examined by field survey. Questionnaires covering 330 respondents affected by land acquisition and urban land development with a turnout of 246 respondents were used for analysis. Yet, the study used remote sensing and imaging as a method to investigate Tanzania's urban land development typology. Dar es Salaam was specifically chosen because it is the fastest expanding and stands for the subject matter under this study.

As mentioned above, Dar es Salaam is the business capital city of Tanzania, and it is Tanzanian's first largest and most populous city due to the economic opportunities it offers [1]. The population of Dar es Salaam encompasses 8.7 % of the total population of Tanzania [75]. The population density of the study area is projected and given in Figure 2 to analyze the populous areas and compare them with the built-up area [36,37]. The most highly and predominantly populous area was seen to be in the middle and coastal areas of the city, where most of the built-up areas were identified to be

upper buildings or tall buildings compared to other areas in the city. On the other hand, southeast parts of the study area were identified to have a very low population distribution as indicated in Figure 2.

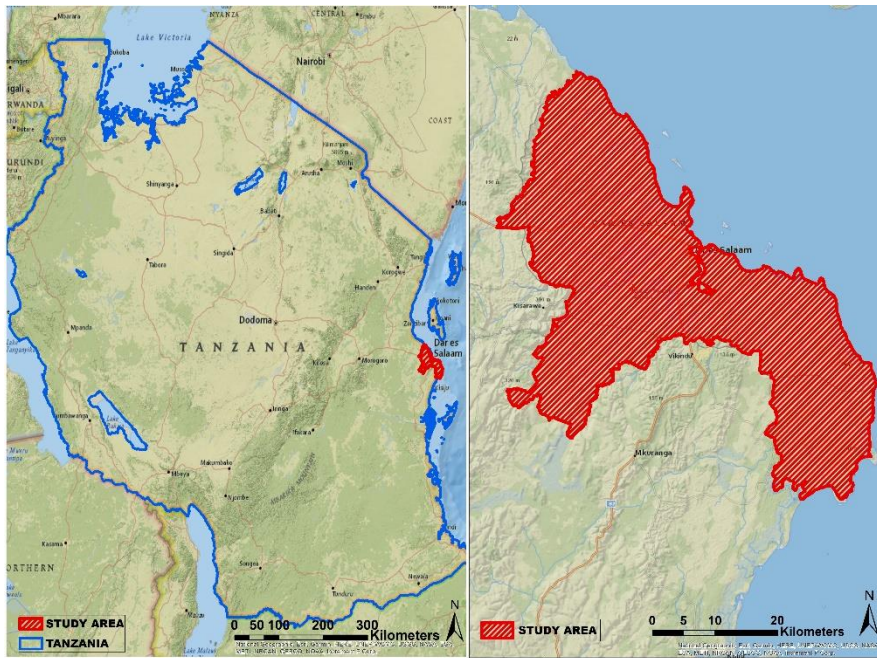**Figure 1.** Tanzania (a), official boundary of Dar es Salaam (b) (Data Source for map ESRI online 2021).
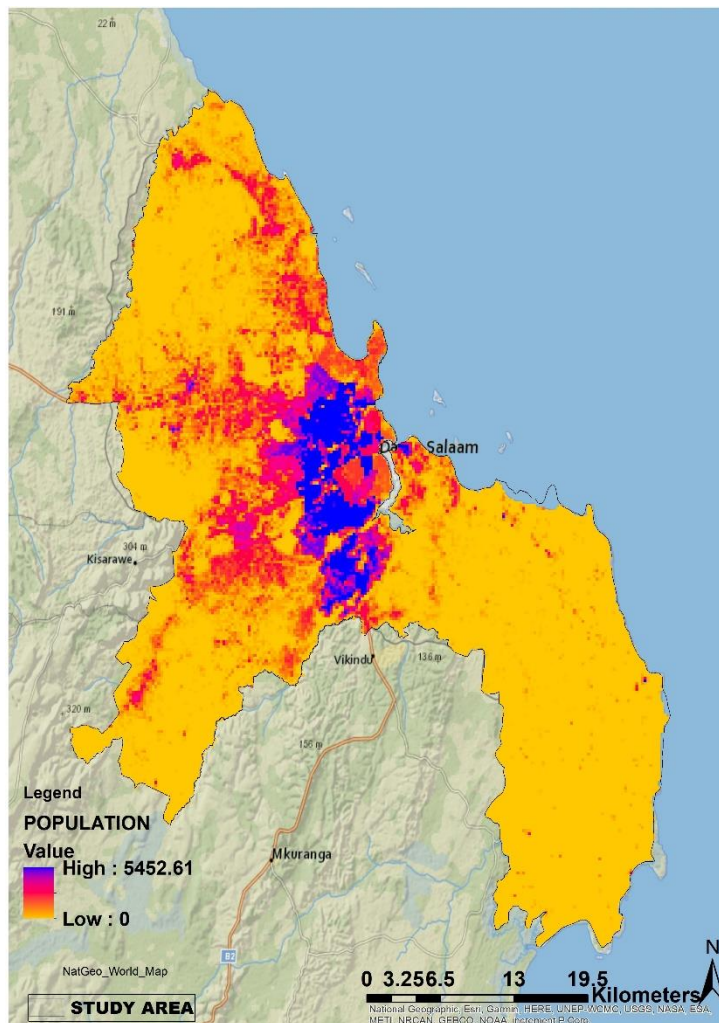

Figure 2. The population density in the study area by the year 2015

The population of Dar es Salaam has been growing over the years (Figure 3, Table 1), The current population of Dar es Salaam in 2021 is estimated to be as 7,047,000, which is a 5.15% increase compared with the 2020

population [38] so that one can easily figure out that the growth of population has been greatly increasing. It is also necessary to analyze the population of Dar es Salaam between 1975-2020 since these years are the subject of the monitoring change detection of built-up areas in Dar es Salaam. According to the official population data, even though the population has shown a significant increase in the last 5 decades, starting from 1975 the growth rate was decreasing up to 1990 whereby the population was identified to rise significantly. One can say that the result of this population growth is the increase in the built-up area within the period. To compare the change in the built-up area and the population growth it was crucial to investigate the correlation between the two variables [1,39].

In detail, Tanzania's total population and Dar es Salaam's population were analyzed at 10 years intervals as seen in Table 1. In 1978 the number of people for km² was 19.65 in 1978, while it was 67.00 in 2020. This data shows that there was a significant increase in both populations and built-up areas.

The population of the city as of now is approximately having a population of 7.04 million [40]. Nevertheless, it is expected to cross the threshold of "megacity" cities with a population of 10 million by having 13.4 million in 2035 (Figure 4). The official boundary surface area of Dar es Salaam is 1590 km². The total land and green land per person have decreased since the 1950s due to population and urban growth. The physical population density in the city is 67 people per km² and the average land per person is 0.45 hectares [54].
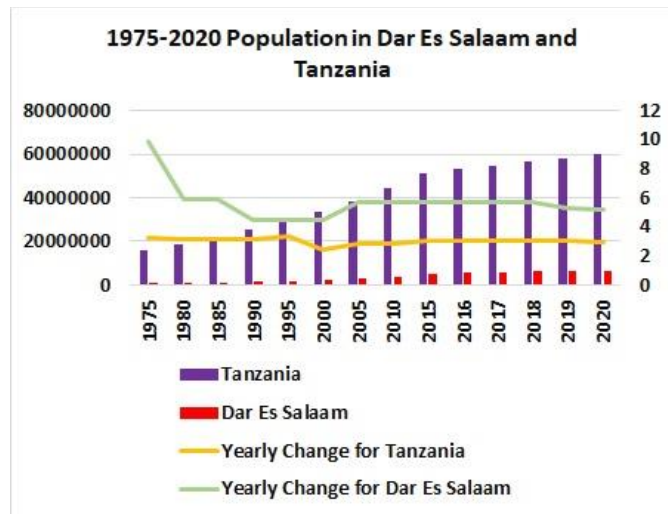

Figure 3. Population and yearly change in Dar es Salaam and Tanzania between 1975-2020

Table 1. Urban growth in Tanzania mainland and Dar es Salaam 1978-2020 [41-42]

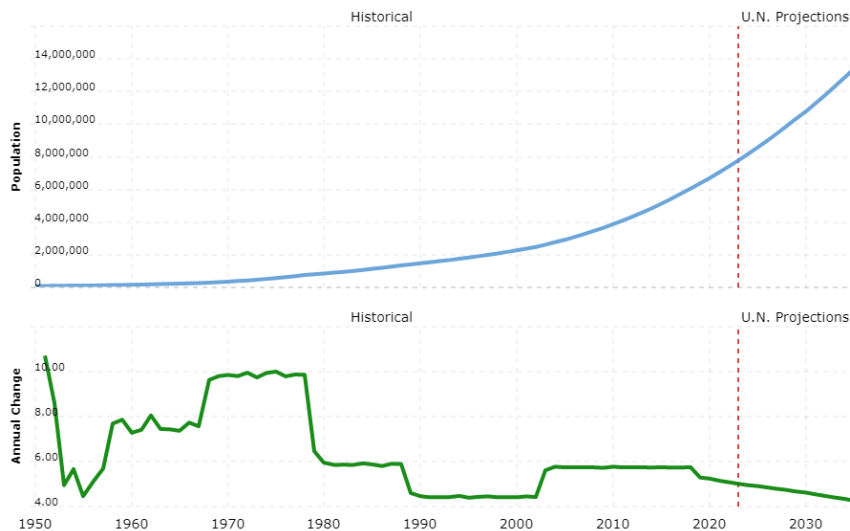| Population Category	Years					
	1978	1988	1998	2008	2018	2020
Total population (000 000)	17.43	23.67	31.92	41.85	56.32	59.73
Urban population (000 000)	2.38	4.31	6.89	11.21	19.02	22.11
Population density (People/Km²)	19.68	26.72	36.04	47.25	63.58	67.00
% of the Urban Population from the Total Population	13.66	18.22	21.59	26.78	33.78	37.00
Dar es Salaam Population (000 000) [40]	0.85	1.36	2.08	3.46	6.048	7.040

Figure 4. Dar es Salaam population future projection [43]

5. Results and Discussion

5.1. The flourishing of unplanned settlements

Several reasons were identified as to why unplanned settlements in urban vicinities were flourishing. Factors such as high population increase which creates a demand for serviced land plots and infrastructures had been leading among the other factors. On the other hand, respondents commented that the lack of financial capacities for the implementation of land development, conventional urban land development tools, and policies do not complement the need and the speed of contemporary urban land development. Factors such as lack of expertise, poor land development, and land development policies are the major factors for informal land development incidences (Figure 5).

5.2. Limitation of implementation of compulsory purchase

The study showed that factors such as inadequate financial resources, and budgetary deficits are the leading factors delimiting the successful compulsory purchase of land acquisition. On the other hand, bottom-up land development (lack of participation), court injunctions, and court cases, obtaining cheap land for land development, and smooth land transfer including holdouts from landowners were identified factors that limiting the implementation of expropriation and land acquisition in urban land development (Figure 6).

5.3. Built-Up area in Dar Es Salaam

Dar es Salaam as the case study area is adjoining the Indian Ocean; therefore, it was very hard to find a cloudless satellite image that covers the total study area. Since this study aims to figure out the built-up area change and examine the urban land development typology, the pre-prepared land cover more specifically built-up area maps from various sources was collected

and used. GHS-BUILT [37] and ESRI Land Cover [45] data were re-symbolized and re-analyzed to monitor change in the built-up area in Dar es Salaam. Change monitoring for built-up areas between 1975-2020 was analyzed in detail. More specifically, built-up area changes in the study area in 1975, 1990, 2000, 2015, and 2020 were conducted and illustrated in Figure 5-7. It is easily seen from Figure 5 that between 1975 to 1990 there was a significant increase in the built-up areas in Dar es Salaam. In 1975 total built-up area of Dar es Salaam was 24.79% of the total study area, while it was almost the same as the 1990 data, where the total built-up area was found to be 24,80% of the total selected study area (Figure 7).

In Figure 8 which shows the built-up area of the study area in 2000 and 2015, it was easily observed from the figure that there is a significant difference between 2000 and 2014. The total built-up area was 30.42% and 33.37% in 2000 and 2014, respectively. As was formerly mentioned that in 1990 the total built-up area was 24,80% while in 2000 was identified to be 30,42%; In comparison, these results show that there is a 5.62% difference as an increase between 1990 and 2000. According to this result, one can say that there is a high construction between 1990 and 2000 in Dar es Salaam. Again, as was previously stated, in these years it experienced rapid population growth which demonstrates the increase in the built-up area for settlement.

Finally, the latest results of the built-up area have been investigated by using the land cover map of 2020 [41]. It is noteworthy to say that the latest built-up area map (2020) has a 10-meters spatial resolution while the other built-up area maps above have a 250-meter spatial resolution, therefore, in the latest built-up map, smaller buildings were easily identified compared to the coarse resolution in previous years land cover maps. In the latest years, it was identified that settlements were scattered and distributed everywhere within the city, while the total built-up area was 35,06% of the total area of the city.
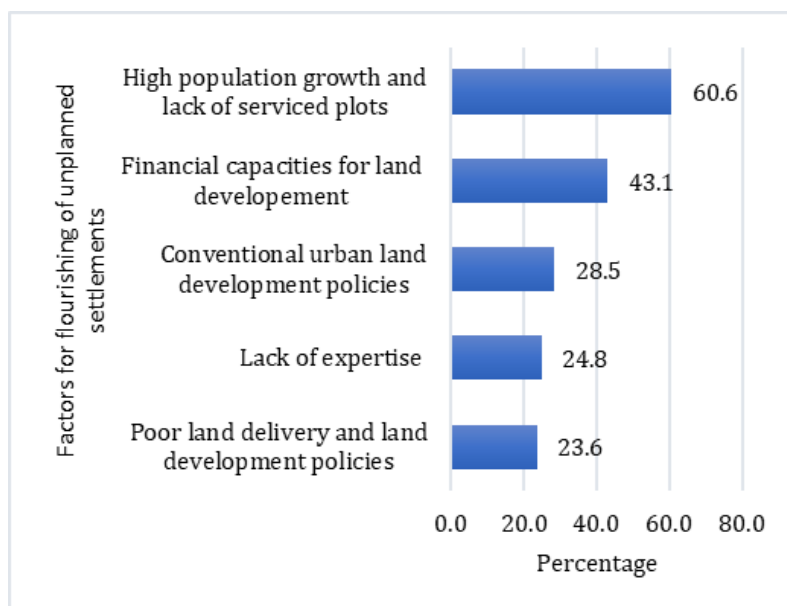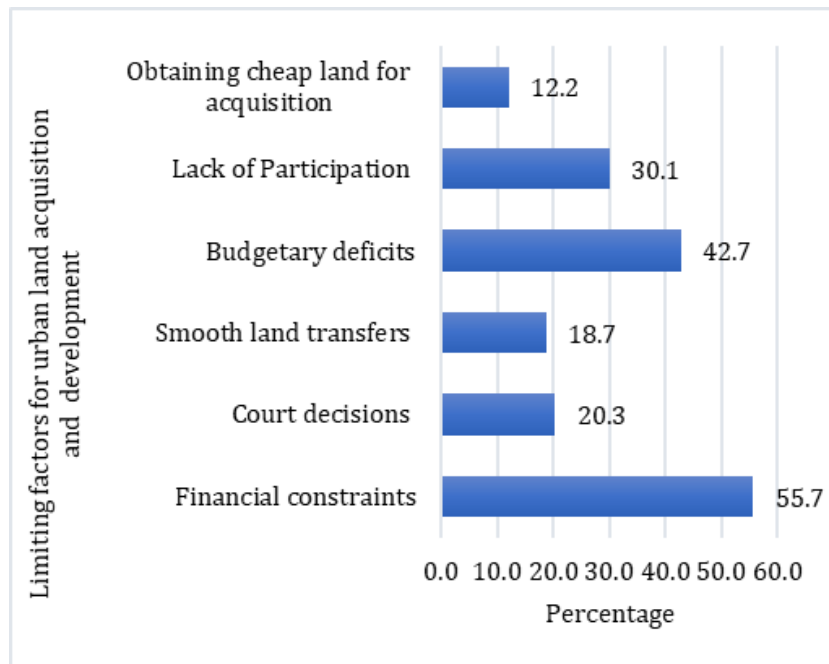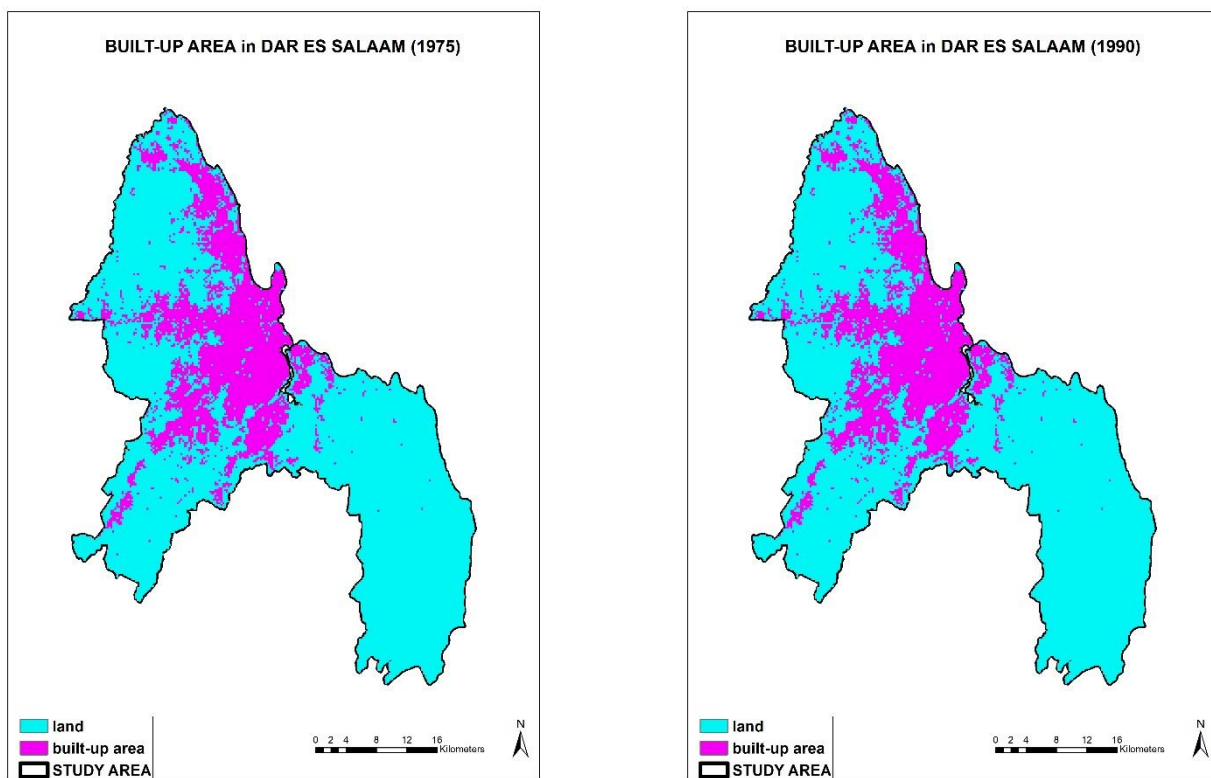

Figure 5. Causes of unplanned settlement and urban sprawl

Figure 6. Limitations in implementing expropriation in land acquisition and urban development

Figure 7. Built-up areas changed in Dar es Salaam between 1975 and 1990

Furthermore, Figure 9 was displaying the change in built-up area by comparing and tracking changes from 1975, 1990, 2000, 2015, and 2020. Consequently, the use of the remotely sensed and processed data demonstrates that Dar es Salaam's built-up area has been continuing to grow in every direction both horizontally and vertically. Therefore, it is necessary to note that initiatives for proper planning and land development must be linked with the trend of population growth in Dar es Salaam and emerging cities of Tanzania.

Figure 10 shows the percentage of built-up area in the selected years with a land cover map. From the image, it can be noted that built-up areas and urban land development changes in Dar es Salaam between 1975-1990 were significantly low, while the growth of the built-up area has been accelerated and took a new pace after 1990 and reached the highest score at 2020 with 35,06%.

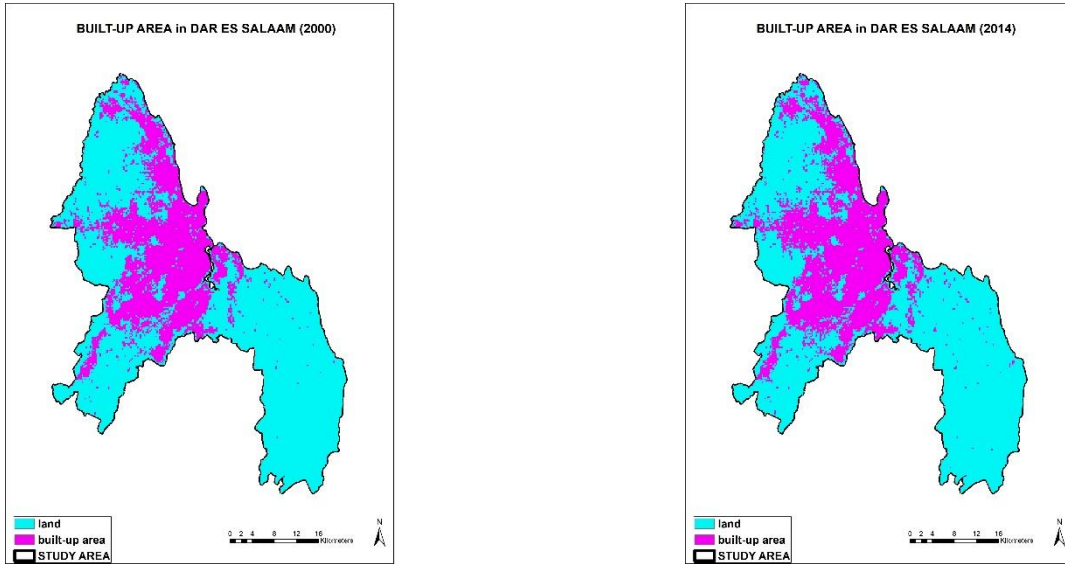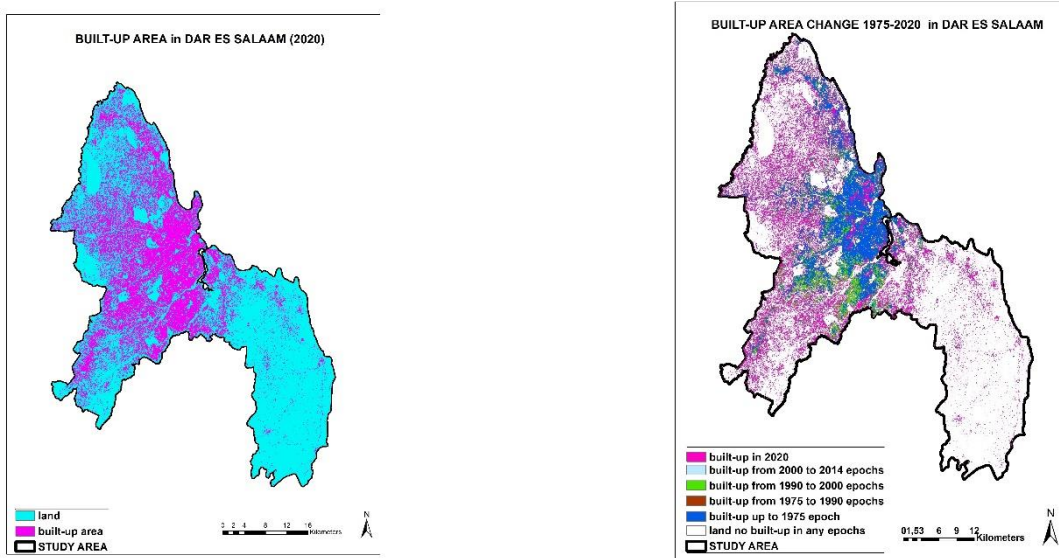**Figure 8.** Built-up area changes in Dar es Salaam between 2000 and 2014

Figure 9. Built-up area of Dar es Salaam in 2020 and change in built-up area between 1975-2020
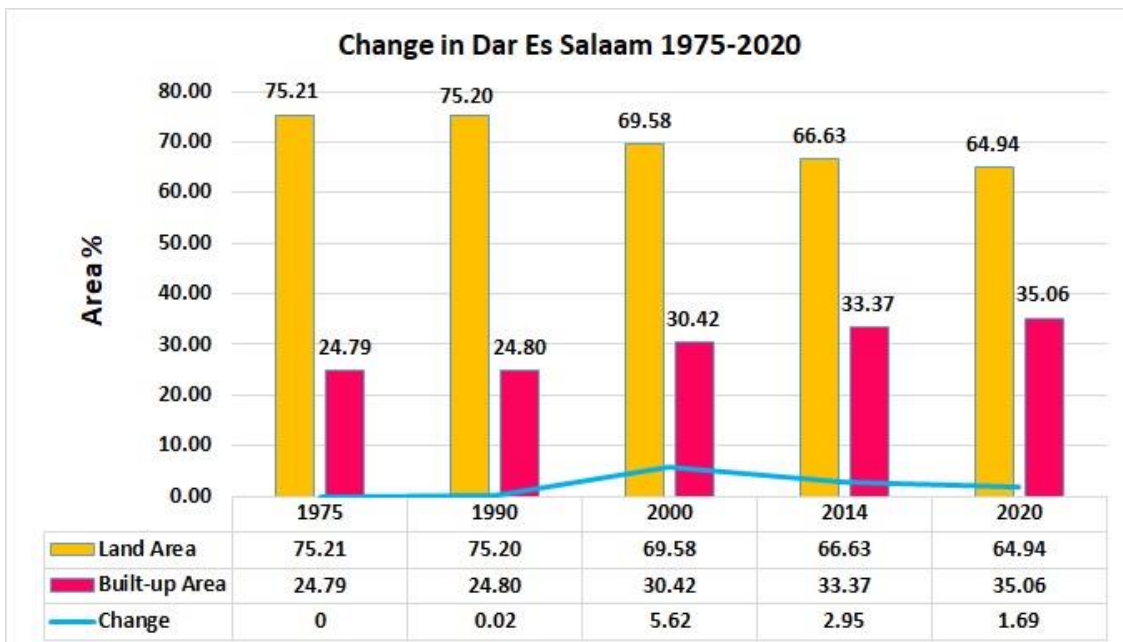

Figure 10. Built-up area changes in Dar es Salaam between 1975-2020

6. Land governance and sustainable urban development

Land governance is all about how policies, institutions, and other procedures by which land resources and natural resources are managed [33,46]. It includes the decisions on access to land, land rights, land use, and land development [33,46]. Good land governance is about the process of making and implementing decisions on land resources; it does not connote implementing "correct decisions" but rather towards enriching the best possible decisions on land resources [5]. It is the governmental side of space and land management [47]. Good land governance has a greater influence on ensuring the proper achievement of global sustainable goals and especially goal 11 of sustainable cities under UN Agenda 21 [33]. Land governance is ideally about determining and implementing sustainable land policies and making sure that urban development is realized [33,46].

Urban land governance and smooth land development were termed as a campaign of alleviation and combating poverty in developing countries and it was launched as the global campaign for good governance in 1999 by the UN-Habitat. The improvement of urban land governance was identified as an important point in urban poverty alleviation and promoting sustainable cities [7]. Urban governance was linked with poverty mitigation procedures and sustainable urban development which are among the common problems recurring in most of the developing countries, especially in the global south [15].

The land governance in Tanzania has its birth and evolved from historical land tenure and ownership, ranging from the traditional alias customary land tenure followed by the colonial system which introduced the statutory land tenure system, and then neo-liberalization and structural adjustment programs (SAPs) adopted in the 1980s [5,48,49]. The adopted SAPs had a greater change on the social, economic, and political structure had a greater impact on land governance, and influenced land development [2,3]. Despite the legal development of structural adjustment programs, land reforms, and relatively progressive land laws, land governance is still dominated by customary and statutory governance [46,47]. While all powers over land remain to the President with the radical title while citizens remain only with a position right [29,49].

Following the historical background land governance in Tanzania is being exercised under legal pluralism in the sense that the implementation of land governance adopts both the wings of customary legal arrangements (village land and trans-urban areas) and the statutory legal arrangements [32,49]. The dualism in land tenure and legal administration which stems from the colonial era is precisely undermining the efforts towards achieving sustainable urban planning and development due to innumerable challenges that appeared in land development, especially in the peri-urban areas [3,48]. The flourishing of informal settlements with formal settlements on the other side, building in hazardous areas, corruption, unequal land access to women, and land use squabbles among the land-based sectors are among the crucial challenges faced by the land sector in Tanzania, precisely because of past precedents and are customarily attributed to poor land governance and policies which guide the urban land development and growth [2,3,5,49]. Sustainable urban growth which has three pillars such as economic, social, and environmental aspects is the good use of resources in recent times without compromising with the future generation. With proper land governance, it could be easier to control resources, land use and planning, and land delivery and distribution while achieving effective land development.

7. Policy and legal provisions for addressing dichotomy urban proliferation

Various policy actions and regulatory approaches had been implemented in the cause of dealing with the unplanned and informal settlement among cities that are more likely thriving along the urban vicinities. Right after the independence officials and politicians had initiated special actions to deal with the continued growth of informal settlements especially in cities like Dar es Salaam and Mwanza due to its high urbanization pace [4]. In this case, the main purpose was meant to prevent all forms of squatter settlement development which happen to be inconsistent with the master plan and modern land development and impose non-payment of compensation to cleared squatter settlements [3,4,30]. However, those measures were not implemented corresponding with the master plan of 1978 which recognizes the informal settlement, and all areas in squatters were zoned as residential areas [4].

The national land policy of 1995 has identified the unplanned settlement by making the provision to all residents found in the unplanned settlements for their land rights to be recognized and registered. The land policy discourages the demolition of the unplanned settlement rather than upgrading them by the provision of basic social infrastructure facilities in non-hazardous areas [74]. On the other hand, the upgrading of the informal settlements in urban settings had been recognized through the National Human Settlements Development Policy of 2000 as the result of the high birth rate which causes population increase and rural-urban migration [74].

The efforts of containing the unplanned settlement were not only ending on recognizing the properties and regularizing them but also in how these regularized properties can be formalized and be accepted as collateral in the eyes of financial institutions [31]. The process entails conducting planning, surveying, and land registration after the due payment of statutory fees [31]. Under this context, the Unplanned Urban Settlements Regularization Program, Property and Business Formalization Program (MKURABITA), and the National Program for Regularization and Prevention of Unplanned Settlements come up with the concern of regularization of informal settlement as the effects of the rapid increase of unplanned settlement in Tanzania [32,49].

The idea of regularization and theoretical perspective originated from the Peruvian economist book by De Soto 2000, which stressed that the significant regularization of the informal settlement could have a greater impact on

the urban economy if the informal extra-legal economy could have been linked up to the formal economy [23,31]. The concept revolving around the whole idea is to unlock the dead capital into live capital or liquid capital and to reduce the poverty impact as financial recognition and inclusion [53]. The regularization is supposed to provide several benefits from the individual property owner to the government; legalization of properties will help to obtain credit as collateral, registration of property and smooth transactions, tax gains to the government, etc. [31].

8. The dichotomy of urban proliferation

In Tanzania, there is a dual structure of land ownership and development, whereby the formal (legal) and informal (illegal) land and structural development is widespread and evolved together (Figure 11a and 11b). The government through its authorities is predominately the regulator and invests little in urban land development by producing public social infrastructure and urban plots productions [4,31]. The private sector has a prime position in urban land production, whereas land development by different landowners is overriding when it comes to property development or land development processes [6,54]. The property owners in the unplanned settlement in Tanzania have nowadays got a legal backup which has not existed before let alone in the colonial era itself. The legal ringfencing of the unplanned settlement (comprising more than 70% of urban cities) in many urban areas, substituted them to be legal owners of the properties with the assurance of having residential licenses or regularized [31]. In addition, it was estimated that in Tanzania approximately 81% of the workforce is employed and operating under the informal sector while the livelihood of the workforce depends on access to public infrastructure services which does not delineate private ownership [54].

Legal acknowledgment of the informal settlements with policies such as regularization and the formalization of informal settlements without any property demolition in the squatter and unplanned settlement generates confidence and the flourishing of the extra-legal urban development and result in a dichotomy urban land development [6,23]. Consequently, the informal landowners develop permanent structures whereby few of them have access to public services such as water and electricity and can be taxpayers and illegal utility purchasers from the main [23]. Again, the development of informal settlements was not limited only to the low-income groups but also the settlement structures show the presence of middle-and higher-income groups in the unplanned alias informal settlements [4,28,56].

The government does not have a well-established social housing policy and leaves the role of providing settlement production to be in the hands of landowners after having land through formal or informal ownership [23,30]. Despite the role of the private sector in the cause of providing urban land plots and infrastructure services,

there are some limitations for the private sector to intervene in the provision of urban land supply and infrastructure services and generate profit by covering the existing demand gap in urban land plots. Nevertheless, some land survey private firms had been devoted themselves to this business, but the problem is still existing at large because of several factors such as inadequate compensations, delay of payments, lack of awareness, political interference, and other complexities in land acquisition procedures [3,54].

Therefore, informal settlement can be considered a land governance failure in carrying out proper land development, distributions, and other land administration and management responsibilities to meet the shelter needs [3,4]. In Tanzania between 50% to 80% of the urban population is living in informal or unplanned settlements [6]. Illegal dwelling leads to poor infrastructure settings and poor quality of housing stocks which impair the efforts of sustainable urban land development.

On the other hand, the dichotomy of urban land development has an inherent effect due to the colonial effects in land laws which leads to the existence of a dual land tenure system; customary land or quasi-customary land ownership especially in the urban fringes areas [2,4,49]. This situation makes land development initiatives face some challenges especially when land acquisition is required for urban land development due to the legal requirement of paying relatively expensive compensation. The major reasons for the dichotomy of urban land development among the challenges stipulated by these scholars are dissatisfaction of the project-affected peoples [9,27], inadequate and delay in payments of the compensation fees [9,29,30], lack of financial resources for projects to regularize land through compensation [57], socioeconomic challenges after the compensation project and incapacity to overcome the relocation and resettlement of project affected people [5], lack of good governance, failure to adhere with the statutory requirements and corruption practices revolving within the land management and administration authorities. Furthermore, other studies revealed that the resettlement actions plan resulted from the compensation in land acquisition and planning which entails reducing the informal settlements, had resulted in the vicious circle of the emergence of new informal settlements because the displaced people were not able to find alternative plots, they could afford with the amount of money they received from compensation in their previous acquired land for development purposes [5,30]. Operation of the land black market and informal marketization of public land development coxed by the landowners at the urban fringes through subdividing land and selling it to other buyers who seek land for dwelling purposes deter the sustainable urban land development and hence dichotomy urban settlement [3,4,28,58,76]. Figures 11 a and 11b represent two scenes of formal (well-planned and serviced land) and informal settlements that evolved together.

(a)   (b)

Figure 11. a) Msasani and Masaki aerial photograph in Dar Es Salaam **b)** Mikocheni aerial photograph in Dar Es Salaam

7. Discussion and policy implications

The current situation is seen in the cities of Tanzania whereby massive population growth, urbanization pace, and higher economic growth it has been the case in the countries such as Japan, Taiwan, Thailand, and South Korea for decades back [77]. Stemming from the foregoing literature and different case studies, the urbanization challenges which had been experienced in different places of the words evolving cities including developing countries, particularly in Tanzania is not a new phenomenon in the cause of land and urban development. It is a common phenomenon that had been experienced by developed countries in the 19th and the early 20th century in the aspect of urban land development and infrastructure land services in most European and Asian countries. Most developed and developing countries show that they had been experiencing similar challenges and pressures from urbanization, such as financial constraints in the land acquisition by local and central authorities, sustainable urban development challenges, how to unlock complex land ownership structures, and supplying of land for the public, environmental issues just to mention few [61,77]. On the cause of finding the solution for urban development, most of the then-developing countries had now adopted and implemented alternative and innovative land development models for land acquisition such as land readjustment, tax increment finance, infrastructure financing models, land value capture, innovative land cadastral, and administration approaches to deal with the urbanization challenges and enhancing the sustainable urban development by evading from the financial and budgetary burdens pinned by conventional land development approaches.

The co-existence of formal and informal urban land development which is purely backed by legal and institutional framework appeared to be a threat to sustainable urban land development and is making public infrastructure, public spaces, and environmental amenities in the cities to be insufficient [74]. The lives of many around the world are merely integrated with the environment while it's true that future survival is tied to an environmental relationship [48]. Alternative urban land development approaches or integrating alternative urban land development approaches are inevitable for sustainable urban land development [61,77].

The only way of reaching sustainable urban development is not only relying on the well planned and cost-effective or self-financing approaches but also should be focused on vertical urban development rather than horizontal urban development since encouraging horizontal urban development whether planned or unplanned will compromise with potential agricultural land in the cause of urbanization. This is because population growth creates demand for affordable food production, decency settlements, and sustainable environmental development.

Tanzania has been facing challenges and struggles in the cause of achieving the aim of sustainable development goals towards achieving sustainable cities as lack of finance for real estate development. The pictorial evidence is revealed under the analysis of satellite imagery of dichotomy settlements. The situation as it is now threatening sustainable urban development, the inadequate fund from the government to finance the urban development process by continuing to implement conventional approaches turns out into environmental problems, impoverishment through loss of land, and resettlement programs.

The urban land development without a proper real estate financing system will make way for the land speculators and endanger the livelihood of the poor or low-income people who will be forced to be displaced from their original premises and as a result, people will seek alternatives and affordable ways to find the land to set up settlements and investment. The government authorities should supply adequate funds, or else should opt for cost recovery models for urban land development and for the implementation of master plans whereby study shows that its implementation is not sufficient to address the urban growth challenges, sustainable growth, and population needs [48].

9. Conclusion

Developing countries had been in a state of challenges in the cause of supplying affordable and sustainable well-serviced land for settlements and infrastructural facilities for urban land development. Most developing countries had been faced with the challenge of supplying infrastructural public services which can support the population growth of rural-urban immigrants, and at the same time achieve sustainable city development and environmental management. Urbanization rate and

population growth in developing countries which has been taking place at a greater momentum in cities undermine the effectiveness of the state's ability on the cause of land development and provision of infrastructural land facilities. Excessive cost and budget constrain which are facing developing countries led to the insufficient supply of serviced land and consequently lead to price hiking of available serviced land which makes it difficult to be affordable among most land seekers. When the government is not in a state of supplying affordable housing settlements and serviced land, the private and informal self-help took part to find a solution and develop informal settlements which as a result challenges the efforts of achieving proper land governance and sustainable urban land development. However, it appeared that the self-initiative actions for settlements are not purposive in achieving environmental amenities, considering public spaces, land economy, and sustainable urban development. It has been found that most people with limited access to housing end up developing land illegally and sometimes in hazardous areas without following the urban land use plan and master plans at large. The low-cost informal settlements are found affordable to most of the people who did not afford the serviced land plots which are scarce and if available are expensive. All these urban land development consequences and land governance misfortunes do not end up in the emergency of informal settlements only but also lead to the emergency of social polarization within the community by the emergency of gated communities.

The key solution to the urban development challenges and dichotomy of informal and formal land rights is to supply affordable housing by means of innovative approaches which can be inclusive and participatory in land-use decisions, land development, and land acquisition. Innovative land development tools are not necessarily to be introduced as a new modal and paradigm shift but rather can be integrated with the existing conventional land development approaches to start with and leverage the land supply and infrastructure services.

The discouragement of top-down land development approaches and encouragement of the bottom-up approach and self-financing land development approaches are found to be relevant and indispensable due to the land development budgetary constraints in developing countries which are facing many economic, social, and environmental issues to achieve.

Having the proper finance is observed as a challenge when it comes to urban land development in many developing countries because of the dichotomy and unsustainable urban growth which was witnessed; it is imperative that innovative policies which have a successive history in other countries such as Japan, Malaysia, South Korea, and India can be applied to get rid of the very same experienced land developmental challenges.

When public governance does not deliver through land governance the proper evidence is the dichotomy of urban settlement development, with the worsening of the urban environment, consequently because sheltering is the basic need of humans, private interest will override

the public interest, and private land governance will rise to fill the void. As a result, social classes, segregation, and even social polarization appeared within formal and informal spatial communities. To contain these challenges the collective actions under the arms of the community and the state as the third part of land development should remain responsible and intact. Urban re-generations and (re)development are among the other issues that developing countries must comprehend and conduct research on the applicability and demonstrability of successful applicable models in sustainable and living cities.

Author contributions

Amani Michael Uisso: Conceptualization, Writing-Original draft preparation, Methodology, Field study
Sibel Canaz Sevgen: Data Analysis, Methodology, Visualization, Image-Data Processing, Software **Harun Tanrıvermiş:** Conceptualization, Supervision, Writing-Reviewing and Editing.

Conflicts of interest

The authors declare no conflicts of interest.

References

1. Wolff, M., Stina, A. K., & Chipman, J. (2018). Urban land governance in Dar es Salaam. *IGC Working Paper.*
2. Kironde, J. L. (2009, March). Improving land sector governance in Africa: The case of Tanzania. In *Workshop on "Land Governance in Support of the MDGs: Responding to New Challenges* (pp. 1-29). Washington, DC: World Bank.
3. Nuhu, S. (2019). Land-access systems in peri-urban areas in Tanzania: Perspectives from Actors. *International Journal of Urban Sustainable Development*, *11*(2), 189-202.
4. Kironde, J. M. L. (2019). Community-Based Settlements Regularization: Lessons for Scaling up from Makongo Juu Informal Settlement, Dar es Salaam, Tanzania. *Current Urban Studies*, *7*(02), 170-192
5. Kironde, J. M. L. (2015). Good governance, efficiency and the provision of planned land for orderly development in African cities: The case of the 20,000 planned land plots project in Dar es Salaam, Tanzania. *Current Urban Studies*, *3*(04), 348-367
6. Kyessi, A., & Tumpale, S. (2013, April). Formalizing property rights in informal settlements and its implications on poverty reduction: The case of Dar es Salaam, Tanzania. In *Proceedings of the Annual World Bank Conference on Land and Poverty. The World Bank, Washington DC* (pp. 8-11).
7. Lupala, J. M. (2010). Sustainable urbanization and spatial growth of cities in least industrialised countries: the case of Dar es Salaam City, Tanzania. *Journal of Building and Land Development*, *17*(1-2), 61-77.
8. Wenban-Smith, H. (2015). Population growth, internal migration, and urbanization in Tanzania,

1967-2012: Phase 2 (final report). International Growth Centre.

9. Komu, F. (2014, June). Urban Land Grabbing and its Implications to Urban Development. In *Being a paper presented at FIG Congress, Kuala Lumpur, Malaysia* (pp. 16-21).

10. Katala, J. N. (2012). The cost of traffic congestion and accidents to the economy in Tanzania. *Dar Es Salaam, Tanzania: http://www. iekenya. org/download/Jumbe% 20N. Katala*, *20*.

11. Msigwa, R., & Kipesha, E. F. (2013). Determinants of youth unemployment in developing countries: Evidence from Tanzania. Journal of Economics and Sustainable Development, 4(14), 67-76.

12. Mfinanga, D., & Fungo, E. (2013). Impact of incidents on traffic congestion in Dar es Salaam city. *International Journal of Transportation Science and Technology*, *2*(2), 95-108.

13. Othman, O. C. (1821). Roadside levels of ambient air pollutants: SO2, NO2, NO, CO and SPM in Dar es Salaam City. *Tanzania Journal of Natural and ISSN*, *7249*.

14. Dasgupta, S., Lall, S. V., & Wheeler, D. (2020). Traffic, air pollution, and distributional impacts in Dar es Salaam: A spatial analysis with new satellite data. *World Bank Policy Research Working Paper*, (9185).

15. Enemark, S. (2017, November). A Fit-For-Purpose approach to Land Administration in Africa in support of the new 2030 Global Agenda. In *The Africa We Want. In Proceedings of the 2017 Conference on Land Policy in Africa UN Economic Commisison for Africa, Addis Ababa, Ethipoia* (pp. 14-17).

16. Union, A. (2009). Land policy in Africa: A framework to strengthen land rights, enhance productivity and secure livelihoods. *Addis Ababa: African Union and Economic Commission for Africa*.

17. UN-HABITAT. (2012). Handling land, Innovative Tools for Land Governance and Secure Tenure: UN-HABITAT

18. Radoki, C. (2006). Social agency and state authority in land delivery processes in African cities: Compliance, conflict and cooperation. *International Development Planning Review*, *28*(2), 263-285

19. Kombe, W. J., & Kreibich, V. (2006). *Governance of informal urbanisation in Tanzania*. Mkuki na Nyota Publishers.

20. Oates, L., Gillard, R., Sudmant, A., & Gouldson, A. (2020). Secure and equal access to land for all: Lessons on land governance and climate resilience from Dar es Salaam, Tanzania.

21. Citizen, T. (2019, 6th February 2019). Only 15 percent of the country's land surveyed, government reveals. Tanzanian Local Newspaper.

22. Bank, A. D. (2013). Urbanization in Africa. African Development Bank Group.

23. Andreasen, M. H., McGranahan, G., Kyessi, A., & Kombe, W. (2020). Informal land investments and wealth accumulation in the context of regularization: case studies from Dar es Salaam and Mwanza. *Environment and Urbanization*, *32*(1), 89-108.

24. Karakuş, P., Karabork, H., & Kaya, S. (2017). A comparison of the classification accuracies in determining the land cover of Kadirli Region of Turkey by using the pixel based and object based classification algorithms. *International Journal of Engineering and Geosciences*, *2*(2), 52-60.

25. Yakup, A. E., & Ayazlı, İ. E. (2022). Investigating changes in land cover in high-density settlement areas by protected scenario. *International Journal of Engineering and Geosciences*, *7*(1), 1-8.

26. Mussa, L. (2016). Urban land use planning legal and institutional issues and challenges in Tanzania: the case of Unplanned Residences in Dar es Salaam and Mwanza.

27. Ndjovu, C. (2016). Understanding causes of dissatisfactions among compensated landowners in expropriation programs in Tanzania. *International Journal of Scientific and Technology Research*, *5*(1), 1-7.

28. Bhanjee, S., & Zhang, C. H. (2018). Mapping latest patterns of urban sprawl in Dar es Salaam, Tanzania. *Papers in Applied Geography*, *4*(3), 292-304.

29. Kombe, W. J. (2010). Land acquisition for public use, emerging conflicts and their socio-political implications. *International Journal of Urban Sustainable Development*, *2*(1-2), 45-63.

30. Lupala, J., & Chiwanga, P. (2014). Urban expansion and compulsory land acquisition in Dodoma National Capital, Tanzania. *Journal of Land Administration in East Africa*, *2*(2).

31. Kusiluka, M. M., Kongela, S., Kusiluka, M. A., Karimuribo, E. D., & Kusiluka, L. J. (2011). The negative impact of land acquisition on indigenous communities' livelihood and environment in Tanzania. *Habitat International*, *35*(1), 66-73.

32. Lugoe, F. N., & Salaam, D. E. (2008, May). A century of government regulated land access in Tanzania. In *Videoconferencing Workshop on Land Administration in Tanzania*.

33. Enemark, S., Bell, K. C., Lemmen, C., & McLaren, R. (2014). *Fit-for-purpose land administration*. International Federation of Surveyors.

34. Agrawal, A., & Ribot, J. (1999). Making decentralization accountable: A framework for analysis and empirical studies from South Asia and West Africa. *Journal of Developing Areas*, *33*, 473-490.

35. Uisso, M. A. (2018). Tanzanya'da Arazi Mülkiyeti, Kullanımı ve Arazi Geliştirme Çalışmalarının Değerlendirilmesi. Ankara University, Master's Thesis.

36. Florczyk, A. J., Corbane, C., Ehrlich, D., Freire, S., Kemper, T., Maffenini, L., ... & Zanchetta, L. (2019). GHSL data package 2019. *Luxembourg, EUR*, *29788*(10.2760), 290498.

37. Corbane, C., Florczyk, A., Pesaresi, M., Politis, P., & Syrris, V. (2018). GHS built-up grid, derived from Landsat, multitemporal (1975-1990-2000-2014), R2018A. European Commission, Joint Research Centre (JRC).

38. Review, W. P. (2021). Retrieved from http://worldpopulationreview.com

39. Canaz, S., Aliefendioğlu, Y., & Tanrıvermiş, H. (2017). Change detection using Landsat images and an

analysis of the linkages between the change and property tax values in the Istanbul Province of Turkey. *Journal of Environmental Management*, *200*, 446-455.

40. Dar Es Salaam population growth data: https://www.macrotrends.net/cities/22894/dar-es-salaam/population Accessed: October 2021.

41. The World Bank Data (2020), FAOSTAT 2020

42. Worldometer (2021), NBS population projection.

43. www.macrotrends.net Accessed: 2021, October

44. Worldometer, C. C. (2021). Worldometer. 2020. Update (Live)

45. Karra, K., Kontgis, C., Statman-Weil, Z., Mazzariello, J. C., Mathis, M., & Brumby, S. P. (2021, July). Global land use/land cover with Sentinel 2 and deep learning. In *2021 IEEE international geoscience and remote sensing symposium IGARSS* (pp. 4704-4707). IEEE.

46. Enemark, S. (2009). Land governance for sustainable development. Paper presented at the Opening keynote address at the FIG/World Bank Conference Land governance in support of the MDGs: Facing the new challenges ", Washington DC.

47. Williamson, I., Enemark, S., Wallace, J., & Rajabifard, A. (2010). *Land administration for sustainable development* (p. 487). Redlands, CA, USA: ESRI Press Academic.

48. Peter, L. L., & Yang, Y. (2019). Urban planning historical review of master plans and the way towards a sustainable city: Dar es Salaam, Tanzania. *Frontiers of Architectural Research*, *8*(3), 359-377.

49. Tenga, R. W. (2015). The Land Governance Assessment Framework (LGAF) Synthesis Report: World Bank -Tanzania.

50. John, P., & Kabote, S. J. (2017). Land governance and conflict management in Tanzania: Institutional capacity and policy-legal framework challenges. American Journal of Rural Development, 5(2), 46-54

51. Fitzgerald, A. (2017). *Wearing an amulet: Land titling and tenure (in) security in Tanzania* (Doctoral dissertation, National University of Ireland, Maynooth (Ireland)).

52. Watson, V. (2009). 'The planned city sweeps the poor away...': Urban planning and 21st century urbanisation. *Progress in planning*, *72*(3), 151-193.

53. De Soto, H., & Diaz, H. P. (2002). The mystery of capital. Why capitalism triumphs in the West and fails everywhere else. *Canadian Journal of Latin American & Caribbean Studies*, *27*(53), 172.

54. Kasala, S. E., Burra, M. M., & Mwankenja, T. S. (2016). Access to Improved Sanitation in Informal Settlements: The Case of Dar es Salaam City, Tanzania. *Current Urban Studies*, *4*(01), 23-35

55. Uisso, A. M., & Tanrıvermiş, H. (2021). Driving factors and assessment of changes in the use of arable land in Tanzania. *Land Use Policy*, *104*, 105359.

56. Kalabamu, F. T. (1992). Tanzania: Developing urban residential land. *Journal of Urban Affairs*, *14*(1), 61-78.

57. Locke, A., & Henley, G. (2016). Urbanisation, land and property rights. *ODI report Jan*.

58. Mercer, C. (2017). Landscapes of extended ruralisation: postcolonial suburbs in Dar es Salaam, Tanzania. *Transactions of the Institute of British Geographers*, *42*(1), 72-83.

59. Tırmanoğlu, B., İsmailoğlu, İ., Kokal, A. T., & Musaoğlu, N. (2023). Yeni nesil multispektral ve hiperspektral uydu görüntülerinin arazi örtüsü/arazi kullanımı sınıflandırma performanslarının karşılaştırılması: Sentinel-2 ve PRISMA Uydusu. *Geomatik*, *8*(1), 79-90.

60. Yakup, A. E., & Ayazlı, İ. E. (2022). Investigating changes in land cover in high-density settlement areas by protected scenario. *International Journal of Engineering and Geosciences*, *7*(1), 1-8.

61. Amirtahmasebi, R., Orloff, M., Wahba, S., & Altman, A. (2016). *Regenerating urban land: A practitioner's guide to leveraging private investment*. World Bank Publications.

62. UN-Habitat, (2016). Urbanization and Development Emerging Futures. World Cities Report. UK: Earthscan Publications

63. Nuhu, S., & Kombe, W. J. (2021). Experiences of private firms in delivering land services in peri-urban areas in Tanzania. *International Planning Studies*, *26*(2), 101-116.

64. Magembe-Mushi, D. L., & Lupala, J. M. (2015). Resettling displaced residents from regularised informal settlements in Dar-es-Salaam, Tanzania: Challenges faced by house owners. *Current Urban Studies*, *3*(02), 71-81

65. Kasala, S. E., & Burra, M. M. (2016). The role of public private partnerships in planned and serviced land delivery in Tanzania. *iBusiness*, *8*(01), 10-17

66. Hong, Y. H., & Brain, I. (2012). Land readjustment for urban development and post-disaster reconstruction. *Land Lines*, *24*(1), 2-9.

67. Briggs, J., & Mwamfupe, D. (1999). The changing nature of the peri-urban zone in Africa: Evidence from Dar-es-Salaam, Tanzania. *Scottish Geographical Journal*, *115*(4), 269-282.

68. Kitay, M. G. (1985). Land acquisition in developing countries: policies and procedures of the public sector with surveys and case studies from Korea, India, Thailand and Ecuador.

69. Gwaleba, M. J., & Masum, F. (2018, June). Participation of informal settlers in participatory land use planning project in pursuit of tenure security. In *Urban Forum* (Vol. 29, pp. 169-184). Springer Netherlands.

70. Locke, A., & Henley, G. (2016). Urbanisation, land and property rights. *ODI report Jan*.

71. United Republic of Tanzania (URT), (1995). National Land Policy. Dar es Salaam: Government Printer.

72. Yılmaz, O. S., Gülgen, F., Güngör, R., & Kadı, F. (2018). Coğrafi Bilgi Sistemleri ve Uzaktan Algılama Teknikleri ile Arazi Kullanım Değişiminin İncelenmesi, Köprübaşı İlçesi Örneği. *Geomatik*, *3*(3), 233-241.

73. Makundi, D. I. (2017). Assessment of policies and practices of land delivery by private sector: a focus on two projects in kigamboni municipality in dar es salaam City (Master's Thesis). *Ardhi University, Dar es Salaam*.

74. Uisso, A. M., Yeşim, A. T., Ahsan, M. M., & Tanrıvermiş, H. (2022). Revisiting land distribution policies among land-based sectors in Tanzania. *African Journal on Land Policy and Geospatial Sciences*, *5*(4), 735-752.

75. URT-United Republic of Tanzania., (2022). National Bureau of Statistics (NBS) Tanzania National Census-2022

76. Briggs, J., & Mwamfupe, D. (1999). The changing nature of the peri-urban zone in Africa: Evidence from Dar-es-Salaam, Tanzania. *Scottish Geographical Journal*, *115*(4), 269-282.

77. Lozano-Gracia, N., Lall, S. V., Young, C., & Vishwanath, T. (2013). Leveraging land to enable urban transformation: Lessons from global experience. *World Bank Policy Research Working Paper*, (6312).

78. United Republic of Tanzania (URT), (2000). National Human Settlements Development Policy, 2000. Dar es Salaam: Ministry of Lands, Housing and Human Settlements Development.

79. Morsy, S., & Hadi, M. (2022). Impact of land use/land cover on land surface temperature and its relationship with spectral indices in Dakahlia Governorate, Egypt. *International Journal of Engineering and Geosciences*, *7*(3), 272-282.

80. Ahady, A. B., & Kaplan, G. (2022). Classification comparison of Landsat-8 and Sentinel-2 data in Google Earth Engine, study case of the city of Kabul. *International Journal of Engineering and Geosciences*, *7*(1), 24-31.

81. https://unequalscenes.com/tanzania. Accessed: December 2021.

Monitoring and classification of karst rocky desertification with Landsat 8 OLI images using spectral indices, multi-endmember spectral mixture analysis and support vector machine

Çağan Alevkayalı [*1] , **Onur Yayla** [2] , **Yıldırım Atayeter** [1]

1Süleyman Demirel University, Geography Department, Türkiye
2Mehmet Akif Ersoy University, Department of Turkish and Social Sciences Education , Türkiye

Abstract

Karst Rocky Desertification (KRD) is the reduction of vegetative productivity of this land with the release of bedrock as a result of the full or partial transportation of the fertile soil through natural processes and human activities in karst landscapes. The purpose of this study is to reveal the effectiveness of Remote Sensing methods in monitoring, mapping and evaluating KRD. Landsat 8 OLI images were used to carry out these procedures. In monitoring this process, Karst Bare Rock Index (KBRI), Normalized Difference Rock Index (NDRI), Carbonate Rock Index 2 (CRI2), Normalized Difference Build-Up Index (NDBI), Normalized Difference Vegetation Index (NDVI), Dimidiate Pixel Model (DPM), Multi Endmember Spectral Mixture Analysis (MESMA) and Support Vector Machine (SVM) were used from the spectral indices. In order to determine KRD with spectral indexes, a strong linear relationship was tested between some indices such as DPM (R^2=0,79), KBRI (R^2=0,66), and NDBI (R^2=0,64) and field measurements. In order to evaluate the results obtained, KRD was divided into 4 basic classes such as none, mild, moderate, and severe. According to these classification levels, it was determined that the SVM method had the highest accuracy (Kappa=0.88). According to the classification results, which have the highest accuracy in the study area, the rate of areas undergoing severe karst desertification is 40%, moderate desertification process is 17%, mild desertification is 14% and non-desertification is 29%. In the study, it was concluded that the KRD strengthens as one goes from south to north and from west to east in the research area. This study points out KRD is one of the effective ecosystem problems in the Mediterranean region, Türkiye.

1. Introduction

The concept of karst is defined as the process of dissolution and deposition realized on carbonates, evaporates and halite with water [1]. This term essentially explains the shapes that are created by the melting of soluble rocks and passing underground through surface streams [2]. The term karst has been associated with the world of science with the German pronunciation of the name of a region between Italy and Slovenia, which is called Carso in Italian and Kras in Slovenian [1]. Karst landscapes are characterized by landforms such as dolines, caves, collapsed sinkholes and carbonate deposits that develop on carbonate rocks (limestone, dolomite, marble) or evaporites (gypsum, anhydrite, rock salt) [2,3].

The total area of karst landscapes around the world is approximately 22 million km² which accounts for approximately 12% of the lithosphere [4,5]. Karst landscapes with heterogeneous and complex land cover, are among the different types of surfaces that make up the lithosphere, are widespread in Türkiye as well as in several parts of the world. Considering the spread of karst landscapes in Türkiye, it is known that these areas correspond to approximately one third of the total area of the country [6].

Karst regions have sensitive ecological characteristics due to geological structures [7]. In karst landscapes, fragmented plant communities that develop on discontinuous soil cover are generally encountered [8]. For this reason, when damage to the soil and vegetation in Karst regions cannot be tolerated in the

---

* Corresponding Author

*(caganalevkayali@sdu.edu.tr) ORCID ID 0000-0001-7044-8183
(oyayla@mehmetakif.edu.tr) ORCID ID 0000-0002-8710-3701
(yatayeter@sdu.edu.tr) ORCID ID 0000-0002-7570-2993

short term, the ecosystem in these regions suffers [9]. One of the most important problems that arise in the ecosystem in karst landscapes is the exposure of the bedrock after the soil cover has been removed due to the destruction of vegetation as a result of natural processes or human effects [10]. This process, which is defined as Karst Rocky Desertification (KRD) in the literature, actually refers to land degradation in karst landscapes in its simplest terms [4,10]. KRD, which means the reduction of soil cover due to deforestation and erosion in karst lands, is a term used to express a land degradation process [11]. According to the explanations in the literature, the erosion of the soil due to human activities such as crop production, animal grazing, extreme climatic events, and changes in land functions are the leading causes that accelerate KRD [12, 13, 7]. The negative effects caused by KRD are both environmental and economic problems such as landslides, floods and erosion [14]. The rapid development of many environmental problems in areas where KRD is effective is important in terms of identifying regions where this process has developed and controlling it by monitoring.

Vegetation cover, exposed bedrock and soil depth are used in expressing or classifying the degree of degradation of the land during the KRD process [11]. However, there is no standard approach to the classification of surfaces on which this problem is effective as regards monitoring, mapping or evaluation of KRD (Table 1). For example, in the study conducted by Yang et al. [13], the regions where the open rock surface is more than 70% in terms of KRD classification were stated as very severe desertification areas. On the other hand, the same surfaces were marked as areas with severe KRD in the study conducted by Bai et al. [15] (Table 1). Moreover, areas with an Exposed Bedrock Rate (EBR) of less than 30% were stated by Jiang et al. [4] as no desertification, while Bai et al. [15] categorized these areas into two groups as non-desertification or potential desertification areas (Table 1). In this study, the class intervals used by Jiang et al. [4] were preferred in the classification of KRD. Because of this complexity, a new classification approach was used in this study, in which the exposed rock rate and soil depth were evaluated together.

Table 1. Classification of exposed bedrock rate (EBR) in different KRD studies

Classification of Karst Rocky Desertification	EBR (Bai, et al. [15])	EBR (Jiang et al. [4])	EBR (Yang et al. [13])
No-Desertification	<%20	<30%	<10%
Potential	21%- 30%	-	-
Mild	31%- 50%	30%- 50%	10%- 30%
Moderete	51%- 70%	50%- 70%	30%- 50%
Severe	71%- 90%	> 70%	50%- 70%
Very Severe	> 91%	-	> 70%

In recent years, remote sensing (RS) methods have replaced labor-intensive and costly traditional methods in monitoring KRD [14,16]. RS methods provide low-cost data collection, wide area coverage and spatial continuity [8].

In the literature, normalized difference spectral indices are the most popular practices for ecological planning that are often used for the detection of Land Use/Land Cover Change and Land Surface Temperature studies which are based on similar conditions to occur KRD [17]. Monitoring, mapping and grading of KRD with RS methods are basically based on determining the land exposure rate (Exposed Bedrock Rate) and vegetation cover rate [18]. Visual interpretation and computer-aided image processing were emphasized in the first studies to detect KRD with the help of satellite images [14]. The advantage of spectral indices over other methods is that they give fast results in monitoring KRD in large areas without classification [14]. In some studies, the best performing indices that gave good results for monitoring KRD were retrieved by spectral unmixing to obtain more effective results on the image in mapping KRD [5]. One of the methods with high accuracy rates in determining the KRD is the support vector machine method [19]. Sub-pixel modeling and machine learning methods (such as Support Vector Machine, Random Forest) were also used to distinguish bare karst surfaces and covered areas in complex areas [7]. SVM, which is used in the classification of karst rock desertification, has been used successfully in different classification

applications and in solving pattern recognition problems [20, 21].

Various indices, mixture analysis and machine learning methods have been used for monitoring KRD at the regional or local level [16]. The aim of this study is to determine the spectral indices and classification method that gives the best results in KRD monitoring and to prove the areas where karst rock desertification is intense in the study area. Moreover, this study compares whether classified spectral indices or different classification practices are more effective in mapping KRD. For this purpose, firstly statistical linear relationships between spectral indices revealing karst rocky desertification and field measurements (In-Situ investigation) of karst rocky desertification were tested in the study area. Afterward, the accuracy rates of the spectral indices which were classified according to the index values and directly applied classification approaches such as machine learning methods were calculated. In addition, examining the human activities that accelerate this problem in the study area is another subject to be clarified. The research questions to be answered in line with these purposes: Is there a statistically significant relation between the spectral indices and the rate of exposed bedrock? What are the most effective methods for the classification of Karst Rocky Desertification in the Mediterranean region of Türkiye? How did the relations between karst landscapes and human activities develop in the study area within the scope of desertification?

2. Method

2.1. Study area

Aksu Stream Basin is a good example of an area where the Mediterranean climate is effective and karstification is common. A large part of the research area is located on the Taurus Mountains mass, which is one of the biggest karst landscapes of Türkiye [22]. The Aksu Stream Basin is located between 36-38° north latitudes and 30-31° east longitudes based on its mathematical location (Figure 1).
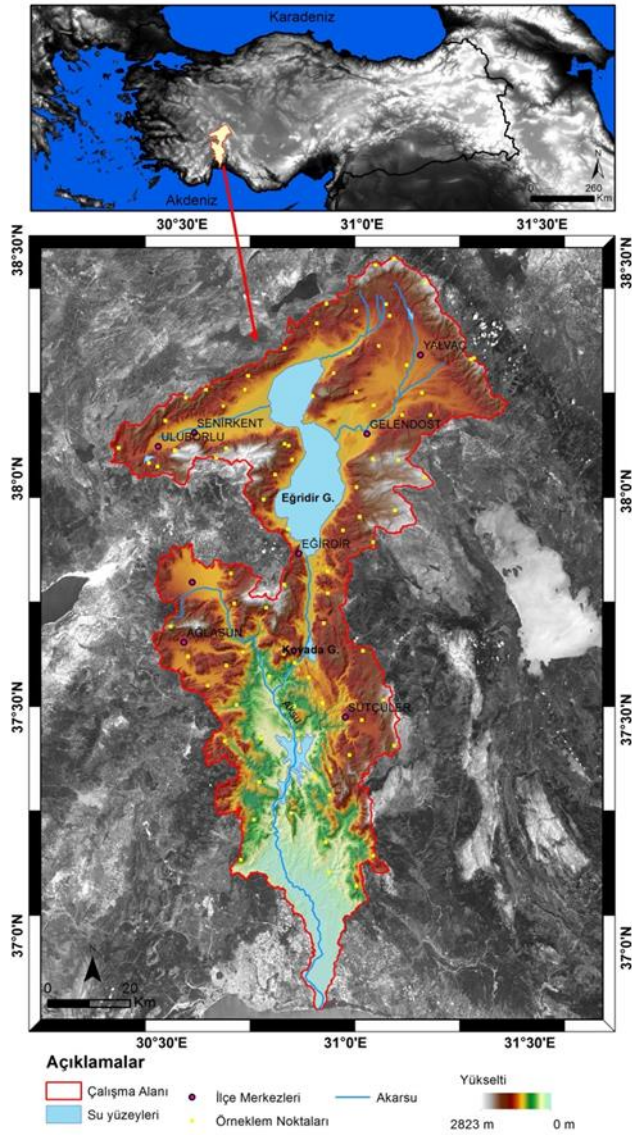
Figure 1. The location of research area and distribution of sample points

Gölcük Lake Basin was not included in the research boundaries as a result of which the boundaries of the research area were determined as 6850 km². Aksu Stream Basin is the largest sub-basin of Antalya Basin, which is one of the 25 major basins of Türkiye [23]. The formations of the land in the Aksu Stream Basin and its immediate surroundings present quite different spreading areas and lithological features. Limestone, which is very important in the formation of the KRD, dominates the study area. Limestone generally consists of units stratified in different formations of Triassic, Jurassic and Cretaceous ages [24]. Karst structures have been shown in the calcareous units indicating a suitable environment for the progress of the KRD in the study area.

Another factor affecting vegetation distribution in terms of KRD is climate. It is not feasible to reach a conclusion that a typical Mediterranean Climate is effective in the entire Aksu Stream Basin. Considering the monthly temperature values, it is known that the annual average temperature in the Western Mediterranean Region is 12.1-12.6 °C in the high regions, the sea impact is effective, and it is in the range of 12.7-13.9 °C in low altitude areas [25]. In the Aksu Stream Basin, the winter season is generally very rainy and humid, the summers are hot and dry, the spring is unstable in terms of precipitation, and the autumn season gains a character similar to the winter season [26].

2.2. Data

Landsat 8 OLI images presented by the United States Geological Survey (http://usgs.com) were used in this study, in which RS methods were employed for monitoring KRD. Landsat 8 satellite was launched by the National Aeronautics and Space Administration on February 11, 2013 with the addition of OLI and a Thermal Infrared sensor [17]. Later, it was transferred to USGS for routine imaging operations [27]. In the selection of images representing the study area, attention was paid to witness that the vegetation period has ended and the study area boundaries are completely cloudless (Table 2). In the next stages, pre-editing operations were performed on the images. The FLAASH (Fast Line-of-Sight Atmospheric Analysis of Hypercubes) tool was used for atmospheric and radiometric arrangements. Lakes in vector data format and non-karst areas obtained from 1/25000 scale geology maps created by MTA (Mining Technical Exploration) were excluded from the combined maps.

Table 2. Landsat 8 OLI images used in the study

Date	Image ID	Column	Row	Sun Angle	Cloud Rate (%)
1 July 2019	LC81780332019182LGN00	178	33	66.02	0.09
1 July 2019	LC81780342019182LGN00	178	34	66.59	1

One of the most important factors in determining the areas where KRD is effective is the exposed bedrock rate. In the determination of EBR, a relationship is established as the EBR increases as the vegetation cover rate decreases. The vegetation cover rate was determined by forest stands obtained from the General Directorate of

Forestry with the help of fieldwork from sampling points (Figure 1). Parameters which contained in forest stands such as average stand height and their distribution are repeated applications [28]. Horizontal vegetation cover in forest stands was determined as separating vegetation into 10x30 or 20x20 diameters with a peak frequency

meter [29]. Soil depth, which is another parameter used in the classification of KRD, was determined with the help of 82 field measurements with a soil auger (Figure 2). In the classification of images, 50 sample points were used for the training process and 32 measurements were utilized for ground truth accuracy.

Figure 2. A view from sampling with a 100cm auger to determine soil depth.

2.3. Method

The methods used in this study for monitoring KRD are Spectral Indices, Dimidiate Pixel Model, Multiple Spectral Mixture Analysis and Support Vector Machine. To understand how effective the spectral indices and sub-pixel segmentation are in monitoring KRD, the linear relationships between field measurements (rock ratio calculated using the tree cover ratio and soil depth) and the indices were tested with simple linear-regression analysis within the scope 82 sampling points (Eşitlik 1).

$$Y = a + b.x \qquad (1)$$

The indices that are frequently used in KRD monitoring studies are:

2.3.1. Karst bare-rock index (KBRI)

The methods applied in KRD are mainly based on the principle of distinguishing vegetation, bedrock surface and soil surface from each other [18]. In this method, the spectral difference between bare rock and other types of land cover becomes evident in the SWIR1 (Landsat 8-OLI image band 6) band (Eşitlik 2). As the index results obtained by making use of this relationship between the bands approach +1 the severity of KRD increases.

$$KBRI = \frac{pSWIR1 - pNIR}{20 \, x \, \sqrt{pSWIR1 + pNIR}} \qquad (2)$$

2.3.2. Normalized difference rock index (NDRI)

This index, derived by Huang and Cai [30] is calculated based on the difference between the strong reflection of visible radiation (band 3) and the complete absorption of mid-infrared wavelengths (band 5) by water. In this method, it is accepted that KRD increases when the results are negative values, and decreases when the results are positive (Eşitlik 3).

$$NDRI = \frac{pNIR - pGreen}{pNIR + pGreen} \qquad (3)$$

2.3.3. Carbonate rock index 2 (CRI2)

This index was prepared by Xie et al. [31] based on the logic that blue and near infrared bands are more effective in reflecting the vegetation cover with soil. In the results obtained by means of this index, karst landscapes become more pronounced in areas where reflection values decrease (Eşitlik 4).

$$CRI2 = \frac{pBlue - pNIR}{pBlue + pNIR} \qquad (4)$$

2.3.4. Normalized difference built-up index (NDBI)

NDBI is one of the indices referenced in the literature for determining KRD [14]. This indice was applied with the use of SWIR1 and NIR bands (Eşitlik 5). The results mean that as the areas where positive values are calculated with NDBI approach up to + 1, the severity of KRD increases.

$$NDBI = \frac{pSWIR1 - pNIR}{pSWIR1 + pNIR} \qquad (5)$$

2.3.5. Normalized difference vegetation index (NDVI)

NDVI is an index used to determine vegetation cover based on the relationship between the near infrared and red bands (Eşitlik 6). these values are close to +1 means that there is dense vegetation in the field, while being close to -1 means that the leaves lose their vitality or the vegetation is sparse [32]. In a region where NDVI shows negative values mean desertification has increased whereas the positive values are not observed below 0.2 [33].

$$NDVI = \frac{pNIR - pRed}{pNIR + pRed} \qquad (6)$$

Another method preferred in KRD monitoring is Dimidiate Pixel Model. This model is generally used for the calculation of Fractional Vegetation Cover [7]. This method is defined as the rate of vertical coverage of the vegetation cover with its projection on the ground surface. Other methods are MESMA and SVM Methods which show the highest accuracy in the literature.

2.3.6. Dimidiate pixel model (DPM)

This model is generally used to calculate fractional vegetation [19]. This method is defined as the rate of the vertical coverage of vegetation to its projection on the ground surface. The Dimidiate Pixel Model used to determine Fractional Vegetation is based on the

relationship between green vegetation and open soil surfaces (Eşitlik 7). Firstly, using NDVI, the areas devoid of vegetation were determined and NDVI$_{Soil}$ was calculated. The regions where vegetation reaches the highest values are calculated as NDVI$_{Vegetation}$:

$$DPM=(NDVI_{Vegetation}NDVI_{Soil})/(NDVI_{Vegetation}+NDVI_{Soil}) \quad (7)$$

### 2.3.7. Multiple endmember spectral mixture analysis (MESMA)

Spectral Mixture Analysis is used to create models of pixel reflections with linear or nonlinear approaches [34]. MESMA is used in studies in the literature for different purposes such as determining the bedrock surface [35], classifying vegetation cover [36], and drawing the boundaries of urban areas [37] (Eşitlik 8). The reason why MESMA was preferred in addition to spectral indices in this study is its high performance in the determination of KRD in previous studies [7].

$$R_i = \sum_{k=1}^{n} f_k R_{ik} + \varepsilon_i \quad (8)$$

2.3.8. Support Vector Machine (SVM)

The Support Vector Machine approach is used to classify images using remote sensing methods and statistical methods [38]. This method tries to find the most suitable sub-pixels between classes by making use of training values [39]. The United States Geological Survey and European Space Agency use different machine learning algorithms including SVM for Spectral Feature extraction [40]. Also, thanks to this method, good classification accuracy with multi-spectral bands such as Landsat images is obtained [41].

KRD Criteria: The criteria for determining areas where KRD is effective in the research area were evaluated by dividing it into 4 classes. Vegetation cover, EBR and soil depth were evaluated together for the classification of KRD (Table 3). The first of these are areas without desertification where the vegetation cover is alive and soil depth is high. Other classes are regions where desertification is mild, moderate and severe. Samples belonging to these four classes in the research area can be easily distinguished in field studies (Figure 3).
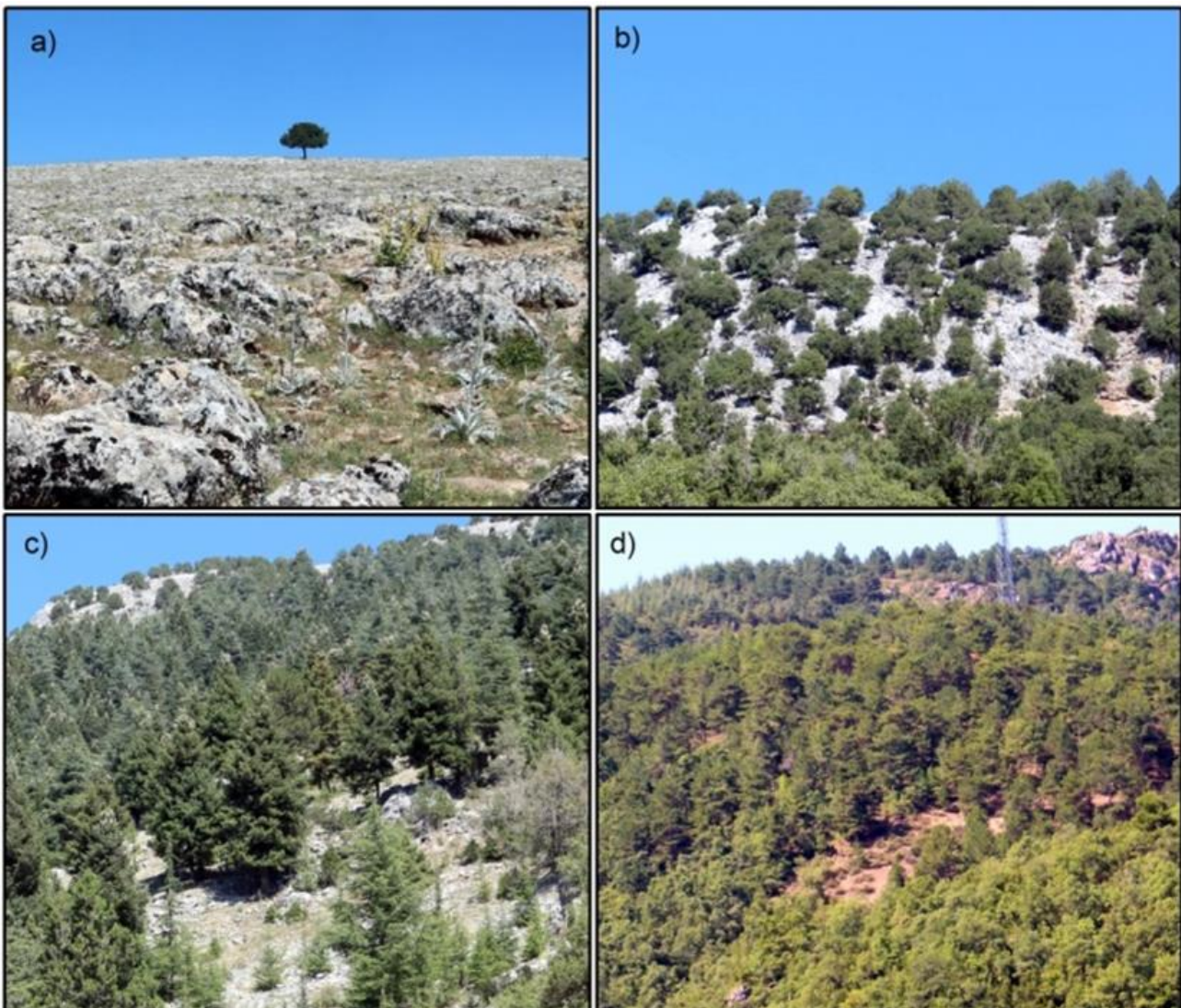
Figure 3. The views from different environments in study area of KRD in the research area; a) Severe KRD b) Moderate KRD c) mild KRD d) no KRD

Table 3. The criteria used in the classification of KRD in this study

Karst Rocky Desertification Classes	Exposed Bedrock Rate (%)	Vegetation Cover (%)	Soil Depth (cm)
No-Desertification	< %20	>80%	More than 75 cm
Mild	20% - 50%	%51-%80	20 -75 cm
Moderete	50%- 80%	20%- 50%	20-75 cm
Severe	> %80	< %20	Less than 20 cm

The performances of all indices used in this study were carried out by statistically testing their accuracy according to their percentage of bedrock. Thus, determination coefficients (R^2) were calculated between index results and spatial measurements (Eşitlik 9).

$$R^2 = \beta_0 + \beta_1 . X + \epsilon \qquad (9)$$

Within the scope of the classification of the results obtained from the methods applied for determining the KRD, determination of manual class ranges, Iso Clustered Unsupervised Classification, MESMA and Support Vector Machine methods were used. Accuracy evaluations of the classified data, 32 out of the 82 randomly selected sample points, were performed by calculating the Kappa Coefficient (Eşitlik 10).

$$K = \frac{P(o) - P(e)}{1 - P(e)} \qquad (10)$$

3. Results

KRD develops in karst landscapes, where there is weak vegetation, vulnerable soil and warm-rainy climate conditions. Considering that agricultural activities have been going on for thousands of years in Anatolia, it is not possible to analyze the land independent from human activities. The weakening of the vegetation, the sensitization of the soil by human processing, and the interaction of human and natural processes increase the KRD effect. In the Aksu Stream Basin, natural processes and human activities were effective jointly in the land to reach its current appearance.

3.1. Comparison exposed bedrock rate between spectral indices

In this study determined by field measurements, higher results were obtained in the linear relationship levels of the spectral indices results calculated. The linear relationship between the various Spectral Indices and Dimidiate Pixel Model results and the EBR obtained from the sample points was tested with the regression model (Figure 4). All of the Indices used for monitoring and mapping KRD have values between +1 and -1 (Figure 4). According to the results, high-level and statistically significant linear relationships were determined between the results of 4 methods and the Exposed Bedrock Rate. Among them, DPM and KBRI were determined to be statistically compatible with terrestrial measurements. There is a statistically positive correlation between EBR values and KBRI, CRI2 and

NDBI results, while there is a negative correlation between NDRI, NDVI and DPM. Highly significant relationships were determined between EBR obtained from sample points and the results of KBRI, NDBI, NDVI and DPM methods (Figure 4). A lower level of linear relationship was found between the other indices NDVI and NDBI and spatial measurements. In this study, the indices in which a low-level linear relationship is determined with local measurements are NDRI and CRI2. The linear relationships at the level between the results obtained within the scope of determining the KRD in this study and the field measurements mean that most of these methods show moderate performance. It is seen that EBR could not represent the bedrock in estimation, but DPM results were successful in predicting EBR.

In all spectral index results of KRD, regions with severe desertification are expressed in red, and areas with healthy vegetation are expressed in green (Figure 5). Considering the results obtained in this study, although there is a difference between the values, some similarities appear in the general outlook (Figure 5). Considering that the best estimate for the estimation of EBR is DPM results, KRD increases from south to north and from west to east in the Aksu Stream Basin (Figure 5).

3.2. Classification of results

The situation that misleads the results obtained by RS methods for determining the KRD most and that causes the occurrence of error margin in classifications is the garrigue formations that develop on thin soil cover and spread continuously over the field. The fact that some areas determined in field observations where KRD is effective are covered with thin soil and garrigue cover which have a good value of vegetation reflection prevents the determination of desertification in these areas by satellite images (Figure 6).

Accuracy analyses of classifications performed within the scope of determining the areas where KRD is effective were carried out within the scope of control points. Accordingly, the reliability of agreement between local examinations carried out with the field studies and the classified results was tested (Table 4). The results presented within the scope of KRD in the research area were classified using the Spectral Indices of Iso-Cluster Unsupervised Classification, MESMA and SVM methods. The accuracy of the classes and spatial measurements were calculated with the Kappa Coefficient (Table 4).

According to these results, it was determined that the classification accuracy in MESMA and SVM methods was considerably higher.
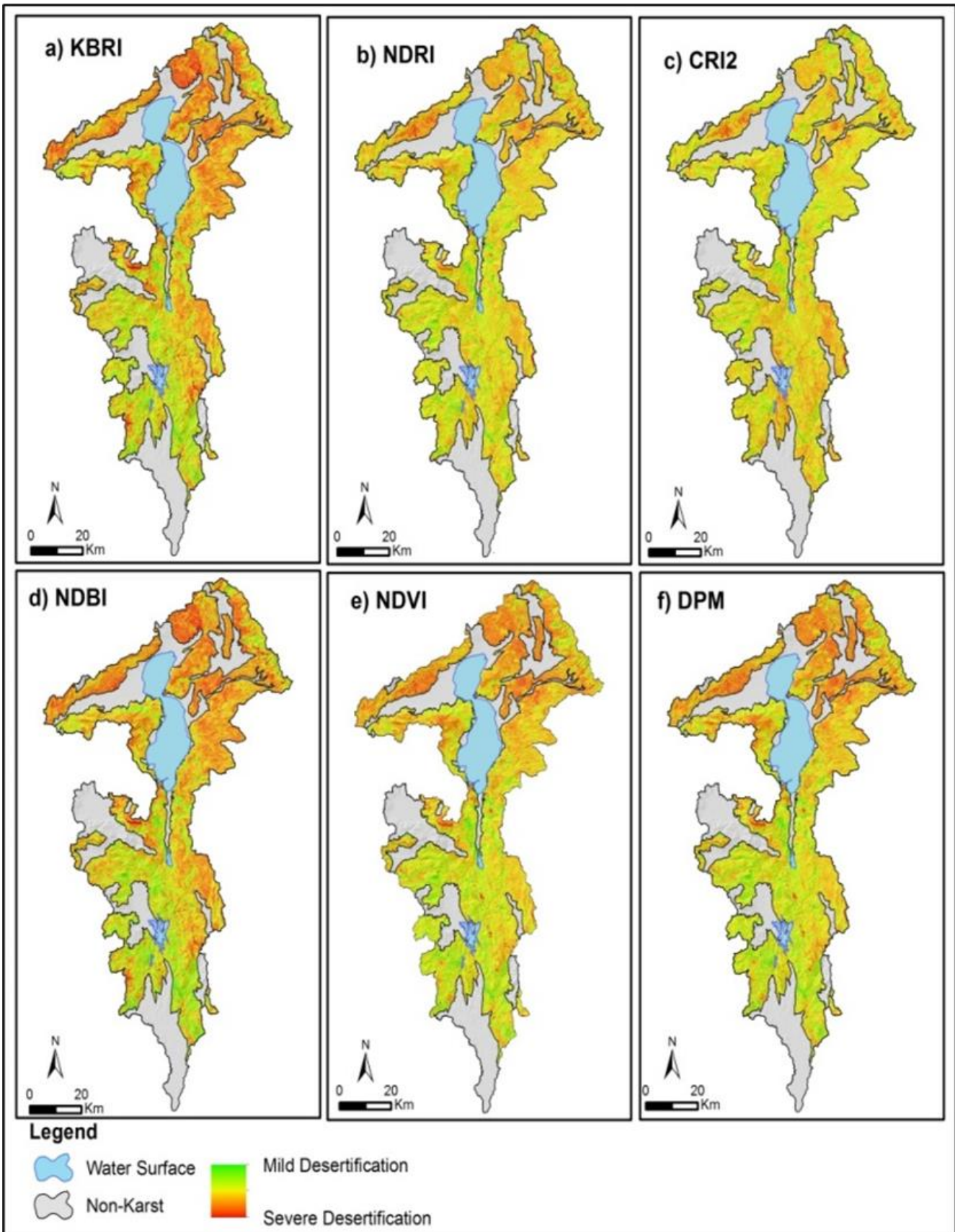
Figure 5. The results of methods used to assess KRD: a) Karst Bare Rock Index (KBRI), b) Normalized Difference Rock Index (NDRI), c) Carbonate Rock Index 2 (CRI2), d) Normalized Difference Build-Up Index (NDBI), e) Normalized Difference Vegetation Index (NDVI), f) Dimidiate Pixel Model (DPM)
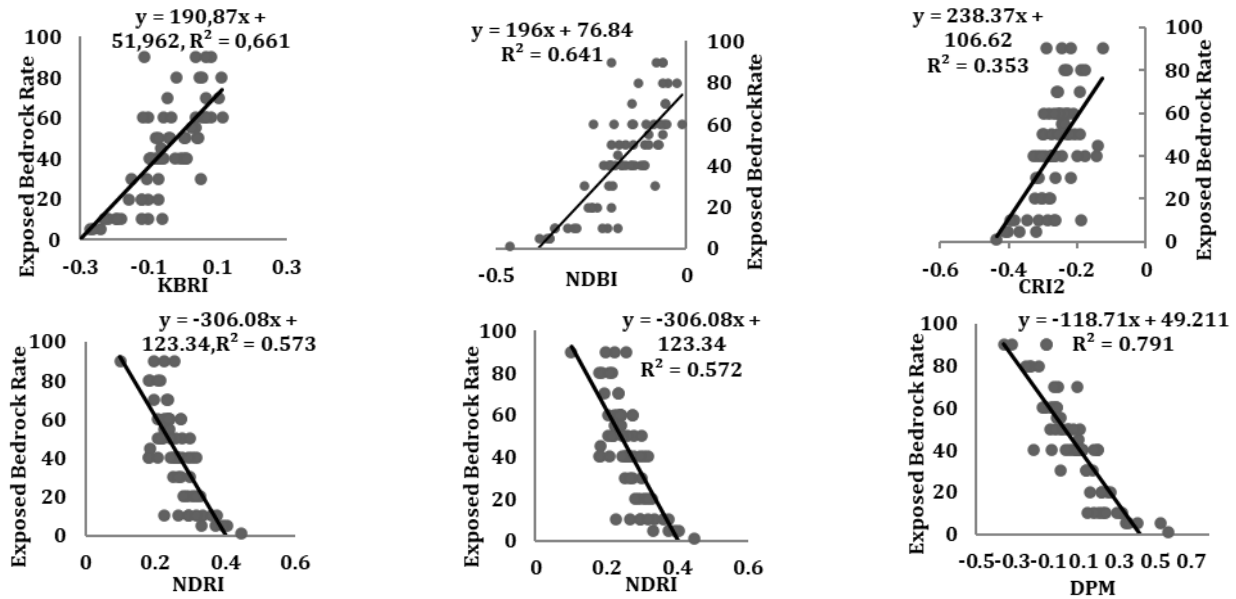
Figure 4. The Linear relationships between exposed bedrock rate and methods which used to assess KRD in this study

Table 4. Kappa coefficient of classification results

Classification	ISO-KBRI	ISO-NDRI	ISO-CRI2	ISO-NDBI
Overall accuracy	0,65	0,61	0,55	0,61
Kappa	0,52	0,46	0,39	0,46
Classification	ISO-NDVI	ISO-DPM	MESMA	SVM
Overall accuracy	0,68	0,69	0,75	0,88
Kappa	0,56	0,57	0,65	0,81

Figure 6. A view of the uninterrupted garrigue formations that prevent to assess KRD based on RS methods around the Uluğbey settlement.

According to the classification results with the highest statistical accuracy, it is seen that the SVM is effective in a significant part of the research area. High-accuracy results show that KRD is high around Lake Eğirdir (Figure 7).

One of the important findings in this study is not only direct measurements of some indexes defined as high accuracy to explain KRD level, but also high overall accuracy was determined when they were classified. In this study, it was concluded that the most effective methods of KRD classification were MESMA and SVM which are two separate methods in the various classification methods used in this study.

3.3. The effects of KRD: Space and People

In the examinations carried out on the surfaces where KRD is effective in the research area, it is understood that human-induced effects accelerate this process. These effects are primarily seen in that the lands lose their productivity as a result of agricultural misuse and intensive land opening applications where the slope is increased (Figure 7). Uncontrolled human activities (overgrazing, improper agricultural practices and improper land use) and extreme natural events (fires) in karst lands play a critical role in desertification. To express the KRD process in the study area gradually, people first clear the area of vegetation where they will carry out agricultural activities. As agricultural activities are carried out in these areas where plowing activities are carried out, the topsoil is eroded. Over time, these areas are left to their fate as the yield decreases. The evidence of the abandonment of agricultural lands is piles of stones between rocks and grass (Figure 8). In this case, since there are sparse plants left to hold the soil cover in the field, bare rocky surfaces are exposed by erosion.
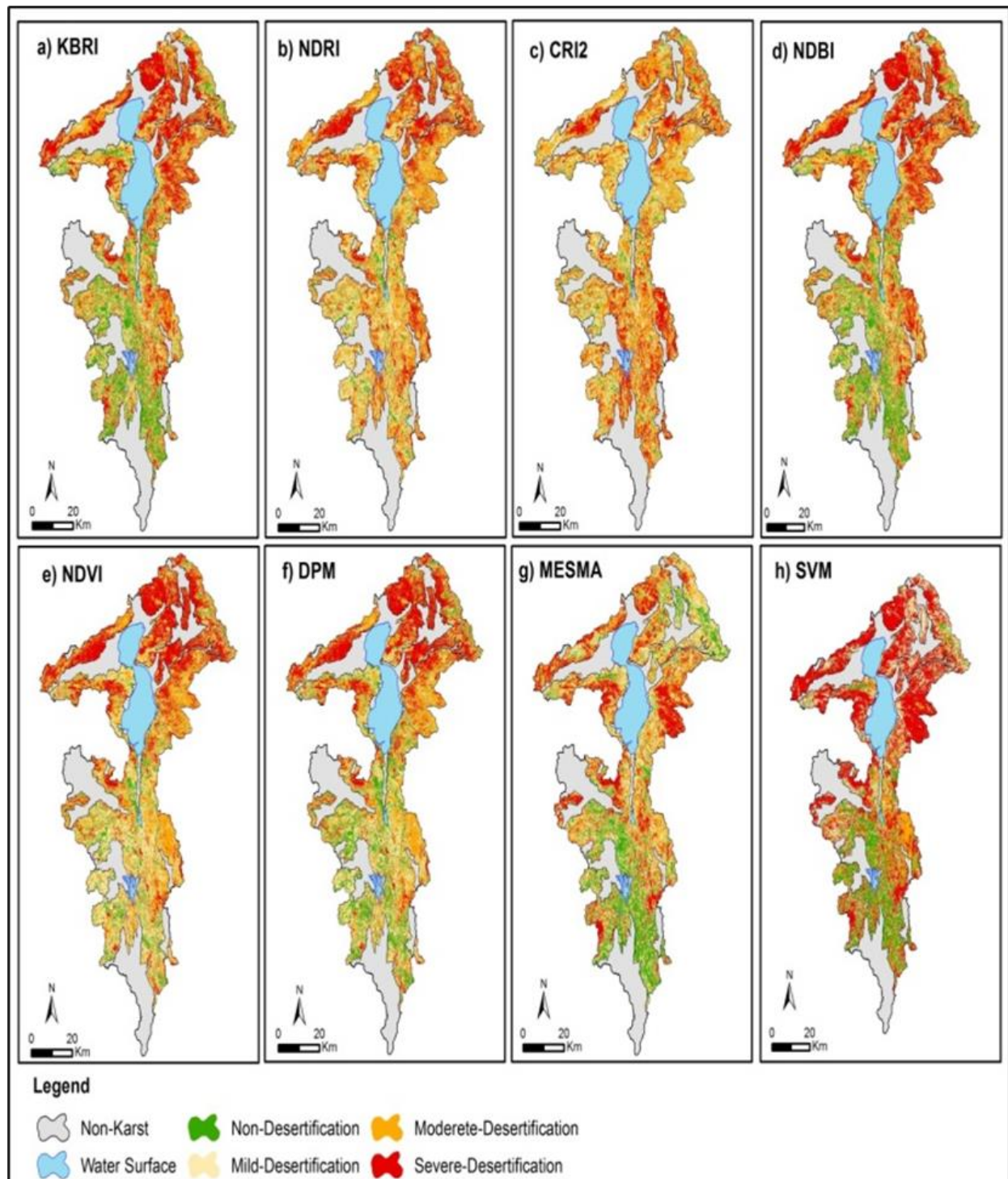
Figure 7. Classification ranges which of KRD results created

4. Discussion

Considering the studies in the literature, it is seen that different results are obtained by using the spectral indices used within the scope of KRD [14, 16]. In terms of general uses, KBRI, NDRI, CRI2 and NDBI indices other than NDVI are used to monitor karst rock desertification. The main indicator for monitoring KRD is the prevalence of EBR in the field. In the literature, there have been many studies on determining the relationship between vegetation and bedrock with remote sensing methods [8, 9, 14, 16,17,31,42].

Natural processes that are effective in the occurrence of KRD in the field are also associated with the slowing of soil development due to the low silicate ratio caused by the geological structure of carbonate rocks [43]. The karst system becomes ecologically fragile due to slow soil development and weak vegetation in direct proportion to this situation [13]. In studies on KRD, classifications are made within the scope of vegetation status and open rocky surfaces [44]. Considering these classifications in general, Li and Wu [16] emphasize that mainly 4 classes can be mentioned in the study and it is stated that an absolute classification method is needed. Thus, by classifying the available data, it is possible to make more effective evaluations of how much of the area has been exposed to desertification and where this desertification is effective.
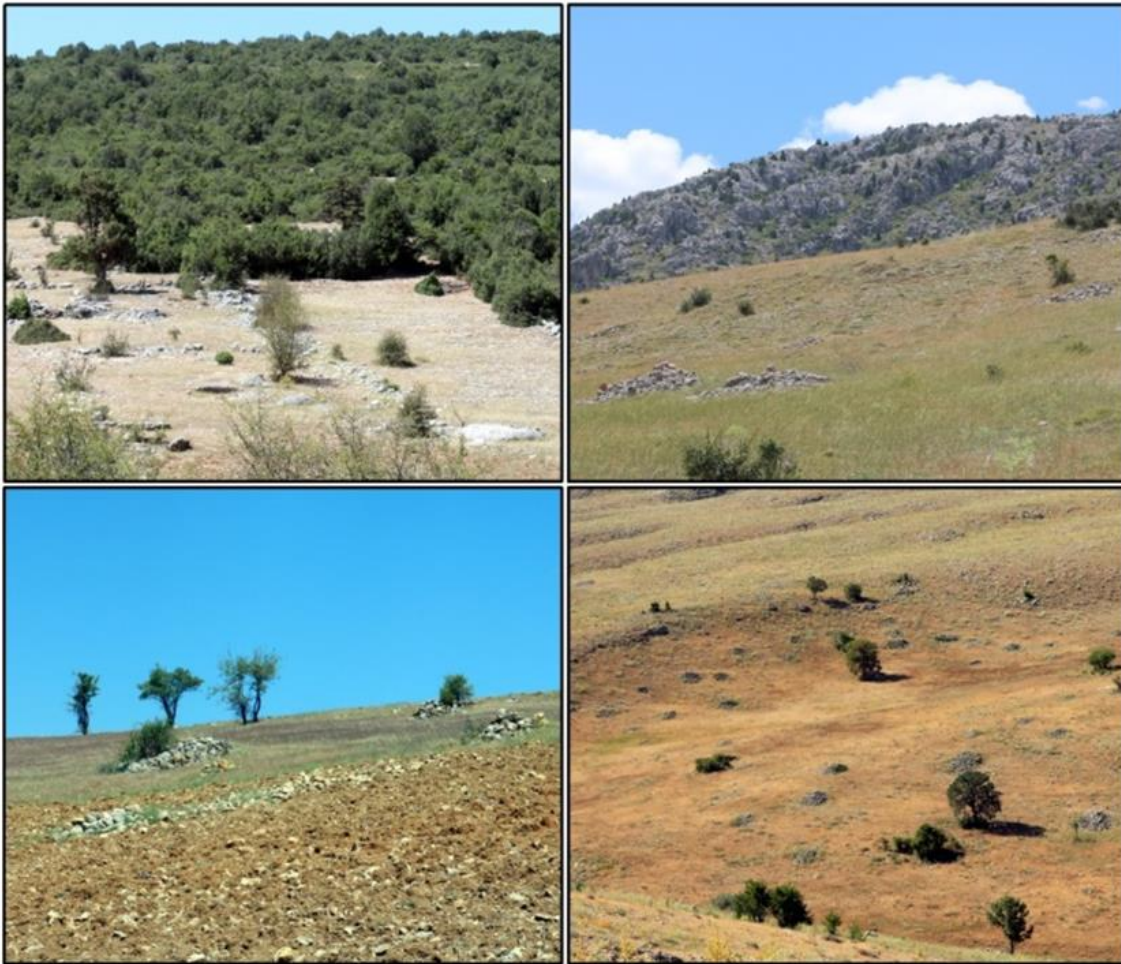
Figure 8. The views from areas where previously cultivated but not now used for agriculture due to desertification

Studies in the literature have reached similar results to the findings of this study, showing that rock exposure rate and vegetation contribute the most to karst rocky desertification inference [42].

Although desertification developed on rocks is not a situation that develops only on carbonate rocks, KRD also has very specific features [43]. This situation arises from the geological properties of karst surfaces. The high chemical dissolution (melting) levels of carbonate rocks slow down soil development [4].

As emphasized in the study by Li and Wu [16] within the scope of evaluating the effects of KRD, it is understood that a classification method is needed instead of spectral indices. In this study, a comparison was made between the spectral indices and the DPM model in terms of the determination of karst rock desertification. This comparison revealed different results from the spectral indexes with a high accuracy rate, as in other studies in the DPM literature [7, 45].

Traditional methods (field studies) for monitoring karst rocky desertification mainly rely on field surveys, which require a quite deal of time and finance. Although using remote sensing images for monitoring karst rocky desertification is not limited by the topography, erosion or land cover, it also has disadvantages, including poor image quality (cloudiness), readily affected by human subjectivity, and strictly guaranteeing the accuracy [46]. In this study, field studies from traditional karst rock desertification methods were also carried out in order to detect the inadequacies that may occur as well as the low

cost and fast decision-making processes of remote sensing. It has been determined that some areas determined in the field studies where KRD is effective are covered with thin soil and garig cover with good vegetation reflectance, and the determination of desertification in these areas by satellite images is prevented.

The most important reason for the natural integrity of the land is erosion becomes stronger as a result of human activities such as destroying vegetation, plowing and contracting roads [47].

Increasing erosion by removing vegetation due to reasons such as fires, overgrazing, improper agricultural practices and improper land use in the Mediterranean Basin is extremely effective KRD development [48, 49].

In addition, the Southern Anatolian mountains, which are described as Taurides, are generally composed of limestones. Widespread karstification in these areas has affected the people living here. Animal husbandry and agricultural activities carried out by people on these surfaces, which have a particularly difficult and faulty topography as karst, take place on the dolines, poljes, and paleo-valleys in these areas [50, 51]. In this study, it was determined that people gradually accelerate KRD directly in karst areas. First of all, people remove the vegetation on the surface where the soil is attached to the karst area. Then, they cultivate the areas with high soil thickness and process them as agricultural land. After the mobilized soil becomes susceptible to erosion, it is carried away by erosion processes and prepares the

ground for karst rock desertification. In the study, it was determined that people wanted to continue agriculture by collecting the rocks exposed in the agricultural lands and left the area as the yield decreased (Figure 8).

5. Conclusion

This study proposes mapping and monitoring of KRD development on karst landscapes in many parts of the World with different RS methods. In this study, high linear relationships were determined between some indices such as KBRI and EBR statistically; also, these indices gave high accuracy results when classified. This means that successful results could not be obtained with monitoring and classification of KRD with spectral indices. One of the possible reasons for not determining a statistically high linear relationship between spectral indices and KRD may be caused by bushes covering the surface. In addition to the poor results in monitoring and classification of KRD, it was determined that SVM (overall accuracy 88%) SVM and MESMA (overall accuracy 77%) methods were found to be successful at a good level. The possible reason why MESMA and SVM methods were more successful than spectral indices is the use of training series based on field measurements. It is understood that the classifications made by these two methods will be efficient in making long-term change detection analyses. In this way, classification results with the highest accuracy in the study area, the proportion of areas subject to severe karst desertification is 40%, those in moderate desertification process 17%, mild desertification 14% and non-desertification 29%.

According to the results, it has been revealed that KRD is quite effective in some parts of the study area. The results obtained in this study, draw attention to the decrease in KRD in the areas where sea impact increases, and in the higher parts, the KRD increases as we move towards the inland areas, similar to the Aksu Stream Basin. In the north of the study area, it was observed that the KRD is particularly effective in the high topography bordered by plain surface. It is noteworthy that the main reason why KRD is effective here is erosion. In addition, it is clearly observed in the field that agricultural production is not efficient enough in the areas where the KRD is effective. The areas with a high Exposed Bedrock Rate where people are trying to conduct agricultural activities make the agricultural conditions worse and reduce agricultural productivity. Uncontrolled agriculture in these lands causes bedrock outcrops to rise to the surface faster. The emergence of bedrock means changing the agricultural land and living conditions for rural people. Thus, increasing difficulties such as inefficiency and limited product diversity show their conditions in rural settlements with many vacant households in the study area. Also, this situation can be accepted as a sign that KRD is effective in the high and sloping parts of the Karst regions in Türkiye.

Acknowledgement

Author contributions

Çağan Alevkayali: Writing-Original draft preparation, Methodology, Software, Data curation, Fieldwork, Validation, Investigation and Visualization; **Onur Yayla:** Fieldwork, Investigation, Visualization and Writing **Yıldırım Atayeter:** Investigation, Fieldwork, Writing and Editing.

Conflicts of interest

The authors declare no conflicts of interest.

References

1. Parise, M., Gabrovsek, F., Kaufmann, G., & Ravbar, N. (2018). Recent advances in karst research: from theory to fieldwork and applications. *Geological Society, London, Special Publications*, *466*(1), 1-24.
2. Erinc, S. (2002). Jeomorfoloji II. İstanbul: DER Yayınları.
3. Theilen-Willige, B., Ait Malek, H., Charif, A., El Bchari, F., & Chaïbi, M. (2014). Remote sensing and GIS contribution to the investigation of karst landscapes in NW-Morocco. *Geosciences*, *4*(2), 50-72.
4. Jiang, Z., Lian, Y., & Qin, X. (2014). Rocky desertification in Southwest China: Impacts, causes, and restoration. *Earth-Science Reviews*, *132*, 1-12.
5. Zhang, X., Shang, K., Cen, Y., Shuai, T., & Sun, Y. (2014). Estimating ecological indicators of karst rocky desertification by linear spectral unmixing method. *International Journal of Applied Earth Observation and Geoinformation*, *31*, 86-94.
6. Ekmekçi, M. (2005). Karst in Turkish Thrace: compatibility between geological history and karst type. *Turkish Journal of Earth Sciences*, *14*(1), 73-90.
7. Qi, X., Zhang, C., & Wang, K. (2019). Comparing remote sensing methods for monitoring karst rocky desertification at sub-pixel scales in a highly heterogeneous karst region. *Scientific reports*, *9*(1), 1-12.
8. Yue, Y. M., Wang, K. L., Liu, B., Li, R., Zhang, B., Chen, H. S., & Zhang, M. Y. (2013). Development of new remote sensing methods for mapping green vegetation and exposed bedrock fractions within heterogeneous landscapes. *International journal of remote sensing*, *34*(14), 5136-5153.
9. Yue, Y. M., Wang, K. L., Zhang, B., Jiao, Q. J., Liu, B., & Zhang, M. Y. (2012). Remote sensing of fractional cover of vegetation and exposed bedrock for karst rocky desertification assessment. *Procedia Environmental Sciences*, *13*, 847-853.
10. Zhang, C., Qi, X., Wang, K., Zhang, M., & Yue, Y. (2017). The application of geospatial techniques in monitoring karst vegetation recovery in southwest China: A review. *Progress in Physical Geography*, *41*(4), 450-477.
11. Xiong, Y. J., Qiu, G. Y., Mo, D. K., Lin, H., Sun, H., Wang, Q. X., ... & Yin, J. (2009). Rocky desertification and its causes in karst areas: a case study in Yongshun County, Hunan Province, China. *Environmental Geology*, *57*, 1481-1488.

12. Liu, Y., Wang, J., & Deng, X. (2008). Rocky land desertification and its driving forces in the karst areas of rural Guangxi, Southwest China. *Journal of Mountain Science*, *5*, 350-357.

13. Yang, W., Chu, W., & Zhou, L. (2019). Evaluating the impact of karst rocky desertification on regional climate in Southwest China with WRF. *Theoretical and Applied Climatology*, *137*, 481-492.

14. Pei, J., Wang, L., Huang, N., Geng, J., Cao, J., & Niu, Z. (2018). Analysis of Landsat-8 OLI imagery for estimating exposed bedrock fractions in typical karst regions of Southwest China using a karst bare-rock index. *Remote Sensing*, *10*(9), 1321.

15. Bai, X. Y., Wang, S. J., & Xiong, K. N. (2013). Assessing spatial-temporal evolution processes of karst rocky desertification land: indications for restoration strategies. *Land Degradation & Development*, *24*(1), 47-56.

16. Li, S., & Wu, H. (2015). Mapping karst rocky desertification using Landsat 8 images. *Remote sensing letters*, *6*(9), 657-666.

17. Guha, S., & Govil, H. (2020). Estimating the seasonal relationship between land surface temperature and normalized difference bareness index using Landsat data series. *International Journal of Engineering and Geosciences*, *7*(1), 9-16.

18. Wang, H., Li, Q., Du, X., & Zhao, L. (2018). Quantitative extraction of the bedrock exposure rate based on unmanned aerial vehicle data and Landsat-8 OLI image in a karst environment. *Frontiers of Earth Science*, *12*, 481-490.

19. Xu, E. Q., Zhang, H. Q., & Li, M. X. (2015). Object-based mapping of karst rocky desertification using a support vector machine. *Land Degradation & Development*, *26*(2), 158-167.

20. Kaynarca, M., Demir, N., & San, B. T. (2020). Yeraltı Suyu Kaynaklarının Uzaktan Algılama ve CBS Teknikleri Kullanarak Modellenmesine Yönelik bir Yaklaşım: Kırkgöz Havzası (Antalya). *Geomatik*, *5*(3), 241-245.

21. Reis, H. Ç., & YılancI, G. (2020). Destek vektör makineleri ve NDVI kullanarak pamuk ekili alanların tespiti: Harran ovası örneği. *Türkiye Uzaktan Algılama Dergisi*, *2*(1), 29-41.

22. Şimşek, M., Utlu, M., Poyraz, M., & Öztürk, M. Z. (2019). Geyik Dağı kütlesinin yüzey karstı jeomorfolojisi ve kütle üzerindeki karst-buzul jeomorfolojisi ilişkisi. *Ege Coğrafya Dergisi*, *28*(2), 97-110.

23. Tokgözlü, A., & Özkan, E. (2018). Taşkın risk haritalarında AHP yönteminin uygulanması: Aksu Çayı Havzası örneği. *Süleyman Demirel Üniversitesi Fen-Edebiyat Fakültesi Sosyal Bilimler Dergisi*, (44), 151-176.

24. Atayeter, Y. (2005). *Aksu Çayı havzası'nın jeomorfolojisi*. Fakülte Kitabevi.

25. Karatepe, Y., Özçelik, R., Gürlevik, N. E. V. Z. A. T., Yavuz, H., & Kiriş, R. (2014). Batı Akdeniz'de farklı yetişme ortamı bölgelerindeki kızılçam (Pinus brutia Ten.) ormanlarının vejetasyon yapısının ekolojik değerlendirilmesi. *Süleyman Demirel Üniversitesi Orman Fakültesi Dergisi*, *15*(1), 1-8.

26. Atayeter, Y. (2011). Eğirdir Gölü Depresyonu ve Yakın Çevresinin Fiziki Coğrafya Özellikleri. Isparta. Fakülte Yayınları

27. Roy, D. P., Wulder, M. A., Loveland, T. R., Woodcock, C. E., Allen, R. G., Anderson, M. C., ... & Zhu, Z. (2014). Landsat-8: Science and product vision for terrestrial global change research. *Remote sensing of Environment*, *145*, 154-172.

28. Sefercik, U. G., Ateşoğlu, A., & Atalay, C. (2021). Orman meşcere yükseklik haritası üretiminde hava kaynaklı lazer tarama performans analizi. *Geomatik*, *6*(3), 179-188.

29. Genç, M., Kasarcı, E., & Kaya, C. (2012). Meşcere Kuruluşu Araştırmaları Üzerine Silvikültürel Bir Değerlendirme. Artvin Çoruh Üniversitesi Orman Fakültesi Dergisi, 13(2), 291-303.

30. Huang, Q., & Cai, Y. (2009). Mapping karst rock in Southwest China. *Mountain Research and Development*, *29*(1), 14-20.

31. Xie, X., Du, P., Xia, J., & Luo, J. (2015). Spectral indices for estimating exposed carbonate rock fraction in karst areas of southwest China. *IEEE Geoscience and Remote Sensing Letters*, *12*(9), 1988-1992.

32. Sabuncu, A., & Ozener, H. (2019). Detection of burned areas by remote sensing techniques: İzmir Seferihisar Forest fire case study. *Journal of Natural Hazards and Environment*, *5*(2), 317-326.

33. Xu, D., Kang, X., Qiu, D., Zhuang, D., & Pan, J. (2009). Quantitative assessment of desertification using Landsat data on a regional scale–a case study in the Ordos Plateau, China. *Sensors*, *9*(3), 1738-1753.

34. Somers, B., Asner, G. P., Tits, L., & Coppin, P. (2011). Endmember variability in spectral mixture analysis: A review. *Remote Sensing of Environment*, *115*(7), 1603-1616.

35. Bedini, E., Van Der Meer, F., & Van Ruitenbeek, F. (2009). Use of HyMap imaging spectrometer data to map mineralogy in the Rodalquilar caldera, southeast Spain. *International Journal of Remote Sensing*, *30*(2), 327-348.

36. Lippitt, C. L., Stow, D. A., Roberts, D. A., & Coulter, L. L. (2018). Multidate MESMA for monitoring vegetation growth forms in southern California shrublands. *International journal of remote sensing*, *39*(3), 655-683.

37. Powell, R. L., & Roberts, D. A. (2008). Characterizing variability of the urban physical environment for a suite of cities in Rondonia, Brazil. *Earth Interactions*, *12*(13), 1-32.

38. Moughal, T. A. (2013, June). Hyperspectral image classification using support vector machine. In *journal of physics: conference series* (Vol. 439, No. 1, p. 012042). IOP Publishing.

39. Tzotsos, A., & Argialas, D. (2008). Support vector machine classification for object-based image analysis. *Object-based image analysis: Spatial concepts for knowledge-driven remote sensing applications*, 663-677.

40. Benbahria, Z., Sebari, I., Hajji, H., & Smiej, M. F. (2021). Intelligent mapping of irrigated areas from Landsat 8 images using transfer learning. *International Journal of Engineering and Geosciences*, *6*(1), 40-50.

41. Melgani, F., & Bruzzone, L. (2004). Classification of hyperspectral remote sensing images with support vector machines. *IEEE Transactions on geoscience and remote sensing*, *42*(8), 1778-1790.

42. Pu, J., Zhao, X., Dong, P., Wang, Q., & Yue, Q. (2021). Extracting information on rocky desertification from satellite images: A comparative study. *Remote Sensing*, *13*(13), 2497.

43. Wang, S. J., Liu, Q. M., & Zhang, D. F. (2004). Karst rocky desertification in southwestern China: geomorphology, landuse, impact and rehabilitation. *Land degradation & development*, *15*(2), 115-121.

44. Xu, E., Zhang, H., & Li, M. (2013). Mining spatial information to investigate the evolution of karst rocky desertification and its human driving forces in Changshun, China. *Science of the Total Environment*, *458*, 419-426.

45. Dai, G., Sun, H., Wang, B., Huang, C., Wang, W., Yao, Y., ... & Zhang, Z. (2021). Assessment of karst rocky desertification from the local to regional scale based on unmanned aerial vehicle images: A case-study of Shilin County, Yunnan Province, China. *Land Degradation & Development*, *32*(18), 5253-5266.

46. Zhang, Y., Tian, Y., Li, Y., Wang, D., Tao, J., Yang, Y., ... & Wu, L. (2022). Machine learning algorithm for estimating karst rocky desertification in a peak-cluster depression basin in southwest Guangxi, China. *Scientific Reports*, *12*(1), 19121.

47. Dindaroğlu, T., & Çelik, H. (2019). Yeşil kuşak orman ekosistemlerindeki orman parçalılığının bazı toprak özellikleri üzerindeki etkilerinin araştırılması (Kahramanmaraş Ahir dağı örneği). *Kahramanmaraş Sütçü İmam Üniversitesi Tarım ve Doğa Dergisi*, *22*(2), 322-332.

48. Chong, G., Hai, Y., Zheng, H., Xu, W., & Ouyang, Z. (2021). Characteristics of changes in karst rocky desertification in southern and western china and driving mechanisms. *Chinese Geographical Science*, *31*, 1082-1096.

49. Haktanir, K., Karaca, A., & Omar, S. M. (2004). The prospects of the impact of desertification on Turkey, Lebanon, Syria and Iraq. In *Environmental Challenges in the Mediterranean 2000–2050: Proceedings of the NATO Advanced Research Workshop on Environmental Challenges in the Mediterranean 2000–2050 Madrid, Spain 2–5 October 2002* (pp. 139-154). Springer Netherlands.

50. Ballut, C., & Faivre, S. (2012). New data on the dolines of Velebit Mountain: An evaluation of their sedimentary archive potential in the reconstruction of landscape evolution. *Acta Carsologica*, *41*(1).

51. Şimşek, M., Öztürk, M. Z., Doğan, U., & Mustafa, U. T. L. U. (2021). Toros polyelerinin morfometrik özellikleri. *Coğrafya Dergisi*, (42), 101-119.

The transformation from e-government to e-land administration in Türkiye: A SWOT-based assessment analysis

Derya Nur Bolat Pak [1], **Osman Sami Kırtıloğlu**[2], **Mert Kayalık**[2], **Zeynel Abidin Polat**[*2]

[1]*İzmir Katip Çelebi University, Graduate School of Natural and Applied Sciences, Türkiye*
[2]*İzmir Katip Çelebi University, Geomatics Engineering Department, Türkiye*

Abstract

The advantage of the developing information and communication technology in terms of both time and cost in service delivery has accelerated the use of these technologies in public administration. With this change, the concept of e-government has taken its place in the literature and has begun to be used in different fields (such as health, safety, tax, education) in many countries. Land management is one of these areas. The Land Registry and Cadastre Directorate and many other public institutions have started to provide many services through e-government within the scope of land management. Thus, the foundations of the transition to e-land administration began to be laid. This study aims to determine the necessary strategies for transition to e-land administration considering the role of the e-government platform in the provision of public services relating to land management in Turkey. Therefore, the current e-service structure related pertaining to land management has been analyzed with the SWOT technique. Thus, the strengths and weaknesses of the existing structure system were revealed. Besides, the opportunities and threats faced by this structure were identified. As a result of the analysis, various suggestions were made for the institutional policies that should be implemented in the transition to e-land administration.

1. Introduction

Rapid information and communication technologies (ICT) developments in recent years have significantly affected social life [1]. With this change, "production and management of information" has come to the fore in the information society instead of "production of material products", which is at the forefront of the industrial society [2]. With the developing information technologies, the citizen-state relationship gains a new dimension in this context [1]. With the rapid increase in internet usage and widespread worldwide since the 1990s, it is seen that a new market understanding in which electronic commerce is widely used has emerged. The fact that electronic commerce is more economical, efficient, and faster in terms of time and cost has accelerated the adaptation of this concept to public administration. Thus, the concept of e-government has taken its place in the literature. As a natural consequence of this, the transfer of public services to digital media has come to the fore, especially in developed western

countries. For this reason, the states had to be more interested in the internet.

Today, using ICT as a tool in the provision of government services is becoming more and more common in the world. These applications, called e-government, provide their users with efficiency, savings, and convenience while simultaneously saving time and strengthening transparency, efficiency, and citizen-oriented service for management. Together with developments in the world, it also increased interest in the concept of e-government in Türkiye quickly. Since the 1990s, computer and internet usage rates have increased due to the investments made in the informatics infrastructure and some state institutions have started to provide their services in digital environments. Especially since the 2000s, many plans and projects of various institutions such as health, safety, tax, and education have been offered via e-government. Land administration is one of these areas. In particular, the General Directorate of Land Registry and Cadastre, which

operates under the Ministry of Environment and Urbanization, and many other public institutions have started to offer many services through e-government within the land management [3-4]. Thus, the foundations of the transition from e-government to e-land administration began to be laid. However, it would be wrong to limit the concept of e-government to the use of information technology. E-government also refers to the distribution of services whose external and internal relations are constantly renewed (innovation), the active participation of citizens in management and supervision processes, and the governance transformation [5]. Public institutions have now started seeing the citizens they serve as a customer, and their priority is to provide customer-citizen satisfaction in their services. Therefore, public institutions must provide new services to citizens more quickly and easily [6] by constantly monitoring and controlling the services offered through e-government. Factors that may affect corporate performance positively or negatively should be considered to increase citizen satisfaction. The aim of this study was to determine the strategies needed in Türkiye in the transition to e-land administration in the provision of public services by introducing the role of the e-government platform for land administration.

For this reason, the existing e-service structure related to land management was analyzed with SWOT technique, the strengths and weaknesses of the existing structure were revealed, and opportunities and threats from the external environment were identified. As a result of the analysis, various suggestions were made for the institutional policies that should be implemented in the transition to e-land administration.

A general introduction to the subject has been made in the first part of the study. In the second part, E-government and E-Land management are discussed, and development processes are mentioned. The third part of study examined the historical development of e-government structure in Turkey is examined. In the fourth part, the services provided by institutions related to land management in Turkey have been identified. In the fifth part, these services are classified according to various criteria, and the current status of this e-service structure is analyzed with the SWOT technique. In the fifth part of the study, the current system is discussed in terms of its strengths and weaknesses with potential opportunities and threats faced. The last part of the study presented results, assessments, and recommendations.

2. e-government and e-land administration concepts

2.1. e-government concept

Citizens are faced with much bureaucracy in various services provided by the government in the classical state understanding. Citizens are faced with a much bureaucracy in various services provided by the government in the classical state understanding. Simple procedures become complex structures for employees, and as a result, many staff and civil servants are hired to run jobs. In addition, numerous forms and signatures

may be required for simple transactions, and transactions can take many months [7].

Today, the rapid development and dissemination of information technologies (especially internet access) have led to the transformation of the traditional state structure into a faster and more flexible state model [8]. Especially towards the end of the 90s, the E-government management model started to be used in terms of public administration [8-9]. E-government is an effective and fast way of doing all kinds of public transactions using information and communication technologies [10-11]. It is means saving time and money for both the public and the citizens.

The characteristics of the traditional state and e-state are given in Table 1 comparatively. According to the Table 1, there have been radical changes in many areas such as the role of the citizen with e-government, the environment in which the service is provided, and the cost of the service. It is possible to say that the emerging and constantly changing social needs, low cost, fast and effective service expectations were caused by the emergence of e-government [12]. Thanks to the strategic use of information technologies in e-government management, it is possible to create a management that can meet the needs of the information society, bring citizens and institutions together in an electronic environment, and ensure efficiency, transparency and development [13].

There are four main internal and external aspects included in the structure of the E-government [8]: 1) the creation of a reliable and accessible government intranet and database for more influence and interoperability among governmental institutions; (2) providing a web-based service; (3) the application of e-commerce for more effectual government-based transaction procedures, such as procurement and contract; and (4) digital accessible democracy for greater transparency and accountability in government affairs. The various technologies have been applied to promote these primary characteristics of e-government, including digital data sahring and transferring, reciprocal voice response, email, Web-based service, and virtual reality [8].

2.2 e-land administration concept

The protection and use of the property right are the basic facts required to create an economically and socially sustainable land administration [15]. There is a direct interaction between the state and citizens / institutions as the protection and use of property rights in many countries are under state control. It determines this level of interaction with the decisions taken by states in this direction [16]. Cadastre and land management system [17] is one of the most intense areas where government and citizens / institutions interact directly. For this reason, the state provides various services related to land management to citizens through public institutions. In order for these services to take place, the citizen must make individual requests. Complex bureaucratic procedures frequently observed in the classical public administration, high service fee, and long application period prevent the citizens from getting

better service. Therefore, the transition to a sustainable land administration system (LAS) is progressing very slowly. With the new land management paradigm [18], the public institutions are encouraged to take up new opportunities for better management of service delivery and implementation LAS policy [19].

Table 1. The comparison of traditional government and e-government [14]

Traditional Government	e-government
Passive Citizen	Active-Customer-Citizen
Paper Based Communication	Electronic Communication
Vertical / Hierarchical Structuring	Horizontal / Coordinated Network Structuring
Data Upload by Institution	Data Upload by Citizen
Staff Response	Automatic Voice Mail, Call Center etc.
Staff Based Control Mechanism	Audit with Automatic Data Update
Uniform Service	Personalized / Differentiated Service
High Transaction Costs	Low transaction costs
Inefficient Growth	Productivity Management
One Way Communication	Versatile Communication
Nationality Relationship	Participation Relationship
Closed State	Open State

Improving and strengthening land administration systems through good policies, legal, institutional frameworks and digital-based applications using ICT are important for national government [20]. The discovering the useful use of the internet and other ICT are increasingly being utilised by public land administration institutions [21-22]. The use of these technologies provides an opportunity to serve better. Thus, while customer satisfaction increases, service delivery costs decrease [21]. However, it is very difficult to design these systems as part of e-land administration.

To propose applicable models and guidelines for e-land administration services, Kalantari et al. [19] emphasize that it is necessary to analyze country experiences and good practices, and identify difficulties and impacts. Australia and the Republic of Korea are examples of countries that have successfully implemented e-land administration. More than ten online land information services have been set up in Australia, covering country arrivals. Australian citizens can easily access information related to land online via web-based services.

Korea Land Information System (KLIS) is one of the main applications of the Republic of Korea's e-government, recognized worldwide as one of the top land information systems [23]. The application was designed to be able to fulfill 530 different procedures in nine land-based areas. It has gathered transparency, efficiency, reliability, and better service for the Republic of Korea's citizens [23]. Many countries recognize the importance of delivering citizen-centric services [19]. They provide a unique and helpful interface for citizens to access all government services.

3. Implementation of e-government in Türkiye

The beginning of transition to e-government in Turkey is based in the 1980s. In this period, while the economic policies gained a more liberal direction, the first studies on the change in the state structure started. Between 1990 and 2000, technology and science policies started to be reformed, and the transition to e-government applications was realized [24]. During this period, the worldwide transformation based on information and technology has affected Türkiye in a very intense way.

Prime Management Information System Center (PMISC) was established to operate e-government activities more efficiently in Türkiye [25]. Subsequently, the e-European initiative launched by the European Union with the member countries and proposed to the candidate countries is referenced. In this respect, after 2000, the e-Turkey Initiative Action Plan was launched. It is plan covering the 2003-2004 e-Transformation Turkey Project Short-Term Action Plan was followed [26]. E-government studies were carried out between 2006-2010 in a comprehensive policy such as the Information Society Strategy and Action Plan. The 2014-2018 draft of the Information Society Strategy and Action Plan, which can be described as the second phase of the Information Society Strategy, which also includes e-government studies, was prepared by the Ministry of Development and shared with the public [27].

As a result of the studies summarized above, an important step has been taken in e-stateization. With the effect of these developments, public administrations within the central government have started to offer some services through e-government [28]. Today, almost all central government units have large e-government projects. The most important of these projects can be listed in Table 2 [28]. The number of services offered via e-government is increasing day by day. According to e-government statistics, while the number of services provided in 2009 was 162, this number reached 6821 in 2023. The institutions that contribute the most to this number of services are "Central Public Institutions", "Municipalities", "Private Institutions" and "Universities", respectively.

The reasons such as the fact that e-government is a universal phenomenon, and that studies are carried out in every country required the determination of indices related e-government and comparisons with other countries. The United Nations (UN) is one of the important institutions calculating E-government

Development Index. It is one of the important institutions calculating the United Nations (UN) e-government Development Index. According to the index made biennially by the UN, the countries' index score is calculated to be a value in the range of 0 to 1. The index value of 1 indicates that the country's e-government development level is high. In calculating the index, three different variables are used: service coverage and quality, human resources, and the status of the telecommunications infrastructure [29]. Turkey's place in the world ranking for e-government applications is changing depending on the development of e-government services. According to various corporate e-

government development rankings, Türkiye is usually located in the middle row. Turkey's e-government Development Index and world ranking by years are given in Table 3. According to Table 3, e-government development index has increased gradually and reached the top ranks in the world ranking in recent years due to the services provided over e-government infrastructure. It is development was also evident in the provision of services related to land management. In addition, many public institutions develop various projects for land management and provide services to citizens through e-government.

Table 2. The most popular e-government projects in Türkiye

| Name of project	The institution that developed the project
Central Population Statistics Project (MERNİS *in Turkish)*	Ministry of the Interior
Identity Sharing System (KPS *in Turkish*)	Ministry of the Interior
MOBESE Projects	General Directorate of Security
Tax Offices Automation Project (VEDOP *in Turkish*)	Ministry of Finance
National Judicial Network Project (UYAP *in Turkish*)	Ministry of Justice
e-Consumer (e-Services) Project	Ministry of Industry
Information Processing Center Project (BİMER *in Turkish*)	Prime Ministry
e-Declaration and MEDULA Projects	Ministry of Labor and Social Security
MEBSİS and e-School Project	Ministry of National Education

Table 3. e-government development index and ranking by years in Türkiye

Year	e-government development index	The world ranking	Total number of countries
2008	0.48	76	192
2010	0.47	69	183
2012	0.52	80	190
2014	0.54	71	193
2016	0.59	68	193
2018	0.71	53	193
2020	0.77	53	193
2022	0.79	48	193

4. e-government-based land administration services in Türkiye

The user interface and system login screen of the application developed for e-government is given in Figure 1. E-government consists of "e-services", "Institutions", "Municipalities", "Companies" and "Quick Solution" sections (Figure 1a). Inquiry, application, and

payment processes related to the service provided in the "e-services" section are carried out. In the "Institutions" section, services and contact information of official institutions are provided. In the "Municipalities" section, the contact information of the municipalities and the services they provide are listed. Invoices and subscriptions are made in companies in the "Companies" section.
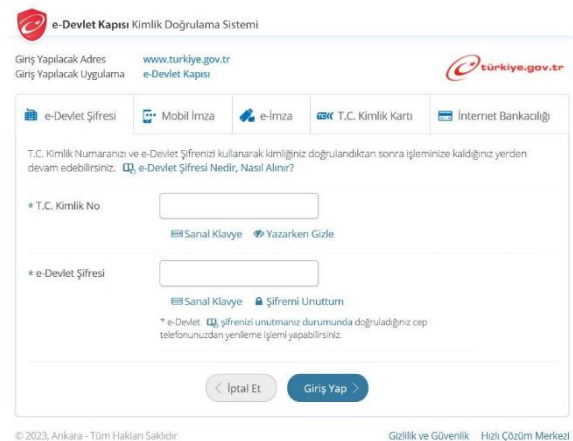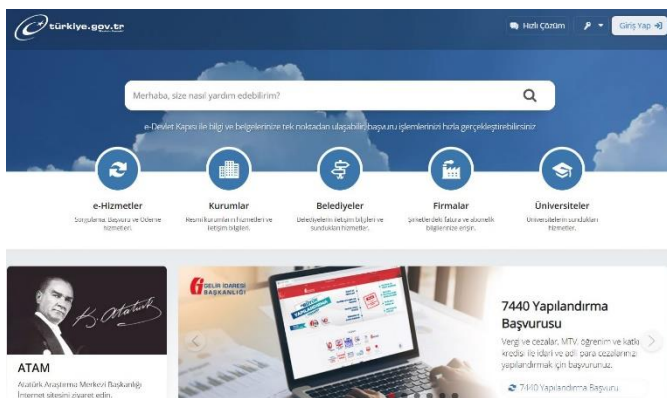
Figure 1. (a) E-government user interface and (b) login the system

The "Quick Solution" section conveys complaints, suggestions, questions and requests regarding the

services provided. Alternative entryways to the system are presented in the e-government entry section (Figure

1b). "E-government password", "mobile signature", "e-signature", "T.C. ID card "and" "internet banking information" can be entered. E-government is increasing in use due to its practical use and easily accessible structure.

For this reason, many public institutions have started offering services through this system. Many institutions, especially those dealing with land management, have begun to transform their services into a structure that can be offered via e-government. Among these institutions the Ministry of Agriculture and Forestry (9 services), Ministry of Justice (1 service), Natural Disaster Insurance Institution (1 service), General Directorate of Forestry (1 service), General Directorate of Land Registry and Cadastre (8 services) and many municipalities (4 services) comes to the fore. The e-services and explanations provided by these institutions are given in Table 4.

Table 4. Institutions taking part in land administration and their e-services

Name and Abbreviation of institution	Name of the E-Service	Definition of E-Service
Ministry of Agriculture and Forestry (MAF)	Investigation of Possible Agricultural Lands to Exclude from Agriculture	Using this service, you can get information on whether the agricultural land you own can be taken out of agriculture.
	Land Consolidation Distribution Inquiry	Using this service, you can view the current and past hang lists of your real estate subject to land consolidation and view the status of your immovables before and after consolidation on the map.
	Farmers register system	It is possible for the farmers registered in the system by the relevant ministry to question their agricultural land and agricultural products.
	Completed Land Consolidation Distribution Inquiry	With this service, you can list the projects of any neighborhood/village where land consolidation is done and view the details.
	Application for Expropriation in Protected Areas	With this service, you can request the expropriation of the real estate in the protected areas.
	Application for Right of Easement in Forest Qualified Areas in National Parks	Opinions may be requested to establish the easement right, except for the strict permits for tourism purposes in forests in the national parks.
	Final Permit application in Forest Qualified Areas in National Parks (e. g. Pre-application, Application, transfer, cancellation)	Permits given in the fields of "pre-application", "application", "transfer," and "cancellation" in forest-qualified areas in national parks can be questioned.
	Tourism Facility Application in Forest Qualified Areas in National Parks	With this application, tourism facility application can be made in forest-qualified areas in national parks.
	Application for Activity Permit Certificate in Wetlands (Real and Legal Person)	With this application, an application can be made for the Permit Certificate required for the Activity in Wetlands.
Ministry of Justice (MJ)	Certificate of inheritance inquiry	With this application, the certificate of inheritance required to share the heritage can be questioned.
Natural Disaster Insurance Institution (NDII)	Earthquake insurance policy inquiry	With this application, an inquiry can be made regarding the policy related to real estate with earthquake insurance.
General Directorate of Forestry (GDF)	Application for Forest Cadastre, Land that has lost its forest quality, Property Dispute, technical error, Renewal, Forest Boundary determination processes.	With this service, applications can be made for the Forest Cadastre, Land that has lost its forest quality, Property Dispute, technical error, Renewal, Forest Boundary determination processes
General Directorate of Land Registry and Cadastre (GDLRC)	Inquiry of Land Registry Information	With this application, you can query the information about the real estate(s) you have.
	Land Registry and Cadastre Fee and Revolving Funds Inquiry and Payment application	With this application, you can inquire about the amount of Fee, and Revolving Capital requested for the Land Registry and Cadastre transactions and made your payments.
	Document verification with an electronic document management system	With this application, the accuracy of the documents issued by the institution can be checked.
	Real estate declaration application	With this application, you can ensure that the real estate you own are registered by entering the necessary information.
	Real estate sales process application	With this application, you can initiate the necessary pretreatments for the sale of real estate you have.
	Land Registry Document	With this application, you can access information about your real estate registered in the land registry
	TUSAGA-Active System User Operations	With this application, you can use the system by registering to TUSAGA-Active System
	Web title transactions (Includes 46 different transactions)	With this application, applications for 46 different transactions can be made.
Municipalities (M)	Land market value inquiry	With this application, the market value of the land's land can be queried.
	Inquiry on Unfinished Zoning Plan	With this application, you can access information about zoning plans that have not been finalized yet.
	Council Decision Inquiry	With this application, Council decisions taken by the relevant municipality can be questioned.
	Zoning status	With this application, information about the zoning status in the location of the real estate can be accessed.

5. Swot analysis of e-government-based land administration services in Türkiye

The easiest way to reveal the current situation and expectations of a sector, an activity, or a company is to perform a SWOT analysis by experts on that subject [30]. The term SWOT is an acronym for the first letters of four words in English. These are Strengths, Weaknesses, Opportunities, and Threats [31]. SWOT analysis is a technique used to identify the strengths and weaknesses of a sector, an activity, or a firm and identify opportunities and threats from the external environment [32-33].

In the literature, various studies using SWOT analysis have been conducted in the process of developing and evaluating the e-government process [34-41]. SWOT analysis has been frequently used in studies on land management. Polat et al. [42] identified strategies that may be necessary to implement the 2034 cadastral vision Turkey. Yan et al. [43] used the SWOT technique to make strategic planning in land consolidation. Halla [44] used SWOT technique to determine the stages of urban planning in Tanzania. Steudler and Williamson [45] analyzed the development of the land administration system in Sweden using the SWOT technique.

Paudel and Thapa [46] used the SWOT technique to determine the competencies of local institutions in land management. Strategic planning is needed to establish sustainable e-services related to land management in Turkey. For this, the strengths and weaknesses of the existing structure and external threats and opportunities must be determined with the SWOT technique. Thus, it will be ensured that strategies suitable for the e-land administration goals of the country are determined.

In this context, a current situation analysis was carried out to assist the e-service process in land management using SWOT analysis. For this, the services provided through e-government related to land management are classified in terms of their characteristics according to various criteria. Explanations about the criteria used in the classification are listed in Table 5, and the result of the classification is listed in Table 6.

Table 5. Explanations of the criteria used in Table 6

Name of e-service	Code	Explanation
E-Service Delivery Level (SDL)	A	Questioning information: gives the applicant information about the service
	B	Application Inquiry: Includes querying the result of an application made for a service
	C	Making an application: Contains only the application process for a service
	D	Completion of all stages: It includes application and finalization stages related to a service or all stages of questioning and concluding information.
E-Service Access Level (SAL)	E	All natural persons can access/query/ apply.
	F	All legal persons can access/query/ apply
	G	Only real persons registered in the system or associated with the service can access
	H	Only legal persons registered in the system or associated with the service can access
E-Service Access Costs (SAC)	K	Paid service
	L	Free service
	M	The application is free but requires a revolving fund/fee/ service fee for the transaction.
Service Access Time (SAT)	N	24/7 access
	P	Access to a specific date/time
E-Service Inquiry Output (SIO)	R	Text (Includes words and numbers)
	S	Map/Image (Includes .KML, .KMZ, JPEG, .TIFF, .PNG, .GIF formats)
	T	Form (.doc, docx, .xls, .xlsx., .pdf)
E-Information and Documents Required for Accessing or Completing the Service (IDS)	U	Requires credentials (e.g., Name-Surname, identity number)
	V	Requires Contact Information (e.g., Phone, mail address)
	W	Requires real estate Information (e.g., Layout, block, parcel number)
	X	Requires location information (e.g., Address, Province-District-Neighborhood, Coordinate)
	Y	Requires other information (eg document code, document number, serial number, date of decision)
	Z	No information required

5.1. Strengths

The five main strengths are determined as follows:

5.1.1. Having a user-friendly interface

The E-government application is designed with a user-friendly interface. Through this interface, citizens easily and quickly benefit from the e-services offered by many institutions. Due to its user-friendly design, the citizen can query a lot of information via e-government and make a pre-application for some transactions.

5.1.2. Providing alternative access

E-government application entered many personal information. Citizens can log in to the e-government system using one of "e-government password", "mobile signature", "e-signature", "T.R. ID card", or "internet banking".

5.1.3. Reducing service cost

Services offered through e-government are realized at a lower cost than normally provided services.

5.1.4. Reducing bureaucracy and paperwork

Many of the services provided by institutions are not performed at any time due to bureaucratic procedures. In addition, various documents are requested in paper form during these processes. Thanks to the e-service offered through e-government, bureaucratic procedures reduced stationery costs.

5.1.5. Access to the service free of charge and at any time

There is no charge for public services provided through e-government. Citizens can access these services at any time.

5.2. Weaknesses

The three main weaknesses are determined as follows:

5.2.1. Not being able to complete every transaction 100% electronically

Only the preliminary application of some transactions is accepted through e-government. For the rest of the procedure, it is necessary to go to the institution.

5.2.2. Incomplete integration of e-service providers into the system

Not all public institutions, municipalities and companies have been able to switch to the e-government system. This weakens the holistic approach in e-service delivery related to land management.

5.2.3. The failure of all citizens to fully utilize e-service

The number of e-government users reached 33 million in 2017, 39 million in 2018, and 44 million in 2019. Turkey is considered to be about 83 million of population; even if the observed increase in the use of E-services, complete success has not been achieved yet.

5.3. Threats

The four main threats are determined as follows:

5.3.1. Cyber-attacks on e-services

Cyber-attacks on e-services cause service disruption and endanger public and personal data security.

5.3.2. Privacy and security gaps

Providing services in an electronic environment brings security risks. Failure to fully protect the personal data of citizens using the service endangers e-service.

5.3.3. Confidence problem

One of the reasons for not benefiting from e-government services sufficiently is the trust problem that citizens have in an electronic environment. To minimize this problem, it is necessary to prevent the risks that cause the problem of trust in the services and to prevent virtual attacks and information leaks that may come from outside.

5.3.4. Low level of computer literacy

The level of computer literacy has not reached the desired level, and the distribution of citizens with computer literacy is not geographically homogeneous, which causes the e-service not to be used sufficiently.

5.4. Opportunities

The five main opportunities are determined as follows:

5.4.1. Developments in information and communication technologies

With the developments in ITC, access to the desired information can be provided independently of time and place. In this way, services related to land management are provided electronically and monitored by citizens.

5.4.2. The increasing desire for public institutions to provide e-services

The spread of e-government and its success in providing services have been preferred by many institutions. According to the Ministry of Environment and Urbanization data, 5180 different services are offered through the e-government Gateway. Of these, 2600 are state institutions, 2123 are municipalities, 403 are private institutions, 54 are water and sewerage services.

5.4.3. The increase in the e-government development index

Because of the services offered via the e-government infrastructure in Türkiye in recent years, the country's e-government development index has been increasing (see Table 3).

5.4.4. Increased e-government usage

As of July 2017, approximately 33 million users benefited from 2165 services provided by 332 institutions [47]. However, it should not be forgotten that these numbers are not constant, and the number of users, institutions, and services increase daily.

5.4.5. Opportunity to convey ideas, complaints, and requests regarding e-service delivery

Citizens can convey their requests, ideas, complaints, and requests to the relevant institutions through the e-government Gateway.

The strengths and weaknesses originating from the internal environment and opportunities and threats originating from the external environment mentioned above are summarized in Table 7 as the SWOT matrix.

Table 6. Comparison of land management-based e-services

Name of Institutions*	Name of E-Service	E-Service Delivery Level (SDL)				E-Service Access Level (SAL)				E-Service Access Costs (SAC)			E-Service Access Time (SAT)		E-Service Inquiry Output (SIO)			Information documents required for accessing or completing the E-service (IDS)					
		A	B	C	D	E	F	G	H	K	L	M	N	P	R	S	T	U	V	W	X	Y	T
MAF	Investigation of agricultural lands to exclude from agriculture	✓				✓					✓		✓		✓					✓	✓		
	Ongoing land consolidation distribution inquiry	✓						✓			✓		✓		✓	✓							✓
	Farmers register system	✓	✓					✓			✓		✓		✓								✓
	Completed land consolidation distribution inquiry	✓				✓					✓				✓							✓	
	Application for expropriation in protected areas		✓			✓					✓		✓		✓	✓	✓			✓		✓	
	Application for right of easement in forest qualified areas in national parks		✓			✓					✓		✓		✓					✓		✓	
	Permit application in forest qualified areas in national parks		✓			✓					✓		✓		✓		✓			✓		✓	
	Tourism facility application in forest qualified areas in national parks		✓			✓					✓		✓		✓	✓	✓			✓		✓	
	Application for activity permit certificate in wetlands		✓			✓	✓				✓		✓		✓		✓	✓				✓	
MJ	Certificate of inheritance inquiry	✓				✓					✓		✓		✓			✓					
NDII	Earthquake insurance policy inquiry	✓				✓		✓			✓		✓		✓								✓
GDF	Application for forest cadastre, land that has lost its forest quality, property dispute, technical error, renewal, forest boundary determination processes.		✓			✓	✓								✓		✓	✓	✓		✓		
GDLRC	Inquiry of land registry information	✓						✓			✓		✓		✓	✓							✓
	Land registry and cadastre fee and revolving funds inquiry and payment			✓				✓		✓	✓	✓	✓	✓	✓				✓			✓	
	Document verification with electronic document management system	✓				✓					✓		✓		✓							✓	
	Real estate declaration application	✓				✓					✓		✓		✓		✓		✓	✓	✓		
	Real estate sales process application		✓					✓			✓		✓		✓	✓	✓						✓
	Land registry document	✓						✓			✓		✓		✓	✓	✓						
	TUSAGA-active system user operations				✓						✓		✓		✓	✓	✓	✓	✓			✓	✓
	Web title transactions (Includes 46 different transactions)		✓	✓				✓			✓		✓		✓		✓	✓	✓	✓	✓	✓	✓
M	Land market value inquiry	✓				✓					✓		✓		✓							✓	
	Inquiry on unfinished zoning plan	✓				✓					✓		✓		✓							✓	
	Council decision inquiry	✓				✓					✓		✓		✓							✓	✓
	Zoning status	✓				✓					✓		✓		✓	✓					✓	✓	

Table 7. SWOT analysis results for e-service-based land management

	Strengths	Weaknesses
Internal factors	➢ Having a user-friendly interface ➢ Providing alternative access ➢ Reducing service cost ➢ Reducing bureaucracy and paperwork ➢ Access to the service free of charge and at any time	➢ Not being able to complete every transaction 100% electronically ➢ Incomplete integration of e-service providers into the system ➢ The failure of all citizens to fully utilize E-service
	Opportunities	**Threats**
External factors	➢ Developments in information and communication technologies ➢ The increasing desire for public institutions to provide e-services ➢ The increase in the E-government development index ➢ Increase in e-government usage ➢ Opportunity to convey ideas, complaints and requests regarding e-service delivery	➢ Cyber-attacks on e-services ➢ Privacy and security gaps ➢ Confidence problem ➢ Low level of computer literacy

3. Discussion

In this study, the presentation of the services related to land management through the e-government platform was evaluated by SWOT analysis. There are many benefits of service delivery via e-government. The most powerful aspects of the e-government structure are lowering service costs, reducing bureaucracy and paperwork, providing continuous service, and providing access at any time and place.

Although it is constantly evolving, the e-government structure has some weaknesses. The weaknesses of this structure are that all institutions operating within the scope of land management are not fully integrated into e-government, the number of services provided is insufficient, and only some of the transaction steps of some services are carried out electronically. Again, not all of our citizens can benefit from these services yet shows that the e-government structure is not known enough.

Some security and privacy problems, some cyber-attacks that may occur in the digital environment are examples of dangerous situations that will prevent or slow down e-service delivery. In addition, the problem of citizens' trust in the electronic environment and the low level of computer literacy can be considered obstacles to the healthy execution of e-government applications.

Developments in information and communication technologies, increasing the tendency of public institutions to provide e-service, increasing e-government use every year, and considering suggestions, complaints and requests related to e-service are opportunities that will make the e-government platform more widespread. Particularly considering the suggestions, complaints and requests regarding the implementation indicates that the citizen plays a significant role in the design of the e-government. This situation has also led to the gradual increase in Turkey's e-government index. In this way, Turkey's worldwide e-government index ranking has become better.

Despite many positive developments, it is observed that various public institutions carry out independent studies on a number of similar services. For example, independent automation projects related to the same administrative and financial affairs of different institutions and organizations are far from effective and shareable. This situation causes the same job to be done more than once, thus wasting labor and resources. To prevent such inefficiencies, necessary e-government coordination efforts should be carried out more effectively. However, it is observed that the culture of electronic service delivery in public institutions and organizations is developing gradually. Therefore, this development is thought to play a facilitating role in e-government studies and the integration of services [27].

4. Conclusion and Suggestions

Turkey's e-government structure with various institutions for the provision of public services (e.g., public institutions, municipalities, corporations) are in cooperation. In this context, the e-government structure has become a dynamic sector that constantly improves the quality of its services by diversifying the services offered.

The land is a scarce social resource directly related to shelter, nutrition, and property. Hence the importance of the land management sector is increasing both in the world and Turkey. Reaching the advanced level of service delivery in an electronic environment and approaching world standards will contribute to the transition to sustainable e-land management in Türkiye. Especially the Ministry of Forestry and Agriculture, the General Directorate of Land Registry, and Cadastre and Municipalities are among the leading e-service institutions related to land management.

This study shows a certain level of culture in e-service in public institutions and organizations, and the studies carried out are following a more positive course daily. In order for e-service to reach the ideal level, weaknesses of e-government and e-land management should be developed, and threats should be eliminated. Various suggestions are needed for this. These suggestions are as follows:

- For the services carried out on the web to be used and accepted efficiently by the citizens, e-government and e-Land management services should provide users with vast opportunities and user satisfaction [48].
- The lack of equal access to information and communication technologies prevents the use of e-government and e-Land management services. Necessary precautions must be taken to minimize the negativities caused by this situation [25].
- National policies and programs should be revised to integrate into e-government and e-Land management practices [49].
- Applications should be organized as "disabled friendly" [50].
- One of the reasons for not getting enough e-government services is the problem of trust. To minimize this problem, it is necessary to prevent risks that cause a problem of trust in services and to prevent virtual attacks and information leaks that may come from outside [51].
- Some administrative and legal regulations need to be made for the widespread use of e-government services by citizens and institutions [25].
- In our country, although the rate of household access to the internet and mobile technology is high, some individuals do not use computers and do not have this skill. For this reason, services should be provided to improve computer literacy [51].

If these suggestions are taken into consideration, it will reach the level of offering all services through e-Land administration, taking into account the demands and needs of citizens and other sectors of public institutions soon.

Author contributions

Derya Nur Bolat Pak: Conceptualization, Methodology, Data curation, Writing, Original draft preparation, **Osman Sami Kirtiloğlu**: Writing, Reviewing and Editing, **Mert Kayalik**: Visualization, Editing and Original draft preparation, **Zeynel Abidin Polat**: Writing, Reviewing and Editing.

Conflicts of interest

The authors declare no conflicts of interest.

References

1. Şahin, A., & Örselli, E. (2003). E-Devlet anlayışı sürecinde Türkiye. *Selçuk Üniversitesi Sosyal Bilimler Enstitüsü Dergisi*, (9), 343-356.

2. Öğüt, A. (2003). Bilgi Çağında Yönetim. Nobel Basımevi, Ankara.

3. İşcan, F., & Ilgaz, A. (2017). Analysis of geographic/urban information system web presentations of local governments in Turkey. *International Journal of Engineering and Geosciences*, *2*(3), 75-83.

4. Ercan, O., & Toker, K. (2022). Assessment of the completion of the forest cadastre considering the legal grounds, collaboration, and the use of technology: The case of Turkey. *International Journal of Engineering and Geosciences*, *7*(1), 49-58.

5. Roy, J. (2006). E-Governmnet in Canada: Transformation İfor Digital Age. Ottawa University: Ottawa Press.

6. İşcan, F., & Vargeloğlu, F. (2019). Boru hattı kamulaştırma çalışmalarında karşılaşılan teknik, ekonomik, hukuki sorunlar ve çözüm önerileri. *Geomatik*, *4*(3), 239-253.

7. Yıldırır, H., & Karakurt, E. (2004). e-Devlet ve Uygulamaları. *İş, Güç Endüstri İlişkileri ve İnsan Kaynakları Dergisi*, *6*(1).

8. Moon, M. J. (2002). The evolution of e-government among municipalities: rhetoric or reality?. *Public administration review*, *62*(4), 424-433.

9. Başar, M. S., & Bölükbaş, A. (2010). Gelişmişlik göstergeleri ve e-devlet indeksi. *Atatürk Üniversitesi Sosyal Bilimler Enstitüsü Dergisi*, *14*(1), 157-170.

10. Lambrinoudakis, C., Gritzalis, S., Dridi, F., & Pernul, G. (2003). Security requirements for e-government services: a methodological approach for developing a common PKI-based security policy. *Computer communications*, *26*(16), 1873-1883.

11. Van der Molen, P., & Wubbe, M. (2007, November). E-government and E-Land Administration-As an example: The Netherlands. In *6th FIG Regional Conference, San Jose, Costa Rica* (pp. 12-15).

12. Marquardt, K., & Orhan, G. (2005). E-Devlet: Gerçek ya da Hayal içinde: E-Devlet: Kavramın Anlamı ve Kapsamı, (Editörler: Karl Marquardt ve Orhan Gökçe), Çizgi Kitapevi Yayınları, Konya, 1-25.

13. Uğur, A. A., & Çütcü, İ. (2009). E-Devlet ve tasarruf etkisi kapsamında VEDOP Projesi. *Sosyal ve Beşeri Bilimler Dergisi*, *1*(2), 1-20.

14. Uçkan, Ö. (2003). E-devlet, e-demokrasi ve e-yönetişim modeli: Bir ilkesel öncelik olarak bilgiye erişim özgürlüğü. *Aylık Strateji ve Analiz E-Dergisi*, *5*(5), 1-19.

15. Zakout, W., Wehrmann, B., & Törhönen, M., P. (2006). Good governance in land administration, The World Bank, FAO, Washington DC.

16. Rhodes, R. A. (1997). *Understanding governance: Policy networks, governance, reflexivity and accountability*. Open University.

17. Döner, F. (2021). Analysis of literature on 3D cadastre. *International Journal of Engineering and Geosciences*, *6*(2), 90-97.

18. Dale, P. F., & McLaughlin, J. D. (1999). Land administration. sl New York: Oxford University Press.

19. Kalantari, M., Rajabifard, A., Wallace, J., & Williamson, I. (2005). Toward e-land administration: Australian online land information services. In *Proceedings of the SSC*.

20. Williamson, I., & Ting, L. (2001). Land administration and cadastral trends—a framework for re-engineering. *Computers, environment and urban systems*, *25*(4-5), 339-366.

21. Kalantari, M., Rajabifard, A., Wallace, J., & Williamson, I. (2005). The role cadastral data modelling in e-Land administration. *Coordinates*, *1*(4), 26-29.

22. Kalantari, M., Rajabifard, A., Wallace, J., & Williamson, I. (2006). An interoperability toolkit for e-Land administration. *Sustainability and Land Administration Systems, Department of Geomatics, Melbourne*, 213-222.

23. Cho, B., & Yoo, J. (2015). Development of a unified land information system in the republic of korea. How Innovations in Land Administration Reform Improve on Doing Business: Cases for Luthuania, the Republich of Korea, Rwanda and the United Kingdom (Editors: Hilhorst, T., & Meunier, F.) Washington DC: The World Bank.

24. Çarıkçı, O. (2010). Türkiyede e-devlet uygulamaları üzerine bir araştırma. *Süleyman Demirel Üniversitesi Sosyal Bilimler Enstitüsü Dergisi*, (12), 95-122.

25. Seferoğlu, S., Çelen, F., & Çelik, A. (2011). Türkiye'deki e-devlet uygulamaları: Sorunlar ve çözüm önerileri üzerine bir inceleme, Türkiye'de E-Öğrenme: Gelişmeler ve Uygulamalar II, Eskişehir: Anadolu Üniversitesi.

26. Güler, D., & Yomralıoğlu, T. (2021). Yapı Ruhsatlandırmadan Kat Mülkiyetine Giden Süreçlerin Dijitalleştirilmesi: Mevcut Durum Analizi ve Öneri. *Geomatik*, *6*(2), 93-106.

27. DPT, (2005), Devlet Planlama Teşkilatı Müsteşarlığı, E-Devlet Proje Ve Uygulamaları.

28. Demirhan, Y., & Türkoğlu, İ. (2014). Türkiye'de E-devlet uygulamalarının bazı yönetim süreçlerine etkisinin örnek projeler bağlamında değerlendirilmesi. *Uluslararası Yönetim İktisat ve İşletme Dergisi*, *10*(22), 235-256.

29. Akgül, E., A. (2015), E-devlet ve yurttaşlık ilişkisi üzerine sosyolojik bir değerlendime: Aydın ili örneği, Doktora Tezi, Adnan Menderes Üniversitesi, Sosyal Bilimler Enstitüsü, Aydın.

30. Akça, H. (2005). Burdur ilinin kırsal turizm potansiyeli ve değerlendirilmesi. *Burdur Sempozyumu*, *16*, 19.

31. İnayet, Z., & Akbulak, C. (2010). Troia Tarihi Milli Parkı'ndaki turizm potansiyelinin SWOT analizi ile değerlendirilmesi. 11. *Ulusal Turizm Kongresi*, *2*(5), 203-213.

32. Ongun, U., Gövdere, B., & Çiçek, U. (2016). Yeşilova'nın kırsal turizm potansiyelinin Swot analizi ile değerlendirilmesi. *Süleyman Demirel Üniversitesi Vizyoner Dergisi*, *7*(16), 75-88.

33. Taktak, F., & Mehmet, I. L. I. (2018). Güneş Enerji Santrali (GES) Geliştirme: Uşak Örneği. *Geomatik*, *3*(1), 1-21.

34. Kahraman, C., Demirel, N. Ç., & Demirel, T. (2007). Prioritization of e-government strategies using a SWOT-AHP analysis: the case of Turkey. *European Journal of Information Systems*, *16*(3), 284-298.

35. Kahraman, C., Demirel, N. Ç., Demirel, T., & Ateş, N. Y. (2008). A SWOT-AHP application using fuzzy concept: e-government in Turkey. *Fuzzy multi-criteria decision making: theory and applications with recent developments*, 85-117.

36. Alshomrani, S., & Qamar, S. (2012). Hybrid SWOT-AHP analysis of Saudi Arabia E-government. *International journal of computer applications*, *48*(2), 1-7.

37. Avny, A. (2007). SWOT analysis of e-government. *Universitatii Bucuresti. Analele. Seria Stiinte Economice si Administrative*, *1*, 43-54

38. Damian, I. P. M., Segundo, J. S., & Merlo, E. M. (2014). SWOT analysis of the services provided by e-government sites in Brazil. *Procedia Computer Science*, *33*, 130-135.

39. Al Salmi, M. A. A., & Hasnan, N. B. (2015). SWOT and TOWS matrix e-government analysis review on Sultanate of Oman. *International Journal of Learning and Development*, *5*(4), 13-23.

40. Elsheikh, Y., & Azzeh, M. (2017). Prioritize E-government Strategies Using SWOT-Ranked Voting Analysis Technique: The Case of Jordan. *International Journal of Computer Science and Network Security (IJCSNS)*, *17*(1), 1-7

41. Rachid, G., & El Fadel, M. (2013). Comparative SWOT analysis of strategic environmental assessment systems in the Middle East and North Africa region. *Journal of environmental management*, *125*, 85-93.

42. Polat, Z. A., Alkan, M., & Sürmeneli, H. G. (2017). Determining strategies for the cadastre 2034 vision using an AHP-Based SWOT analysis: A case study for the turkish cadastral and land administration system. *Land use policy*, *67*, 151-166.

43. Yan, J., Xia, F., & Bao, H. X. (2015). Strategic planning framework for land consolidation in China: A top-level design based on SWOT analysis. *Habitat International*, *48*, 46-54.

44. Halla, F. (2007). A SWOT analysis of strategic urban development planning: The case of Dar es Salaam city in Tanzania. *Habitat international*, *31*(1), 130-142.

45. Steudler, D., & Williamson, I. P. (2005). Evaluation of national land administration system in Switzerland. *Survey review*, *38*(298), 317-330.

46. Paudel, G. S., & Thapa, G. B. (2001). Local Organizational Capability for Land Management: A SWOT Analysis of Organizations in the Hills of Nepal. *Asia-Pacific Journal of Rural Development*, *11*(2), 15-34.

47. Bozkurt, A. (2017). Türkiye'de e-devlet uygulamaları. Bilgi Toplumu ve E-Devlet. Eskişehir: Anadolu Üniversitesi Yayınları. ISBN: 978-975-06-1958-8, 90-111.

48. West, D. M. (2004). E-government and the transformation of service delivery and citizen attitudes. *Public administration review*, *64*(1), 15-27.

49. Şişman, A., Alkış, Z., & Maraş, E. E. (2011). E-Devlet ve M-Devlet'in Geliştirilmesinin Önündeki Engel; Sayısal Uçurum. *Harita Teknolojileri Elektronik Dergisi*, *3*(1), 27-37.

50. Akcagündüz, E. (2013). Türkiye'de e-Devlet sistemine farklı bir bakış: e-Devlet ve tasarruf ilişkisi. *Doğuş Üniversitesi Dergisi*, *14*(2), 127-140.

51. Ateş, H., & Yavuz, Ö. (2019). Elektronik devletten mobil devlete geçiş: Fırsatlar, tehditler ve uygulama örnekleri. *Bilgi Ekonomisi ve Yönetimi Dergisi*, *14*(2), 155-177.

Methodology of real-time 3D point cloud mapping with UAV lidar

Levent Candan *[1] , **Elif Kaçar** [2]

1Kocaeli University, Laser Technologies Research and Application Center, Türkiye
2Kocaeli University, Department of Physics, Türkiye

Abstract

Accurate and timely availability of LiDAR data is vital in some cases. To facilitate monitoring of any environmental changes, LiDAR systems can be designed, and carried by UAV platforms that can take off without major preparation. In this study, the methodology of the real-time LiDAR mapping system was developed in the laboratory. The designed system shortens the target-based flight planning and post-flight data processing. In this system, the data is taken instantly and thus the change in the mapping area can be detected quickly. The simulation system, produce 3D point cloud, and data was stored in a database for later analysis. The 3D visualization of the data obtained from our developed UAV-LiDAR system was carried out with a platform-independent interface designed as web-based. The X3D file format used in the study to produce 3D point data provide an infrastructure for AI and ML-based systems in identifying urban objects in systems containing big data such as LiDAR.

check for updates

1. Introduction

Remote sensing systems allow for obtaining a repeatable and consistent image at spatial, spectral, radiometric, and temporal resolutions to monitor the impact of short/long-term environmental changes and human activities on the earth [1–5]. Environmental assessment/monitoring, detection/monitoring of global change, agriculture, meteorology, mapping and military surveillance/reconnaissance are some of the important applications of remote sensing technology [5,6]. Many remote sensing systems have been developed that offer a wide variety of spatial, spectral and temporal parameters to meet the needs of data users working in different application areas [4,5]. Technological developments in these systems increase the number of studies on forest ecology management and water use on a global scale [7, 8]. In recent years, the use of LiDAR data obtained by aircraft or satellites has been preferred to examine urban areas (buildings, roads, vegetation, etc.) where the fastest changes can be observed on earth [9–11].

Platforms used to acquire LiDAR data (3D point cloud) over large and continuous areas are airplanes, satellites, and helicopters [1]. The spatial and temporal resolutions of high-cost inflexible manned aerial LiDAR systems are limited, especially when collecting high-resolution data in small areas [12,13]. When higher data density is required for smaller areas, UAV systems that provide high temporal and spatial resolution data; it has become a widely used remote sensing platform in various applications due to their features such as low cost and flexible data collection [11,14–17].

Accurate and timely acquisition of LiDAR data is vital for monitoring environmental change and post-disaster emergency response [18]. LiDAR data obtained over a certain region (street, city) in different periods is an important resource that can be used in these processes [19]. However, examining and making available LiDAR data at the ground station after each flight takes place through a series of processes/steps and temporal processes [20]. When evaluating the suitability of the UAV LiDAR system for the 3D point cloud at a precise scale, it is encountered that the repeatability and comparability are limited due to the unsystematic flights and the potential effects of flight parameters [21]. To improve this situation, studies are carried out on long-term flight planning, autopilot systems, regular

trajectory determination, and post-flight data processing processes [16,22].

In addition to the accurate and timely acquisition of LiDAR data, it is also important that the relevant LiDAR data can be easily accessed by experts and the public via remote access for various applications and can take action accordingly [23]. The limitations of many of the online tools owned by individual researchers may not allow 3D visualization. The disadvantage of the existing tools is that they are not flexible enough for them to create 3D scenes of a mixture of point-based and triangle-based models when the density of the 3D point cloud is also taken into account [24]. Given the wide availability of the internet world, transmitting remote sensing data via browsers is a good choice [23]. In addition, developments in HTML5 technology and cloud systems have enabled Web-based 3D visualization. In various applications (forestry, environment, etc.) where LiDAR data is used, it is necessary to develop simulations using accurate geospatial information. Developed high-resolution simulations need a real-time 3D simulation infrastructure that can provide a base platform for these various fields and can be shared. The use of this data in 3D environments is possible with the provision of a platform-independent web-based infrastructure. This can be achieved using the extensible 3D (eXtensible 3D: X3D) standard [25]. 3D data can be visualized with X3DOM (X3D+DOM: DOM that describes the concepts of interaction and hierarchical representations associated with the content of HTML documents.), which allows X3D elements to be included as part of any HTML5 DOM (Document Object Model) tree. X3DOM is a WebGL-based library built on the extensible 3D (X3D) standard, allowing users to create 3D scenes with little knowledge of computer graphics [23,24].

The main motivation of this study is to contribute to the solution of the problems arising from pre-flight (long-term flight planning, autopilot systems, regular trajectory determination etc.) and post-flight processes (data processing) of the UAV-LiDAR systems. One of the results of this motivation is to produce a real-time 3D point cloud that can be used effectively in rapid decision-making processes in disaster situations.

In this study, a methodology that allows instant visualization of LiDAR data is presented. Within the scope of this methodology; the real-time processing processes of the data obtained from the UAV LiDAR system are described. This system provides instant visualization with a web-based interface that can be constantly renewed/improved with the development of web technology. With this system, besides the production of an instant 3D point cloud that can be used in areas where fast access to data is needed, this data is also instantly stored in a database (PostgreSQL or MySQL) for later analysis. There are exponential increases in information processing capability and storage capacity with the increase in big data on a global scale. Therefore, artificial intelligence (AI) and machine learning (ML) are becoming important in data processing processes. One of the systems containing big data is LiDAR. AI and ML provide important information and predictions in LiDAR applications which is used natural disasters that require quick decision-making.

2. Method

Accurate and timely availability of LiDAR data is vital in some cases. For this purpose, an effective methodology has been put forward that provides instantaneous 3D point cloud generation that can be used easily in disaster situations as well as eliminating the problems arising from the pre-flight (long-term flight planning, autopilot systems, regular trajectory determination etc.) and post-flight processes (data processing) of UAV-LiDAR systems.

A two-component system was designed to realize the Real-Time 3D Point Cloud Mapping Methodology with UAV LiDAR. The structure of this methodology developed in this context, suitable for the real environment, is shown schematically in Figure 1. The first of these two main components are the Remote Sensing Platform (Unmanned Aerial Vehicle and LiDAR), and the second is the Ground Control & Recording Station. These two components interact with each other simultaneously. The first thing to do for this methodology to work is real-time data acquisition. This data acquisition process is detailed in section 2.1. The second thing to do is to make these LiDAR data obtained in real time available as a 3D point cloud with a platform-independent web interface. The development of this web interface using X3D file format, PHP programming language and MySQL database is explained in detail in section 2.2.

The methodology developed here is platform independent and was first simulated in a laboratory environment to test the data from all sensors used in real systems. This methodology, which is simulated in a laboratory environment, has features that can be adapted to the desired remote sensing platform and its limits can be expanded. Thanks to the telemetry technologies in use and the rapidly developing innovative technologies (5G), it allows to transfer data wirelessly over longer distances. The development of X3D graphics libraries is continued in a fast and stable manner, increasing their use on more platforms [26]. Although some web-based (HTML5) studies have made geographic visualizations in X3D file format, LiDAR data previously obtained by manned/unmanned aerial vehicles have been used in the relevant systems [23, 27]. In addition to these features of the X3D file format, it is very successful in defining objects in accordance with AI and ML.

The components (X3D, MySQL, PHP, Real-time LiDAR data, etc.) brought together to implement this methodology are not yet available in the literature and are open to development.

### 2.1. Laser scanning process

In this study, a simulation system that can be adapted to real environment components in the laboratory environment has been created for any flight platform (Figure 2), to reveal the methodology of the "Real-Time 3D Point Cloud Mapping with UAV LiDAR". Here, instead of UAV, a platform that is moved at a constant speed on a sled with a constant height was used for real-time scanning processes. In order to develop the methodology, the SF45B (micro-LiDAR, LightWare

Optoelectronics (Pty) Ltd) model laser scanner, which is a suitable micro-LiDAR for small areas such as laboratory environments, was selected. The selected SF45B laser scanner was placed on the carrier platform, viewing the scanning area (Figure 2). The field of view (FOV) of the laser scanner was adjusted to approximately 60º to obtain more detailed data. The distances from successive positions of the platform moving at a constant speed to the ground were measured by making a series of scans.

SF45B model laser scanner has a 1 cm linear resolution, ±10 cm precision, and angular resolution of less than 0.2º. In addition, the scanner makes 5000 readings per second at a scanning angle of 340º and up to 50 m measuring distance. Generally, GPS systems are used to determine the location of Remote Sensing Platforms (RSPs). In the system created in the laboratory, location information was obtained by using a VL53L0XV2 model laser range finder (LRF), which measures horizontally sensitive distance, instead of GPS due to the short distance (~1 m). Acceleration, roll, pitch, and yaw data are also utilized by using an Inertial Measurement Unit (IMU: usually includes an accelerometer, a gyroscope, and a magnetometer) to determine the position of the UAV platforms. In this system, MPU6050 model IMU was adopted to get information from acceleration, roll, pitch, and yaw sensors (Figure 2).
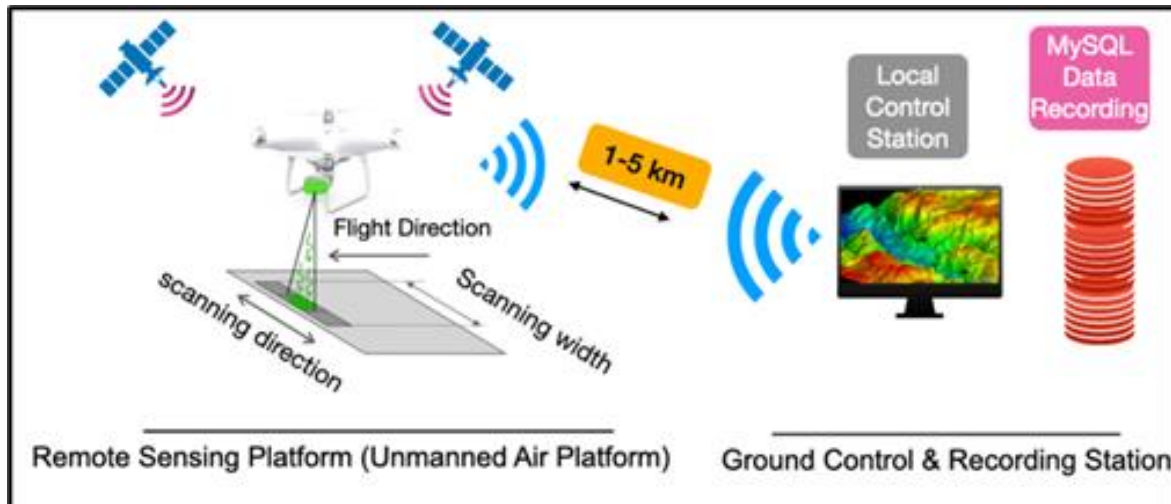
Figure 1. Schematic representation of Real-Time 3D Point Cloud Mapping System with UAV LiDAR providing data transfer for real environment. Remote Sensing Platform (Unmanned Aerial Vehicle) and Ground Control & Recording Station
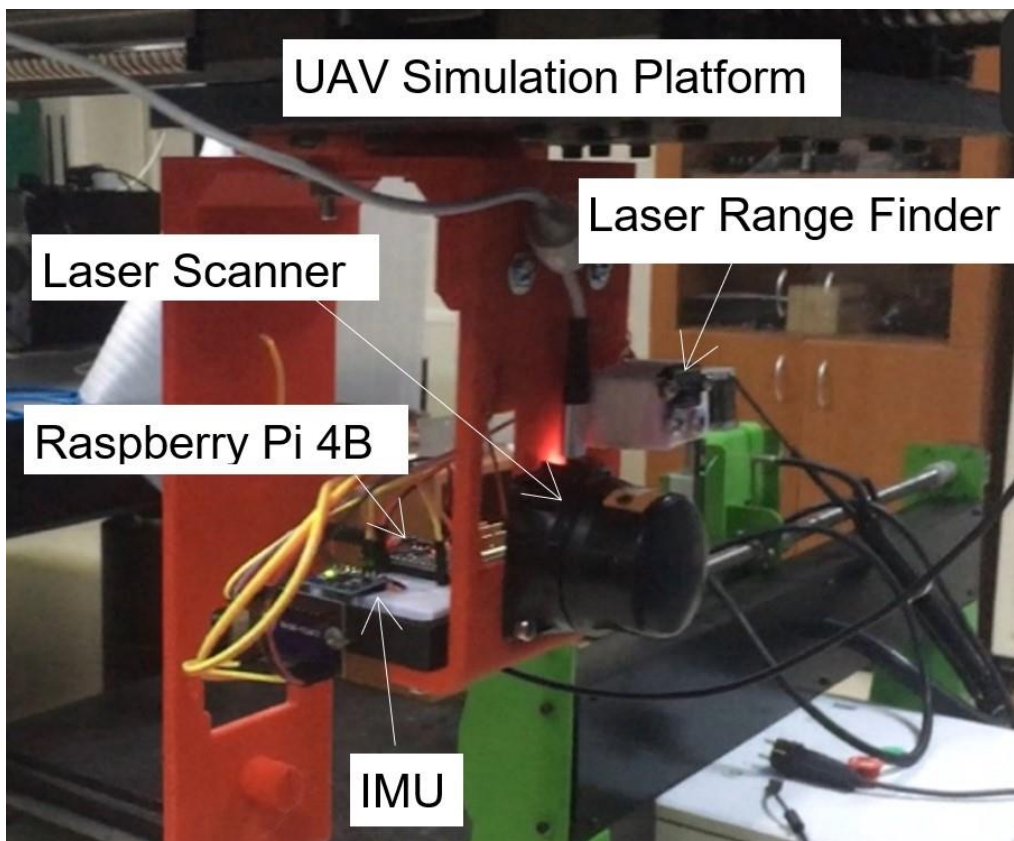
**Figure 2.** UAV Simulation Platform: Scanning system, LRF, recording system, and IMU

In the environment where the platform is used, objects of various shapes of known sizes (Table 1) were placed on the floor and the external environment was simulated (Figure 3). The LRF used to obtain position information (r_{LRF}) during the scanning process was positioned to move parallel to the ground. While the system was moving, different angle values were obtained for each measurement by making right angles to the laser scanner movement direction. By using the angle values (θ_n) and distance values (hypotenuse = r_n) measured from the laser scanner, the vertical edge distances of the right triangles formed as shown in Figure 3 were calculated with the equations in Table 2.

Table 1. Dimensions of target objects labeled in Figure 3

Target	Size (m)
First (yellow)	x = 0.215, y =0.075, z = 0.180
Second (pink)	x = 0.21, y = 0.190, z = 0.08
Third (blue)	x = 0.20, y = 0.025, z = 0.05
Fourth (white)	h= 0.20, r=0.028

Table 2. Coordinate equations of the transformed point in accordance with the X3D scene

Terms	Defined as
measured distance for point n (cm)	r_n
advance distance for point n (mm)	r_{LRF}
x coordinate of point n (m)	$x_n= (\sin\theta_n. r_n)/100$
y coordinate of point n (m)	$y_n= (\cos\theta_n. r_n)/100$
z coordinate of point n (m)	$z_n= r_{LRF}/1000$
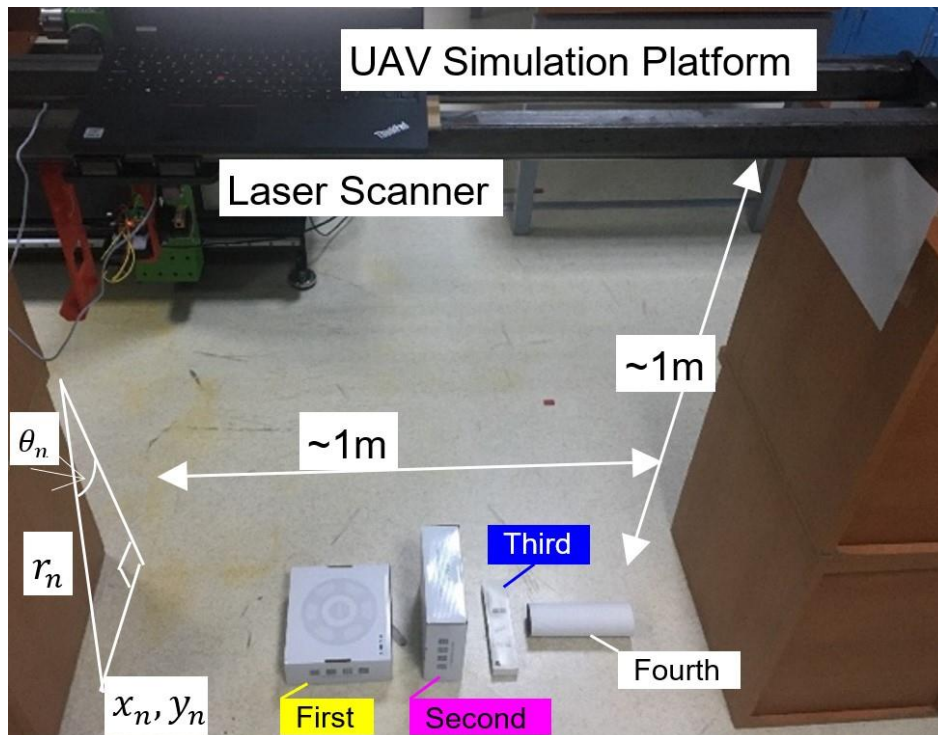
Figure 3. Overview of the experimental workspace for realistic simulation in the laboratory environment

2.2. Data processing

Data from all sensors were recorded on Raspberry Pi 4B (Raspi4B), a computer with a single board structure. The Raspi4B (Raspberry Pi Foundation) used in this study has 8 GB LPDDR4-3200 SDRAM, Broadcom BCM2711-Quad core Cortex-A72 (ARM v8) processor with 64-bit architecture, and 64 GB data storage. In this microcomputer, on which C codes were compiled, all data from the sensors were instantly recorded in the MySQL database on it. In about 1 minute, 114.438 3D point coordinates (x, y, z) were obtained. Raspi4B can connect to a common internet network (modem) in a laboratory environment with its built-in 2.4/5.0 GHz WiFi module. By using this feature, connection with another computer defined as Ground Control & Recording Station can be established by using the SSH (Security SHell) protocol, which is a secure remote login method. With this connection method, the real-time 3D point cloud was obtained by providing online wireless remote access to the instant data obtained from the MySQL database

running on Rasp4B via the web interface developed on the Ground Control & Recording Station. The web interface was developed using the PHP programming language and the X3D file format. In approximately 1 minute, x, y, z coordinate information was obtained for each point measured with the data taken from the laser scanner and other sensors. During this period, 3D visualization was made for 114.438 x, y, z point coordinates.

3. Results

In the Ground Control & Recording Station of the "Real-Time 3D Point Cloud Mapping with UAV LiDAR" System, whose methodology was given in the previous section, instant data were received with the web interface created using PHP programming language. By selecting the relevant data table in the web interface and clicking the "Show 3D Point Cloud" button, it was directed to the web page where the 3D point cloud obtained by scanning was displayed (Figure 4).
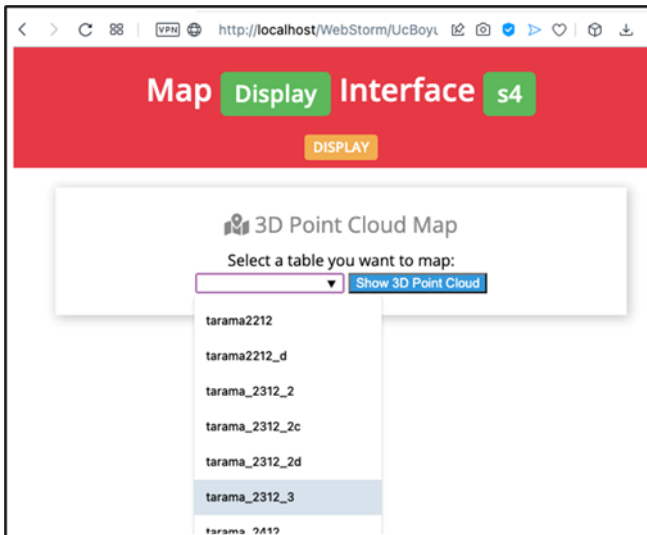
Figure 4. 3D Point Cloud visualization web interface.

These data were obtained by instant, wireless and remote access. The obtained data was visualized as a 3D point cloud using the XML-based X3D (Extensible 3D) file format, which is the Web3D standard that can run on a platform-independent web browser. Figure 5 shows the point cloud map that is extracted simultaneously with the real-time data. Figure 6 shows 3D point cloud overlapping with objects in X3D scene.

As seen in Figure 5 and Figure 6, coordinate transformations were made between IMU and X3D file format during the scanning process. According to these transformations, the +y axis of the IMU is the +z axis in X3D file format and is outward from the page plane (Figure 5). The +z-axis of the IMU is the +y-axis (green colored axis) in X3D file format, pointing upwards (Figure 5). The +x axis of the IMU is the same as the +x axis (red color axis) in X3D file format and is to the right (Figure 5).
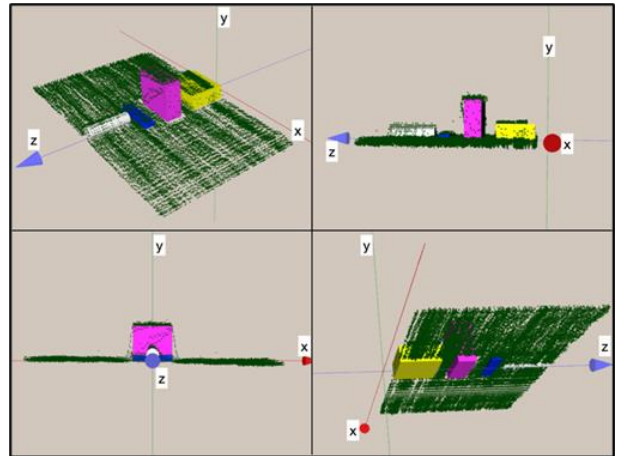

Figure 5. 3D point clouds of objects in X3D scene

Figure 6. 3D point cloud overlapping with objects in X3D scene

The altitude value initially measured by the laser scanner moved at a constant height was accepted as a reference (0.985 m). The distances from all measured successive positions to the ground were obtained by subtracting (for y-axis) from this reference value. Then, the accuracy of the 3D point cloud of the data obtained simultaneously and wirelessly with the developed simulation was evaluated. For this, the real dimensions of the relevant objects in the X3D scene were created in the Ground Control & Recording Station. Figure 6 shows the overlap of the 3D point cloud obtained with the objects in the X3D scene. Although this system is a remote sensing platform at a constant height and constant speed, the information obtained from the IMU is also considered to process the data realistically. The data obtained from the IMU consists of acceleration values in m/s^2 unit for x, y, z axis separately and gyroscope angle values in rad/s unit separately for x axis roll, y axis pitch, z axis yaw.

The appearance of real objects on the scanned surface at various time intervals in the X3D scene is given in Figure 7.

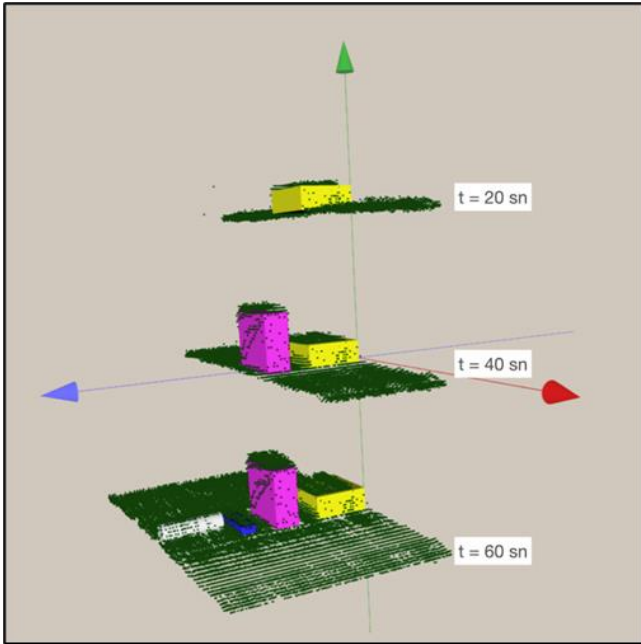The accuracy comparison was made between the height of the objects measured by laser scanning and the

actual height of the objects as in Figure 8. Root Mean Square Error (RMSE) was calculated as 0.020158 m in the comparison. In other words, a 2% variation was observed between the actual object heights and the measured heights. It was observed that the measurements were within the accuracy values of the laser scanner used.

The acceleration changes and gyroscope changes obtained for all three axes during the scanning process are shown respectively in Figure 9 and Figure 10. In addition, the gravitational acceleration was measured as ~9.80 m/s^2 according to the sensitivity of the IMU in the z-axis of the IMU (Figure 9). Although these data did not change in the laboratory environment, they were used in the calculations. Thus, adaptive simulations of this methodology to systems containing a relatively high-altitude UAV LiDAR system (for real environments) have been obtained.

4. Discussion

Real-time 3D Point Cloud Mapping with UAV LiDAR system, whose methodology was given in the previous sections, was simulated in a laboratory environment in a

realistic way. The structure of this methodology developed in this context, suitable for the real environment, is shown schematically in Figure 1. The first thing to do for the methodology to be successful is the real-time data acquisition process. For this, a LiDAR system that receives real-time data was designed.

Accurate and timely acquisition of LiDAR data is vital for monitoring environmental change and post-disaster emergency response [18]. LiDAR data obtained over a certain region (street, city) in different periods is an important resource that can be used in these processes [19].

Figure 7. The appearance of real objects on the scanned surface in the X3D scene at various time intervals
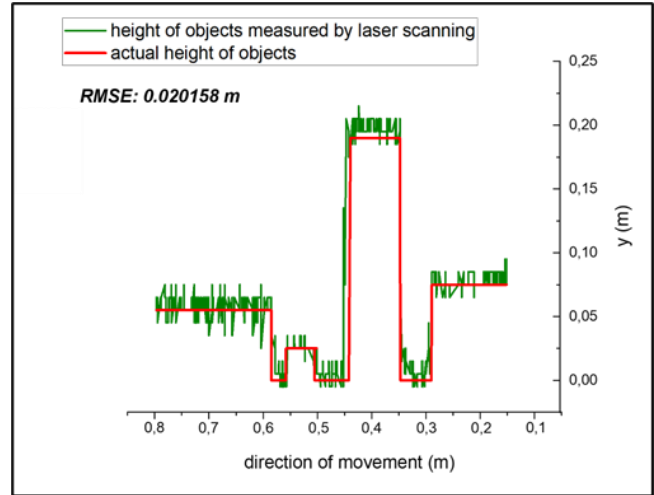
Figure 8. Accuracy comparison between the height of objects measured by laser scanning and the actual height of objects
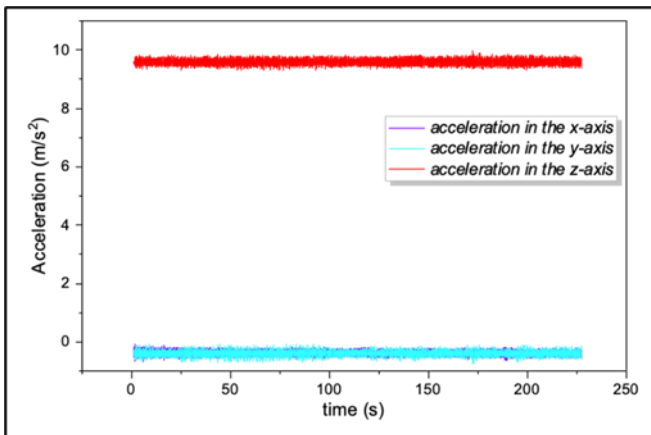
Figure 9. Changes in acceleration in all three axes
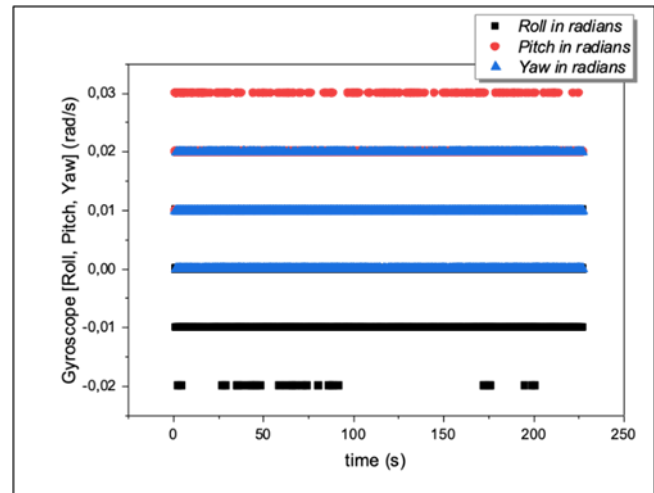
Figure 10. Changes in roll, pitch, and yaw

The UAV-LiDAR platform, which constitutes the first part of the methodology, has the feature of acquiring and recording real-time data on itself. The reason for recording on the platform is to avoid data loss in case of any disconnection with the Ground Control & Recording Station, which is the second part of the methodology. Georeferencing points are obtained from the GPS data of the relevant area in the systems used in the real environment. Although GPS is not used in this system designed for the laboratory environment, it is possible to record these data in a related way.

Another aim of this study is that LiDAR data can be easily accessed by experts and individual researchers in various fields via remote access. With this system, besides the production of an instant 3D point cloud that can be used in areas where fast access to data is needed, this data is also instantly stored in the MySQL database for later analysis. In addition to the accurate and timely acquisition of LiDAR data, it is also important that the relevant LiDAR data can be easily accessed by experts and individual researchers via remote access for various applications and can take action accordingly [23]. This designed system is very useful in making retrospective

research or comparisons by recording the data with date stamps. Developed in accordance with the methodology, this design ensures that data can be accessed by more than one user at the same time. With this access, users have the opportunity to easily search, filter, and quickly visualize the desired data range on the data.

In various applications (forestry, environment, etc.) where LiDAR data is used, it is necessary to develop simulations using accurate geospatial information. Developed high-resolution simulations need a real-time 3D simulation infrastructure that can provide a base platform for these various fields and can be shared. The use of this data in 3D environments is possible with the provision of a platform-independent web-based infrastructure [25]. Also, many of the online tools owned by individual researchers are limited in rendering 3D scenes, given the density of the 3D point cloud [24]. Given the wide availability of the Internet world, transmitting remote sensing data via web browsers is a good choice [23]. In addition, developments in HTML5 technology and cloud systems have enabled Web-based 3D visualization. The 3D visualization of the data obtained from our developed UAV-LiDAR system was carried out with a platform-independent interface designed as web-based. This infrastructure, available to multiple users, is visualized with X3DOM, which allows X3D elements to be included as part of any HTML5 DOM tree. X3DOM is a WebGL-based library built on the extensible 3D (X3D) standard, allowing users to create 3D scenes with little knowledge of computer graphics [23,24]. X3D is a standard maintained by the Web3D Consortium and approved by the International Organization for Standardization (ISO). This developed design provides a compliant complement to existing GIS standards produced by the Open Geospatial Consortium (OGC) and Web Architecture supported by the World Wide Web Consortium (W3C 2004).

In our study, a LiDAR mapping system was designed that shortens target-based flight planning, regular trajectory determination and post-flight data processing. As it is understood from the literature research, examining and making available LiDAR data at the ground station after each flight takes place through a series of processes/steps and temporal processes [20]. When evaluating the suitability of the UAV LiDAR system for the 3D point cloud at a precise scale, it is encountered that the repeatability and comparability are limited due to the unsystematic flights and the potential effects of flight parameters [21]. To improve this situation, studies are carried out on long-term flight planning, autopilot systems, regular trajectory determination, and post-flight data processing processes [16,22].

The Real-time 3D Point Cloud Mapping with UAV LiDAR System, whose methodology is presented, has the advantage of enabling rapid rescanning of the area when missing data is detected. Identifying urban objects, producing accurate and timely information about the location of these objects, is important in urban planning and disaster management.

Another aim of this study to provide an infrastructure for AI and ML-based systems. The X3D file format we used in our study forms the basis of artificial intelligence (AI) and machine learning (ML) based applications. This file format is very successful in identifying relevant urban objects in accordance with AI and ML. AI and ML can be used to create 3D maps using LiDAR data or to identify and classify surrounding objects. AI and ML can improve the accuracy and speed of LiDAR applications when used to process, filter and extract meaningful information from LiDAR data. In addition, AI and ML allow modeling and forecasting about the environment using large volumes of LiDAR data. This valuable information and estimates can assist institutions and organizations in making decisions in natural disasters.

This study can be easily extended for real environments with more advanced and currently in use telemetry and GPS technologies. In addition, thanks to rapidly developing innovative technologies such as 5G, allow faster wireless data transfer over longer distances. The results of this simulation study in the laboratory environment, whose methodology is presented, can be easily integrated into the relatively high-altitude UAV LiDAR system with all its components in the real environment. We also believe that the presented methodology is in line with OGC's mission, which connects people, communities, and technology to solve global challenges and meet daily needs.

5. Conclusion

In this study, a real-time LiDAR measurement system was established. The designed system shortens the processes of target-based flight planning and post-flight data processing. With this developed real-time LiDAR mapping system in laboratory, data is obtained instantly, so that the change in the area in question can be detected and fast solutions can be produced to the problems. The simulation system, produce 3D point cloud, and data was stored in a database for later analysis. The X3D scene used in the study to produce 3D point data provide an infrastructure for AI and ML-based systems in identifying urban objects in systems containing big data such as LiDAR.

Acknowledgement

Author contributions

Levent Candan: Conceptualization, Methodology, Software, Field study, Writing-Original draft preparation, Data curation, Validation. **Elif Kaçar:** Investigation, Writing-Reviewing, and Editing. All authors provided critical feedback and helped shape the research, analysis and manuscript.

Conflicts of interest

The authors declare no conflicts of interest.

References

1. Toth, C., & Józków, G. (2016). Remote sensing platforms and sensors: A survey. *ISPRS Journal of Photogrammetry and Remote Sensing*, *115*, 22-36. https://doi.org/10.1016/j.isprsjprs.2015.10.004

2. Lechner, A. M., Foody, G. M., & Boyd, D. S. (2020). Applications in remote sensing to forest ecology and management. *One Earth*, *2*(5), 405-412. https://doi.org/10.1016/J.ONEEAR.2020.05.001

3. Levin, N., Kyba, C. C., Zhang, Q., de Miguel, A. S., Román, M. O., Li, X., ... & Elvidge, C. D. (2020). Remote sensing of night lights: A review and an outlook for the future. *Remote Sensing of Environment*, *237*, 111443. https://doi.org/10.1016/J.RSE.2019.111443

4. Diaz, B. S., Mata-Zayas, E. E., Gama-Campillo, L. M., Rincon-Ramirez, J. A., Vidal-Garcia, F., Rullan-Silva, C. D., & Sanchez-Gutierrez, F. (2022). LiDAR modeling to determine the height of shade canopy tree in cocoa agrosystems as available habitat for wildlife. *International Journal of Engineering and Geosciences*, *7*(3), 283-293. https://doi.org/10.26833/ijeg.978990

5. Sishodia, R. P., Ray, R. L., & Singh, S. K. (2020). Applications of remote sensing in precision agriculture: A review. *Remote Sensing*, *12*(19), 3136. https://doi.org/10.3390/RS12193136

6. Ørka, H. O., Jutras-Perreault, M. C., Næsset, E., & Gobakken, T. (2022). A framework for a forest ecological base map–An example from Norway. *Ecological Indicators*, *136*, 108636. https://doi.org/10.1016/j.ecolind.2022.108636

7. Calera, A., Campos, I., Osann, A., D'Urso, G., & Menenti, M. (2017). Remote sensing for crop water management: From ET modelling to services for the end users. *Sensors*, *17*(5), 1104. https://doi.org/10.3390/S17051104

8. Jiang, D., & Wang, K. (2019). The role of satellite-based remote sensing in improving simulated streamflow: A review. *Water*, *11*(8), 1615. https://doi.org/10.3390/W11081615

9. Keleş, M. D., & Aydın, C. C. (2020). Mobil Lidar Verisi ile Kent Ölçeğinde Cadde Bazlı Envanter Çalışması ve Coğrafi Sistemleri Entegrasyonu-Ankara Örneği. *Geomatik*, *5*(3), 193-200. https://doi.org/10.29128/geomatik.643569

10. Awad, M. M. (2017). Toward robust segmentation results based on fusion methods for very high resolution optical image and lidar data. *IEEE Journal of Selected Topics in Applied Earth Observations and Remote Sensing*, *10*(5), 2067-2076. https://doi.org/10.1109/JSTARS.2017.2653061

11. Yao, H., Qin, R., & Chen, X. (2019). Unmanned aerial vehicle for remote sensing applications—A review. *Remote Sensing*, *11*(12), 1443. https://doi.org/10.3390/rs11121443

12. Yang, B., & Chen, C. (2015). Automatic registration of UAV-borne sequent images and LiDAR data. *ISPRS Journal of Photogrammetry and Remote Sensing*, *101*, 262-274. https://doi.org/10.1016/j.isprsjprs.2014.12.025

13. Li, J., Yang, B., Chen, C., & Habib, A. (2019). NRLI-UAV: Non-rigid registration of sequential raw laser scans and images for low-cost UAV LiDAR point cloud quality improvement. *ISPRS Journal of Photogrammetry and Remote Sensing*, *158*, 123-145. https://doi.org/10.1016/j.isprsjprs.2019.10.009

14. Jiang, S., Jiang, W., Huang, W., & Yang, L. (2017). UAV-based oblique photogrammetry for outdoor data acquisition and offsite visual inspection of transmission line. *Remote Sensing*, *9*(3), 278. https://doi.org/10.3390/rs9030278

15. Fuad, N. A., Ismail, Z., Majid, Z., Darwin, N., Ariff, M. F. M., Idris, K. M., & Yusoff, A. R. (2018, June). Accuracy evaluation of digital terrain model based on different flying altitudes and conditional of terrain using UAV LiDAR technology. In *IOP conference series: earth and environmental science* (Vol. 169, No. 1, p. 012100). IOP Publishing. https://doi.org/10.1088/1755-1315/169/1/012100

16. Sofonia, J. J., Phinn, S., Roelfsema, C., Kendoul, F., & Rist, Y. (2019). Modelling the effects of fundamental UAV flight parameters on LiDAR point clouds to facilitate objectives-based planning. *ISPRS journal of photogrammetry and remote sensing*, *149*, 105-118. https://doi.org/10.1016/j.isprsjprs.2019.01.020

17. Jiang, S., Jiang, C., & Jiang, W. (2020). Efficient structure from motion for large-scale UAV images: A review and a comparison of SfM tools. *ISPRS Journal of Photogrammetry and Remote Sensing*, *167*, 230-251. https://doi.org/10.1016/j.isprsjprs.2020.04.016

18. Awrangjeb, M. (2015). Effective generation and update of a building map database through automatic building change detection from LiDAR point cloud data. *Remote Sensing*, *7*(10), 14119-14150. https://doi.org/10.3390/RS71014119

19. He, M., Zhu, Q., Du, Z., Hu, H., Ding, Y., & Chen, M. (2016). A 3D shape descriptor based on contour clusters for damaged roof detection using airborne LiDAR point clouds. *Remote Sensing*, *8*(3), 189. https://doi.org/10.3390/rs8030189

20. Meng, X., Currit, N., & Zhao, K. (2010). Ground filtering algorithms for airborne LiDAR data: A review of critical issues. *Remote Sensing*, *2*(3), 833-860. https://doi.org/10.3390/rs2030833

21. Tulldahl, H. M., Bissmarck, F., Larsson, H., Grönwall, C., & Tolt, G. (2015, October). Accuracy evaluation of 3D lidar data from small UAV. In *Electro-Optical Remote Sensing, Photonic Technologies, and Applications IX* (Vol. 9649, p. 964903). SPIE. https://doi.org/10.1117/12.2194508

22. Thiel, C., & Schmullius, C. (2017). Comparison of UAV photograph-based and airborne lidar-based point clouds over forest from a forestry application perspective. *International Journal of Remote Sensing*, *38*(8-10), 2411-2426. https://doi.org/10.1080/01431161.2016.1225181

23. Zhou, S., & Wu, Z. (2013). Social Media Retrieval and Mining. *IOP Conference Series: Earth and Environmental Science* (Vol. 387). Berlin, Heidelberg: Springer Berlin Heidelberg. https://doi.org/10.1007/978-3-642-41629-3

24. Sun, Y., & Polys, N. (2020, November). The Scalability of X3D4 PointProperties: Benchmarks on WWW Performance. In *The 25th International Conference on 3D Web Technology* (pp. 1-8). https://doi.org/10.1145/3424616.3424707

25. Yoo, B., & Brutzman, D. (2009, June). X3D earth terrain-tile production chain for georeferenced simulation. In *Proceedings of the 14th international conference on 3D Web technology* (pp. 159-166). https://doi.org/10.1145/1559764.1559791

26. Han, S., Brutzman, D., Lee, J., Yoo, K. H., Marchetti, V., Mouton, C., ... & Jia, J. (Eds.). (2020). *The 25th International Conference on 3D Web Technology*. ACM.

27. Kim, J. S., Polys, N., & Sforza, P. (2015, June). Preparing and evaluating geospatial data models using X3D encodings for web 3D geovisualization services. In *Proceedings of the 20th International Conference on 3D Web Technology* (pp. 55-63). https://doi.org/10.1145/2775292.2775304

Using GIS for the allowable soil bearing capacity estimation according to the Terzaghi (1943) equation in Eskişehir city center, Türkiye

Ebru Civelekler[*1]

¹Eskişehir Osmangazi University, Department of Civil Engineering, Türkiye

Abstract

In foundation engineering, it is necessary to calculate the bearing capacity of soils. The allowable soil bearing capacity required for foundation design is calculated through various empirical methods using geotechnical parameters such as specific gravity and angle of internal friction. Standard Penetration Test (SPT) values of the soil are used in these calculations. Therefore, soil tests which engineers need, are costly and time-consuming. This study aims to determine the soil bearing capacity of Eskişehir city according to the Terzaghi (1943) equation and present soil bearing capacity maps for shallow foundations. The geotechnical parameters of the soil were obtained from 40 borehole data made in the field. Within the scope of the study, according to the Terzaghi (1943) equation bearing capacity maps were created for 0-5 m depth to provide an overview of the bearing capacity of Eskişehir soil. These maps were made in the Geographic Information System (GIS), which has a database that stores and analyses regular data. In addition, these maps can assist engineers working on shallow foundation design on the site.

1. Introduction

Soil is the main material used in the construction of building foundations. The foundation should be designed according to the parameters obtained after determination of the soil properties in the area of construction. The most important of these soil parameters is the bearing capacity of the soil [1]. Soft soil layers often cannot carry the load from the superstructure causing problems such as settlement and loss of bearing capacity. Therefore, extensive soil survey studies are required to be conducted to construct a building. These studies are expensive, time-consuming and labour-intensive. Many researchers have suggested empirical equations for calculating the bearing capacity of the soil to this date [2-7]. Different engineering parameters of the soil are utilized in these empirical equations. Some researchers suggest these equations utilizing the physical and mechanical properties of the soil, while others suggest these equations according to the dynamic properties of the soil.

In the last thirty years, with the advances in computer technologies, Geographic Information Systems (GIS) are a frequently used tool for storing, processing and analysing spatial data [8]. In the last thirty years, with the advances in computer technologies, GIS is frequently used for civil engineering applications and contributes to studies such as spatial data management, the creation of smart city models and risk analysis [9,10].

It has become very important to predict the engineering properties of the soil using Geographic Information Systems (GIS) technologies in terms of geotechnical engineering. Today, there are many studies that calculate the allowable soil bearing capacity using empirical equations and present site-specific maps in GIS from the calculated data [11-13].

Allowable soil bearing capacity is the geotechnical parameter of the soil used to decide the most suitable foundation in the design of constructions. The bearing capacity should be calculated in order to determine the type and depth of foundations, as well as to prevent damage caused by building loads and earthquakes [12].

Geotechnical properties such as relative density, cohesion and internal friction angle are used to calculate the allowable soil bearing capacity. These geotechnical properties are obtained from studies on the field such as Standard Penetration Test (SPT) and Cone Penetration Test (CPT). These studies are comprehensive survey studies conducted in field conditions and time-consuming. It costs very high to conduct such studies on the field and the engineering properties of the soil should be determined in the construction of the building foundation. A database of soil geotechnical properties may help to save from a large portion of the total project cost. Inverse distance weighting method is an interpolation method used to estimate non-spatial points from existing data [14]. Therefore, using interpolation methods by creating a database of geotechnical data for a particular site allows to obtain economical and effective results for construction design. Dungca [15] created soil bearing capacity maps from the surface to a depth of 5 meters using GIS technologies for the city of Quezon, Philippines. Al Mamoori et al. [16] determined that Inverse distance weighting (IDW is the best GIS interpolation method for the estimation of the bearing capacity of the soil in Najaf, Iraq. Al Maliki et al. [12] used

IDW interpolation method in GIS to generate soil bearing capacity maps of Najaf and Kufa cities of Iraq. In this study, the geotechnical parameters of the soil obtained from the boring works carried out in the field in a certain part of Eskişehir city center were used. The allowable soil bearing capacity calculations were made using the Terzaghi (1943) equation, among these geotechnical parameters, for shallow foundations. All geotechnical parameters were stored in the Geographical Information Systems (GIS) database and maps containing the soil bearing capacity of the study area were produced by use of the Inverse of Distance (IDW) method.

2. Method

2.1. Study area

The study area, Eskişehir, is located in the Central Anatolia Region in the northwest of Turkey. The study area covers a significant part of Eskişehir city center and is located in an area of approximately 53 km² between 280.000-290.200 E and 4.404.000-4.410.000 N (UTM Zone 36, ED50) (Figure 1). The most important stream of the region is the Porsuk River.
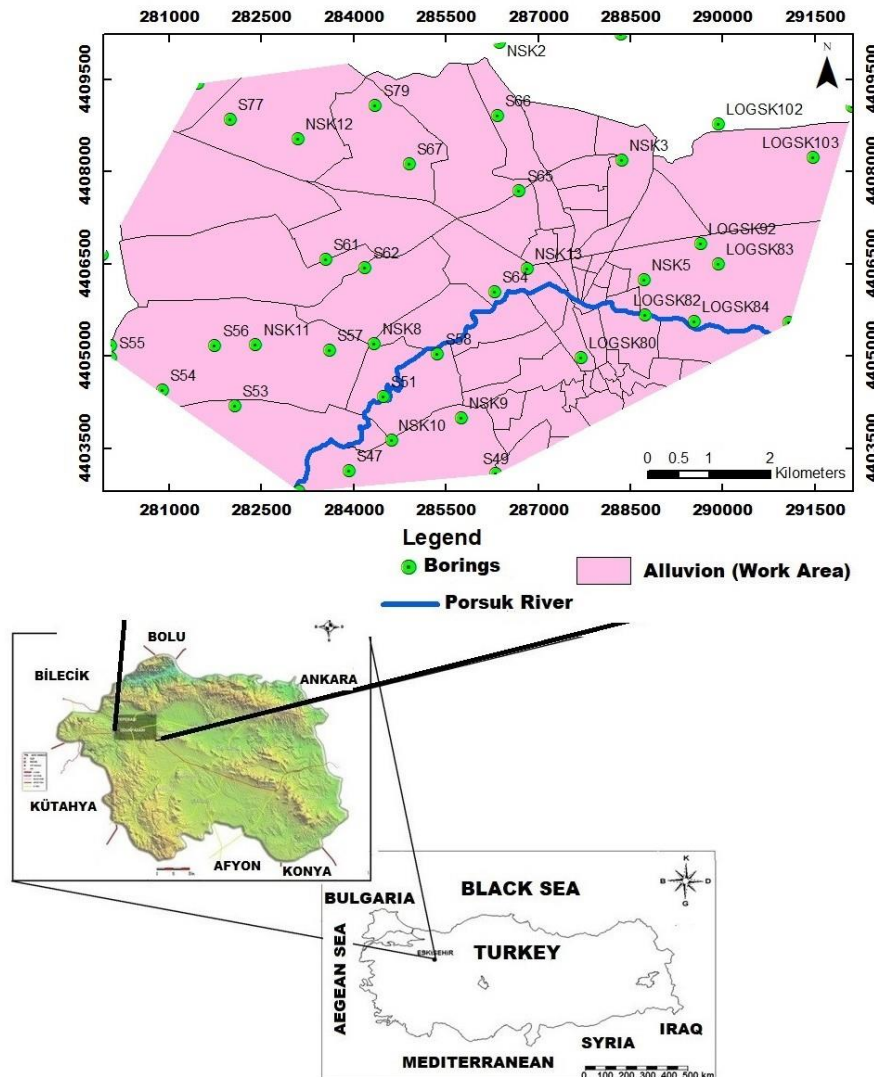

Figure 1. Boring location map of the study area

2.2. Geotechnical properties of the study area

Alluvial soil extends in most of Eskişehir city center. Geological map of the study area is presented in Figure 2. This alluvial soil is divided into two as old alluvium and new alluvium by some researchers [17]. Some parts of the study area are located on the soil, which is geologically defined as new alluvium consisting of younger and loose material. In the north-west of the study area, the soil defined as old alluvium, which was formed relatively earlier than the new alluvium, and where more compact soil layers are located. When the soil properties of the alluvial soil are examined for 30 meters, there are clay, silt, sand and gravel levels. Generally, high plasticity clay-silt levels are found up to

5-6 m from the surface, while at lower levels, it alternates from low plasticity stratified strata to sand and gravel levels [18]. In addition, there are poorly graded sand and silty sand-clay sand layers at the middle levels of some soundings at 30 m depth. In the southern part of the Porsuk River, sandstone-conglomerate units also extend as bedrock within the boundaries of the study area.

We made the local soil class map of the study area according to the Turkish Building Earthquake Code (2018) in our previous study [20] (Figure 3). We created this local soil class map by use of the Inverse Distance Weighting interpolation approach in ArcGIS program. It is understood, according to this map, that the local soil class of the site is mostly ZD, ZE and ZF.
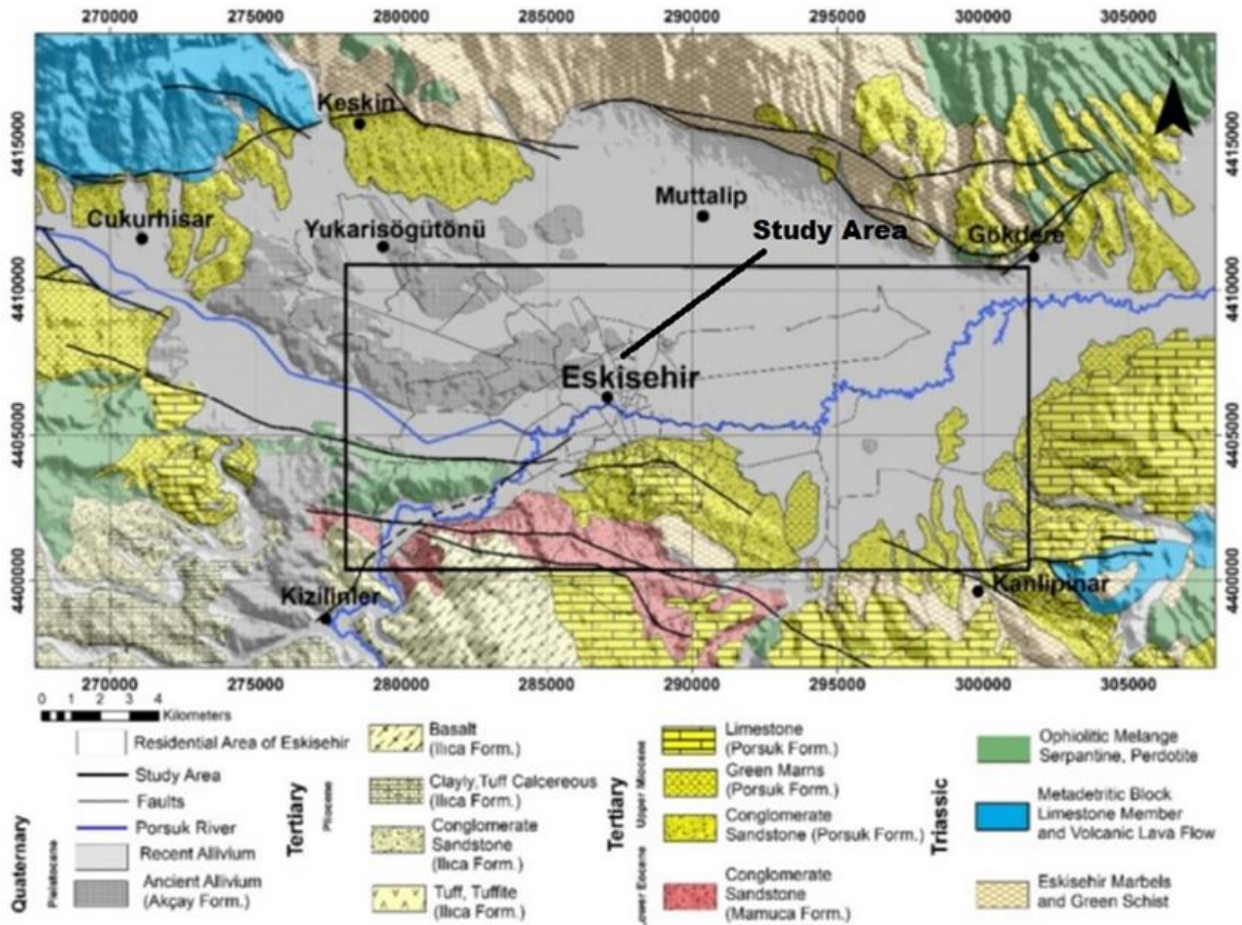

**Figure 2.** Geological map of the study area [19]

3. Methodology

Shallow foundations transmit the applied constructional loads to the soil close to the surface. Meanwhile, they generate shear stresses in the soil. Bearing strength failures occur when shear stresses exceed the shear strength of soil or rock. The relationship between foundation dimensions, load and soil properties should be known in order to prevent failure of bearing capacity of shallow foundations [1].

In the design of shallow foundations, the ultimate bearing capacity calculation is made by using the geotechnical properties of the soil. According to Terzaghi (1943), soil bearing capacity is calculated using the

corrected SPT-N values of the drilling logs. This calculation is given in Equation 1.

$$N_{60} = \frac{E_m C_B C_S C_R C_N N}{0.6} \tag{1}$$

In Equation 1, N_{60} is the corrected SPT-N value (pulses/ft) determined by considering the number of blows. The corrected SPT-N_{60} values are used to determine the geotechnical properties of the soil such as relative density, undrained shear strength and internal friction angle. The E_m ram efficiency is the C_B borehole diameter correction. C_S is the sampler correction. C_R is rod length correction. C_N is the cover pressure correction and N is the SPT-N value recorded in the field.
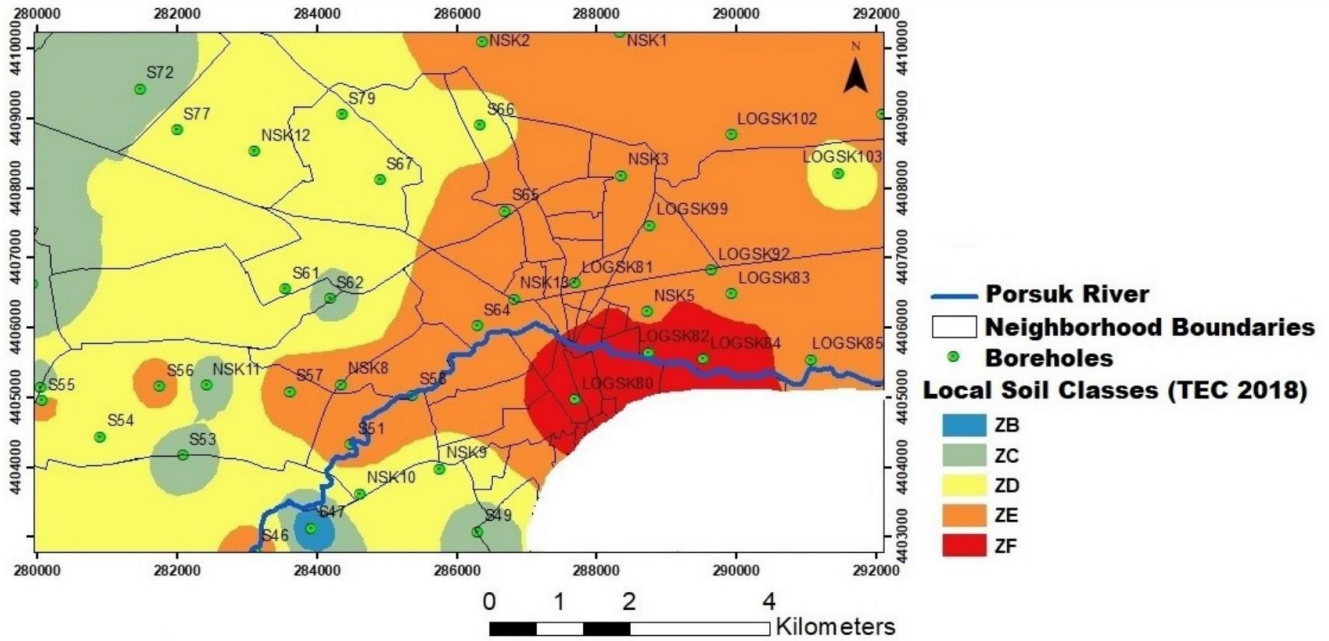
Figure 3. Local soil classes of investigated area according to Turkish Earthquake Code 2018

Soil has two mechanical properties, namely shear strength and bearing capacity. Soil bearing capacity, which is one of the most important features in foundation design, represents the contact pressure between the foundation and the soil. Various boundary balance methods used to calculate soil bearing capacity were developed in the first half of the twentieth century. However, it is the method of Terzaghi (1943) that is widely accepted. Terzaghi (1943) considers three zones in soil as wedge zone, radial slip zone and linear slip zone. He assumes that the sliding surface stops at this depth and that the overlying soil is displaced by the surcharge pressure because the soils between soil surface and foundation depth neglect the shear strength. This approach is conservative and limits the method to relatively shallow foundations (D≤ B) [1].

Terzaghi developed his theory for continuous foundations (that is, foundations with a very large L/B ratio), which is one of the shallow foundation types. However, in the ongoing process, he suggested similar approaches for square and rectangular foundations, using his experimental results. Accordingly, in this study, the bearing capacity equation developed by Terzaghi for continuous foundations was used to determine the soil bearing capacity and this is presented in Equation 2 [2].

$$q_n = c'N_C + \sigma'_Z N_q + 0.5\gamma'BN_\gamma \qquad (2)$$

Here, q_n indicates the Ultimate bearing capacity of the soil, c' indicates the Effective cohesion of the soil under the foundation, σ'_z indicates the Effective vertical stress at foundation depth, γ' indicates the Effective unit weight of the soil, B indicates the Foundation width, N_c, N_q and N_γ: Terzaghi indicates the bearing power factors. Although bearing capacity calculation of Terzahgi was developed for effective stresses, this calculation can also be used in total stress analysis [2].

In calculating the allowable bearing capacity (q_a): the ultimate bearing capacity (q_u) is divided by a factor of

safety (Equation 3). The foundation is then designed so that the contact pressure (q) does not exceed the allowable bearing capacity (q_a).

$$q_a = \frac{q_u}{F} \qquad (3)$$

Safety factors are not stated clearly in most of the building codes. However, constructional engineers determine the safety factor by taking into account the design loads depending on the soil type, terrain structure, soil variability and construction type. The factor of safety varies between 2.5-4.5. The one commonly used in foundation engineering is 3 [1].

In this study, the allowable soil bearing capacity values of 40 boreholes were calculated using the corrected SPT-N values and soil parameters. The factor of safety was taken as 3, divided by the ultimate bearing capacity in order to determine the allowable bearing capacity of the soil. Allowable soil bearing capacities at different locations are calculated for depths of 1.5 meters, 3 meters and 4.5 meters. Allowable bearing capacity maps of the soil were produced using GIS technologies for a certain part of Eskişehir city center,

4. Estimation of soil bearing capacity

Theoretically, the ultimate bearing capacity of the soil is the acceptable load bearing capacity of the soil layers without any collapse [21,22]. The issue of ultimate bearing capacity can be expressed in terms of the contact pressure between the soil and the construction and the pressure allowing optimization of the superstructures interacting with the soil. In this study, the ultimate bearing capacity of the soil was calculated by considering the soil properties obtained from area studies for 1.5, 3.0 and 4.5 depths from the surface. In the study, the physical and mechanical properties obtained from 40 boreholes representing the land made in different locations were used (Table 1).

Table 1. Soil parameters used in the study

Study Type	Unit	Value
Boreholes	amount	40
Total Borehole Length	meters	1200
SPT	amount	800
Definition Test (such as cohesion, internal friction angle, unit weight of the soil	amount	689

Inverse distance weighting (IDW) is a popular interpolation method that estimates values at unknown points using the value and distance of a nearby known point. In this method, connection and resemblance rate is proportional to the distance between the points (that is, those that are closest to the known point have more weight than those that are far away) [23].

In the IDW method, the unknown points value is estimated using the following equation (Equation 3) [23].

$$z(x_0) = \left(\frac{\sum_{i=1}^{n} \frac{x_i}{h_{ij}^{\beta}}}{\sum_{i=1}^{n} \frac{1}{h_{ij}^{\beta}}} \right) \qquad (4)$$

Calculations were made according to the empirical approach of Terzaghi (1943) for shallow foundations. Maps were produced by creating a database in GIS from the calculated soil bearing capacity data. These maps were created using the IDW interpolation method from the Geostatistical Analyst Wizard (GAW) methods in ArcGIS 10.7 software. Geotechnical maps representing the bearing capacity at these 3 depths were produced for the settlement area within the scope of the study. Figure 4, among these maps, shows the permissible soil bearing capacity of the study area at a depth of 1.5 meters from the ground surface. Here, the carrying capacity values are as low as 289 kPa in some places, while maximum values of 539 kPa have been obtained in some places.

The allowable soil bearing capacity map of the study area at a depth of 3.0 meters was created based on the calculated data within the scope of the study (Figure 5). As can be seen from Figure 5, allowable soil bearing capacity values for the 3.0 meters depth of the study area range between 369 kPa and 773 kPa.

The allowable soil bearing capacity map of the study area at a depth of 4.5 meters was created based on the calculated data within the scope of the study (Figure 6). According to the map presented in Figure 6, the carrying capacity values have been seen to vary between 849 and 1.533 kPa. It is observed that the bearing capacity values increase as the depth increases.

Also, a groundwater level map of the study area was created taking into account the studied geotechnical field data (Figure 7). The groundwater level of the city center varies between 2-13.40 m according to this map (shallow depths).
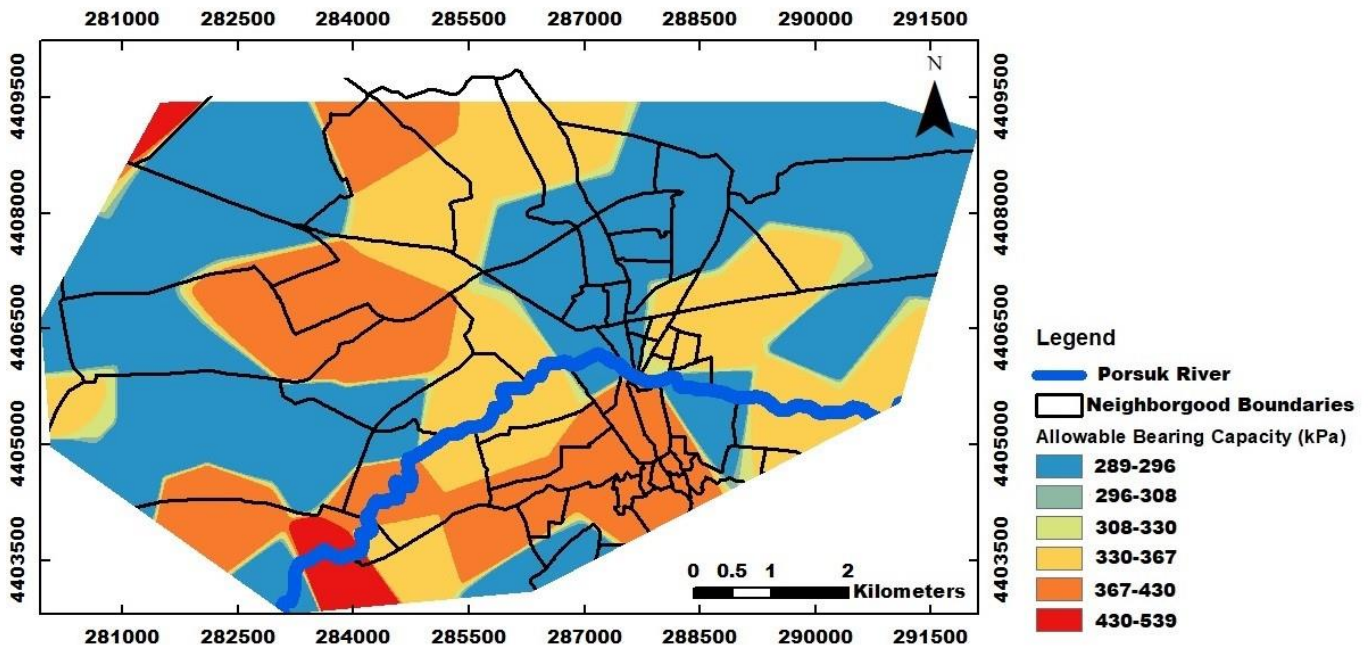
Figure 4. Allowable Bearing Capacity Map of the Study Area at 1.5 meters

5. Conclusion

It is determined that the soil bearing capacity has lower values (0-290 kPa) in some parts of the study area with younger geological units, while it has relatively higher values in some regions according to the maps created. The bearing capacity values are higher on the soil consisting of old alluvium units on the north side of the study area. Low values where the carrying capacity may pose a problem noticed in the units defined as new alluvium on the northern side of the study area. The zone consisting of rock units as soil features in the south of the study area has bearing capacity values greater than 1500 kPa. It has been determined that ZB, ZC class soils have higher soil bearing capacity when the local soil properties are taken in to account. In addition, in soils

where the groundwater level is high, the allowable soil bearing capacity was obtained as lower values.

In the construction of shallow foundations, it is one of the most accurate methods to determine the bearing capacity of soils by performing loading tests that force them to collapse. However, these experiments are not economical and are rarely performed due to some uncertainties in practice. Therefore, today, the bearing capacity calculation of the soil using SPT-N and soil properties is more preferred due to its practicality in practice. In this study, site-specific allowable soil bearing

capacity maps were created according to the Terzaghi (1943) approach by using the data obtained as a result of the calculations in GIS. It has been determined that especially the new alluvial ground has a risky bearing capacity according to the maps obtained as a result of this study. The estimated maps presented in this study were created using the Terzaghi (1943) method only. For this reason, it is necessary to make general bearing capacity calculations for the Turkish Building Earthquake Regulation (2018), which is used in earthquake-resistant building design today.
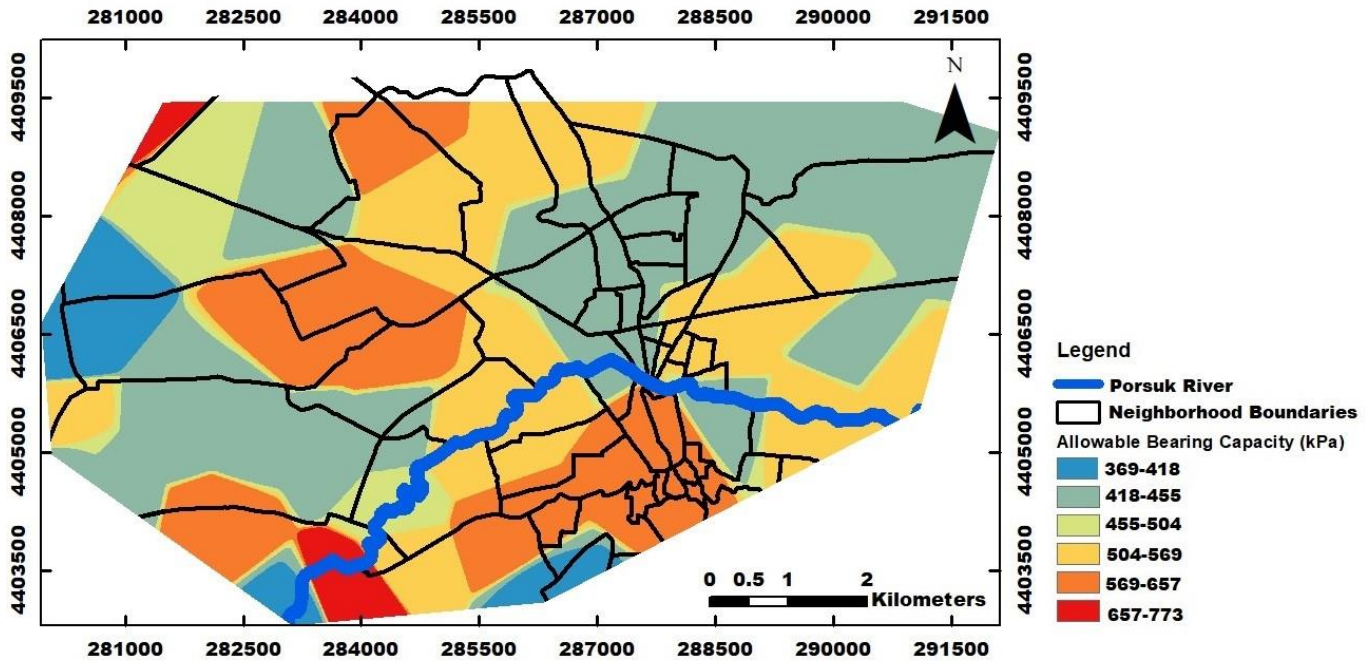

Figure 5. Allowable Bearing Capacity Map of the Study Area at 3.0 meters
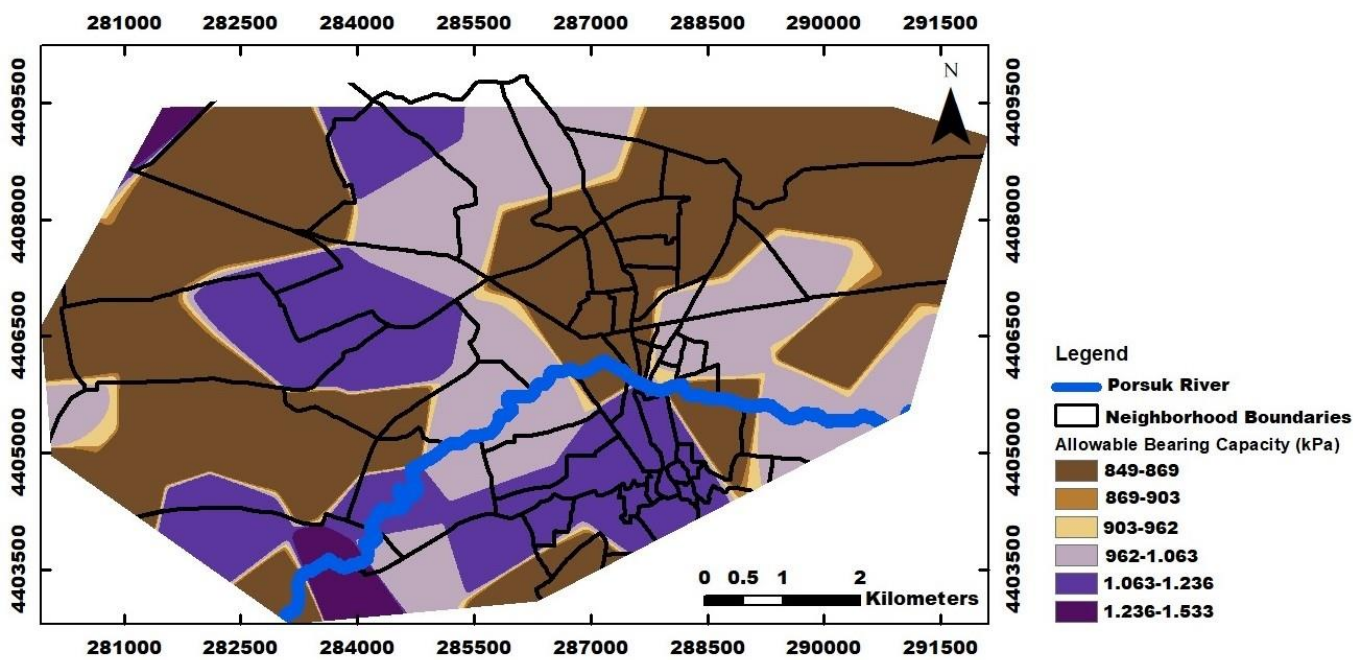

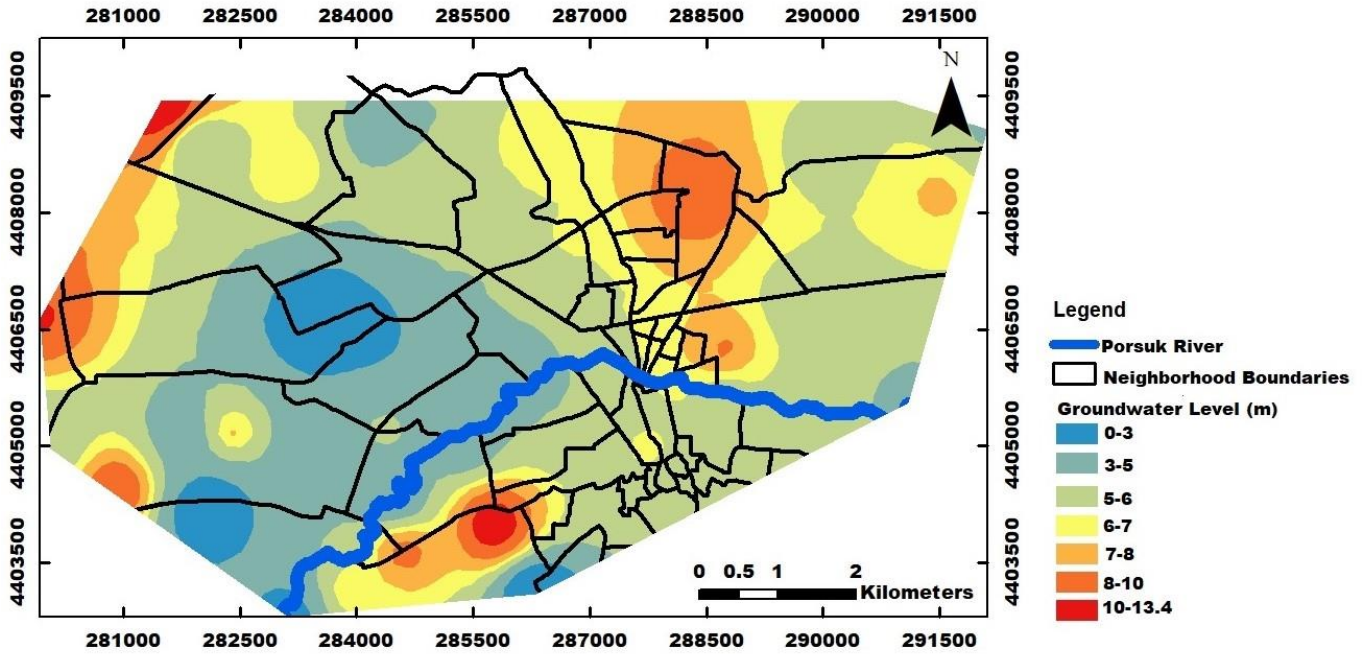**Figure 6.** Allowable Bearing Capacity Map of the Study Area at 4.5 meters

Figure 7. Groundwater level map of the study area

Conflicts of interest

The authors declare no conflicts of interest.

References

1. Coduto, D. P. (2001). Foundation design principles and practices. 2nd ed., New Jersey, USA, Prentice Hall. ISBN:0135897068.
2. Terzaghi, K. (1943). Theoretical Soil Mechanics John Wiley and Sons Inc. *New York*, *314*.
3. Meyerhof, G. G. (1963). Some recent research on the bearing capacity of foundations. *Canadian geotechnical journal*, *1*(1), 16-26.
4. Richards Jr, R., Elms, D. G., & Budhu, M. (1993). Seismic bearing capacity and settlements of foundations. *Journal of Geotechnical Engineering*, *119*(4), 662-674.
5. Çinicioğlu, S. F. (2005). Zeminlerde statik ve dinamik yükler altında taşıma gücü anlayışı ve hesabı. *Seminer, IMO İstanbul Şubesi*.
6. Keçeli, A. (2010). Sismik yöntem ile zemin taşıma kapasitesi ve oturmasının saptanması. *Uygulamalı Yerbilimleri Dergisi*, *9*(1), 23-41.
7. Tezcan, S. S., & Ozdemir, Z. (2011). A refined formula for the allowable soil pressure using shear wave velocities. *The Open Civil Engineering Journal*, *5*(1), 1-8
8. Şimşek, Ç. K., Türk, T., Ödül, H., & Çelik, M. N. (2018). Detection of paragliding fields by GIS. *International Journal of Engineering and Geosciences*, *3*(3), 119-125. https://doi.org/10.26833/ijeg.413833
9. Kılıçer, S. T., Cömert, Ç., & Akıncı, H. 3B Kent Modelleri İçin Yeni Bir Silüet Analizi Modülünün Geliştirilmesi. *Geomatik*, *3*(3),183-195. https://doi.org/10.29128/geomatik.390081
10. Oğuz, E., Oğuz, K., & Öztürk, K. (2022). Düzce bölgesi taşkın duyarlılık alanlarının belirlenmesi. Geomatik, *7*(3),220-234. https://doi.org/10.29128/geomatik.972343
11. Dungca, J. R., Concepcion Jr, I, Limyuen, M. C. M., See, T. O., & Vicencio, M. R. (2017). Soil bearing capacity reference for Metro Manila, Philippines. *Geomate Journal*, *12*(32), 5-11.
12. Al-Maliki, L. A. J., Al-Mamoori, S. K., El-Tawel, K., Hussain, H. M., Al-Ansari, N., & Al Ali, M. J. (2018). Bearing capacity map for An-Najaf and Kufa cities using GIS. *Engineering*, *10*(05), 262-269. https://doi.org/10.4236/eng.2018.105018
13. Khan, F., & Das, B. (2021, June). Geospatial approach to determine Soil bearing capacity of Nagpur city, Maharashtra India. In *IOP Conference Series: Earth and Environmental Science* (Vol. 796, No. 1, p. 012069). IOP Publishing.
14. Hastaoğlu, K. Ö., Göğsu, S., & Gül, Y. (2022). Determining the relationship between the slope and directional distribution of the UAV point cloud and the accuracy of various IDW interpolation. *International Journal of Engineering and Geosciences*, *7*(2), 161-173. https://doi.org/10.26833/ijeg.940997
15. Dungca, J. R. (2020). A reference for the allowable soil bearing capacities in Quezon city, Philippines. *Geomate Journal*, *19*(71), 42-47. https://doi.org/10.21660/2020.71.9203
16. Al-Mamoori, S. K., Al-Maliki, L. A., Al-Sulttani, A. H., El-Tawil, K., & Al-Ansari, N. (2021). Statistical analysis of the best GIS interpolation method for bearing capacity estimation in An-Najaf City,

Iraq. *Environmental Earth Sciences*, *80*(20), 683. https://doi.org/10.1007/s12665-021-09971-2

17. Civelekler, E., & Pekkan, E. (2022). The application of GIS in visualization of geotechnical data (SPT-Soil Properties): a case study in Eskisehir-Tepebaşı, Turkey. *International Journal of Engineering and Geosciences*, *7*(3), 302-313. https://doi.org/10.26833/ijeg.980611

18. Akdeniz, E., Güney, Y., Pekkan, E., Avdan, U., Tün, M., & Ecevitoglu, B. (2011). Using Geographical Information Systems in Interpretation of Geo-Engineering Properties of Ground: Yenibaglar and Bahçelievler District Sample in Eskisehir. In *6th International Advanced Technologies Symposium (IATS'11), Elazıg, Turkey*.

19. Güney, Y., Ecevitoğlu, B., Pekkan, E., Avdan, U., Tün, M., Kaplan, O., Mutlu, S., & Akdeniz, E. (2013). Evaluation of the geotechnical, structural and geophysical information systems of Eskisehir using GIS Technics. Project No:080240.

20. Civelekler, E., Okur, V. D., & Afacan, K. B. (2021). A study of the local site effects on the ground response for the city of Eskişehir, Turkey. *Bulletin of Engineering Geology and the Environment*, *80*(7), 5589-5607. https://doi.org/10.1007/S10064-021-02285-4

21. Kadhim, M. M., Al-Saoudi, N. K., & Ziboon, A. R. T. (2013). Digital geotechnical maps of Basrah city using geographical information systems technique. *Engineering & Technology Journal*, *31*, 599-617.

22. Castelli, F., & Motta, E. (2012). Seismic Bearing Capacity of Shallow Foundations, Earthquake-Resistant Structures—Design, Assessment and Rehabilitation. *InTech. https://www. tandfonline. com/doi/abs/10.1179 Y, 1939787915*.

23. Bhunia, G. S., Shit, P. K., & Maiti, R. (2018). Comparison of GIS-based interpolation methods for spatial distribution of soil organic carbon (SOC). Journal of the Saudi Society of Agricultural Sciences, 17, 114–126.

Identification of groundwater potential for urban development using multi-criteria decision-making method of analytical hierarchy process

Rajaveni Sundara Pandian **1* [iD] **, Sidesh Udayakumar** *1* [iD] **, Kalyana Kumar Prasanna Balaji** *1* [iD] **, Ramabalan Lakshmi Narayanan** *1* [iD]

1Mepco Schlenk Engineering College, Department of Civil Engineering, Sivakasi, India

Abstract

Detailed knowledge regarding the availability of potential groundwater sources is a prerequisite for the sustainable development of cities and towns in a planned manner. The present study is carried out to identify the potential groundwater sources for the growth of towns and cities around Virudhunagar district, India by integrated geospatial techniques and analytical hierarchy method. The groundwater potential zones are divided into four groups: low, medium, high, and very high. It is obtained that 1.71% and 51.86% fall under the low and medium zones, respectively. The area with high and very high groundwater potential accounts for 45.7% and 0.73% of the total area, respectively. Finally, potential areas identified for groundwater are validated with data on the potential yield of various wells, demonstrating a good correlation. The results of this research will help planners and decision-makers to better plan and develop future cities.

1. Introduction

Water is essential for all kinds of living organisms; groundwater found in the aquifer beneath the earth's surface is a precious source for mankind. Groundwater is the primary source of water for a variety of purposes, including industrial, domestic, and agricultural needs. The availability of water varies with space and it is characterized by a hydrological cycle. The increase in population has led to serious deterioration of surface and subsurface water. Groundwater is something that needs to survive, and also needs water for agriculture, domestic and industrial developments. Groundwater depletion occurs due to the frequent pumping of water from the ground with the use of bore wells. Pumping of water more quickly than it can replenish itself which in turn leads to the depletion of groundwater at a faster rate than it is not sustainable anymore.

Groundwater is the primary source of water used for domestic purposes in rural areas. Furthermore, it is the primary source of agriculture due to its greater distribution, low development cost, and good quality when compared to surface water [1]. The United Nations reveal an estimation that by the year 2025, two-thirds of the human population will face an acute shortage of freshwater across all parts of the world. According to a report by the United Nations Educational, Scientific, and Cultural Organization (UNESCO), India withdraws a significant portion of groundwater in comparison to other countries. It has also been stated that 21 major cities of India are in a critical stage of groundwater which would distress almost 100 million people.

Groundwater recharge mechanisms have been altered by rapid urbanization, necessitating a focus on new methods to increase groundwater recharge. This urban development is impacting the groundwater quality in major cities and downstream of the alluvial aquifer. Carmon and Shamir [2] discussed the water considerations for planning urban and regional areas. The author of [3] characterized the watersheds that bear dynamic structures with large land. Sustainable development requires the proper guidelines for urban planning which takes the effects on environmental resources including groundwater resources. In this paper, it is stressed that sustainable development also includes the development of urban settlements based on natural resources, which includes factors like

---

* Corresponding Author

**(spveni4112@gmail.com) ORCID ID 0000-0003-3470-2142
(sidesh99@gmail.com) ORCID ID 0000-0001-5101-2376
(prasannakalyan123@gmail.com) ORCID ID 0000-0001-5297-5924
(narayananl634@gmail.com) ORCID ID 0000-0001-8679-7054

groundwater availability, rainfall, rainwater harvesting, surface water availability, and planning of settlement based on natural resources.

Satellite images with high spatial resolution are provided by sensors onboard satellites launched by leading countries, e.g., US, Germany, France, India, etc. These images are used to create large-scale geo-referenced data, which are required to assess groundwater potential. The rapid advancement of computer technology and Geographic Information Systems (GIS) in the twentieth century enables more support in storing and analyzing large amounts of spatial and non-spatial data in a shorter period of time and with greater accuracy. Analytic Hierarchy Process (AHP) was proposed by [4] to solve complex decision-making through pairwise comparisons. Integration of remote sensing imageries, GIS, and AHP can help to handle a large number of geo-referenced data for the demarcation of groundwater potential zones (GWPZ) more accurately. Sajil Kumar [5] demarcated the groundwater potential zones in the Chennai River basin using the GIS-based AHP method. An integrated approach of RS, GIS, and AHP has been used by several researchers [6-9] for monitoring and assessing groundwater potential. As Virudhunagar is a rapidly developing district it is without a doubt an absolute necessity to find the regions having good groundwater resources and develop the settlements-based availability and sustainability of groundwater. The

objective of the present study is to recognize the hydrogeology, and categorize the GWPZ of Virudhunagar district, Tamilnadu, India.

2. Study area

The current study was conducted in the Virudhunagar district of Tamil Nadu, India, over a 4126 km² region (Figure 1). It is one of the rapidly developing districts in Tamil Nadu as a nearby district of Madurai is turning into a smart city. Thus, the development of population settlement based on groundwater availability will be sustainable manner. Hence, this district was chosen as the study area. Minerals such as limestone, sand clay, gypsum, and granite abound in the studied region. The study area's climatic condition is semiarid tropical monsoon, and it has been experiencing hot and dry conditions. A maximum temperature of 28°C to 32°C was recorded in December, while 38°C to 42°C was recorded in June. The least temperature ranged from 17.6°C to 23°C experienced in the months of January. The Northeast monsoon is mostly responsible for the district's rainfall. The majority of the rain falls in the form of cyclonic storms brought on by depressions in the Bay of Bengal. The district's average yearly rainfall ranges from 724 to 913 mm. In the district's south-eastern corner, it is at a bare minimum. It progressively rises in the direction of the west, north, and northwest.
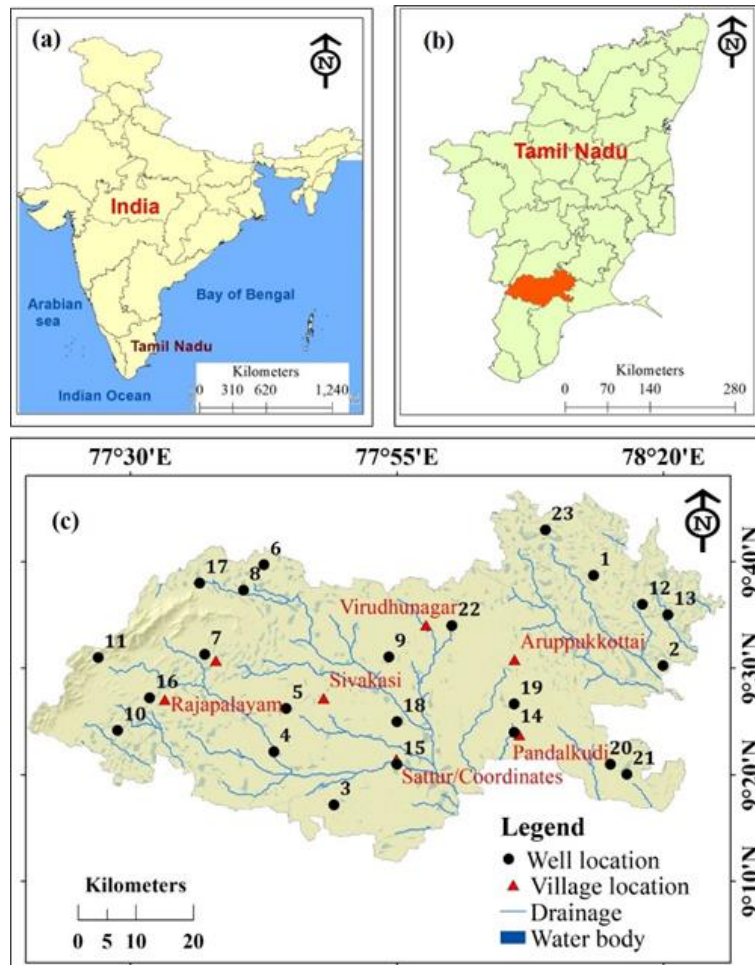
Figure 1. Study area illustrating (a) overview of India with different states; (b) Overview of Tamil Nadu state divided with district boundary; (c) The actual area covered by Virudhunagr district includes drainage streams, water bodies, town, and monitoring well locations

3. Materials and Methodology

3.1 Data collection

Slope, geology, drainage density, roughness, topographic wetness index, geomorphology, land use, lineament density, and soil were examined and selected for determining GWPZ across the Virudhunagar district based on numerous studies [10,11]. These parameters were collected from various sources such as the Bhuvan website, the Geological Survey of India (GSI), the USGS earth explorer, and the National Bureau of Soil Survey (NBSS). Cartosat-1 Digital Elevation Model (DEM) (30 m) downloaded from the Bhuvan thematic map web portal is used to create different thematic maps such as slope, drainage, roughness, and topographical wetness index. Geological Survey of India and Linear Imaging Self Scanning III (LISS III) satellite images are used to create geology and lineament density maps. The soil information of the Virudhunagar district was derived from the National Bureau of Soil Survey's (NBSS) map. The geomorphology and land use maps were collected from Bhuvan thematic map web portal which was updated with LISS III satellite image and verified with field investigations.

3.2 Methodology

The general methodology used in the current study is clearly illustrated in Figure 2. This work structure is grouped into three: geo-reference database preparation, identification of GWPZ, and validation of identified sites. In the first step of the geo-referenced database, the data was derived from satellite imagery, and secondary data was collected from GSI and NBSS. Then, weights are assigned to individual sublayers based on the manual and AHP methods. Further, rank was given to each geo-referenced data and determined the GWPZ. The results of delineated zones of groundwater potential were validated with the available groundwater head data.
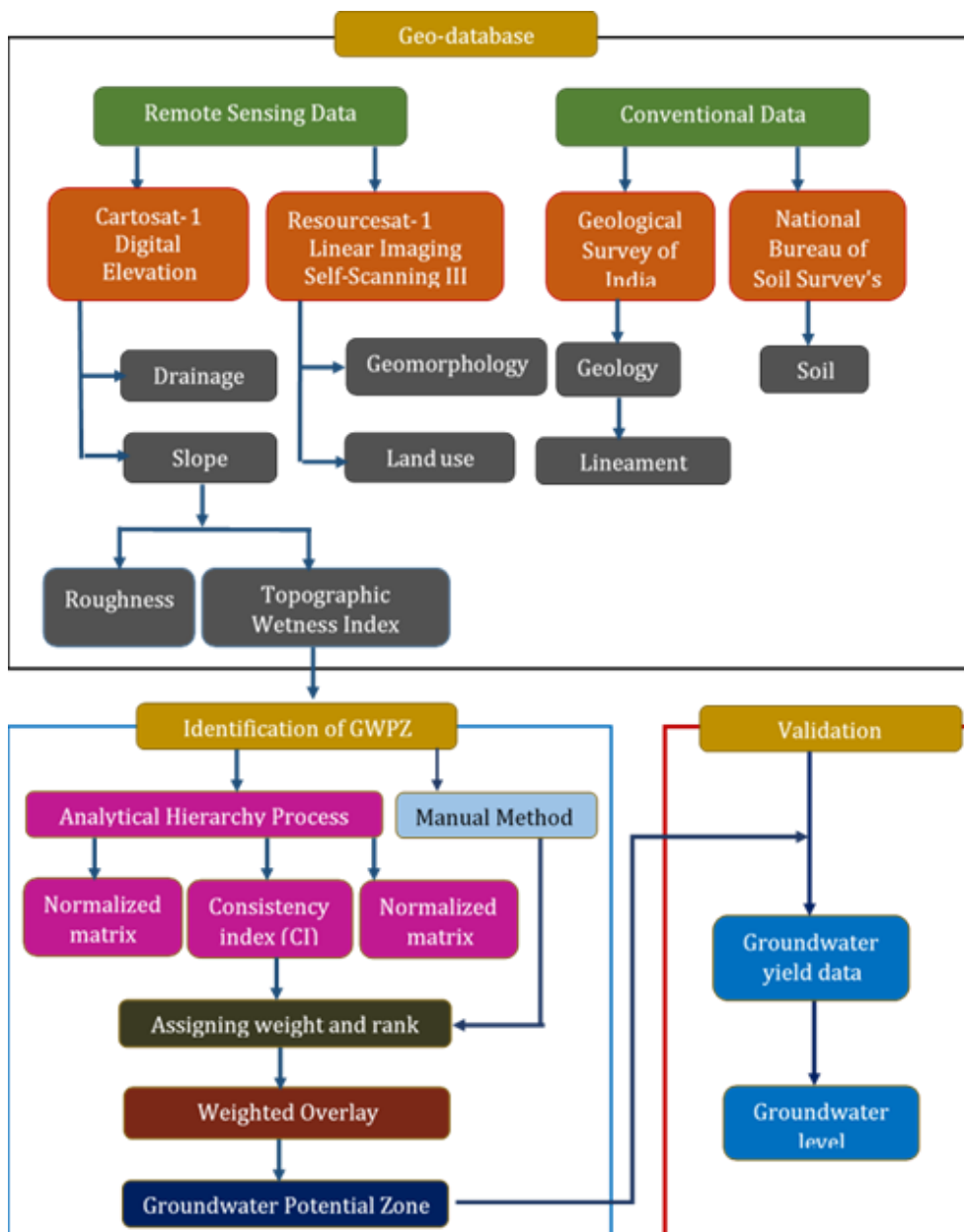

Figure 2. Flowchart represents the methodology adopted to delineate groundwater potential

3.2.1 Creation of geo-database

The slope is the difference in ground elevation that is used to locate a good source of groundwater. Rainwater may have drained away from the steep slope, causing soil erosion. Rainwater has enough time to contact the ground surface in the leveled ground and gentle slope regions, resulting in water recharge. The slope map for this study area was created using a Cartosat DEM with a spatial resolution of 30 m.

Drainage is the path where the rainwater flows on the ground. It normally flows from higher elevation to lower elevation and lithology. Drainage density is defined as the rate of drainage lines flow per square km of the area. This is one indicator that shows groundwater availability, which means higher drainage lines, more runoff, and less infiltration. Thus, groundwater recharge is inversely proportional to drainage density. The groundwater source is less in the high drainage line region; it shows a negative impact on groundwater potential. Because low drainage density equates to high infiltration, it contributes more to groundwater potential. The drainage density map was generated from a digital elevation model of CARTOSAT with a resolution of 30 x 30 m. The first flow direction and flow accumulation map were prepared in ArcGIS using the Hydrology tool. Then the drainage line was generated which was further taken as input to create a drainage density map.

The amount of elevation variation between consecutive cells is expressed by the roughness index of a digital elevation model (DEM). The roughness index often describes the topography's undulation. The rougher the surface, the more undulation there is, and vice versa. Over time, weathering and erosion processes smooth out a rocky landscape into a flat surface. Then, the surface roughness was created from slope data.

The Topographic Wetness Index (TWI) is a measurement of the potential for groundwater infiltration due to topographic parameters. It is frequently used to evaluate topographic control over hydrological processes. TWI was created in ArcGIS 10.2 using slope data. This was accomplished by using Equation (1) and (2) to calculate the rate of change of an aspect of a cell grid within its neighborhood [12]. The impacts of slope, elevation, and geomorphologic on groundwater development were integrated using the TWI map [13]. Then the TWI was calculated in ArcGIS.

$$TWI = \ln\left[\frac{a}{\tan(\beta)}\right] \quad (1)$$

$$a = \frac{A}{L} \quad (2)$$

Where A is the catchment area, a is the specific catchment area, tan(β) is the slope and L is the contour length

The LISS III image was used to update the geology supplied by the Geological Survey of India. Lineaments are delineated from the geological data and satellite imagery. Then, a lineament density was generated using the line density tool in ArcGIS 10.2 software. The lineaments are the joints and fractures present in the study region; hence these joints and fractures allow the water to infiltrate into the ground.

The recharge of groundwater is based on this land use map. LlSS-III satellite data and extensive field verification were used to construct these land use classes [14]. Moderate medium red tone and fine/medium texture were used to identify agricultural land [15]. Water bodies were shown in a black tone and had high groundwater sources [16]. Forest plantations were pale reddish-brown in color, with a fine medium texture and uneven shape and size. Wasteland had a light to dark bluish tone with coarse texture, whereas built-up land had a pale bluish-white color with fine texture and uniform shape and size [16].

Soil is another major factor that influences the store and distribution of sub-surface water, as well as the recharge of groundwater, hence affecting groundwater recharge [17]. The texture of the soil and its hydraulic qualities are important considerations for determining infiltration rates. Soil texture, an important part of analyzing the physical characteristics of the soil, is closely related to the structure, porosity, adhesion, and consistency of soil qualities. The data collected from the NBSS includes seven different types of soil.

3.2.2 Identification of GWPZ using AHP method

Multi-Criteria Decision Analysis (MCDA) of AHP is an important and commonly used methodology to delineate groundwater prospecting zones [18]. AHP technique was employed to assign significance to each thematic layer for zoning groundwater potential recharge region in this study. Saaty's scale is used to figure out the relative significance of each parameter of scale 1-9, with a score of 1 indicating the equal value of both thematic layers and a score of 9 indicating the exceptional significance of one layer over the other [19]. According to Saaty's relative importance scale, a value of 9 indicates extreme importance, 8 indicates very to very strong importance, 7 specifies very extreme importance, 6 specifies strong plus, 5 shows strong importance, 4 shows moderate plus, 3 shows moderate importance and 2 shows weak importance. The higher weights are assigned based on the stronger influence of one thematic layer on another thematic layer, that is the relative importance between the thematic layers is high [20,21].

The themes were described using Saaty's scale of rank and priority, which assists in the hierarchical arrangement of the criteria using a pair-wise comparison matrix. The expertise in the field of hydrogeology helps to find out the weight allocation of the various thematic maps and their respective classes. The suitable ranks and weights were assigned to determine a good source of groundwater location [22]. Detailed literature surveys were done before assigning ranks and weights in order to get a thorough knowledge of the ranking of thematic layers under various environmental conditions in the current study [23,24]. The principal Eigenvalue and the index of consistency (Equation 3) in the AHP determine the likelihood of uncertainty. The following equation gives the Consistency Index (CI), which is a measure of consistency.

$$CI = \frac{\lambda_{\max} - n}{n - 1} \qquad (3)$$

$$CR = \frac{CI}{RCI} \qquad (4)$$

Where $\lambda_{\max}$ is the significant eigenvalue of the pairwise comparison matrix, and n is the number of thematic layers used in this analysis. Consistency ratio (CR), described as the indicator of consistency between pairwise comparison matrix, is calculated to regulate the assessment of consistency analysis (Equation 4) and scale.

Where RCI = Random consistency Index value, whose values were attained from Saaty's standard. According to Saaty, a CR of 0.10 or less is appropriate for further analysis. Each layer and its corresponding classes are given ranks and weights based on their proportional groundwater potential contribution (Table 1).

Table 1. Weightage and rank assigned based on AHP method

Thematic Layer & Weight (%)	Sub-layer / Class	Ranks (High = 5; Low = 1)
Slope (Degree) & 9 (%)	Flat (0 - 4.7)	5
	Gentle (4.8 - 14)	4
	Moderate (15 - 23)	3
	Steep (24 - 33)	2
	Very steep (34 - 63)	1
Drainage Density (km/km²) & 9 (%)	Very low (0 - 0.08)	5
	Low (0.09 - 0.23)	4
	Moderate (0.24 - 0.36)	3
	High (0.37 - 0.49)	2
	Very High (0.50 - 0.84)	1
Roughness & 7 (%)	0.03 - 0.30	5
	0.31 - 0.42	4
	0.43 - 0.49	3
	0.50 - 0.56	2
	0.57 - 0.85	1
Topographic wetness index & 8 (%)	4.03 - 7.60	1
	7.61 - 9.58	2
	9.59 - 10.96	3
	10.97 - 12.78	4
	12.79 - 18.06	5
Geology & 13 (%)	Charnockite	1
	Gneiss	2
	Limestone / Marble	3
	Quartzite	4
	Sand and Silt	5
	Shaly sandstone	4
Lineament density (km/km²) & 11 (%)	Very low (0 - 0.07)	1
	Low (0.08 -0.19)	2
	Moderate (0.20 - 0.31)	3
	High (0.32 - 0.43)	4
	Very high (0.44 - 0.72)	5
Land use & 15 (%)	Agricultural land	4
	Built-up land	1
	Forest	3
	Waste land	2
	Water body	5
Geomorphology & 17 (%)	Hills and Plateaus	-
	Pediment	2
	Plateaus	3
	Sedimentary High ground	1
	Structural Hills	1
	Valleys	5
	Alluvial Plain	5
	Bajada	3
	Deflection slope	2
	Denudational hills	1
	Flood Plain	4
Soil & 11 (%)	Alfisols	3
	Entisols	5
	Forest unsurvey	1
	Hill soil	2
	Inceptisols	5
	Reserve forest	2
	Vertisols	4

3.2.3 Identification of GWPZ using manual method

The influence of thematic layers and their related classes in controlling the potential groundwater recharge over an area is first considered while reclassifying particular layers and assigning ranks. The objective of establishing numerous classes and their weights in groundwater regions is to demonstrate the best potential options. Rank and weights were assigned to each parameter and their sub-classes by manual method. This is accomplished by the author's knowledge and observations of existing literature, as well as the area-specific qualities in this study region [25,26]. The Equation 5 is used to carry out a raster-based weighted overlay of all of these layers using ArcGIS 10.2 software.

$$GWPZ = (SL_w x SL_r) + (DD_w x DD_r) + (R_w x R_r) + (TWI_w x \ TWI_r) + (G_w x \ G_r) + (LD_w x LD_r) + (GM_w x GM_r) + (L_w x L_r) + (S_w x S_r) \quad (5)$$

Where GWPZ indicates the groundwater potential zones, SL is the slope, DD is the drainage density, R is the roughness, TWI is the topographic wetness index, G is the geology, LD is the lineament density, GM is the geomorphology, L is the land use and S is soil, w is the normalized weight of the thematic layers calculated by AHP and r is the rank of individual features.

3.2.4 Validation

The groundwater potential zones obtained through AHP and manual method must be validated, so the result obtained is cross-verified by groundwater head which was officially gathered from the PWD Hydrology Department Virudhunagar during the process of data collection.

4. Results

4.1 Slope

The slope map was classified into five based on the degree of their gradient. The degree of gradient ranges from 0 degrees to 63 degrees present in this study region. The major areas fall under very low to low slope, nearly flat land with a slope less than 10 degrees (Figure 3a). The study area is assigned as very low (0 – 4.70 degrees); low (4.80 – 14 degrees); moderate (15 -23 degrees); steep (24 – 33 degrees); and very steep (34 – 63 degrees) based on the slope values calculated using the DEM data. As a result, approximately 95% of the total area seems to be gentle and nearly level land, allowing for maximum recharge rather than runoff.

4.2 Drainage density

The prepared drainage map shows the pattern of dendritic. Then drainage density was created from drainage data. The drainage density values vary from 0 to 0.84 per km². It was then divided into five classes (Figure 3b). These classes have been assigned to very good (0.50 – 0.84 /km²), good (0.37 – 0.49 /km²), moderate (0.24 – 0.36 /km²), poor (0.09-0.23 /km²), and very poor (0 - 0.08 /km²) respectively. The central and northeastern parts of the study area have a high drainage density (0.84 /km²) which indicates that the availability of groundwater resources may be low.

4.3 Roughness

The roughness map of the study area is shown in Figure 3c, with values ranging from 0.03 to 0.85. The values were divided into five groups: 0.03 -0.30, 0.3 - 0.42, 0.4 - 0.50, 0.50 - 0.56, and 0.57 - 0.85. Low roughness values are given high ranks and vice versa.
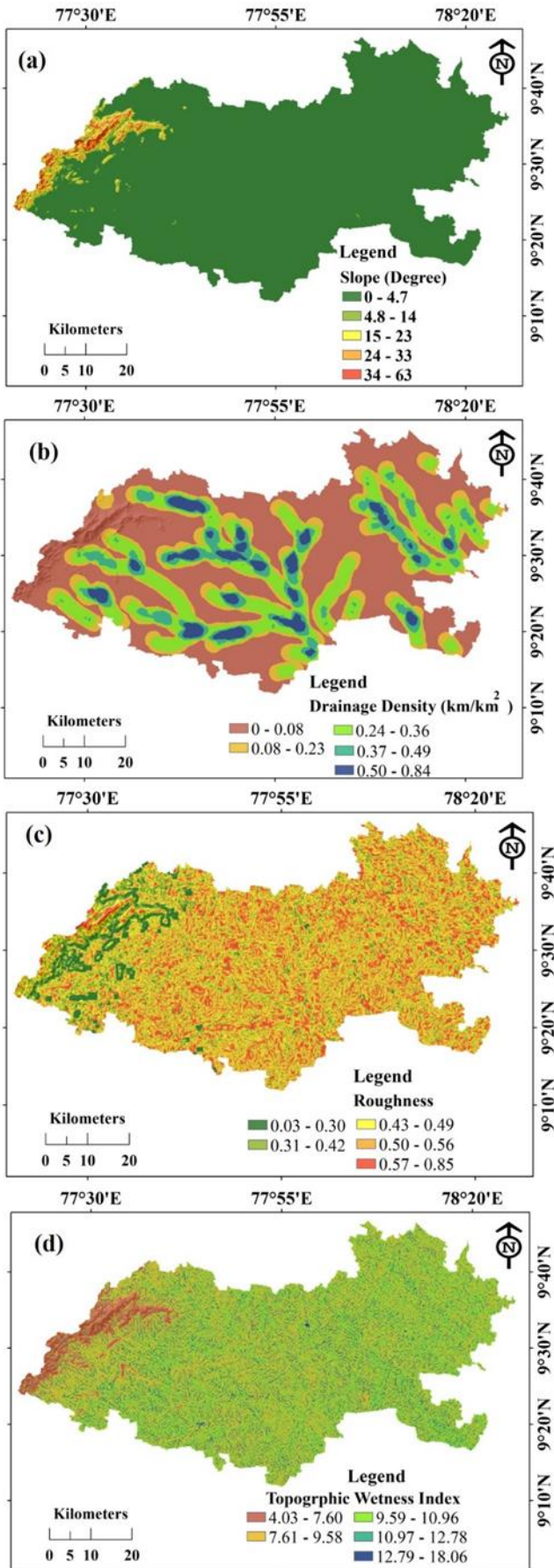
4.4 Topographic wetness index (TWI)

TWI-rich areas allow for the determination of locations with high soil moisture accumulation and infiltration potential, which are unique to foothills [27, 28]. The study area's TWI ranged from 4.03 to 18.06 (Figure 3d). The results were divided into five groups; 4.03 – 7.60, 7.61 – 9.58, 9.59 – 10.96, 10.97 – 12.78, and 12.79 – 18.06. The regions having high TWI are assigned to high ranks and weights, and vice versa.

4.5 Geology

The geology map of the study area is shown in Figure 4a. Sandstones and clays of recent to sub-recent and Tertiary age are among the porous formations. Alluvial formations, which mostly consist of sands, clays, and gravels, are limited to major drainage channels. The gneiss is a metamorphic rock created by high pressure and temperature acting on sedimentary and igneous rocks. Crystalline formations sorely missing primary porosity have different water-bearing properties depending on the degree of secondary intergranular porosity development. The availability and movement of groundwater in crystalline rocks are mainly limited. Even within short distances, these aquifers are very varied in nature due to huge variations in sub-surface lithology, soil texture, fold, fault, and joint features. At deeper levels, groundwater is found in unconfined conditions in the weathered portion and in semiconfined circumstances in the fractured regions [29].

4.6 Lineament density

The study region has a smaller number of lineaments. Figure 4b shows the lineament density map with values ranging from 0 to 0.72 km/km². It was then divided into five. These classes have been assigned to very good (0.44 – 0.72 km/km²), good (0.32 – 0.43 km/km²), moderate (0.20 – 0.0.31 km/km²), poor (0.08-0.19 km/km²), and very poor (0 - 0.07 /km²) respectively. It shows that high lineament density can be found in the north, center, and western parts of the study area. Lineament density is ranked according to the distance between lineaments. For high-density groups, a high rank is assigned, while for low-density classes, a low weight is assigned.

Figure 3. (a) Slope map derived from SRTM DEM data; **(b)** Drainage density; **(c)** Roughness map; **(d)** Topographic Wetness Index map of the study region

4.7 Geomorphology

The various geomorphological features namely pediment, hills and plateaus, structural hills, valleys, alluvial plain, sedimentary high ground, Denudational hills, flood plain, deflection slope, and bajada (Figure 4c) are formed in the study area. The study area comprises mostly of the pediment (76%) followed by Sedimentary high ground (10%), Flood plain (5%), and deflection slope (5%), and the remaining features are covered very less area.
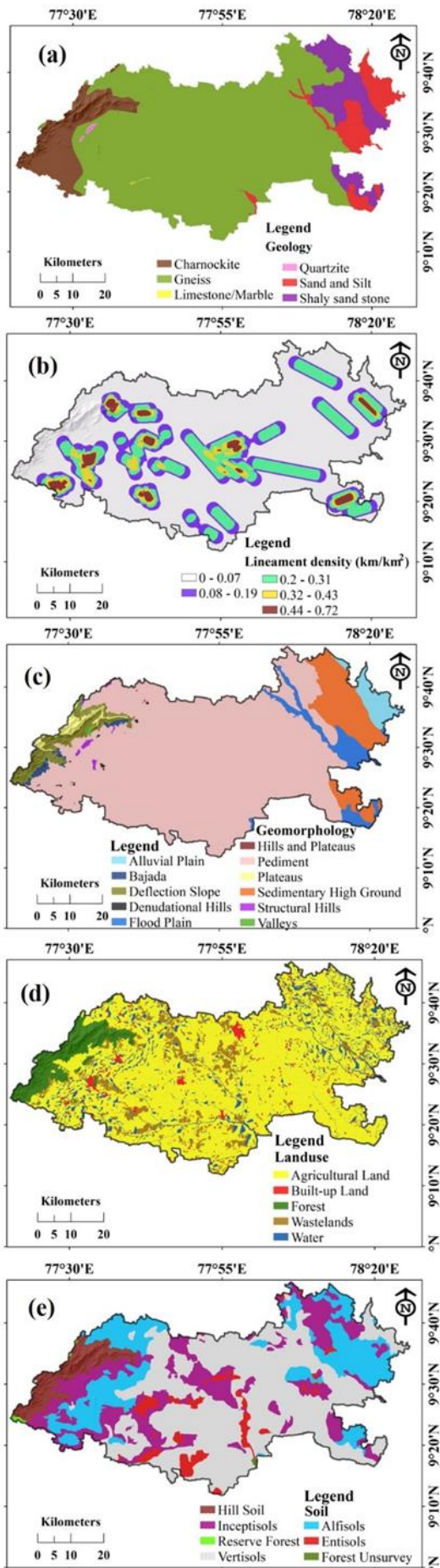
4.8 Land use

The change in land uses significantly influences the dynamics of groundwater recharge and storage. The land use map is divided into agricultural land, built-up land, forest, wasteland, and water bodies (Figure 4d). Higher percentage of 75% of land in this district is covered by agricultural land. The crops grown are horticulture crops that are fruits crops like mango, banana, and guava, vegetables like tomato, brinjal, chilies, and onion, and spices like coriander. The water bodies and wasteland encompass each 8 % of the area. The built-up land and forest cover 3 % and 6.5 % of the area respectively.

4.9 Soil

The characteristics of soil play a major role in the control of groundwater recharge. Figure 4e represents the various soil groups. The different types of soil found in this study area are vertisols, inceptisols, alfisols, reserve forest, entisols, hill soil, and forest unsurvey. Vertisols cover 48 %, inceptisols cover 21 %, reserve forest covers 0.2 %, alfisols cover 20 %, entisols cover 4.3 %, hill soils cover 6 %, and forest unsurvey cover a very low portion of 0.09 % of the total area. Entisols and inceptisols were given higher rankings. Vertisols and alfisols are assigned a moderate ranking since they include a large amount of clay and expansive clay. Hill soils and reserve forest soils are given a low rank, indicating that they receive less groundwater recharge than other soils.

4.10 Manual method to delineate GWPZ

Weightage is assigned to each of these parameters using a manual method and different levels within the parameters are ranked according to the influence they have over groundwater potential. The delineated GWPZ by the manual method is shown in Figure 5a. GWPZ was classified into four i.e., low potential, moderate potential, high potential, and very high potential. The results revealed that 2837.31 km² of the area covers moderate potential which is 68.76 %, high potential covers 1231.06 km² (29.84 %), low potential covers 35.69 km² (0.87 %), and very high potential covers 22.17 km² (0.54 %) of the total area.

Figure 4. (a) Geology map; **(b)** Lineament density map; **(c)** Geomorphology map**; (d)** Land use map; **(e)** Soil map of the study area

4.11 AHP method to delineate the GWPZ

The parameters namely geology, geomorphology, lineament, drainage, land use, soil, and slope are comprehended in the ArcGIS platform and a groundwater potential zone map is prepared which is illustrated in Figure 5b. Four different classes such as 'less potential', 'moderate potential', 'high potential', and 'very high potential' are classified. The 'less potential' zones within the study area are spread randomly it covers over 70.45 km² which covers over 1.71% of the overall area, Low potential areas are not suitable for industrial and urban development. However, 'moderate potential' zones have the highest area coverage of 2139.83 km² which makes around 51.86% of the overall area spread almost all over Virudhunagar district. And 'high potential' zone has the second most area coverage with 1885.09 km² which is a 45.70% of the overall area. And 'Very high' zones are the least with 30.01 km² which is 0.73 % of the overall area.
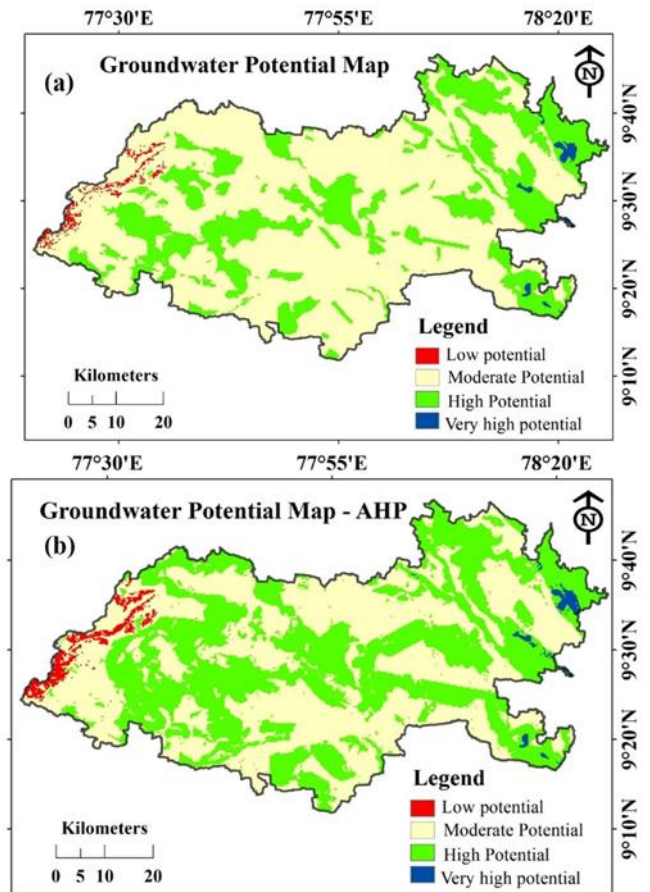
Figure 5. Groundwater potential map prepared by using **(a)** manual method; **(b)** AHP method

5. Discussion

The result of GWPZ created through manual and AHP methods are discussed in this section. Initially, the effects of each sub-layers of all the parameters related to groundwater recharge are explained here. The highly rough topographical regions may have a thin layer of weathered soil which shows less recharge of water to the ground. The regions where the weathered soil is thick

have good groundwater recharge. High roughness equates to a lot of undulation. High-undulation regions are usually mountainous, with continuous weathering and erosion processes causing destruction on the terrain. The groundwater recharge rate is high in the low drainage density regions and vice versa.

TWI-rich areas allow for the determination of locations with high soil moisture accumulation and infiltration potential. A pediment is a gradually sloping surface created between the hill and the plain surface. These have a low potential for groundwater. Structural hills, denudational hills, hills, and plateaus features are covered in very small areas on the western side the groundwater potential is low. The groundwater source is moderate in Bajada. Flood plains, valleys, and alluvial plains percolated a good amount of water into the ground which has a good source of groundwater potential. Agricultural lands are considered to be high groundwater prospecting locations. The groundwater potential in forest areas was rated as low because despite the fact that these areas have good sources of groundwater. Entisols and inceptisols soil have more porosity which recharges high amounts of water. Vertisols and alfisols soil make moderate levels of recharge of water.

The very low potential is located in the western side of the area which is formed by Charnokite rock, low surface roughness, very low TWI, deflection slope of landform, forest type of land use, very low percentage of lineament density, and hill soil. Moderate groundwater potential encompasses of about more than 50 % of the total area, ie. 68.76 % shown in the manual and 51.86 % shown in the AHP method. High groundwater potential covers mostly in central, east, and northeastern sides of the study area. The high groundwater potential derived in the AHP method is greater than the manual method, which shows the GWPZ is determined more accurately by considering each sub-layers of all the parameters in AHP. Very high groundwater potential covers almost less than 1 % of the total area, i.e., 0.54 % in manual and 0.73 % in the AHP method. The AHP method result shows more area covers high groundwater potential which means these locations are suitable for urbanization. Proper sustainable plans and regulations must be put in place so that the available potential doesn't get overexploited.

6. Validation of groundwater potential zones

The groundwater potential thus obtained through AHP and the manual method was cross verified with pre-monsoon and post-monsoon groundwater heads (Figure 6). Around seven wells located in low (well No. 11), moderate (well No. (1,17,22), high (well No. 5, 6) and very high (well No. 13, 21) GWPZ were selected to represent the groundwater head. The plotted groundwater head clearly shows that wells located in low and moderate zones have very deep groundwater, and the fluctuation between pre-monsoon and post-monsoon is very small. The wells located in the high and very high GWPZ are recharged with more water, hence, the groundwater is available at a lower depth with more fluctuation, which means more water infiltrates after

rainfall. Well number 5 is located in the moderate zone in the manual method of determination, and it is located in the high GWPZ in the determination of AHP. The groundwater head at well no. 5 shows less depth below ground level, which clearly shows that the AHP method of delineating groundwater potential zones is more accurate than the manual method.
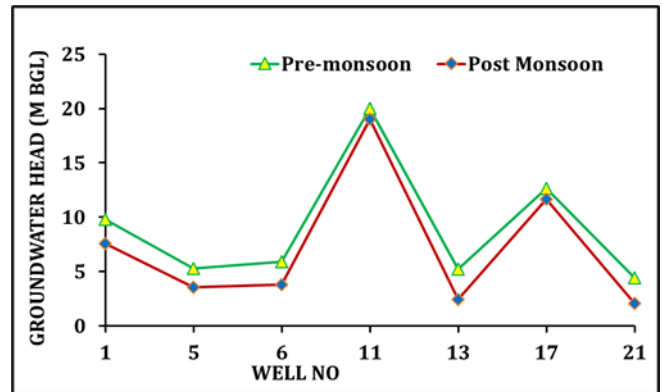

Figure 6. Groundwater head during pre- and post-monsoon

6. Conclusion

This study used the integrated approach of RS, GIS, and AHP for the delineation of GWPZ in the Virudhunagar district. As this district is a rapidly developing district, it is necessary to find regions having good groundwater resources. Nine different parameters of Slope, geology, drainage density, roughness, topographic wetness index, geomorphology, land use, lineament density, and soil were used to carry out weighted overlay analysis. In both, the method of GWPZ delineation results shows that more than 50 % of the land has moderate potential and less than 1 % of very high groundwater potential. There is a huge difference in the area of high groundwater potential determined by manual and AHP methods. AHP result is more accurate than the manual because it includes rank and weights for each sub-layers. The identification of groundwater potentiality zones for predicting built-up area development sites around the Virudhunagar district was emphasized in this study. The findings of this study will support the Virudhunagar municipality in the sustainable management of its water resources, including regional land use planning, future bore well construction, and groundwater protection.

Author contributions

Sundara Pandian Rajaveni: Conceptualization, Methodology, Analysis in Software, Writing-Original draft preparation; **Udayakumar Sidesh**: Data collection, Analysis in Software, Writing, Validation, Field study; **Kalyana Kumar Prasanna Balaji**: Writing-Reviewing and Editing, Data collection, Field work; **Ramabalan Lakshmi Narayanan**: Writing, Editing, Data collection, and Field work.

Conflicts of interest

The authors declare no conflicts of interest.

References

1. Foster, S., Chilton, J., Nijsten, G. J., & Richts, A. (2013). Groundwater—a global focus on the 'local resource'. *Current opinion in environmental sustainability*, *5*(6), 685-695.
2. Carmon, N., & Shamir, U. (2010). Water-sensitive planning: integrating water considerations into urban and regional planning. *Water and Environment Journal*, *24*(3), 181-191.
3. Yağmur, N., Tanık, A., Tuzcu, A., Musaoğlu, N., Erten, E., & Bilgilioglu, B. (2020). Oppurtunities provided by remote sensing data for watershed management: Example of konya closed basin. *International Journal of Engineering and Geosciences*, *5*(3), 120-129.
4. Saaty, T.L. (1980) The Analytic Hierarchy Process: Planning, Priority Setting, Resources Allocation; McGraw: New York, NY, USA, ISBN 978-0070543713.
5. Sajil Kumar, P. J., Elango, L., & Schneider, M. (2022). GIS and AHP based groundwater potential zones delineation in Chennai River Basin (CRB), India. *Sustainability*, *14*(3), 1830.
6. Uc Castillo, J. L., Martínez Cruz, D. A., Ramos Leal, J. A., Tuxpan Vargas, J., Rodríguez Tapia, S. A., & Marín Celestino, A. E. (2022). Delineation of groundwater potential zones (GWPZs) in a semi-arid basin through remote sensing, GIS, and AHP approaches. *Water*, *14*(13), 2138.
7. Maity, B., Mallick, S. K., Das, P., & Rudra, S. (2022). Comparative analysis of groundwater potentiality zone using fuzzy AHP, frequency ratio and Bayesian weights of evidence methods. *Applied Water Science*, *12*(4), 63.
8. Raihan, A. T., Bauer, S., & Mukhopadhaya, S. (2022). An AHP based approach to forecast groundwater level at potential recharge zones of Uckermark District, Brandenburg, Germany. *Scientific Reports*, *12*(1), 6365.
9. Polat, Z. A., Alkan, M., & Sürmeneli, H. G. (2017). Determining strategies for the cadastre 2034 vision using an AHP-Based SWOT analysis: A case study for the turkish cadastral and land administration system. *Land use policy*, *67*, 151-166.
10. Arulbalaji, P. & Gurugnanam, B. (2016) An Integrated Study to Assess the Groundwater Potential Zone Using Geospatial Tool in Salem District, South India, Journal of Hydrogeology & Hydrologic Engineering, 5(2), 1-7
11. Arulbalaji, P., Padmalal, D., & Sreelash, K. (2019). GIS and AHP techniques-based delineation of groundwater potential zones: a case study from southern Western Ghats, India. *Scientific reports*, *9*(1), 2082.
12. Hojati, M., & Mokarram, M. (2016). Determination of a topographic wetness index using high resolution digital elevation models. *European Journal of Geography*, *7*(4), 41-52.
13. Pourali, S. H., Arrowsmith, C., Chrisman, N., Matkan, A. A., & Mitchell, D. (2016). Topography wetness index application in flood-risk-based land use planning. *Applied Spatial Analysis and Policy*, *9*, 39-54.
14. Aghayev, A. (2018). Determining of different inundated land use in Salyan plain during 2010 the Kura River flood through GIS and remote sensing tools. *International Journal of Engineering and Geosciences*, *3*(3), 80-86.
15. Lone, M. S., Nagaraju, D., Mahadavesamy, G., & Siddalingamurthy, S. (2013). Applications of GIS and remote sensing to delineate artificial recharge zones (DARZ) of groundwater in HD Kote taluk, Mysore district, Karnataka, India. *International Journal of Remote Sensing and Geosciences*, *2*(3), 92-97.
16. Lillesand, T., Kiefer, R. W., & Chipman, J. (2007) Remote Sensing and Image Interpretation, Wiley, Hoboken.
17. Ibrahim-Bathis, K., & Ahmed, S. A. (2016). Geospatial technology for delineating groundwater potential zones in Doddahalla watershed of Chitradurga district, India. *The Egyptian Journal of Remote Sensing and Space Science*, *19*(2), 223-234.
18. Rahmati, O., Nazari Samani, A., Mahdavi, M., Pourghasemi, H. R., & Zeinivand, H. (2015). Groundwater potential mapping at Kurdistan region of Iran using analytic hierarchy process and GIS. *Arabian Journal of Geosciences*, *8*, 7059-7071.
19. Saaty, T. L. (1990) Decision making for leaders: the analytic hierarchy process for decisions in a complex world (RWS publications).
20. Magesh, N. S., Chandrasekar, N., & Soundranayagam, J. P. (2011). Morphometric evaluation of Papanasam and Manimuthar watersheds, parts of Western Ghats, Tirunelveli district, Tamil Nadu, India: a GIS approach. *Environmental Earth Sciences*, *64*, 373-381.
21. Yeh, H. F., Lee, C. H., Hsu, K. C., & Chang, P. H. (2009). GIS for the assessment of the groundwater recharge potential zone. *Environmental geology*, *58*, 185-195.
22. Das, S. (2017). Delineation of groundwater potential zone in hard rock terrain in Gangajalghati block, Bankura district, India using remote sensing and GIS techniques. *Modeling Earth Systems and Environment*, *3*(4), 1589-1599.
23. Khorrami, B., & Kamran, K. V. (2022). A fuzzy multi-criteria decision-making approach for the assessment of forest health applying hyper spectral imageries: A case study from Ramsar forest, North of Iran. *International Journal of Engineering and Geosciences*, *7*(3), 214-220.
24. Kumar, M. G., Agarwal, A. K., & Bali, R. (2008). Delineation of potential sites for water harvesting structures using remote sensing and GIS. *Journal of the Indian Society of Remote Sensing*, *36*, 323-334.
25. Jaiswal, R. K., Mukherjee, S., Krishnamurthy, J., & Saxena, R. (2003). Role of remote sensing and GIS techniques for generation of groundwater prospect zones towards rural development--an approach. *International Journal of Remote Sensing*, *24*(5), 993-1008.
26. Krishnamurthy, J., Venkatesa Kumar, N., Jayaraman, V., & Manivel, M. (1996). An approach to demarcate ground water potential zones through remote sensing and a geographical information system. *International journal of Remote sensing*, *17*(10), 1867-1884.

27. Altunel, A. O. (2023). The effect of DEM resolution on topographic wetness index calculation and visualization: An insight to the hidden danger unraveled in Bozkurt in August, 2021. *International Journal of Engineering and Geosciences*, *8*(2), 165-172.

28. Pourali, S. H., Arrowsmith, C., Chrisman, N., Matkan, A. A., & Mitchell, D. (2016). Topography wetness index application in flood-risk-based land use planning. *Applied Spatial Analysis and Policy*, *9*, 39-54.

29. Rajaveni, S. P., Brindha, K., & Elango, L. (2017). Geological and geomorphological controls on groundwater occurrence in a hard rock region. *Applied water science*, *7*, 1377-1389.